

# Amplitude analysis of $\Lambda_c^+ \rightarrow pK^-\pi^+$ decays from semileptonic production

L. Henry<sup>1,2</sup>, D. Marangotto<sup>2</sup>, F. Martinez Vidal<sup>1</sup>, A. Merli<sup>2</sup>, N. Neri<sup>2</sup>, J. Ruiz Vidal<sup>1</sup>.

<sup>1</sup> IFIC and Universitat de València-CSIC, Spain

<sup>2</sup> INFN and Università degli Studi di Milano, Italy

## Abstract

The full 5-dimensional phase space amplitude analysis of the  $\Lambda_c^+ \rightarrow pK^-\pi^+$  decay is performed. The simultaneous determination of an amplitude model of the decay and the measurement of the  $\Lambda_c^+$  polarisation vector is obtained. The  $\Lambda_c^+$  polarisation is measured in two  $\Lambda_c^+$  helicity systems, with orthogonal polarisation components determined from the muon momentum: one reached from the laboratory system and the second from an approximate beauty hadron rest frame. The  $\Lambda_c^+ \rightarrow pK^-\pi^+$  decays from beauty hadron semileptonic decays are selected from the 2016  $pp$  collision sample, with very small background contamination. A fit dataset of 400'000 candidates, corresponding to  $\approx 0.5 \text{ fb}^{-1}$  integrated luminosity is employed. The precision of almost all the measured quantities are limited by systematic uncertainties.



# 1 Contents

2	Document history	4
3	1 Introduction	6
4	1.1 Motivation . . . . .	6
5	1.2 Analysis strategy . . . . .	7
6	1.3 Analysis preservation . . . . .	7
7	2 Data and simulation samples	8
8	2.1 Selection and invariant mass fit . . . . .	8
9	2.2 Choice of the fit dataset . . . . .	12
10	2.3 Misidentified backgrounds . . . . .	13
11	2.4 Data/MC comparison and simulation weighting . . . . .	16
12	3 The helicity formalism for baryon amplitude analyses and polarisation measurements	32
13	3.1 Helicity amplitudes . . . . .	32
14	3.2 Differential decay rate and extraction of the decaying particle polarisation	33
15	3.3 Properties of the polarised decay rate . . . . .	34
16	4 The $\Lambda_c^+ \rightarrow pK^-\pi^+$ amplitude model	36
17	4.1 $\Lambda_c^+$ baryon polarisation system . . . . .	36
18	4.2 Three-body decay phase space . . . . .	37
19	4.3 Combination of $CP$ -conjugated events . . . . .	39
20	4.4 Amplitude model for the $\Lambda_c^+ \rightarrow pK^-\pi^+$ decay . . . . .	40
21	4.4.1 Model with Dalitz-plot decomposition . . . . .	40
22	4.4.2 Model without Dalitz-plot decomposition . . . . .	43
23	4.5 Polarised decay rate . . . . .	45
24	4.6 Relation between amplitude model determination and polarisation mea-	
25	surement . . . . .	46
26	5 Test and comparison of amplitude models written with different proton spin matching methods	46
27	5.1 Interference patterns over the Dalitz plot . . . . .	52
28	6 Amplitude fit	59
29	6.1 Maximum-likelihood fit . . . . .	59
30	6.2 Code . . . . .	60
31	6.3 Fit strategy . . . . .	60
32	6.4 Fit quality . . . . .	62
33	6.5 Resonance lineshapes . . . . .	63
34	6.6 Efficiency and background parametrisation . . . . .	65
35	6.7 Amplitude model building . . . . .	70
36	6.8 Definition of the amplitude fit parameters . . . . .	73
37	6.8.1 Resonances . . . . .	73
38	6.8.2 Lineshape parameters . . . . .	73
39	6.8.3 Helicity couplings . . . . .	73

42	6.8.4	Polarisation components . . . . .	74
43	6.9	Nominal amplitude fit results . . . . .	74
44	6.10	Resolution effects . . . . .	82
45	<b>7</b>	<b>Systematic uncertainties</b>	<b>87</b>
46	7.1	Amplitude model choice . . . . .	87
47	7.1.1	Breit-Wigner parameters for $K^*(892)$ , $\Lambda(1670)$ , $\Lambda(1690)$ , $\Delta(1232)$ contributions . . . . .	87
48	7.1.2	Breit-Wigner parameters for broad $\Lambda(1600)$ , $\Delta^{++}(1600)$ and $\Delta^{++}(1700)$ contributions . . . . .	87
49	7.1.3	$\Lambda(1405)$ widths . . . . .	88
50	7.1.4	$\Lambda(1800)$ contribution . . . . .	88
51	7.1.5	$\Lambda(1810)$ contribution . . . . .	88
52	7.1.6	$\Delta^{++}(1620)$ contribution . . . . .	89
53	7.1.7	Relativistic Breit-Wigner for $K_0^*(700)$ . . . . .	89
54	7.1.8	$K_0^*(700)$ parameters . . . . .	89
55	7.1.9	$K^*(1410)$ contribution . . . . .	89
56	7.1.10	Relativistic Breit-Wigner for $K_0^*(1430)$ . . . . .	89
57	7.1.11	$K_0^*(1430)$ width . . . . .	90
58	7.1.12	Overall exponential form factor for Bugg lineshape . . . . .	90
59	7.1.13	$\Lambda_c^+ d$ radial parameter . . . . .	90
60	7.1.14	$\Lambda_c^+ \rightarrow Rh$ decay orbital angular momentum . . . . .	90
61	7.2	Other amplitude models not considered for evaluating systematic uncertainties	90
62	7.2.1	“PDG extended” model . . . . .	90
63	7.2.2	$\Lambda(1890)$ contribution . . . . .	92
64	7.2.3	$\Lambda(2000)$ spin-parity assignment . . . . .	92
65	7.2.4	Addition of $\Sigma^*$ states . . . . .	92
66	7.2.5	Removal of resonance barrier factors . . . . .	93
67	7.2.6	$K\eta$ , $K\eta'$ decay channel widths in Bugg lineshape . . . . .	93
68	7.2.7	$K^*$ spin zero as a single contribution . . . . .	93
69	7.2.8	Pole model for $K_0^*(700)$ state . . . . .	93
70	7.2.9	Flatté lineshape for $K_0^*(1430)$ state . . . . .	93
71	7.2.10	$K_0^*(1430)$ floating mass . . . . .	93
72	7.2.11	Change of $\Lambda_c^+ \rightarrow Rh$ decay orbital angular momentum assignment	94
73	7.3	Background contribution . . . . .	94
74	7.4	Simulation weighting . . . . .	94
75	7.5	PID . . . . .	94
76	7.6	Fit bias and finite MC integration statistics . . . . .	95
77	7.7	Summary of systematic uncertainties . . . . .	95
78	<b>8</b>	<b>Cross-checks</b>	<b>100</b>
79	8.1	MagDown data sample . . . . .	100
80	8.2	MagUp data sample . . . . .	100
81	8.3	$\Lambda_c^+$ -only data sample . . . . .	100
82	8.4	$\Lambda_c^-$ -only data sample . . . . .	100
83	8.5	Polarisation in $\Lambda_b^0$ rest frame from “Full reconstruction” algorithm . . . . .	101
84	8.6	Polarisation in $\Lambda_b^0$ rest frame from “Equal boost” algorithm . . . . .	101

87	8.7 Data split according to $\Lambda_c^+$ transverse momentum . . . . .	101
88	8.8 Data split according to $\Lambda_c^+$ lifetime . . . . .	102
89	<b>9 Final results</b>	<b>103</b>
90	9.1 Interpretation of the measured $\Lambda_c^+$ polarisation . . . . .	108
91	<b>A ReDecay faster simulation validation</b>	<b>112</b>
92	<b>B Additional misidentified background plots</b>	<b>115</b>
93	<b>C Rotation of reference frames</b>	<b>117</b>
94	<b>D Cross-checks fit results</b>	<b>119</b>
95	<b>References</b>	<b>148</b>

## 96 Document history

- 97     ● v0: Version for first WG reading
- 98     - Analysis up to first full phase space fits with correct amplitude model, showing quite  
99       good quality. Impact of background, data/MC discrepancies checked to be small,  
100      not included in amplitude fits. Red text: highlighted ongoing/planned work towards  
101      analysis completion.
- 102     x r1: Added simulation weighting, efficiency and background parametrisation, more  
103       detailed plan to evaluate systematic uncertainties and cross-checks, more amplitude  
104       model tests
- 105     x r2: Extended data/simulation comparison to more variables
- 106     ● v1: First “complete” version
- 107     - Added alternative invariant mass fit with signal shape fixed from simulation and  
108       estimation of signal “contamination” in background sidebands. More plots for  
109       misidentified background study and data/simulation comparison. New simulation  
110       weighting targeting  $\Lambda_c^+$  kinematics. Studies on resolution effects. Approximate  
111       reconstruction algorithms for  $\Lambda_b^0$  rest frame. Relation between  $\Lambda_c^+$  polarisation and  
112       time-reversal. Updated test and comparison of spin matching methods, equivalence  
113       with the Dalitz-plot decomposition method. Determination of nominal amplitude  
114       model, with different polarisation frames. Systematic uncertainties, cross-checks  
115       and final results.
- 116     x r1: Tried inclusion of  $\Sigma^*$  states. Updated comparison of cross-check results with  $\chi^2$   
117       test. Tested variation of mass and width parameters for  $K^*(892)$ ,  $\Lambda(1670)$ ,  $\Lambda(1690)$ ,  
118        $\Delta(1232)$  contributions. Tested RBW lineshape for  $K_0^*(1430)$ , removal of  $K_0^*(700)$ .  
119       Cross-checks splitting data according to  $\Lambda_c^+ p_T$  and  $\Lambda_c^+$  lifetime. Tried changing  
120       orbital angular momentum assignment for  $\Lambda_c^+ \rightarrow Rh$  decays. Added interference  
121       effects plot.
- 122     ● v2: Version for RC, after WG review
- 123     - Added justification for limited fit dataset, new subsection “analysis strategy”. Added  
124       analysis preservation information. Effects of orbital angular momentum added to  
125       systematic uncertainties, checked with LS couplings. Added relation between effective  
126        $\alpha$  parameters and effective ones. Added results and systematic uncertainties for  $\Lambda_c^+$   
127       polarisation measured in “Equal boost” approximate  $\Lambda_b^0$  rest frame.
- 128     x r1: Added more momentum asymmetry plots for physical background search. Added  
129       Dalitz plot comparison between entire 2016 datasample and amplitude model, Fig. 44.  
130       Minor rewording.
- 131     ● v3: Version after major changes requested during RC review and last WG comments
- 132     - Updated amplitude analysis with new parametrisation of the  $K\pi$  spectrum (using  
133       Bugg parametrisation instead of LASS one), increase of fit statistics (from 100k to  
134       400k), and mixing of baryon charge and polarities: includes update of amplitude

model, systematic uncertainty evaluation and cross-checks. Updated justification for limited fit dataset. Added Sec. 4.6 on relation between amplitude model determination and polarisation measurement. Added Sec. 5.1 with interference patterns for toy amplitude model. Added LS couplings fit results. Quoting decay asymmetry parameters computed from helicity couplings for single two-body contributions, effective decay asymmetry parameter reported only for the  $\Lambda_c^+ \rightarrow pK^-\pi^+$  model.

- x r1: Moved definition of amplitude model parameters from appendix to Sec. 6. Split total systematic uncertainty between amplitude model choice component and the other contributions. Added Sec. 9.1 with the simulation study for the interpretation of the measured  $\Lambda_c^+$  polarisation. Renamed the effective three-body  $\alpha$  parameter throughout the note to avoid confusion with usual definition of decay asymmetry parameters. Integrated introduction part, following paper draft.

# <sup>147</sup> 1 Introduction

## <sup>148</sup> 1.1 Motivation

<sup>149</sup> The weak, charged-current, Cabibbo favoured  $\Lambda_c^+ \rightarrow pK^-\pi^+$  decay is the most abundant  
<sup>150</sup> decay mode of the  $\Lambda_c^+$  baryon, with a branching fraction of  $(6.35 \pm 0.33)\%$  [1], making  
<sup>151</sup> it the most suited channel to study the  $\Lambda_c^+$  baryon properties with the best statistical  
<sup>152</sup> precision. Indeed, two-body decays like  $\Lambda_c^+ \rightarrow pK_S^0$  or  $\Lambda_c^+ \rightarrow \Lambda\pi^+$ , which are characterised  
<sup>153</sup> by simple angular distributions, feature lower branching fractions  $\lesssim 1\%$  and reduced  
<sup>154</sup> detector efficiencies for the presence of strange particles with lifetimes of order  $10^{-10}$  s.  
<sup>155</sup> The latter is particularly relevant for fixed-target experiments where the large Lorentz  
<sup>156</sup> boost increases the typical strange particle flight distances.

<sup>157</sup> Nonetheless, the  $\Lambda_c^+ \rightarrow pK^-\pi^+$  decay structure is very poorly known, the only  
<sup>158</sup> amplitude analysis of  $\Lambda_c^+ \rightarrow pK^-\pi^+$  decays was performed by the E791 experiment at  
<sup>159</sup> Fermilab on a data sample of  $\approx 1000$  events only [2]; moreover the amplitude model  
<sup>160</sup> employed in that analysis missed the matching of proton spin states among different decay  
<sup>161</sup> chains. The LHCb experiment has recorded millions of  $\Lambda_c^+ \rightarrow pK^-\pi^+$  events, allowing  
<sup>162</sup> to perform detailed studies of the intermediate resonances contributing to the decay. By  
<sup>163</sup> including the  $\Lambda_c^+ \rightarrow pK^-\pi^+$  decay plane orientation in the amplitude analysis it is also  
<sup>164</sup> possible to measure the full polarization vector of the  $\Lambda_c^+$  baryon. The analytical study of  
<sup>165</sup> the  $\Lambda_c^+ \rightarrow pK^-\pi^+$  decay rate shows that the full phase space amplitude analysis of this  
<sup>166</sup> decay is able to measure simultaneously helicity amplitudes (real and imaginary parts of  
<sup>167</sup> the helicity couplings) and the polarization vector [3].

<sup>168</sup> The interest in the measurement of the  $\Lambda_c^+ \rightarrow pK^-\pi^+$  decay amplitudes and polarisation  
<sup>169</sup> ranges from New Physics searches to low-energy QCD studies. The amplitude analysis  
<sup>170</sup> of the  $\Lambda_c^+ \rightarrow pK^-\pi^+$  decay allows to study parity-violation, *e.g.* measuring the unknown  
<sup>171</sup> decay asymmetry parameters  $\alpha$  relating the  $\Lambda_c^+$  polarization to the quasi two-body decay  
<sup>172</sup> distribution of the intermediate resonances. Knowledge of the decay structure is also  
<sup>173</sup> useful for performing localized  $CP$ -violation searches in the decay phase space. These can  
<sup>174</sup> be carried out in a model-dependent way by comparing amplitude model fits to baryon  
<sup>175</sup> and antibaryon decays, or in a model-independent way by tailoring the partition of the  
<sup>176</sup> phase space according to the known intermediate resonances to localize and optimize the  
<sup>177</sup> sensitivity to  $CP$ -violation [4].

<sup>178</sup> The knowledge of the  $\Lambda_c^+ \rightarrow pK^-\pi^+$  decay amplitude increases the sensitivity to  
<sup>179</sup> possible beyond the Standard Model physics contributions in  $\Lambda_b^0 \rightarrow \Lambda_c^+ l^- \bar{\nu}_l$  angular  
<sup>180</sup> analyses, strongly motivated by the anomalies seen in  $b \rightarrow cl\nu$  processes but also for  
<sup>181</sup> CKM angles measurement and  $CP$ -violation searches [5–20]. Methods to perform angular  
<sup>182</sup> analyses of semileptonic  $b \rightarrow cl\nu$  processes even at LHCb have been proposed [21–23].

<sup>183</sup> Polarization measurements for  $\Lambda_c^+$  baryons are a fundamental probe for the baryon  
<sup>184</sup> spin structure and its formation process via hadronization of the heavy charm quarks:  
<sup>185</sup> according to heavy quark effective theory most of the  $c$ -quark polarization is expected to  
<sup>186</sup> be retained by the charm baryon, similarly to beauty baryons [24–26]. The measurement  
<sup>187</sup> of the  $\Lambda_c^+$  polarization has been advocated for different baryon production processes:  $\Lambda_b^0$   
<sup>188</sup> semileptonic decays [7, 10, 11, 16, 20, 27, 28], weak interaction vector boson decays [25, 26]  
<sup>189</sup> and strong interactions [25, 29, 30]. Besides the interest for the baryon formation in  
<sup>190</sup> weak decays, the  $\Lambda_c^+$  polarization also constitutes an additional probe for New Physics  
<sup>191</sup> effects, like for the  $b \rightarrow cl\nu$  processes mentioned before. For strong force production, the

baryon polarization is hardly predictable in QCD, being related to its non-perturbative regime, and its measurement provide anchor points to discriminate among low energy QCD models.

The extraction of the  $\Lambda_c^+ \rightarrow pK^-\pi^+$  amplitude model enables different studies related to  $\Lambda_c^+$  polarisation measurements, for instance:  $\Lambda_c^+$  polarization in fixed-target p-Ne SMOG collisions; the measurement of charm baryon electric and magnetic dipole moments using bent crystals via spin precession at LHC(b) [31, 32]; the study of excited  $\Omega_c$  spin and  $\Lambda_c^+ - \bar{\Lambda}_c^-$  correlation studies at BESIII experiment.

## 1.2 Analysis strategy

In the present analysis, the full phase space 5D  $\Lambda_c^+ \rightarrow pK^-\pi^+$  amplitude analysis with extraction of the decaying baryon polarisation is performed, selecting  $\Lambda_c^+$  baryons produced in beauty hadron semileptonic decays. The full Run 2 LHCb datasample allows a statistics of some million events: an amplitude analysis of such a big datasample is very challenging, requiring huge computational resources (for both performing the amplitude fits and generating a sufficiently large simulation sample) and a very precise study of the amplitude model. For the present analysis it has been decided to limit the fit statistics to 400'000 candidates. This value has been fixed after studying the scaling of statistical and systematic uncertainties with the fit statistics: at this level the leading uncertainty, being the systematic uncertainty associated to the amplitude model choice, is observed to not reduce with increasing statistics.

The chosen fit datasample allows to perform the first detailed amplitude analysis of the  $\Lambda_c^+ \rightarrow pK^-\pi^+$  decay, more than two orders of magnitude more than the previous done by E791. Moreover, all the analyses needing a  $\Lambda_c^+ \rightarrow pK^-\pi^+$  amplitude model mentioned before, notably the  $\Lambda_c^+$  polarisation measurement in SMOG collisions, will employ datasets much smaller than the one being used for the present amplitude analysis.

## 1.3 Analysis preservation

- TWiki page: [Lc2pKpiAmplitudeAnalysisSLTagged](#)
- Code Gitlab repository: [Hc2pKpi/Lc2pKpi-SL\\_AmAn](#)
- Data EOS repository: [/eos/lhcb/wg/Charm/Lc2pKpi-SL\\_AmAn](#)

## 2 Data and simulation samples

The real  $\Lambda_c^+ \rightarrow pK^-\pi^+$  data samples from semileptonic  $\Lambda_b^0$  decays are selected from 2015 and 2016  $pp$  collision data recorded by the LHCb experiment by the stripping line `B2DMuNuX_Lc` of the `Semileptonic` stream, versions `Stripping24r1p1` and `Stripping28r1p1` for 2015 and 2016 years, respectively. The stripping selection criteria are listed in Table 1.

Candidates are required to be triggered on signal (TOS) by the `L0Muon`, the `Hlt1TrackMuon` and one of the topological `Hlt2TopoMuNBodyDecision`,  $N = 2, 3, 4$ , trigger lines.

The particles momenta are calibrated using the `TrackScaleState` algorithm (momentum scaling).

The  $\Lambda_c^+ \rightarrow pK^-\pi^+$  phase-space variables are computed applying the kinematic fitter `DecayTreeFitter` [33], performing a refitting of the entire decay chain fixing the reconstructed  $\Lambda_c^+$  invariant mass to the PDG value [1]. No origin vertex constraints are applied.

Two simulation samples are used in the analysis. The first reproduces semileptonic  $\Lambda_b^0$  decays to  $\Lambda_c^+$ , for  $\mu^-$  and  $\tau^-$  leptons (event type 15874000). The  $\Lambda_c^+ \rightarrow pK^-\pi^+$  decay is simulated with a simple decay model including the three main resonances  $\Lambda^*(1520)$ ,  $\Delta^{++}(1232)$ ,  $K^*(892)$  seen in the E791  $\Lambda_c^+ \rightarrow pK^-\pi^+$  amplitude analysis [2] plus a flat phase space component. No interferences among the contributions are simulated. This sample consist of 10 million generated events, of which  $\approx 130$  thousands passing stripping and trigger requirements, and will be referred to as “full simulation”.

A second simulation sample with higher statistics is generated using the faster-simulation option `ReDecay` [34], which reduces by 10 times the CPU consumption by re-using each complete simulated event by generating 100 signal decays which are added to the same rest of the event. This sample reproduces  $\Lambda_c^+ \rightarrow pK^-\pi^+$  flat phase space decays from semileptonic  $\Lambda_b^0 \rightarrow \Lambda_c^+ \mu^- \bar{\nu}_\mu$  events (event type 15574001) and it is used for describing the detector efficiency. Distributions for different physical quantities have been compared between the two simulation samples, to check the assumptions behind the `ReDecay` method are suitable for the detector efficiency studies. The validation plots are reported in Appendix A, in which only flat phase space  $\Lambda_c^+ \rightarrow pK^-\pi^+$  events are selected in the full simulation samples (this is possible using MCDecayTree information because the full simulation sample is an incoherent sum of different contributions). Non-signal events are removed from the simulation samples (truth-matching). The `ReDecay` sample consists of 1452828 events after truth-matching, stripping and trigger requirements.

Both simulation samples were generated with `Sim09c` simulation version with CondDB tag `sim-20170721-2-vc-mu100` and DDDBtag `dddb-20170721-3`.

### 2.1 Selection and invariant mass fit

A tight selection is developed to reduce the combinatorial background contamination to a very small level. A cut-based selection has been studied on real data, its requirements reported in Table 2. The selection has been studied first on 2015 data, then applied to 2016 data checking its performances to be similar; the 2015 data sample used for optimizing the selection is not used for the amplitude analysis that is based on 2016 data. The selection requires  $\Lambda_c^+ \rightarrow pK^-\pi^+$  candidates to have: a limited displacement between  $\Lambda_c^+$  and  $\Lambda_b^0$  vertex  $z$  positions; a  $\Lambda_b^0$  vertex separated from the primary vertex, measured by the logarithm of the flight distance  $\chi^2$ ,  $\log(\text{FD}\chi^2)(\Lambda_b^0)$ ; good particle identification

Particle	Quantity	Cut
$\mu$	min $p_T$	1 GeV
	min $p$	6 GeV
	track ghost probability	< 0.35
	track $\chi^2/\text{ndf}$	< 3
	min primary vertex IP $\chi^2$	9
	min PID $_\mu$	0
	hadron	
	min $p_T$	250 MeV
	track ghost probability	< 0.35
	track $\chi^2/\text{ndf}$	< 3
$K$	min primary vertex IP $\chi^2$	4
	min $p$	2 GeV
	min PID $_K$	-2
	$\pi$	
$\pi$	min $p$	2 GeV
	max PID $_K$	10
	$p$	
	min $p$	8 GeV
$\Lambda_c^+$	min PID $_p$	0
	min PID $_p - \text{PID}_K$	0
	$m(pK\pi)$ interval	$m(\Lambda_c^+)_{\text{PDG}} \pm 80$ MeV
	DOCA $\chi^2$ limit between daughter tracks	20
	max vertex $\chi^2/\text{ndf}$	6.0
	min $\chi^2$ distance from primary vertex	25
	min $\cos(\text{DIRA})$	0.99
	$m(\Lambda_c^+ \mu)$ interval	2.2-8.0 GeV
	DOCA $\chi^2$ limit between daughter tracks	10
	max vertex $\chi^2/\text{ndf}$	9.0
$\Lambda_b^0$	min $\cos(\text{DIRA})$	0.999
	$\Lambda_c^+$ vertex $z$ position - $\Lambda_b^0$ vertex $z$ position	> -2 mm

Table 1: B2DMuNuX\_Lc stripping line selection criteria. DOCA is the distance of closest approach between a pair of tracks; DIRA is the angle between the momentum of the particle and the direction of flight from the best PV to the decay vertex.

responses for proton and kaon hadrons, measured from the neural-network based ProbNN variables. The separation between signal and background distributions for the employed variables, obtained applying the *sPlot* statistical technique [35] to the 2015 data sample, is displayed in Fig. 1. The requirement on the proton identification ProbNN $_p(p)$  is by far the most effective.

To evaluate the amount of combinatorial background passing the selection requirements, its contribution is separated from  $\Lambda_c^+ \rightarrow pK^-\pi^+$  candidates by means of a fit to the  $pK^-\pi^+$  invariant mass distribution. The  $\Lambda_c^+ \rightarrow pK^-\pi^+$  candidates are modelled using two Crystal-Ball (CB) PDFs with asymmetric power-law tails, while the combinatorial background is parametrised by an exponential PDF  $\propto e^{cx}$ . The Crystal Ball PDF is a four-parameter function made of a Gaussian connected with a power-law tail in such a

Quantity	Requirement
$\Lambda_c^+ \text{ vertex } z \text{ position} - \Lambda_b^0 \text{ vertex } z \text{ position}$	< 6 mm
$\log(\text{FD}\chi^2)(\Lambda_b^0)$	> 6.5
$\text{ProbNN}_p(p)$	> 0.95
$\text{ProbNN}_K(K^-)$	> 0.7

Table 2: Selection requirements for  $\Lambda_c^+ \rightarrow p K^- \pi^+$  candidates.

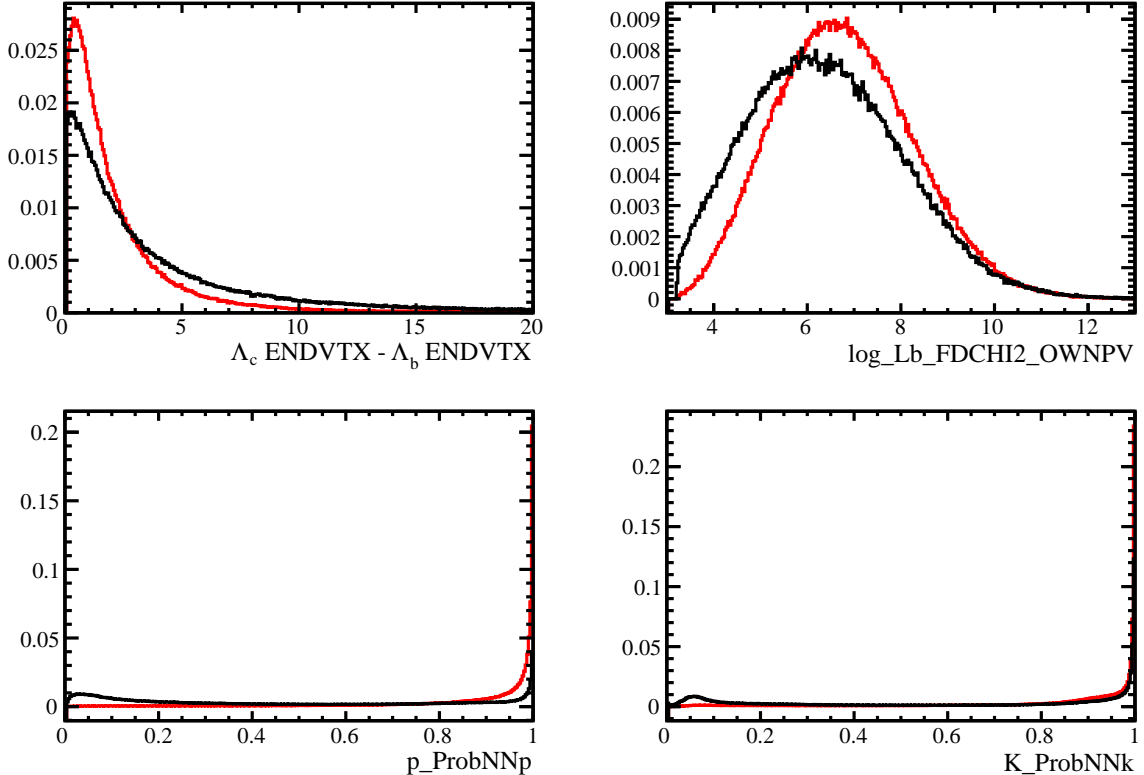


Figure 1: Separation between (red) signal and (black) background s-Weighted normalised distributions of the selection variables for 2015 data.

way to have continuous derivative,

$$CB(x|\bar{x}, \sigma, \alpha, n) = N \begin{cases} \exp\left(\frac{(x-\bar{x})^2}{2\sigma^2}\right) & \text{for } \alpha > 0, \frac{(x-\bar{x})}{\sigma} > -\alpha \\ A \left(B - \frac{(x-\bar{x})}{\sigma}\right)^{-n} & \text{for } \alpha < 0, \frac{(x-\bar{x})}{\sigma} < -\alpha \\ & \text{for } \alpha > 0, \frac{(x-\bar{x})}{\sigma} < -\alpha \\ & \text{for } \alpha < 0, \frac{(x-\bar{x})}{\sigma} > -\alpha \end{cases}, \quad (1)$$

in which  $A = \left(\frac{n}{|\alpha|}\right)^n \exp\left(-\frac{|\alpha|^2}{2}\right)$ ,  $B = \frac{n}{|\alpha|} - |\alpha|$  and  $N$  is the normalisation factor. The two CB PDFs share the same  $\bar{x}$  value and have power-law tails in opposite mass direction.

The fit to the  $pK^-\pi^+$  invariant mass distribution for 2016 data selected candidates is shown in Fig. 2 (log-scale plot in Fig. 3), results reported in Table 3. The selection retains 1.281 millions of  $\Lambda_c^+ \rightarrow pK^-\pi^+$  candidates, reducing the combinatorial background

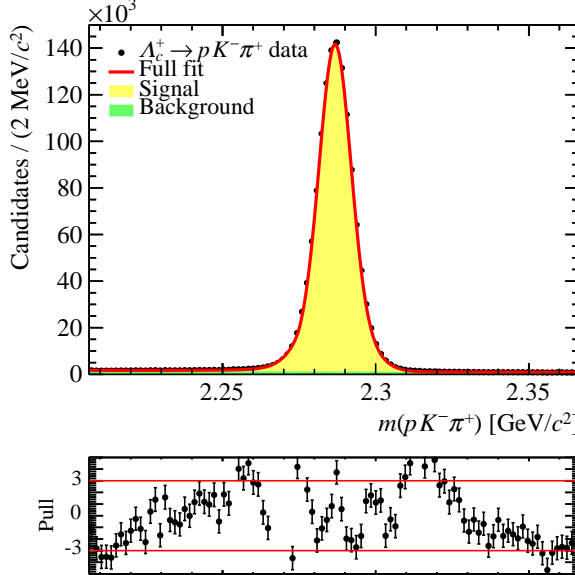


Figure 2: Fit to the  $pK^- \pi^+$  invariant mass of 2016 data selected candidates.

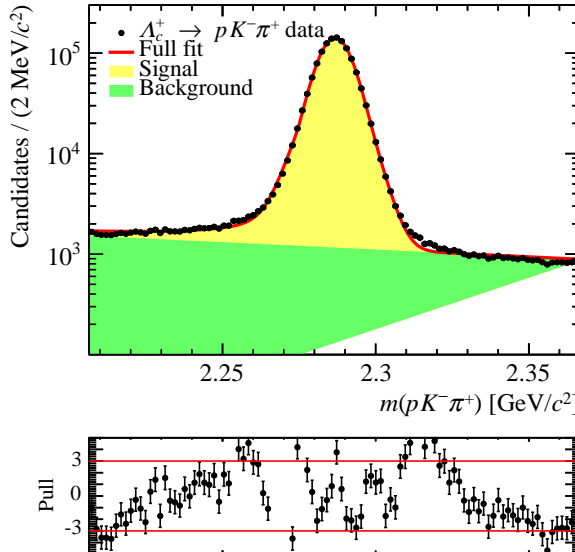


Figure 3: Fit to the  $pK^- \pi^+$  invariant mass of 2016 data selected candidates, in logarithmic scale.

contribution in the signal region chosen as  $|m(pK^- \pi^+) - m(\Lambda_c^+)_{\text{PDG}}| < 15 \text{ MeV}$  to 1.69% of the candidates. Only candidates from this signal region will be employed for the amplitude fits. The signal region contains the 95.1% of the  $\Lambda_c^+ \rightarrow pK^- \pi^+$  signal candidates.

The fit quality is good but for some discrepancies at the signal peak sides. However a precise agreement between data and the effective fit model is almost impossible given the very high number of events, since the fit becomes sensitive to fine details of the invariant mass distribution.

An alternative invariant mass fit is performed first studying the  $\Lambda_c^+ \rightarrow pK^- \pi^+$  invariant

Parameter	Central value $\pm$ Uncertainty
Signal events	$1281200 \pm 1450$
Background events	$117150 \pm 1950$
CB $\bar{x}$ [GeV/ $c^2$ ]	$2.2868 \pm 0.00000280$
CB1 $\sigma$ [MeV/ $c^2$ ]	$4.9518 \pm 0.00388$
CB2 $\sigma$ [MeV/ $c^2$ ]	$8.2588 \pm 0.0340$
CB1 $\alpha$	$2.3119 \pm 0.00212$
CB2 $\alpha$	$-4.7914 \pm 7.51$
CB1 $n$	$1.0774 \pm 0.00364$
CB2 $n$	$15.166 \pm 29.6$
CB1 fraction	$0.67358 \pm 0.000798$
Exp $c$ [(GeV/ $c^2$ ) $^{-1}$ ]	$-3.3642 \pm 0.217$

Table 3: Results of the fit to the  $pK^-\pi^+$  invariant mass of 2016 data selected candidates.

mass shape on simulation. A good fit of simulated events is found exploiting three CB PDFs, two having power-law tails towards lower mass and one towards higher mass directions, Fig. 4. The fitted  $\Lambda_c^+ \rightarrow pK^-\pi^+$  mass shape is introduced in the data mass fit leaving only the overall mass and width of the CB PDF combination as free parameters. The combinatorial background is parametrised this time using a second-order Chebyshev polynomial.

The alternative fit to the  $pK^-\pi^+$  invariant mass distribution for 2016 data selected candidates is shown in Fig. 5 (log-scale plot in Fig. 6), results reported in Table 4. The number of  $\Lambda_c^+ \rightarrow pK^-\pi^+$  candidates is found to be 1.275 millions with a combinatorial background contribution in the signal region of 1.79% of the candidates. The difference in background fraction found between the two fits is at the 0.1% level. The fit quality is similar with respect to the previous fit, with discrepancies probably due to differences in the invariant mass shape between data and simulation.

The alternative fit is used to estimate the signal contribution to the sidebands later employed for background parametrisation. Considering signal sidebands defined as  $|m(pK^-\pi^+) - m(\Lambda_c^+)_\text{PDG}| > 40$  MeV (limited by the stripping requirement  $|m(pK^-\pi^+) - m(\Lambda_c^+)_\text{PDG}| < 80$  MeV) the signal contribution  $S/(S + B)$  is estimated to be 11.9% (5.59%) in the lower (upper) mass sideband. For smaller sidebands  $|m(pK^-\pi^+) - m(\Lambda_c^+)_\text{PDG}| > 60$  MeV the signal contribution is 8.79% (2.93%) in the lower (upper) mass sideband.

The  $\Lambda_c^+ \rightarrow pK^-\pi^+$  phase space one-dimensional projections of 2016 data selected candidates are reported in Fig. 7. The residual background distributions are estimated from the signal sidebands defined as  $|m(pK^-\pi^+) - m(\Lambda_c^+)_\text{PDG}| > 40$  MeV.

## 2.2 Choice of the fit dataset

Following the discussion in Sec. 1.2, the dataset used for the amplitude analysis is limited to 400'000 candidates passing selection, chosen in order to have 100'000 candidates per each baryon charge and magnet polarity category. To select the dataset in a reproducible way, data have been taken between some dates, one interval for each magnet polarity, reported in Table 5.

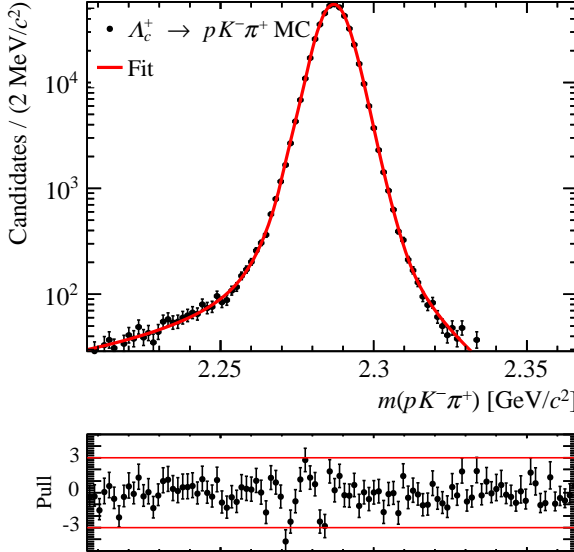


Figure 4: Fit to the  $pK^{-}\pi^{+}$  invariant mass of *ReDecay* simulated events, in logarithmic scale.

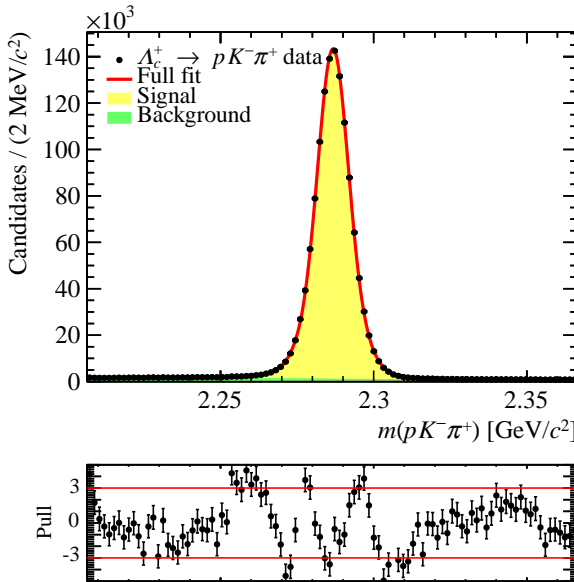


Figure 5: Alternative fit to the  $pK^{-}\pi^{+}$  invariant mass of 2016 data selected candidates.

### 319 2.3 Misidentified backgrounds

320 Three-body hadronic decays of charm hadrons can constitute potential backgrounds  
 321 to the  $\Lambda_c^+ \rightarrow pK^- \pi^+$  decays if some of the final-state hadrons are wrongly identified.  
 322 The Cabibbo-favoured  $D^+ \rightarrow K^+ \pi^- \pi^+$  and  $D_s^+ \rightarrow K^+ K^- \pi^+$  may enter the signal  
 323 region due to a proton mis-identification, while Cabibbo-suppressed  $\Lambda_c^+ \rightarrow pK^- K^+$  and  
 324  $\Lambda_c^+ \rightarrow p\pi^- \pi^+$  may fake signal candidates due to a wrong kaon or pion assignment; also  
 325 possible  $\Xi_c^+ \rightarrow pK^- K^+$  and  $\Xi_c^+ \rightarrow p\pi^- \pi^+$  contributions are searched for. Moreover,  
 326 four-body decays of charm mesons in which one hadron is not reconstructed may contribute  
 327 as well to the  $\Lambda_c^+$  signal region. The presence of these backgrounds is searched for by

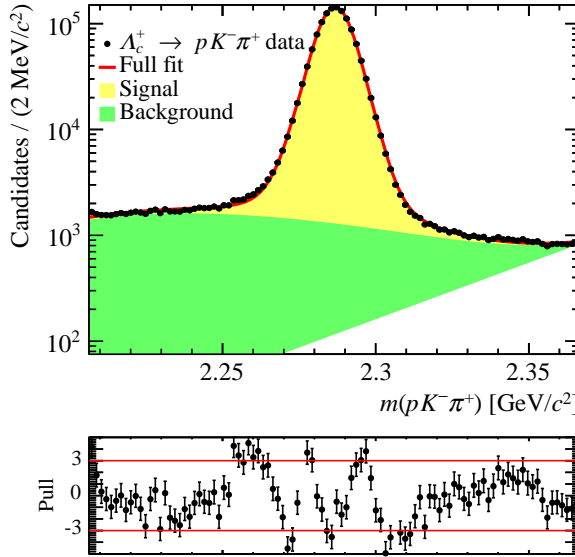


Figure 6: Alternative fit to the  $pK^-\pi^+$  invariant mass of 2016 data selected candidates, in logarithmic scale.

Parameter	Central value $\pm$ Uncertainty
Signal events	$1275100 \pm 1190$
Background events	$123970 \pm 507$
CB $\bar{x}$ [ $\text{GeV}/c^2$ ]	$2.2867 \pm 0.00000560$
CB $\sigma$ [ $\text{MeV}/c^2$ ]	$7.4103 \pm 0.00663$
$c_0$	$-0.33893 \pm 0.00560$
$c_1$ [ $(\text{GeV}/c^2)^{-1}$ ]	$-0.068789 \pm 0.00674$
$c_2$ [ $(\text{GeV}/c^2)^{-2}$ ]	$0.11592 \pm 0.00521$

Table 4: Results of the alternative fit to the  $pK^-\pi^+$  invariant mass of 2016 data selected candidates.  $c_i$  is the coefficient of the  $i$ -th order Chebyshev polynomial.

Magnet Polarity	Initial Run #	Date	Final Run #	Date
Up	178547	27/06/16	179780	13/07/16
Down	182001	18/08/16	183160	09/09/16

Table 5: Time and Run intervals of the data employed as fit dataset.

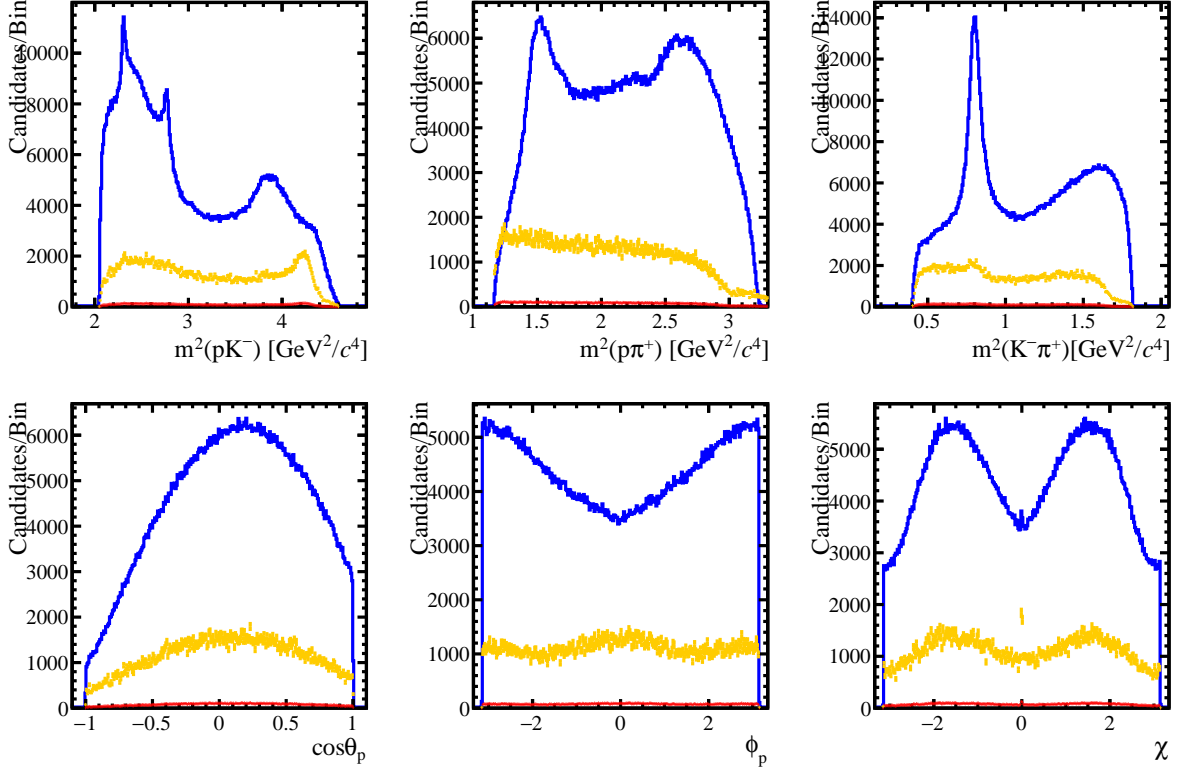


Figure 7: (blue)  $\Lambda_c^+ \rightarrow pK^-\pi^+$  phase space one-dimensional projections of 2016 data selected candidates, in  $|m(pK^-\pi^+) - m(\Lambda_c^+)_\text{PDG}| < 15$  MeV, for angular variables defined in the laboratory  $\Lambda_c^+$  helicity frame (defined in Sec. 4.1). (red) background contribution estimated from the signal sidebands scaled to reproduce the background fraction in the signal region measured in the invariant mass fit: its contribution is very small compared to the signal  $\Lambda_c^+ \rightarrow pK^-\pi^+$  decays. (orange) background contribution magnified by a factor 15.

reconstructing the invariant mass of the three daughter particles with different mass hypothesis plotted versus the  $pK^-\pi^+$  invariant mass. Fig. 8 shows the invariant mass distributions for candidates passing stripping and trigger requirements only, Fig. 9 being the same plot in log scale. Contributions from  $D^+ \rightarrow K^+\pi^-\pi^+$  and  $D_s^+ \rightarrow K^+K^-\pi^+$  decays due to single mis-identifications are visible as horizontal lines corresponding to  $D^+$  and  $D_s^+$  invariant masses, while  $\Lambda_c^+ \rightarrow pK^-K^+$  and  $\Lambda_c^+/\Xi_c^+ \rightarrow p\pi^-\pi^+$  decays do not contribute because outside the range covered by  $\Lambda_c^+ \rightarrow pK^-\pi^+$  candidates (the horizontal band corresponding to the  $\Lambda_c^+$  mass is empty). No  $\Xi_c^+ \rightarrow pK^-K^+$  contributions are found. No broader structures at  $K^+\pi^-\pi^+$  and  $K^+K^-\pi^+$  invariant masses are visible, indicating that there are no partially reconstructed decays present. After application of the selection requirements no evidence of residual physical backgrounds is visible, Fig. 10, log scale plots in Fig. 11. In fact, charm meson decays are effectively rejected by the tight proton PID requirement. One-dimensional invariant mass projections are reported in Appendix B.

A complementary study, which is more sensitive to partially reconstructed backgrounds, is performed by plotting the momentum asymmetries of the  $\Lambda_c^+$  daughters versus the  $pK^-\pi^+$  invariant mass. The three momentum asymmetries  $\beta_h$  for  $h = p, K^-, \pi^+$  hadrons

versus the other two hadrons in the decay  $h_1, h_2$  is defined as

$$\beta_h = \frac{p(h_1) + p(h_2) - p(h)}{p(h_1) + p(h_2) + p(h)}. \quad (2)$$

Along with the  $\Lambda_c^+$  invariant mass under the nominal  $\Lambda_c^+ \rightarrow pK^-\pi^+$  mass assignment, it fully parametrises alternative mass hypotheses in which the assignment of the  $h$  hadron is changed. The  $\beta_h - m(pK^-\pi^+)$  plane therefore provides an additional check. Fig. 12 shows the momentum asymmetry distributions for the three hadrons, for candidates passing stripping and trigger requirements only: sharp bands are visible only for  $\beta_p$ , these corresponding to the already observed  $D^+ \rightarrow K^+\pi^-\pi^+$  and  $D_s^+ \rightarrow K^+K^-\pi^+$  backgrounds. Log scale plots in Fig. 13. No broader structures highlighting partially reconstructed decays are present. After application of the full selection no evidence of residual misidentified backgrounds is visible, Fig. 14, log scale plot in Fig. 15. Therefore, no selection cuts against misidentified backgrounds are applied.

## 2.4 Data/MC comparison and simulation weighting

Simulated data are used in this analysis to describe the efficiency of the detector as a function of the  $\Lambda_c^+ \rightarrow pK^-\pi^+$  decay phase space variables. To properly subtract the detector efficiency reconstruction effects it is therefore crucial for the simulation to reproduce real data as accurately as possible.

The variables used to select  $\Lambda_c^+ \rightarrow pK^-\pi^+$  candidates, listed in Table 2, have been chosen not only for their ability to separate signal from combinatorial background, but also because their distributions are well reproduced in simulation. Fig. 16 reports the comparison between s-Weighted  $\Lambda_c^+ \rightarrow pK^-\pi^+$  real data and simulated ReDecay sample distributions for the selection variables. ProbNN variables have been corrected using the **PIDCorr** tool, which transform the simulated PID variables to match those from calibration data samples: the *p\_LbLcPi\_MC15TuneV1\_ProbNNp\_Brunel* and *K\_MC15TuneV1\_ProbNNK\_Brunel* combinations are employed for proton and kaon ProbNN variables, respectively; moreover the number-of-tracks distribution employed is rescaled by a factor 1.15 to reproduce that of  $\Lambda_c^+ \rightarrow pK^-\pi^+$  data. The agreement is quite good, even if not perfect for ProbNN variables.

The comparison between data and simulation distributions for variables other than those employed in the selection are checked in Figs. 17, 18, 19: they describe  $\Lambda_c^+$  and daughter hadron kinematics,  $\Lambda_c^+$  lifetime and number-of-tracks, and stripping related variables, (see Table 1). Discrepancies are present in the  $\Lambda_c^+$  and daughter particle kinematic distributions, **nTracks**, track quantities (ghost probability and track  $\chi^2/\text{ndf}$ ) and PID. Since no requirement is placed on these variables the effect of these discrepancies is not expected to be critical.

To correct for residual data/simulation discrepancies the *ReDecay* simulation sample is weighted event-per-event in order to reproduce the data distribution of the selection variables. The weights are computed using the gradient boost weighting technique of the **hep\_ml** package, trained on a subset of 2016  $\Lambda_c^+ \rightarrow pK^-\pi^+$  data, targeting  $\Lambda_c^+$  momentum and transverse momentum, this way correcting the  $\Lambda_c^+$  baryon production kinematics.

The comparison between data and simulation distributions after gradient boost weighting are reported in Figs. 20-23. Besides correcting the  $\Lambda_c^+$  momentum distributions, the weighting procedure automatically corrects the final particle kinematic distributions, which

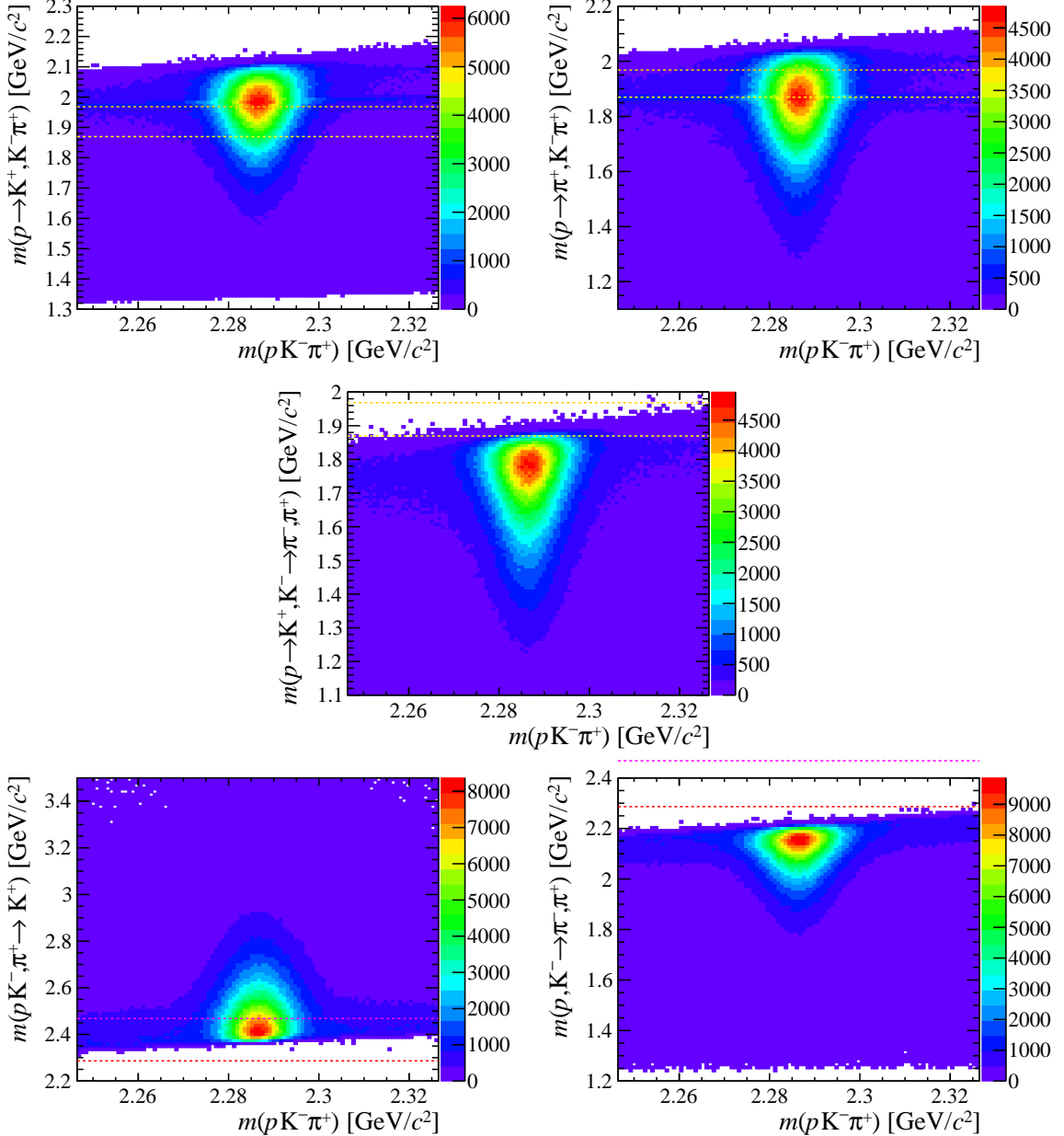


Figure 8: Invariant mass distributions for  $pK^-\pi^+$  mass hypothesis versus (Top, Center)  $D_{(s)}^+ \rightarrow h^+h^-h^+$  and (Bottom)  $\Lambda_c^+/\Xi_c^+ \rightarrow ph^-h^+$  alternative mass hypothesis for candidates passing stripping and trigger requirements. Horizontal dashed lines correspond to (yellow)  $D^+$ , (orange)  $D_s^+$ , (red)  $\Lambda_c^+$  and (magenta)  $\Xi_c^+$  PDG masses [1].

match to a high degree of precision even though the MC sample is generated flat in phase space: this distributions are therefore basically independent of the  $\Lambda_c^+ \rightarrow pK^-\pi^+$  decay dynamics. Also ProbNN distributions are improved by the simulation weighting.

The simulation weighting presented is used to correct the detector efficiency effects in the amplitude fits. Variations of this weighting procedure are studied by evaluating the change in fit quality for the nominal amplitude model, see Section 6. The addition of track variables in the gradient boost training like `nTracks`, track ghost probability and/or track  $\chi^2/\text{ndf}$  does not produce significant better fits, while the addition of ProbNN variables

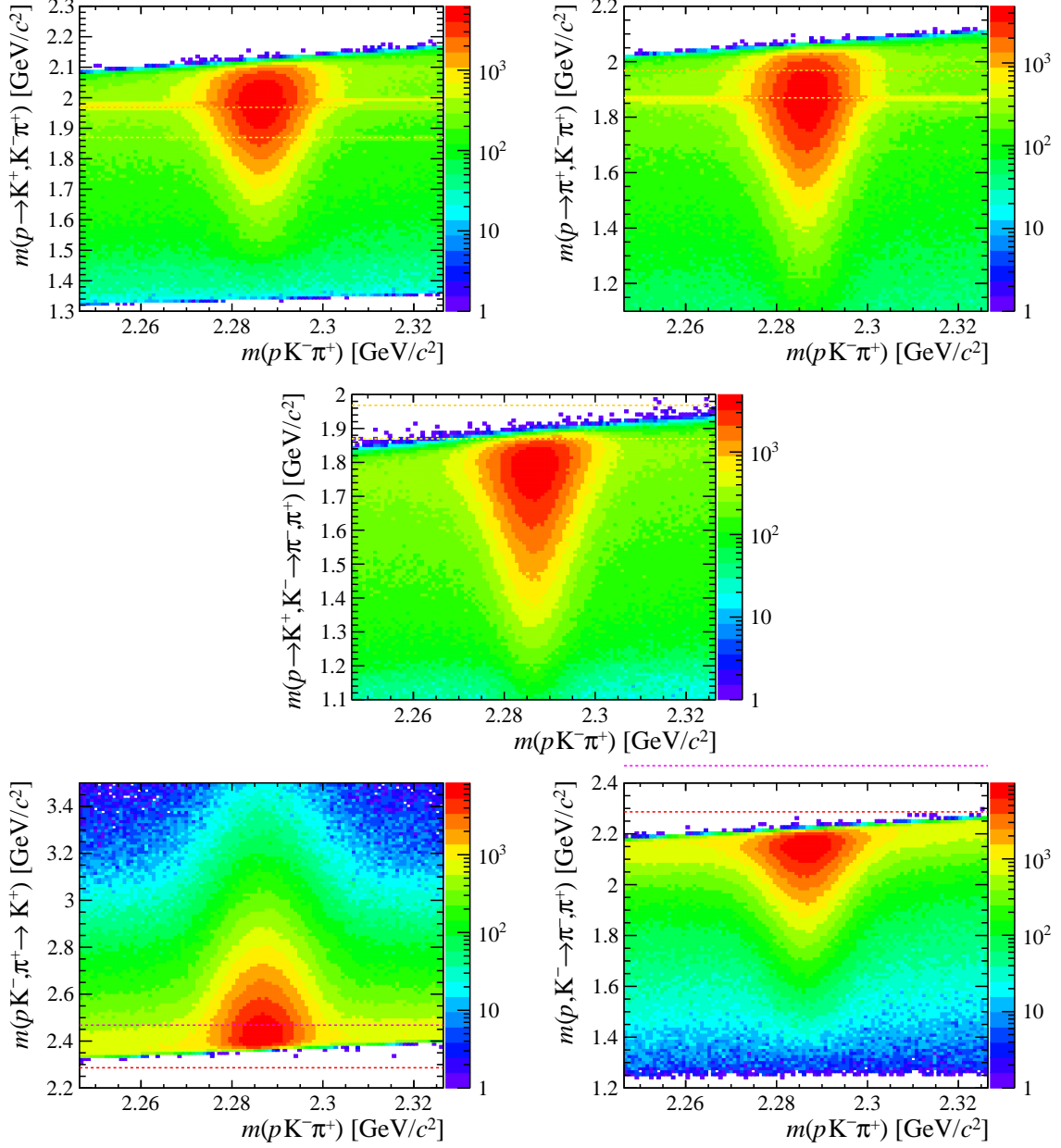


Figure 9: Invariant mass distributions for  $pK^-\pi^+$  mass hypothesis versus (Top, Center)  $D_{(s)}^+ \rightarrow h^+h^-h^+$  and (Bottom)  $\Lambda_c^+/\Xi_c^+ \rightarrow ph^-h^+$  alternative mass hypothesis for candidates passing stripping and trigger requirements, log scale applied. Horizontal dashed lines correspond to (yellow)  $D^+$ , (orange)  $D_s^+$ , (red)  $\Lambda_c^+$  and (magenta)  $\Xi_c^+$  PDG masses [1].

<sup>394</sup> yields a worser description of the detector efficiency.

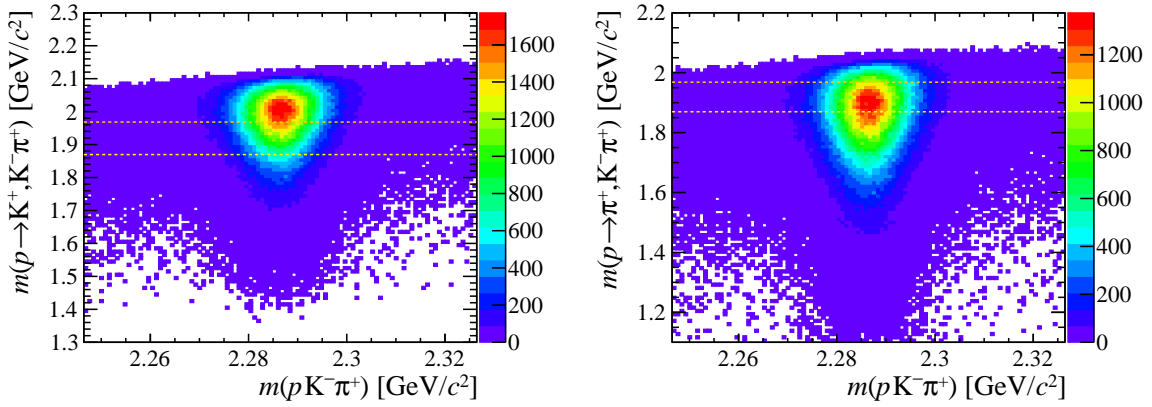


Figure 10: Invariant mass distributions for  $pK^-\pi^+$  mass hypothesis versus  $D_{(s)}^+ \rightarrow h^+h^-h^+$  alternative mass hypothesis for candidates passing the full selection process. Horizontal dashed lines correspond to the (yellow)  $D^+$  and (orange)  $D_s^+$  PDG masses [1]

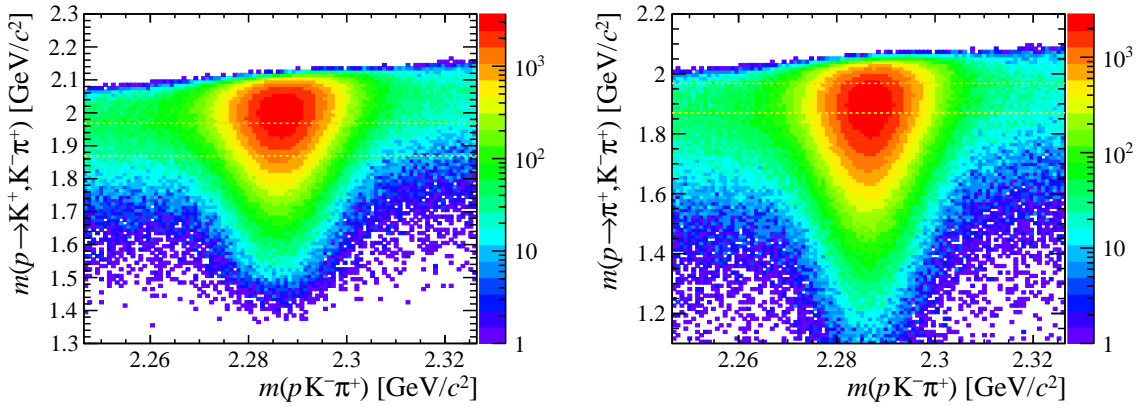


Figure 11: Invariant mass distributions for  $pK^-\pi^+$  mass hypothesis versus  $D_{(s)}^+ \rightarrow h^+h^-h^+$  alternative mass hypothesis for candidates passing the full selection process. Log scale applied. Horizontal dashed lines correspond to the (yellow)  $D^+$  and (orange)  $D_s^+$  PDG masses [1]

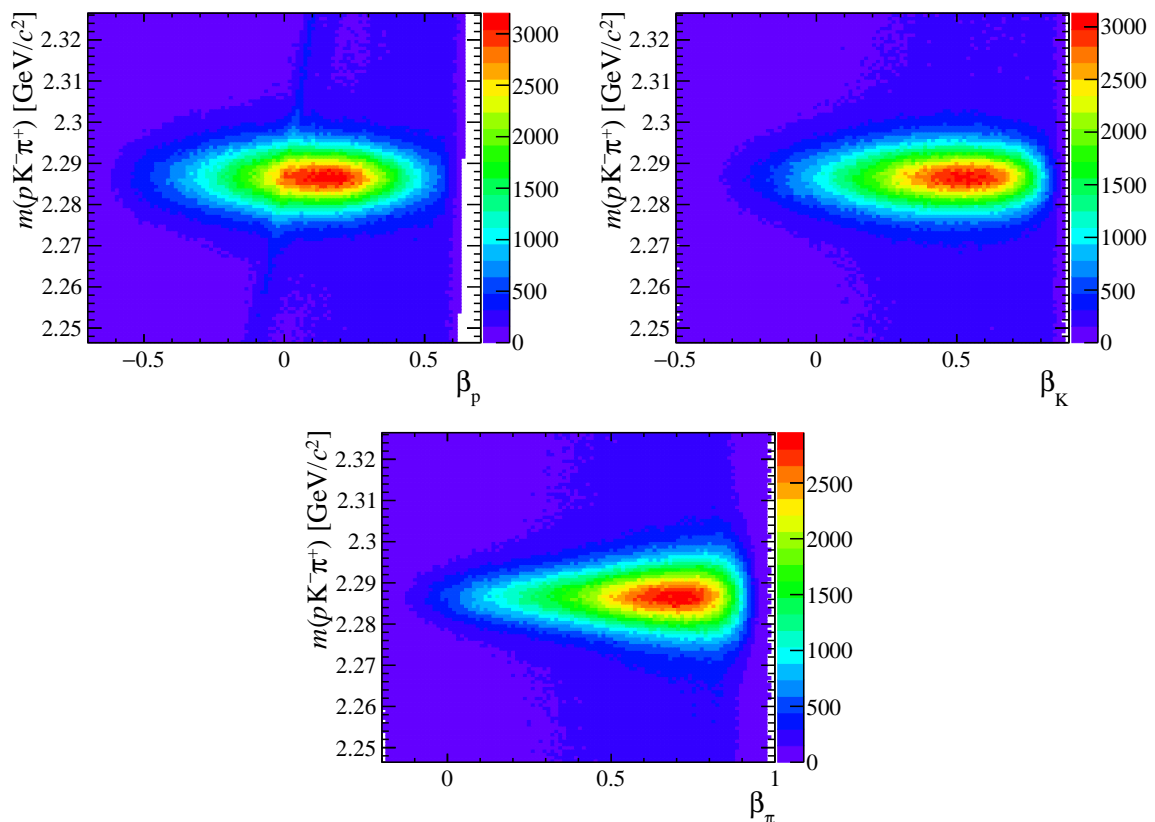


Figure 12: Invariant mass distributions for  $pK^-\pi^+$  mass hypothesis versus hadron momentum asymmetries for candidates selected with stripping and trigger requirements only.

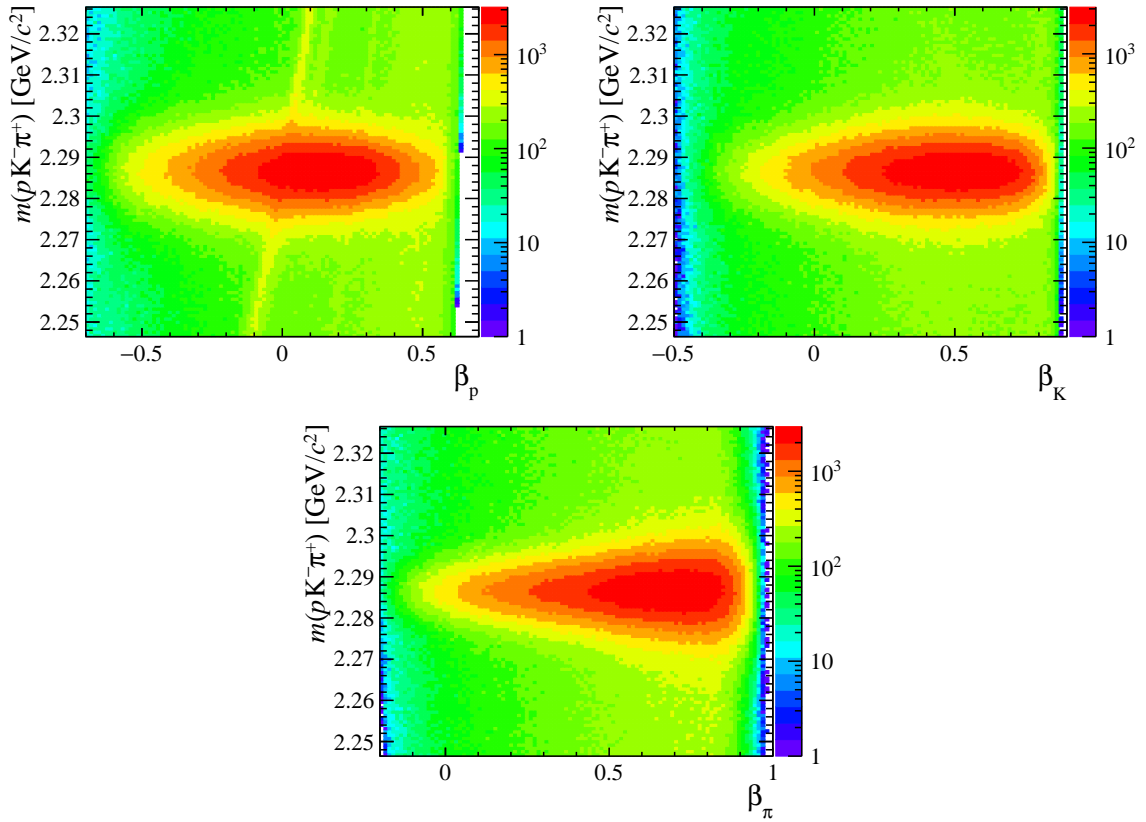


Figure 13: Invariant mass distributions for  $pK^-\pi^+$  mass hypothesis versus hadron momentum asymmetries for candidates selected with stripping and trigger requirements only, log scale applied.

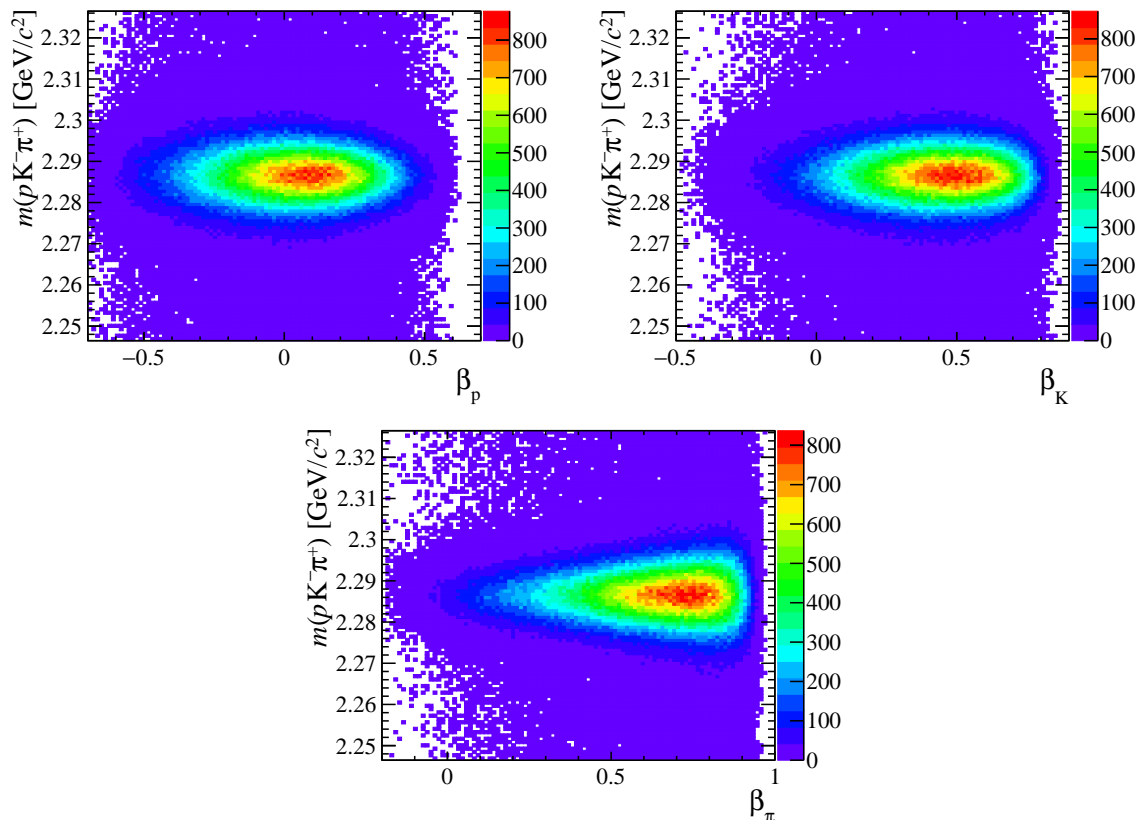


Figure 14: Invariant mass distributions for  $pK^-\pi^+$  mass hypothesis versus proton momentum asymmetry for candidates passing the full selection process.

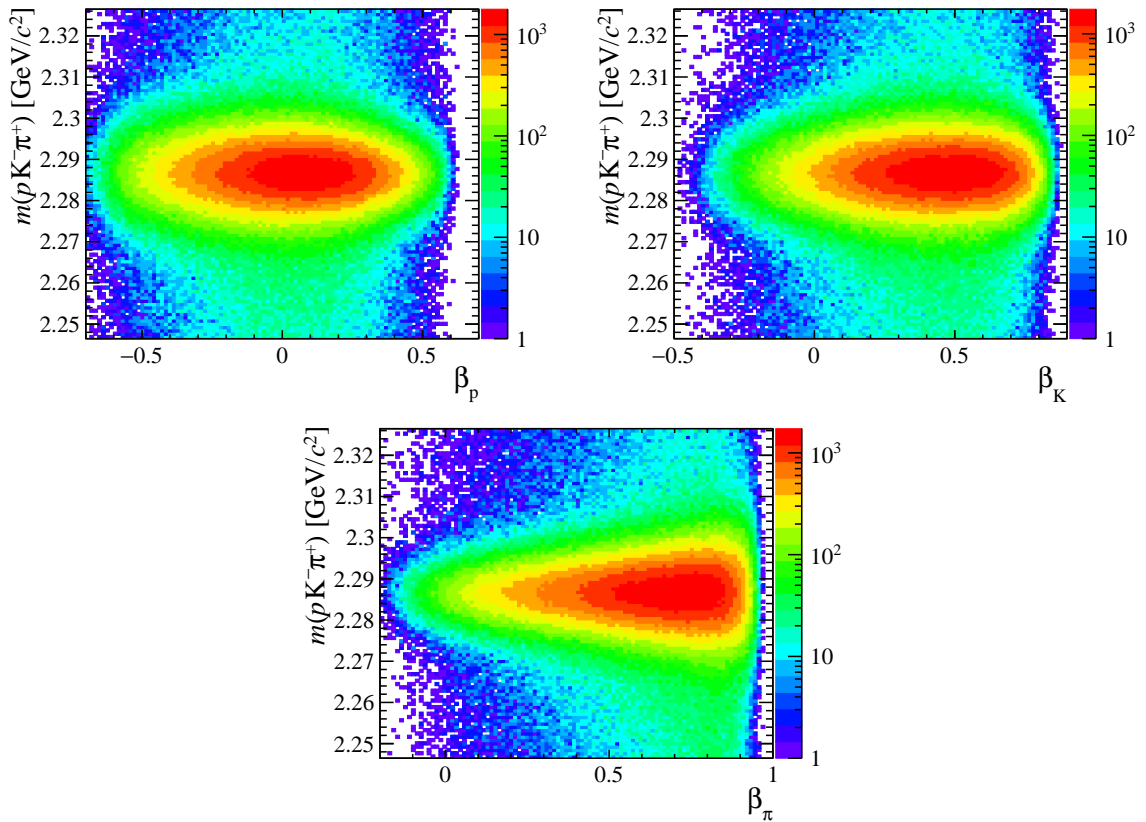


Figure 15: Invariant mass distributions for  $pK^-\pi^+$  mass hypothesis versus proton momentum asymmetry for candidates passing the full selection process. Log scale applied.

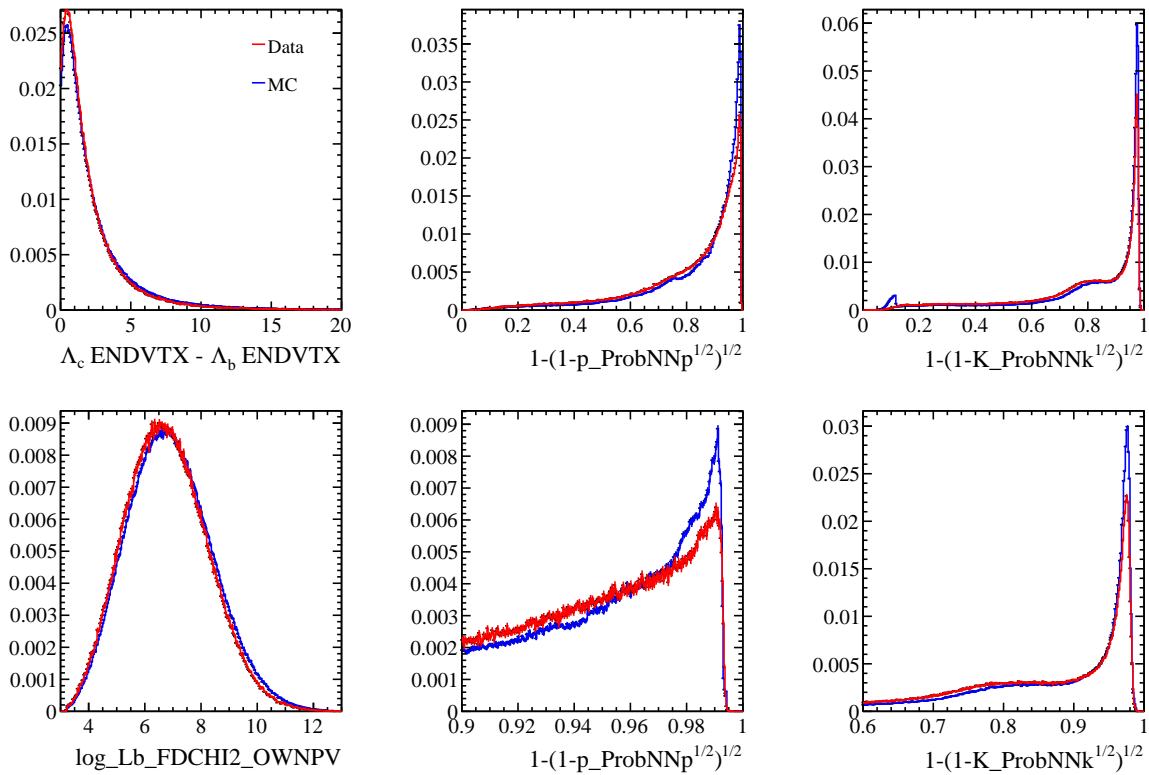


Figure 16: Selection variable normalised distributions for s-Weighted  $\Lambda_c^+ \rightarrow pK^-\pi^+$  data candidates (red) and simulated ReDecay sample (blue), after PIDCorr correction. ProbNN distributions are also zoomed in the region where the associated selection cut is placed

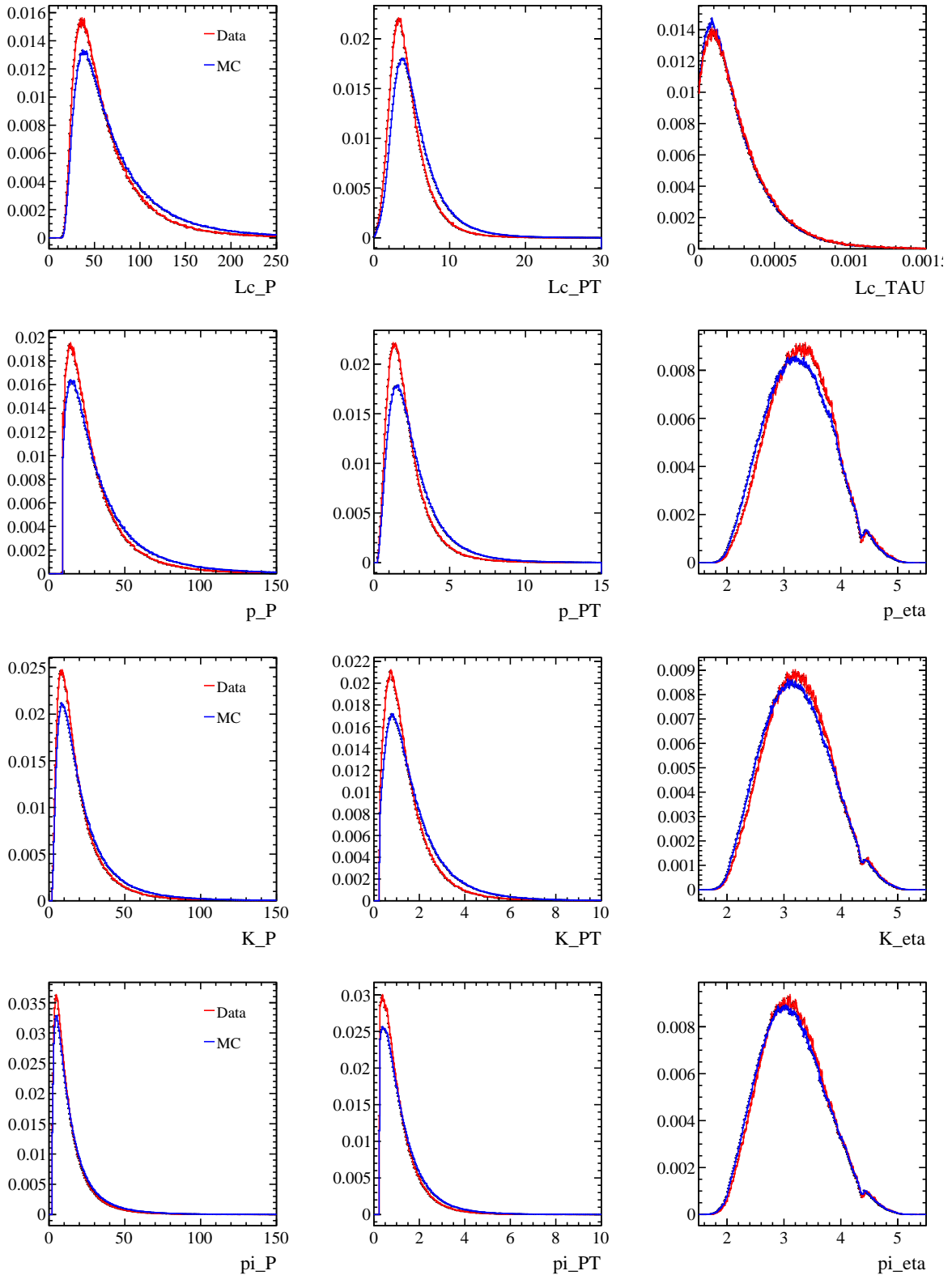


Figure 17:  $\Lambda_c^+$  kinematics,  $\Lambda_c^+$  lifetime and final particle kinematic normalised distributions for s-Weighted  $\Lambda_c^+ \rightarrow pK^-\pi^+$  data candidates (red) and simulated ReDecay sample (blue), after PIDCorr correction.

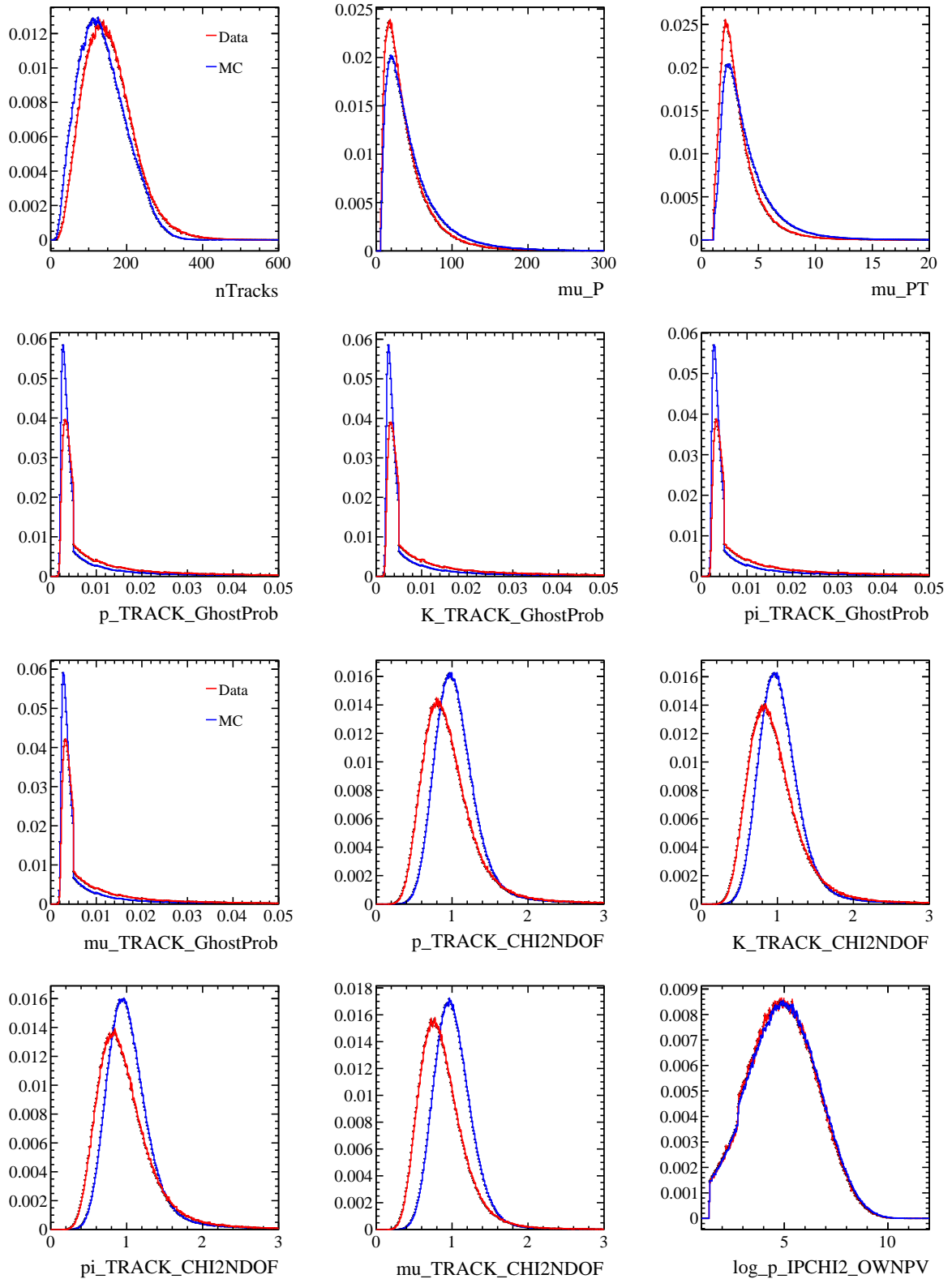


Figure 18: nTracks and stripping-related (see Table 1) normalised distributions for s-Weighted  $\Lambda_c^+ \rightarrow pK^-\pi^+$  data candidates (red) and simulated ReDecay sample (blue), after PIDCorr correction.

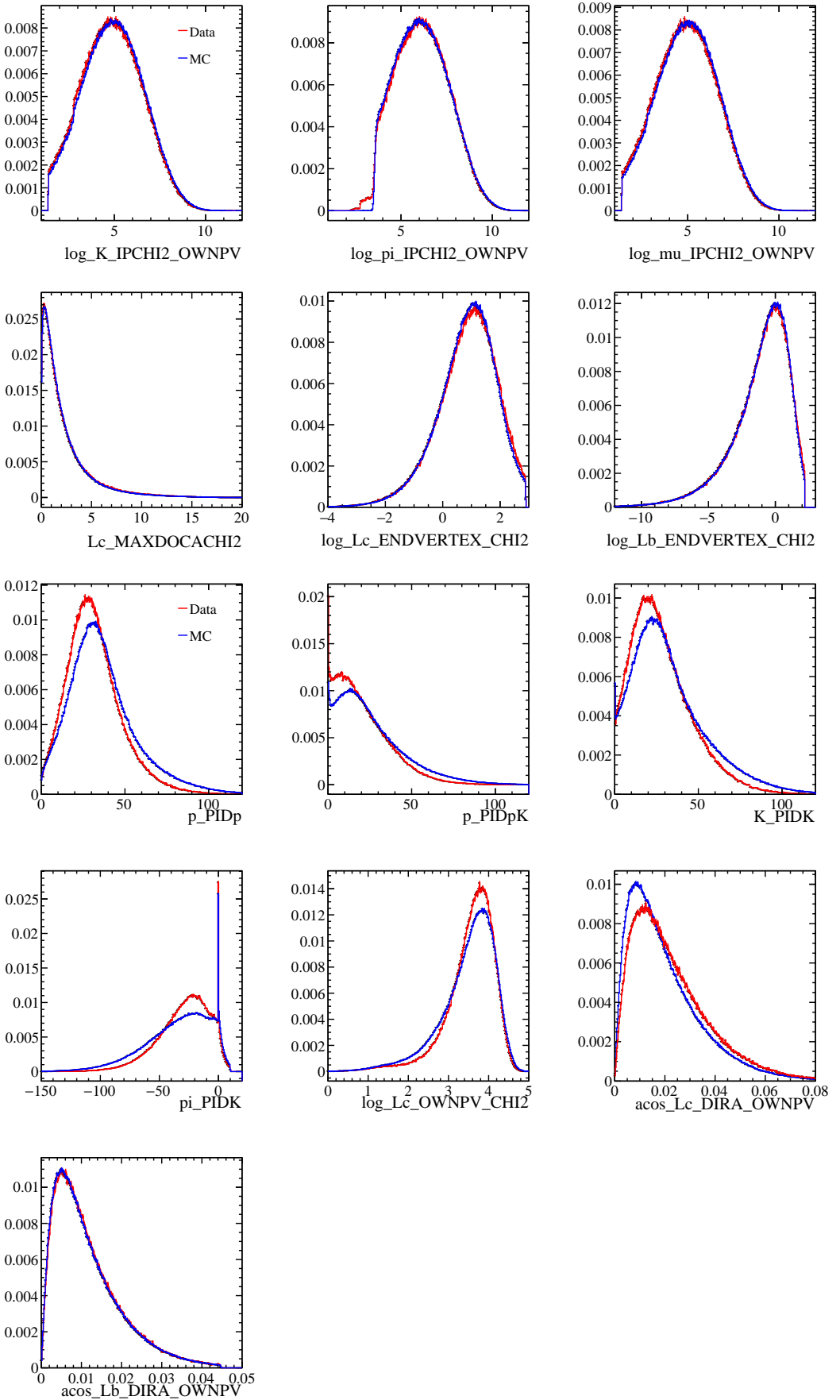


Figure 19: More stripping-related (see Table 1) normalised distributions for s-Weighted  $\Lambda_c^+ \rightarrow pK^-\pi^+$  data candidates (red) and simulated R2D decay sample (blue), after PIDCorr correction.

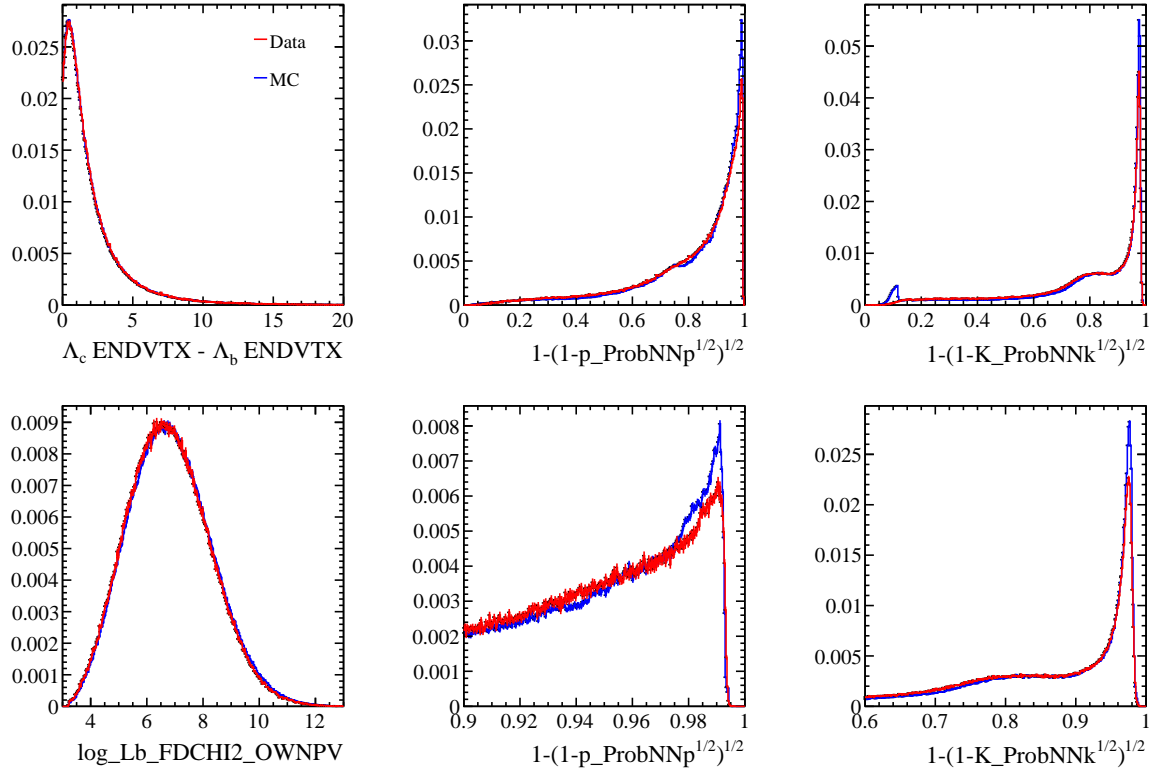


Figure 20: Selection variable normalised distributions for s-Weighted  $\Lambda_c^+ \rightarrow pK^-\pi^+$  data candidates (red) and simulated ReDecay sample (blue), after gradient boosting weighting. ProbNN distributions are also zoomed in the region where the associated selection cut is placed

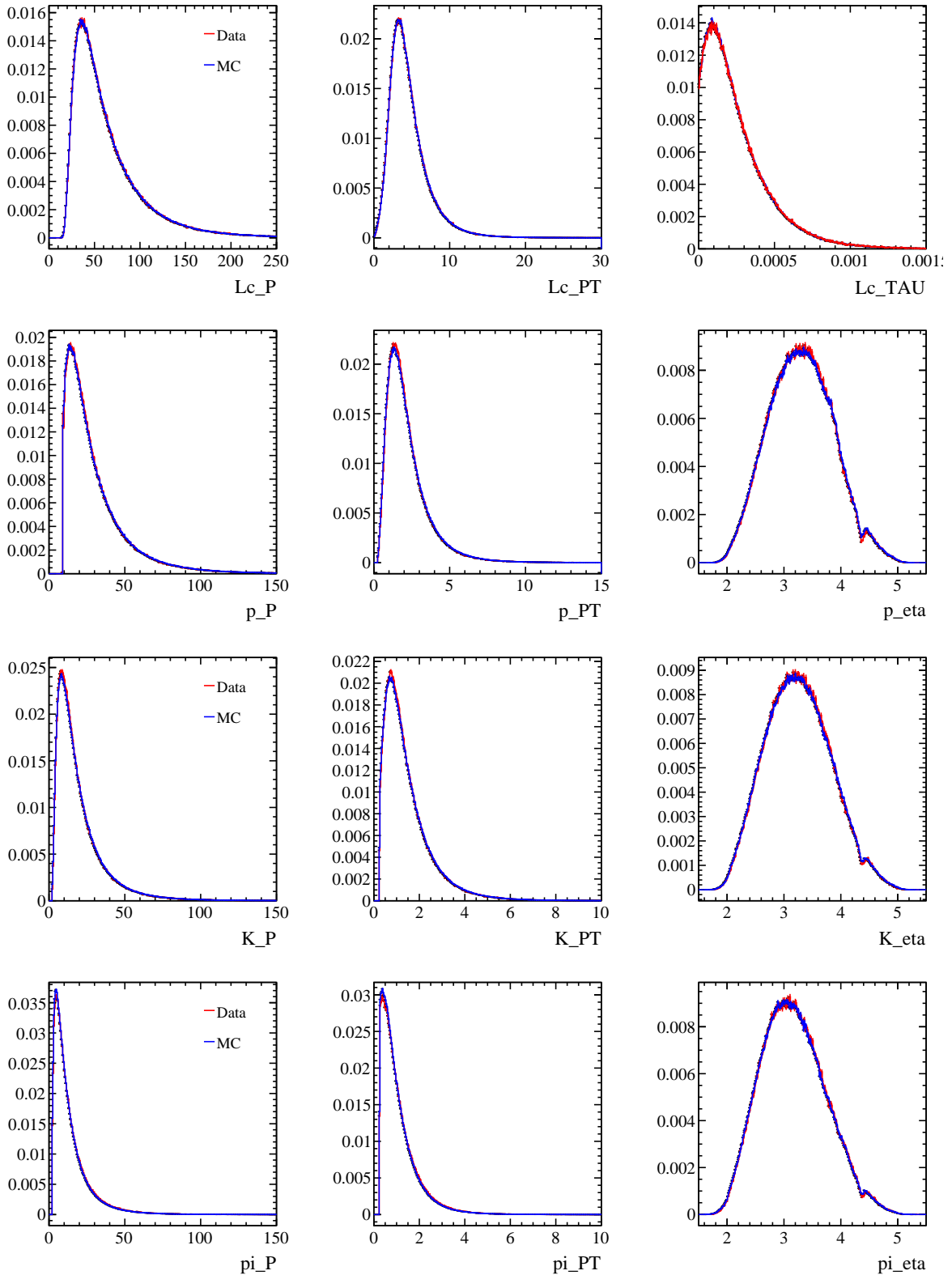


Figure 21:  $\Lambda_c^+$  kinematics,  $\Lambda_c^+$  lifetime and final particle kinematic normalised distributions for s-Weighted  $\Lambda_c^+ \rightarrow p K^- \pi^+$  data candidates (red) and simulated ReDecay sample (blue), after gradient boosting weighting.

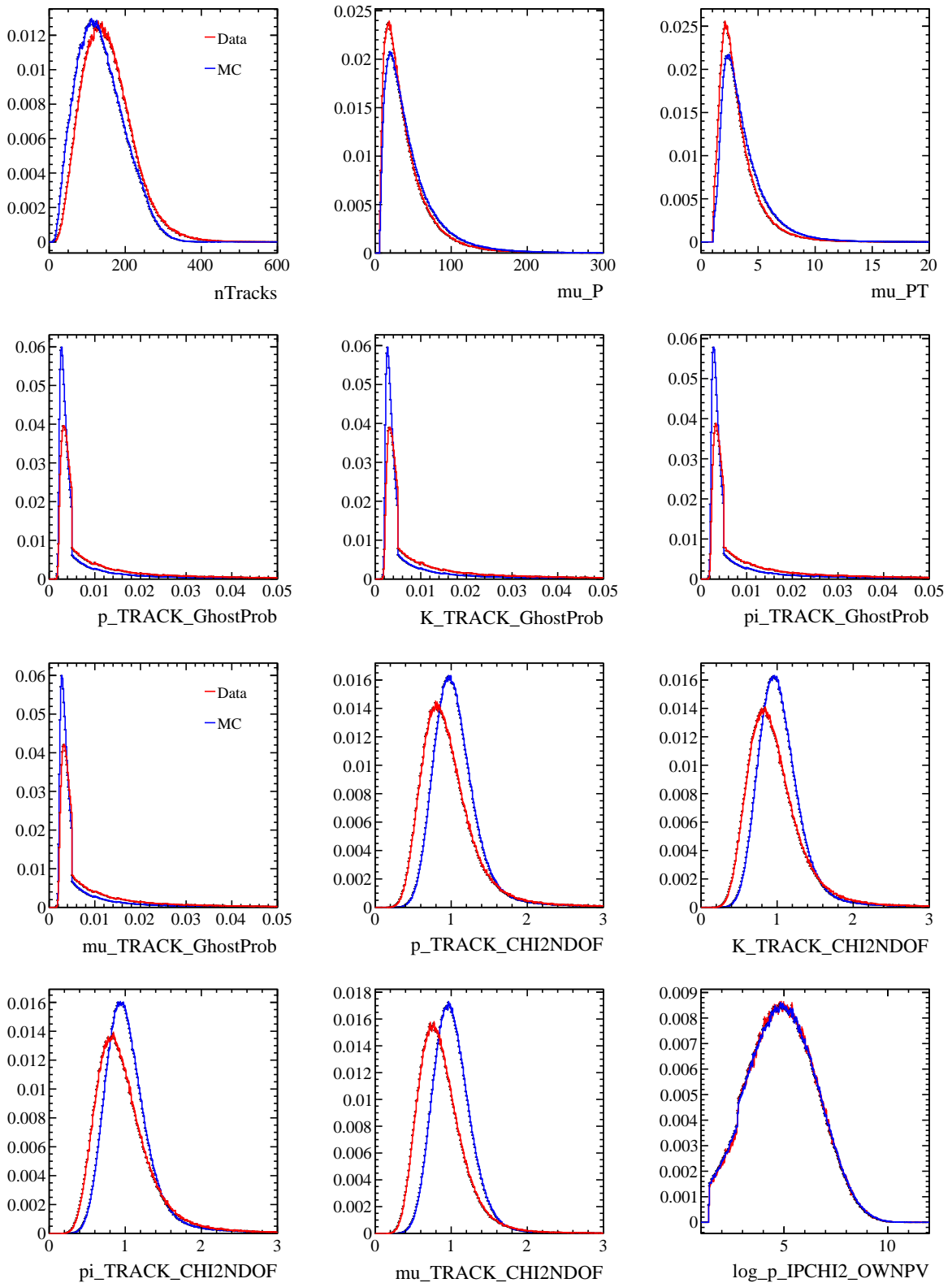


Figure 22: nTracks and stripping-related (see Table 1) normalised distributions for s-Weighted  $\Lambda_c^+ \rightarrow pK^-\pi^+$  data candidates (red) and simulated ReDecay sample (blue), after gradient boosting weighting.

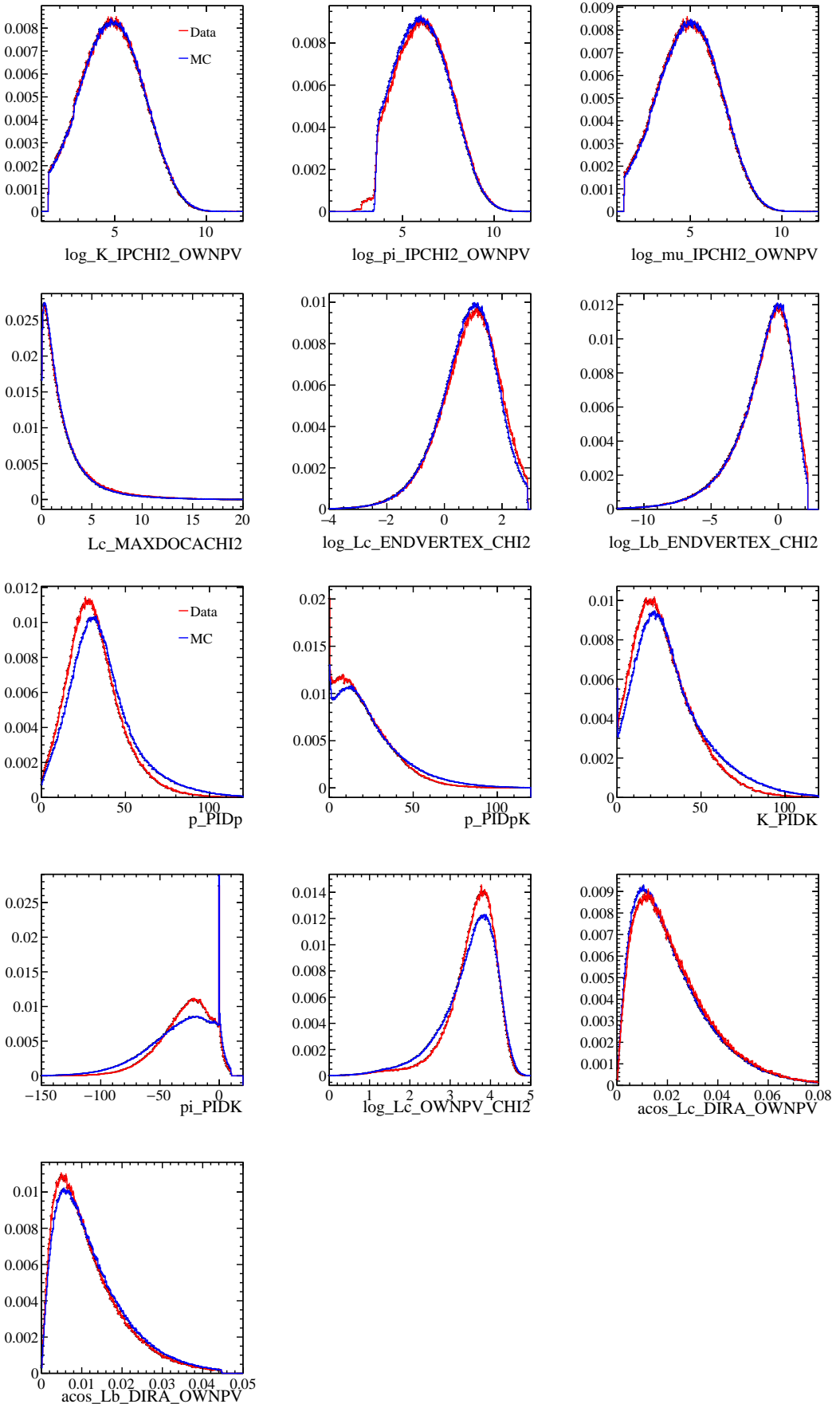


Figure 23: More stripping-related (see Table 1) normalised distributions for s-Weighted  $\Lambda_c^+ \rightarrow pK^-\pi^+$  data candidates (red) and simulated McDecay sample (blue), after gradient boosting weighting.

395 **3 The helicity formalism for baryon amplitude analyses and polarisation measurements**

397 **3.1 Helicity amplitudes**

398 The  $\Lambda_c^+ \rightarrow pK^-\pi^+$  amplitude model is written in the helicity formalism [36], which  
 399 generalises the spin-orbit formalism for combining particle spins to relativistic processes  
 400 by using helicity states. In the following a quick overview of the formalism employed is  
 401 given. The discussion follows that of Ref. [37] and Refs. therein.

402 The helicity formalism establishes a relation between two sets of two-particle states:  
 403 plane-wave helicity states describing propagating particles with well defined momentum  
 404 and spherical-wave helicity states, describing states of definite total angular momentum.

405 We consider a couple of particles in their centre-of-mass rest frame, with a given  
 406 reference system. For two-body particle decays, this system is given by the set of spin  
 407 operators expressing the mother particle spin states. A single-particle plane-wave helicity  
 408 state is labelled by the particle momentum  $\mathbf{p}$  in that reference frame, spin  $s$  and helicity  $\lambda$ ,  
 409  $|\mathbf{p}, s, \lambda\rangle$ . In Eqs. (13), (14) of Ref. [36] two-particle plane-wave helicity states are defined  
 410 as

$$|p, \theta_1, \phi_1, \lambda_1, \lambda_2\rangle \equiv |\mathbf{p}_1, s_1, \lambda_1\rangle \otimes (-1)^{s_2-\lambda_2} \exp(-i\pi J_y) |\mathbf{p}_2, s_2, \lambda_2\rangle. \quad (3)$$

411 in which  $(-1)^{s_2-\lambda_2}$  is an optional phase factor and the rotation  $\exp(-i\pi J_y)$  inverts the  
 412  $z$  quantisation axis of the particle 2 helicity state. So, particle 2 enters Eq. (3) not via  
 413 its helicity state, but via an opposite-helicity state: a state with quantisation axis in the  
 414 opposite direction to that determined by the particle momentum.

415 In the two-particle centre-of-mass (CM) frame the two momenta are back-to-back,  
 416  $\mathbf{p}_1 = -\mathbf{p}_2$ , and the same state can be described using the spherical coordinates of  $\mathbf{p}_1$ : its  
 417 modulus  $p = |\mathbf{p}_1| = |\mathbf{p}_2|$ , and the polar and azimuthal angles  $\theta_1$  and  $\phi_1$  with respect to a  
 418 given coordinate frame, being

$$\begin{aligned} \theta_1 &= \arccos(\hat{\mathbf{z}} \cdot \hat{\mathbf{p}}_1), \\ \phi_1 &= \text{atan2}[\hat{\mathbf{y}} \cdot \hat{\mathbf{p}}_1, \hat{\mathbf{x}} \cdot \hat{\mathbf{p}}_1]. \end{aligned} \quad (4)$$

419 These states can be now related to two-particle states with definite value of total  
 420 angular momentum  $J$ , with  $M$  its projection along the  $z$  axis, denoted  $|p, J, M, \lambda_1, \lambda_2\rangle$ .  
 421 These states transform irreducibly under rotations according to Eq. (94), while plane-wave  
 422 helicity states do not. The relation between plane- and spherical-wave helicity states  
 423 is [36]

$$|p, \theta_1, \phi_1, \lambda_1, \lambda_2\rangle = \sum_{J,M} \sqrt{\frac{2J+1}{4\pi}} D_{M,\lambda_1-\lambda_2}^J(\phi_1, \theta_1, 0) |p, J, M, \lambda_1, \lambda_2\rangle, \quad (5)$$

424 in which  $D$  is a Wigner  $D$ -matrix, defined in Appendix C. The crucial point of this  
 425 derivation is that invariance under rotations of the helicity allows to consider the state  
 426  $|p, 0, 0, \lambda_1, \lambda_2\rangle$  (in which particles are aligned to the  $z$  axis) which is eigenstate of  $J_z$  with  
 427 eigenvalue  $\lambda_1 - \lambda_2$ . Then, exploiting the invariance of the helicity under rotations, this  
 428 state is rotated to  $|p, \theta, \phi, \lambda_1, \lambda_2\rangle$  with unchanged helicities.

429 Note that the inversion  $\exp(-i\pi J_y)$  applied to particle 2 states is essential for Eq. (5) to  
 430 be valid, so the treatment of particle 1 and 2 states is not symmetric under the interchange

431 of their role. The third argument of the Wigner  $D$ -matrix refers to a rotation around the  
432 helicity state  $z$  quantisation axis: given an angle  $\psi$ , one has

$$R_z(\psi) |s, \lambda\rangle = e^{-i\psi \hat{J}_z} |s, \lambda\rangle = e^{-i\psi \lambda} |s, \lambda\rangle, \quad (6)$$

433 so that the choice of the  $\psi$  angle is equivalent to a choice of the helicity state phase. In  
434 the following, the conventional choice  $\psi = 0$  is taken.

435 In Ref. [37] it is proposed a definition of the two-particle state Eq. (3) in which a pair  
436 of helicity and opposite-helicity states are employed,

$$|p, \theta_1, \phi_1, \lambda_1, \bar{\lambda}_2\rangle = |\mathbf{p}_1, s_1, \lambda_1\rangle \otimes |\mathbf{p}_2, s_2, \bar{\lambda}_2\rangle, \quad (7)$$

437 and Eq. (5) holds with the substitution  $-\lambda_2 \rightarrow \bar{\lambda}_2$ ,

$$\begin{aligned} |p, \theta_1, \phi_1, \lambda_1, \bar{\lambda}_2\rangle &= \sum_{J,M} \sqrt{\frac{2J+1}{4\pi}} D_{M,\lambda_1+\bar{\lambda}_2}^J(\phi_1, \theta_1, 0) \\ &\quad \times |p, J, M, \lambda_1, \bar{\lambda}_2\rangle. \end{aligned} \quad (8)$$

438 With respect to the standard choice of two-particle helicity states Eq. (3), now both  
439 particle 1 and particle 2 spins are already defined by the same helicity rotation  $R(\phi_1, \theta_1, 0)$   
440 (details in Ref. [37]), without the need of inverting the particle 2 helicity states as in  
441 Eq. (3). This choice of the two-particle state ease the handling of phase differences and  
442 the matching of proton spin states, which will be addressed later in the construction of  
443 the  $\Lambda_c^+ \rightarrow p K^- \pi^+$  amplitude model.

444 The amplitude associated to a two-body decay  $A \rightarrow 1, 2$  is

$$\begin{aligned} \mathcal{A}_{m_A, \lambda_1, \bar{\lambda}_2}(\theta_1, \phi_1) &= \left\langle p, \theta_1, \phi_1, \lambda_1, \bar{\lambda}_2 \middle| \hat{T} \right| s_A, m_A \rangle \\ &= \mathcal{H}_{\lambda_1, \bar{\lambda}_2} D_{m_A, \lambda_1+\bar{\lambda}_2}^{*s_A}(\phi_1, \theta_1, 0), \end{aligned} \quad (9)$$

445 in which the terms

$$\mathcal{H}_{\lambda_1, \bar{\lambda}_2} \equiv \left\langle p, s_A, m_A, \lambda_1, \bar{\lambda}_2 \middle| \hat{T} \right| s_A, m_A \rangle, \quad (10)$$

446 called helicity couplings, encode the decay dynamics and can not depend on  $s_A, m_A$  for  
447 rotational invariance. The helicity values allowed by angular momentum conservation are

$$|\lambda_1| \leq s_1, \quad |\bar{\lambda}_2| \leq s_2, \quad |\lambda_1 + \bar{\lambda}_2| \leq s_A. \quad (11)$$

448 If the decay conserves parity symmetry, the helicity couplings for opposite helicities  
449 are constrained by the relation

$$\mathcal{H}_{\lambda_1, \bar{\lambda}_2} \equiv \eta_A \eta_1 \eta_2 (-1)^{s_1+s_2-s_A} \mathcal{H}_{-\lambda_1, -\bar{\lambda}_2}, \quad (12)$$

450 in which  $\eta$  are the parity eigenvalues of the particle states.

### 451 3.2 Differential decay rate and extraction of the decaying parti- 452 cle polarisation

453 The differential decay rate for a particle  $A$  decaying to a final-state  $f$  is described by the  
454 probability density  $p(\Omega, \mathbf{P})$ , function of the phase-space variables  $\Omega$ , and the  $A$  particle

455 spin polarisation vector  $\mathbf{P}$ . The final particle polarisations do not enter the decay rate  
456 unless measurable, which is not usually the case. The decay probability for definite spin  
457 states is the squared modulus of the amplitude of the multi-body decay between the  $A$   
458 particle initial state  $|s_A, m_A\rangle$  and the final particle state  $|\{\mathbf{p}_i\}, \{\lambda_i\}\rangle$ ,

$$p(A \rightarrow f) = |\langle s_A, m_A | T | \{\mathbf{p}_i\}, \{\lambda_i\} \rangle|^2 = |\mathcal{A}_{m_A, \{\lambda_i\}}^{A \rightarrow f}(\Omega)|^2. \quad (13)$$

459 In practice, it is not possible to measure event-by-event particle polarisations, therefore  
460 statistical mixtures of pure quantum spin states must be considered, expressing the  
461 probability density in terms of spin density operators

$$\rho = \sum_i p_i |\psi_i\rangle \langle \psi_i|, \quad (14)$$

462 having matrix elements in the  $|s, m\rangle$  basis

$$\rho_{m, m'} = \langle s, m | \rho | s, m' \rangle. \quad (15)$$

463 Eq. (13), rewritten by inserting suitable identity operators, becomes

$$p(A \rightarrow f) = \text{tr} [\rho_A T \rho_f T^\dagger], \quad (16)$$

464 in which  $\rho_A$  and  $\rho_f$  are the  $A$  and  $f$  spin density matrices expressed in their own spin  
465 reference frames, respectively, and  $T$  now represents the transition operator matrix  
466 elements between  $A$  and  $f$  spin states,

$$T_{m_A, \{\lambda_i\}} = \mathcal{A}_{m_A, \{\lambda_i\}}^{A \rightarrow f}(\Omega). \quad (17)$$

467 If final particle polarisations are not measured, the final spin state is a maximally mixed  
468 state,  $\rho_f = \mathbb{I}/(2s+1)$ , in any spin reference frame [38]. By making explicit the sum over  
469 spin states, the differential decay rate is written as

$$p(\Omega, \mathbf{P}) = \sum_{m, m' = -s_A}^{s_A} \sum_{\{\lambda_i\} = \{-s_i\}}^{\{s_i\}} (\rho_A)_{m, m'} \mathcal{A}_{m', \{\lambda_i\}}^{A \rightarrow f}(\Omega) \mathcal{A}_{m, \{\lambda_i\}}^{*A \rightarrow f}(\Omega). \quad (18)$$

470 The differential decay rate of a particle with spin can be therefore exploited to extract  
471 its (statistically-averaged) polarisation. The polarisation can be extracted together with  
472 the amplitude model of the decay by means of an amplitude analysis over the full decay  
473 phase space  $\Omega$ .

### 474 3.3 Properties of the polarised decay rate

475 Let's consider the decay of a particle  $A$ , having polarisation vector  $\mathbf{P}$ . The polarisation  
476 vector is the only quantity specifying a direction in the  $A$  particle system. If  $\mathbf{P}$  is zero,  
477 nothing specifies a direction in the  $A$  system and its decay rate must be isotropic with  
478 respect to a reference frame independent of the decay, *e.g.* a given  $A$  spin reference frame.  
479 In other words, the decay rate specifies the relative angular distribution among daughter  
480 particles, but not their orientation relative to an external reference frame. This provide  
481 a benchmark test for codes implementing amplitude models: the angular distributions

482 describing the orientation of the decay with respect to an external reference frame must  
483 be isotropic irrespective of the amplitude model.

484 Now let us suppose  $\mathbf{P} \neq 0$ . Under rotations of the polarisation frame, the polarisation  
485 vector rotates too, but, for rotational invariance, the decay phase space variables of the  
486 differential decay rate must rotate consistently. This implies that the relative orientation  
487 of the daughter particles can not depend on the orientation of the decay with respect to an  
488 external reference frame. The kinematic distributions describing the relative orientation of  
489 daughter particles must be therefore the same for any value of the  $A$  polarisation vector,  
490 this providing another benchmark test for the amplitude model.

## 491 4 The $\Lambda_c^+ \rightarrow pK^-\pi^+$ amplitude model

492 The amplitude model for the  $\Lambda_c^+ \rightarrow pK^-\pi^+$  decay is built exploiting the helicity formalism  
 493 described in Sec. 3.1. In Sec. 4.1 the definition of the  $\Lambda_c^+$  baryon polarisation system is  
 494 defined. Sec. 4.2 presents the description of the  $\Lambda_c^+ \rightarrow pK^-\pi^+$  phase space employed.  
 495 In Sec. 4.3 it is shown how  $CP$ -conjugate  $\Lambda_c^+$  and  $\bar{\Lambda}_c^-$  events can be combined. The  
 496  $\Lambda_c^+ \rightarrow pK^-\pi^+$  amplitude model is built in Sec. 4.4 using two equivalent approaches.  
 497 Finally, the polarised decay rate is introduced in Sec. 4.5.

### 498 4.1 $\Lambda_c^+$ baryon polarisation system

499 Charm baryons originated in  $\Lambda_b^0$  semileptonic decays can be polarised thanks to the  
 500 structure of the charged current weak force mediating semileptonic decays. Since parity is  
 501 maximally violated in such transitions, the baryon polarisation is expected to be mostly  
 502 parallel to the  $\Lambda_c^+$  momentum as seen from the  $\Lambda_b^0$  rest frame. Therefore, the “ideal”  
 503 polarisation system would be the helicity system of the  $\Lambda_c^+$  baryon reached from the  $\Lambda_b^0$   
 504 rest frame. However, the presence of an undetectable neutrino in the  $\Lambda_b^0$  decay prevents a  
 505 precise reconstruction of the  $\Lambda_b^0$  rest frame, making the mentioned polarisation system  
 506 hardly accessible.

507 In this analysis two  $\Lambda_c^+$  helicity systems are considered to express the  $\Lambda_c^+$  polarisation:  
 508 one reached from the laboratory frame, which is well defined since the  $\Lambda_c^+$  decay is fully  
 509 reconstructed; and one reached from an approximate  $\Lambda_b^0$  rest frame, obtained using a  
 510 partial reconstruction algorithm for the estimation of the  $\Lambda_b^0$  momentum. Both lead to a  
 511 dilution of the original polarisation since the actual quantisation axis will be uncontrollably  
 512 rotated event-by-event from the “ideal” one, because of the unknown orientation of the  
 513  $\Lambda_b^0$  decay in the laboratory frame or the impossibility of precisely determining the  $\Lambda_b^0$  rest  
 514 frame.

515 The muon momentum is used to define the orthogonal polarisation axes, by choosing  
 516 the  $x$ -axis as the component of the muon momentum orthogonal to the  $\Lambda_c^+$  momentum.  
 517 The three polarisation system axes are thus defined as follows, Fig. 24,

$$\begin{aligned}\hat{z}_{\Lambda_c^+} &= \hat{\mathbf{p}}(\Lambda_c^+) \\ \hat{x}_{\Lambda_c^+} &= \frac{\mathbf{p}(\mu^-) - [\mathbf{p}(\mu^-) \cdot \hat{\mathbf{p}}(\Lambda_c^+)] \hat{\mathbf{p}}(\Lambda_c^+)}{|\mathbf{p}(\mu^-) - [\mathbf{p}(\mu^-) \cdot \hat{\mathbf{p}}(\Lambda_c^+)] \hat{\mathbf{p}}(\Lambda_c^+)|} \\ &= \frac{\mathbf{p}(\Lambda_c^+) \times \mathbf{p}(\mu^-)}{|\mathbf{p}(\Lambda_c^+) \times \mathbf{p}(\mu^-)|} \times \hat{\mathbf{p}}(\Lambda_c^+) \\ \hat{y}_{\Lambda_c^+} &= \hat{z}_{\Lambda_c^+} \times \hat{x}_{\Lambda_c^+} \\ &= \frac{\mathbf{p}(\Lambda_c^+) \times \mathbf{p}(\mu^-)}{|\mathbf{p}(\Lambda_c^+) \times \mathbf{p}(\mu^-)|},\end{aligned}\tag{19}$$

518 in which the  $\Lambda_c^+$  and muon momenta are expressed in the laboratory or in the approximate  
 519  $\Lambda_b^0$  rest frames.

520 For the approximate reconstruction of the  $\Lambda_b^0$  rest frame two algorithms are employed.  
 521 The first, named hereafter “Full reconstruction”, assumes that the  $\Lambda_c^+$  originates from  
 522 a  $\Lambda_b^0 \rightarrow \Lambda_c^+ \mu^- \nu_\mu$  decay: exploiting all the available information (the momentum of the  
 523 detectable part of the decay, the  $\Lambda_b^0$  meson flight direction from primary vertex to the  
 524  $\Lambda_c^+ \mu^-$  vertex, the  $\Lambda_b^0$  and neutrino masses) determines the  $\Lambda_b^0$  momentum up to a two-fold

ambiguity [39]. The two solutions correspond to the forward or backward orientation of the neutrino in the  $\Lambda_b^0$  rest frame with respect to the  $\Lambda_b^0$  flight direction. If the neutrino is orthogonal to the  $\Lambda_b^0$  flight direction a unique, degenerate solution is found. Of the two solutions one is chosen randomly. If no solution is available, for an apparent unphysical configuration due to resolution effects or a different decay than the expected one, the degenerate configuration is assumed. No solution is found in the 24.8% of MC events.

The second, named hereafter ‘‘Equal boost’’, assumes that the proper velocity along the beam axis,  $\gamma\beta_z$ , of the detectable part of the decay ( $\Lambda_c^+\mu^-$ ) is equal to that of the  $\Lambda_b^0$  baryon [40]. The magnitude of the  $\Lambda_b^0$  momentum in terms of the visible decay system  $V$  and the angle  $\theta$  between flight direction and beam axis is set as

$$|p(\Lambda_b^0)| = p_z(V) \frac{m(\Lambda_b^0)}{m(V)} \sqrt{1 + \tan^2 \theta}. \quad (20)$$

The first algorithm is in principle more precise, but the assumption that the  $\Lambda_c^+$  originates from  $\Lambda_b^0 \rightarrow \Lambda_c^+ \mu^- \nu_\mu$  decays is not always true: the selection criteria applied do not reject other decay modes, *e.g.*  $\Lambda_b^0 \rightarrow \Lambda_c^+ \tau^- \nu_\tau$ , for which the assumptions behind the algorithm do not apply. The second is in principle less precise but it is applicable also to decays with two or more missing particles.

In this analysis we use by default the  $\Lambda_c^+$  helicity system reached from the laboratory, which does not suffer from uncertainties in the definition of the starting reference frame.

The three polarisation components determined by this polarisation system are

$$\begin{aligned} P_z &= \mathbf{P} \cdot \hat{\mathbf{z}}_{\Lambda_c^+}, \\ P_x &= \mathbf{P} \cdot \hat{\mathbf{x}}_{\Lambda_c^+}, \\ P_y &= \mathbf{P} \cdot \hat{\mathbf{y}}_{\Lambda_c^+}, \end{aligned}$$

known in the literature as longitudinal, transverse and normal polarisation. Considering the effect of the time-reversal operator, reversing both momenta and spin, one sees that longitudinal and transverse components are  $\hat{T}$ -even quantities, while normal polarisation is  $\hat{T}$ -odd. This implies that the  $P_y$  component can be produced only by time-reversal violating effects or final-state interactions between particles produced in the semileptonic decay [41]. The firsts can be expected to have the same order of magnitude of  $CP$ -violating effects, which are tiny for  $b \rightarrow c$  transitions, while the latter can only be electromagnetic interactions between  $\Lambda_c^+$  and  $\mu^-$  particles, which are order  $1/\alpha_{EM} \sim \mathcal{O}(1\%)$  at maximum. Therefore, the  $\Lambda_c^+$  polarisation vector is expected to lie basically in the  $x - z$  plane.

## 4.2 Three-body decay phase space

A particle three-body decay is described by 5 degrees of freedom, resulting from 12 four momentum components constrained by 3 mass requirements and 4 energy-momentum conservation relations, which confines the daughters momenta to a plane in the rest frame of the mother particle. For an unpolarised particle, there is no preferred direction in space and the decay is isotropic for rotational invariance. In such a case, the decay plane orientation is irrelevant and the decay is described by two variables only, which are usually chosen to be two of the three available two-body invariant mass-squared (Dalitz variables) since the phase space density is uniform over them. For the  $\Lambda_c^+ \rightarrow pK^-\pi^+$  decay,  $m_{pK^-}^2$  and  $m_{K^-\pi^+}^2$  are selected. For non-zero polarisation the decay is not isotropic and the decay

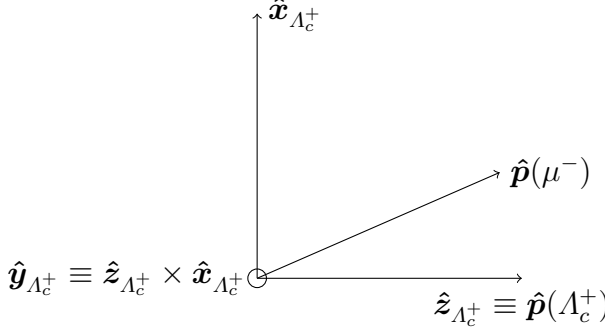


Figure 24: Definition of the  $\Lambda_c^+$  polarisation system. The  $\hat{y}_{\Lambda_c^+}$  axis is orthogonal to the page, towards the reader.

562 spatial orientation must be specified by the three Euler angles describing the rotation  
 563 from the  $\Lambda_c^+$  polarisation system to the decay plane reference system. See Appendix C for  
 564 the definition of Euler rotations.

565 The decay plane (DP) reference system is chosen in such a way that the proton  
 566 momentum defines the  $z$  axis, while the component of the kaon momentum orthogonal to  
 567 the proton momentum defines the  $x$  axis (see Fig. 24 with  $\Lambda_c^+ \leftrightarrow p$ ,  $\mu \leftrightarrow K^-$  substitutions),

$$\begin{aligned}
 \hat{z}_{\text{DP}} &= \hat{\mathbf{p}}(p) \\
 \hat{x}_{\text{DP}} &= \frac{\mathbf{p}(K^-) - [\mathbf{p}(K^-) \cdot \hat{\mathbf{p}}(p)] \hat{\mathbf{p}}(p)}{|\mathbf{p}(K^-) - [\mathbf{p}(K^-) \cdot \hat{\mathbf{p}}(p)] \hat{\mathbf{p}}(p)|} \\
 &= \frac{[\hat{\mathbf{p}}(p) \times \hat{\mathbf{p}}(K^-)] \times \hat{\mathbf{p}}(p)}{|[\hat{\mathbf{p}}(p) \times \hat{\mathbf{p}}(K^-)] \times \hat{\mathbf{p}}(p)|} \\
 \hat{y}_{\text{DP}} &= \hat{z}_{\text{DP}} \times \hat{x}_{\text{DP}} \\
 &= \frac{\mathbf{p}(p) \times \mathbf{p}(K^-)}{|\mathbf{p}(p) \times \mathbf{p}(K^-)|}
 \end{aligned} \tag{21}$$

568 in which the momenta are expressed in the  $\Lambda_c^+$  rest frame. With this definition the  $\alpha$   
 569 Euler angle is the azimuthal angle of the proton in the  $\Lambda_c^+$  polarisation system,  $\phi_p$ , the  $\beta$   
 570 angle is the polar angle of the proton,  $\theta_p$ , and the  $\gamma$  angle is the signed angle formed by  
 571 the proton and the  $\Lambda_c^+$  quantisation axis  $\hat{z}_{\Lambda_c^+}$  and the plane formed by the kaon and the  
 572 pion, named  $\chi$ , Fig. 25. In formulae, following from Eq. (90),

$$\begin{aligned}
 \phi_p &= \text{atan2}(\hat{\mathbf{p}}(p) \cdot \hat{y}_{\Lambda_c^+}, \hat{\mathbf{p}}(p) \cdot \hat{x}_{\Lambda_c^+}) \\
 \theta_p &= \arccos(\hat{\mathbf{p}}(p) \cdot \hat{z}_{\Lambda_c^+}) \\
 \chi &= \text{atan2} \left\{ \hat{z}_{\Lambda_c^+} \cdot \frac{\hat{\mathbf{p}}(p) \times \hat{\mathbf{p}}(K^-)}{|\hat{\mathbf{p}}(p) \times \hat{\mathbf{p}}(K^-)|}, -\hat{z}_{\Lambda_c^+} \cdot \frac{[\hat{\mathbf{p}}(p) \times \hat{\mathbf{p}}(K^-)] \times \hat{\mathbf{p}}(p)}{|[\hat{\mathbf{p}}(p) \times \hat{\mathbf{p}}(K^-)] \times \hat{\mathbf{p}}(p)|} \right\}
 \end{aligned} \tag{22}$$

573 The five phase space variables are therefore chosen to be

$$\Omega = (m_{pK^-}^2, m_{K^-\pi^+}^2, \cos \theta_p, \phi_p, \chi), \tag{23}$$

574 so that the phase space density is uniform over the five variables. Their allowed range  
 575 is  $\cos \theta_p \in [-1, 1]$  and  $\phi_p, \chi \in [-\pi, \pi]$ , while the mass distributions are constrained to a  
 576 rounded-triangle shape in the  $(m_{pK^-}^2, m_{K^-\pi^+}^2)$  plane (Dalitz plot, see Fig. 42).

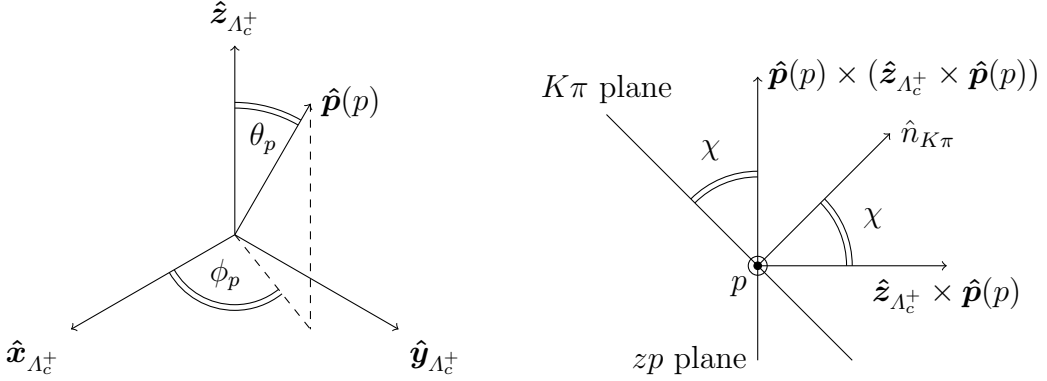


Figure 25: Definition of the Euler angles describing the rotation from the  $\Lambda_c^+$  polarisation system to the decay plane reference system: (left) proton polar and azimuthal angles and (right)  $\chi$  angle.

### 577 4.3 Combination of $CP$ -conjugated events

578 The amplitude fit with extraction of the polarisation vector can be performed separately  
 579 for  $\Lambda_c^+ \rightarrow pK^-\pi^+$  and  $\bar{\Lambda}_c^- \rightarrow \bar{p}K^+\pi^-$  decays, or by merging the two samples under  
 580 the hypothesis of  $CP$  symmetry. In the latter case,  $\Lambda_c^+ \rightarrow pK^-\pi^+$  decays must be  
 581 compared with  $\bar{\Lambda}_c^- \rightarrow \bar{p}K^+\pi^-$  decays in which momenta are reversed. This is possible for  
 582  $\Lambda_c^+ \rightarrow pK^-\pi^+$  decays from semileptonic production because, assuming  $CP$ -symmetry in  
 583 the  $\Lambda_b^0$  decay, the polarisation is expected to be identical for  $\Lambda_c^+$  and  $\bar{\Lambda}_c^-$  baryons<sup>1</sup>. For  
 584 cases in which the baryon production mechanism is different from the antibaryon one,  
 585 as for prompt  $pp$  collisions, the polarisation is in general different between baryon and  
 586 antibaryon, and the two samples can not be combined.

587 The definition of the polarisation system for  $CP$ -conjugated decays, following from  
 588 Eq. (19) substituting  $p(\Lambda_c^+) \rightarrow -p(\bar{\Lambda}_c^-)$  and  $p(\mu^-) \rightarrow -p(\mu^+)$ , is

$$\hat{z}_{\bar{\Lambda}_c^-} = -\hat{z}_{\Lambda_c^+} \quad \hat{x}_{\bar{\Lambda}_c^-} = -\hat{x}_{\Lambda_c^+} \quad \hat{y}_{\bar{\Lambda}_c^-} = \hat{y}_{\Lambda_c^+}, \quad (24)$$

589 that is, with respect to  $\Lambda_c^+$  decays,  $z$  and  $x$  axes are reversed, while the  $y$  axis is the  
 590 same. Similarly, the definition of the decay plane coordinate system Eq. (21), substituting  
 591  $p(p) \rightarrow -p(\bar{p})$  and  $p(K^-) \rightarrow -p(K^+)$  is

$$\hat{z}_{\overline{DP}} = -\hat{z}_{DP} \quad \hat{x}_{\overline{DP}} = -\hat{x}_{DP} \quad \hat{y}_{\overline{DP}} = \hat{y}_{DP}. \quad (25)$$

592 The decay orientation variables for  $\bar{\Lambda}_c^- \rightarrow \bar{p}K^+\pi^-$  decays change due to the different  
 593 definition of polarisation and decay plane systems; following Eq. (22), decay orientation  
 594 angles must be transformed for  $\bar{\Lambda}_c^-$  decays as

$$\theta_{\bar{p}} = \theta_p \quad \phi_{\bar{p}} = -\phi_p \quad \bar{\chi} \rightarrow -\chi. \quad (26)$$

595 In the amplitude fit, the reversal of  $\phi_p$  and  $\chi$  angles is the only transformation to be  
 596 applied to the phase space variables of  $\bar{\Lambda}_c^- \rightarrow \bar{p}K^+\pi^-$  decays; no transformation is needed  
 597 for invariant masses, apart from the charge conjugation substitutions  $m_{pK^-}^2 \rightarrow m_{\bar{p}K^+}^2$  and  
 598  $m_{K^-\pi^+}^2 \rightarrow m_{K^+\pi^-}^2$ .

---

<sup>1</sup>Angular momentum does not change under  $CP$  transformation.

With this definition of the polarisation system for  $CP$ -conjugate decays, the polarisation value must coincide for  $\Lambda_c^+$  and  $\bar{\Lambda}_c^-$  decays, allowing to fit simultaneously the two datasamples. Given the large statistics available, actually there is no need to fit simultaneously  $\Lambda_c^+$  and  $\bar{\Lambda}_c^-$  decays in this analysis:  $\Lambda_c^+ \rightarrow pK^-\pi^+$  decays are used for the nominal amplitude fit, while  $\bar{\Lambda}_c^- \rightarrow \bar{p}K^+\pi^-$  decays are fit separately as a cross-check, Sec. 8.

## 4.4 Amplitude model for the $\Lambda_c^+ \rightarrow pK^-\pi^+$ decay

The amplitude model for the  $\Lambda_c^+ \rightarrow pK^-\pi^+$  decay is built exploiting the helicity formalism described in Sec. 3.1 using two equivalent approaches. Intermediate states can contribute to the decay for all the three possible two-particle systems, so that amplitudes for  $\Lambda_c^+ \rightarrow \Lambda^*(\rightarrow pK^-)\pi^+$ ,  $\Lambda_c^+ \rightarrow \Delta^{++*}(\rightarrow p\pi^+)K^-$  and  $\Lambda_c^+ \rightarrow K^*(\rightarrow K^-\pi^+)p$  decay chains must be considered.

### 4.4.1 Model with Dalitz-plot decomposition

To simplify the amplitude model, it is useful to separate invariant mass and decay orientation angle degrees-of-freedom applying the Dalitz plot decomposition proposed in Ref. [42], which allows to factorise the decay amplitude separating invariant mass and orientation angles dependence. This way, properties following from rotational invariance are enforced. For the  $\Lambda_c^+ \rightarrow pK^-\pi^+$  decay the decomposition is written as

$$\mathcal{A}_{m_{\Lambda_c^+}, m_p}(\Omega) = \sum_{\nu_{\Lambda_c^+}} D_{m_{\Lambda_c^+}, \nu_{\Lambda_c^+}}^{*1/2}(\phi_p, \theta_p, \chi) \mathcal{O}_{\nu_{\Lambda_c^+}, m_p}(m_{pK^-}^2, m_{K^-\pi^+}^2), \quad (27)$$

in which the Wigner  $D$  matrix describes the rotation of the  $\Lambda_c^+$  spin states from the polarisation system Eq. (19),  $|1/2, m_{\Lambda_c^+}\rangle$ , to the decay plane system Eq. (21),  $|1/2, \nu_{\Lambda_c^+}\rangle$ . The term  $\mathcal{O}_{\nu_{\Lambda_c^+}, m_p}(m_{pK^-}^2, m_{K^-\pi^+}^2)$  describes the  $\Lambda_c^+$  decay amplitude in terms of  $\Lambda_c^+$  spin states  $|1/2, \nu_{\Lambda_c^+}\rangle$  and proton states defined in the canonical spin system reached from the  $\Lambda_c^+$  decay plane system,  $|1/2, m_p\rangle$ . These proton states are needed for the matching of proton spin states among different decay chains.

Let's first consider the decay chain  $\Lambda_c^+ \rightarrow pK^*(\rightarrow K^-\pi^+)$ . The weak decay  $\Lambda_c^+ \rightarrow pK^*$  can be described by Eq. (9) applied starting from the decay plane coordinate system,

$$\mathcal{A}_{\nu_{\Lambda_c^+}, m_p, \bar{\lambda}_{K^*}}^{\Lambda_c^+ \rightarrow pK^*} = \mathcal{H}_{m_p, \bar{\lambda}_{K^*}}^{\Lambda_c^+ \rightarrow pK^*} \delta_{\nu_{\Lambda_c^+}, m_p + \bar{\lambda}_{K^*}}, \quad (28)$$

in which the decay plane coordinate system is used to express spin states, so that the amplitude is written in terms of the proton helicity  $m_p$  and the  $K^*$  opposite helicity  $\bar{\lambda}_{K^*}$ . Since no rotation of spin states is involved, the  $D$ -matrix becomes a constraint on the helicity values  $m_p + \bar{\lambda}_{K^*} = \nu_{\Lambda_c^+}$ .

For spin zero  $K^*$  resonances the angular momentum conservation relations Eq. (11) allow two complex couplings corresponding to  $m_p = \pm 1/2$ , for higher spin resonances four couplings are allowed, corresponding to  $\{m_p = 1/2; \bar{\lambda}_{K^*} = 0, -1\}$  and  $\{m_p = -1/2; \bar{\lambda}_{K^*} = 0, 1\}$ . The couplings are independent of each other because of parity violation in weak decays. The strong decay  $K^* \rightarrow K^-\pi^+$  contribution is

$$\mathcal{A}_{\bar{\lambda}_{K^*}}^{K^* \rightarrow K^-\pi^+} = \mathcal{H}_{0,0}^{K^* \rightarrow K^-\pi^+} d_{\bar{\lambda}_{K^*}, 0}^{*J_{K^*}}(\bar{\theta}_K) \mathcal{R}(m_{K^-\pi^+}^2), \quad (29)$$

in which  $\mathcal{R}(m_{K^-\pi^+}^2)$  is the lineshape of the  $K^*$  resonance and  $\bar{\theta}_K$  is the kaon momentum signed polar angle in the  $K^*$  opposite-helicity coordinate system,

$$\bar{\theta}_K = \text{atan2}\left(p_x^{K^*}(K^-), p_z^{K^*}(K^-)\right). \quad (30)$$

Signed polar angles are used as helicity angles in order to have rotations only around the  $y$  axis of the decay plane system<sup>2</sup>.

In the fit model the coupling  $\mathcal{H}_{0,0}^{K^*\rightarrow K^-\pi^+}$  can not be determined independently of  $\mathcal{H}_{m_p, \bar{\lambda}_{K^*}}^{A_c^+\rightarrow K^*p}$  couplings, therefore it is set equal to 1 and absorbed into the latter.

Considering the decay chain  $A_c^+ \rightarrow A^*(\rightarrow pK^-)\pi^+$ , the weak decay  $A_c^+ \rightarrow A^*\pi^+$  is described by Eq. (9) as

$$\mathcal{A}_{\nu_{A_c^+}, \lambda_{A^*}}^{A_c^+\rightarrow A^*\pi^+} = \mathcal{H}_{\lambda_{A^*}, 0}^{A_c^+\rightarrow A^*\pi^+} d_{\nu_{A_c^+}, \lambda_{A^*}}^{1/2}(\theta_{A^*}), \quad (31)$$

in which  $\lambda_{A^*}$  is the  $A^*$  helicity system reached from the  $A_c^+$  system and  $\theta_{A^*}$  is the signed polar angle of the  $A^*$  momentum, defined as

$$\theta_{A^*} = \text{atan2}\left(p_x^{A_c^+}(A^*), p_z^{A_c^+}(A^*)\right). \quad (32)$$

The angular momentum conservation relations Eq. (11) allow two helicity couplings,  $\lambda_{A^*} = \pm 1/2$ , to fit for each resonance whatever  $J_{A^*}$  is.

The strong decay  $A^* \rightarrow pK^-$  is described by

$$\mathcal{A}_{\lambda_{A^*}, \lambda_p^{A^*}}^{A^*\rightarrow pK^-} = \mathcal{H}_{\lambda_{A^*}, 0}^{A^*\rightarrow pK^-} d_{\lambda_{A^*}, \lambda_p^{A^*}}^{J_{A^*}}(\theta_p^{A^*}) \mathcal{R}(m_{pK^-}^2), \quad (33)$$

in which  $\lambda_p^{A^*}$  is the proton helicity,  $\theta_p^{A^*}$  the proton signed polar angle in the helicity coordinate system reached from the  $A^*$  resonance, while  $\mathcal{R}(m_{pK^-}^2)$  is the lineshape of the  $A^*$  resonance. Since strong decays conserve parity the two helicity couplings corresponding to  $\lambda_p^{A^*} = \pm 1/2$  are related by Eq. (12),

$$\mathcal{H}_{-\lambda_p^{A^*}, 0}^{A^*\rightarrow pK^-} = -P_{A^*}(-1)^{J_{A^*}-1/2} \mathcal{H}_{\lambda_p^{A^*}, 0}^{A^*\rightarrow pK^-}, \quad (34)$$

in which  $P_{A^*}$  is the parity of the  $A^*$  resonance and the proton and kaon parities  $P_p = 1$ ,  $P_K = -1$  have been inserted. In the fit model these couplings can not be determined independently of  $\mathcal{H}_{\lambda_{A^*}, 0}^{A_c^+\rightarrow A^*\pi^+}$  couplings, so that they are absorbed into the latter setting them as  $\mathcal{H}_{+1/2, 0}^{A^*\rightarrow pK^-} = 1$  and  $\mathcal{H}_{-1/2, 0}^{A^*\rightarrow pK^-} = -P_{A^*}(-1)^{J_{A^*}-1/2}$ , with zero imaginary parts.

The matching of proton spin states from the  $A^*$  helicity system to the canonical system it is performed applying the method of Ref. [37] to the case of the Dalitz-plot decomposition. Indeed, the transformation sequence applied to reach the proton helicity system must be undone step-by-step in order to ensure a consistent phase definition of fermion spin states. Three rotations must be applied to the proton spin system: two of angles  $\theta_p^{A^*}$  and  $\theta_{A^*}$ , plus the Wigner rotation accounting for the different boost sequence applied to reach the two systems. The Wigner rotation can be written in angle-axis decomposition [43], with angle

$$\alpha_{A^*}^W = \arccos \left[ \frac{\left(1 + \gamma_p^{A_c^+} + \gamma_{A^*}^{A_c^+} + \gamma_p^{A^*}\right)^2}{(1 + \gamma_p^{A_c^+})(1 + \gamma_{A^*}^{A_c^+})(1 + \gamma_p^{A^*})} - 1 \right], \quad (35)$$

---

<sup>2</sup>Otherwise, the use of positive polar angles would require additional azimuthal rotations around the  $z$  axis (to flip the  $y$  axis direction) complicating unnecessarily the expression of the helicity amplitudes.

663 and axis

$$\mathbf{a}_{\Lambda^*}^W = \frac{\mathbf{p}^{A_c^+}(\Lambda^*) \times \mathbf{p}^{\Lambda^*}(p)}{|\mathbf{p}^{A_c^+}(\Lambda^*) \times \mathbf{p}^{\Lambda^*}(p)|} = \hat{\mathbf{y}}_{\text{DP}}, \quad (36)$$

664 which coincides with the  $y$  axis of the decay plane coordinate system. All these rotations are  
665 around the same  $y$  axis, so they can be combined into just one rotation  $R_y(\theta_p^{\Lambda^*} + \theta_{\Lambda^*} + \alpha_{\Lambda^*}^W)$ .

666 Considering the third decay chain  $\Lambda_c^+ \rightarrow \Delta^{++*} (\rightarrow p\pi^+) K^-$ , the weak decay  $\Lambda_c^+ \rightarrow$   
667  $\Delta^{++*} K^-$  is described by

$$\mathcal{A}_{\nu_{\Lambda_c^+}, \lambda_{\Delta^*}}^{\Lambda_c^+ \rightarrow \Delta^{++*} K^-} = \mathcal{H}_{\lambda_{\Delta^*}, 0}^{\Lambda_c^+ \rightarrow \Delta^{++*} K^-} d_{\nu_{\Lambda_c^+}, \lambda_{\Delta^*}}^{1/2}(\theta_{\Delta^*}), \quad (37)$$

668 in which  $\lambda_{\Delta^*}$  is the  $\Delta^*$  helicity and  $\theta_{\Delta^*}$  is the signed polar angle of the  $\Delta^*$  momentum in  
669 the  $\Lambda_c^+$  rest frame with decay plane coordinate system. As for the  $\Lambda^*$  decay chain, there  
670 are two helicity couplings corresponding to  $\lambda_{\Delta^*} = \pm 1/2$  to fit for each resonance. The  
671 strong decay  $\Delta^{++*} \rightarrow p\pi^+$  amplitude is written as

$$\mathcal{A}_{\lambda_{\Delta^*}, \lambda_p^{\Delta^*}}^{\Delta^{++*} \rightarrow p\pi^+} = \mathcal{H}_{\lambda_{\Delta^*}, 0}^{\Delta^{++*} \rightarrow p\pi^+} d_{\lambda_{\Delta^*}, \lambda_p^{\Delta^*}}^{J_{\Delta^*}}(\theta_p^{\Delta^*}) \mathcal{R}(m_{p\pi^+}^2), \quad (38)$$

672 in which  $\lambda_p^{\Delta^*}$  is the proton helicity and  $\theta_p^{\Delta^*}$  the signed polar angle defined in the  $\Delta^*$  helicity  
673 coordinate system. In the fit model the strong decay helicity couplings are absorbed into  
674  $\mathcal{H}_{\lambda_{\Delta^*}, 0}^{\Lambda_c^+ \rightarrow \Delta^{++*} K^-}$  setting them to  $\mathcal{H}_{+1/2, 0}^{\Delta^{++*} \rightarrow p\pi^+} = 1$  and  $\mathcal{H}_{-1/2, 0}^{\Delta^{++*} \rightarrow p\pi^+} = -P_{\Delta^*}(-1)^{J_{\Delta^*}-1/2}$ .

675 The matching of proton spin states from the  $\Delta^*$  helicity system to the canonical system  
676 is performed similarly to the  $\Lambda^*$  decay chain. The Wigner rotation angle is

$$\alpha_{\Delta^*}^W = \arccos \left[ \frac{\left(1 + \gamma_p^{A_c^+} + \gamma_{\Delta^*}^{A_c^+} + \gamma_p^{\Delta^*}\right)^2}{(1 + \gamma_p^{A_c^+})(1 + \gamma_{\Delta^*}^{A_c^+})(1 + \gamma_p^{\Delta^*})} - 1 \right], \quad (39)$$

677 around the axis

$$\mathbf{a}_{\Delta^*}^W = \frac{\mathbf{p}^{A_c^+}(\Delta^*) \times \mathbf{p}^{\Delta^*}(p)}{|\mathbf{p}^{A_c^+}(\Delta^*) \times \mathbf{p}^{\Delta^*}(p)|} = -\hat{\mathbf{y}}_{\text{DP}}, \quad (40)$$

678 which is opposite to the  $y$  axis of the decay plane coordinate system. Therefore, the  
679 proton spin rotation can be written as  $R_y(\theta_p^{\Delta^*} + \theta_{\Delta^*} - \alpha_{\Delta^*}^W)$ , with reversed Wigner angle  
680 sign.

681 The decay amplitudes for each decay chain are the product of the two two-body decay  
682 amplitudes, summed over the proton helicities for  $\Lambda^*$  and  $\Delta^*$  chains,

$$\begin{aligned} \mathcal{A}_{\nu_{\Lambda_c^+}, m_p, \bar{\lambda}_{K^*}}^{K^*} &= \mathcal{H}_{m_p, \bar{\lambda}_{K^*}}^{\Lambda_c^+ \rightarrow pK^*} \delta_{\nu_{\Lambda_c^+}, m_p + \bar{\lambda}_{K^*}} d_{\bar{\lambda}_{K^*}, 0}^{J_{K^*}}(\bar{\theta}_K) \mathcal{R}(m_{K^-\pi^+}^2) \\ \mathcal{A}_{\nu_{\Lambda_c^+}, \lambda_{\Lambda^*}, m_p}^{\Lambda^*} &= \sum_{\lambda_p^{\Lambda^*}} d_{m_p, \lambda_p^{\Lambda^*}}^{1/2}(\theta_p^{\Lambda^*} + \theta_{\Lambda^*} + \alpha_{\Lambda^*}^W) \\ &\quad \times \mathcal{H}_{\lambda_{\Lambda^*}, 0}^{\Lambda_c^+ \rightarrow \Lambda^*\pi^+} d_{\nu_{\Lambda_c^+}, \lambda_{\Lambda^*}}^{1/2}(\theta_{\Lambda^*}) d_{\lambda_{\Lambda^*}, \lambda_p^{\Lambda^*}}^{J_{\Lambda^*}}(\theta_p^{\Lambda^*}) \mathcal{R}(m_{pK^-}^2) \\ \mathcal{A}_{\nu_{\Lambda_c^+}, \lambda_{\Delta^*}, m_p}^{\Delta^{++*}} &= \sum_{\lambda_p^{\Delta^*}} d_{m_p, \lambda_p^{\Delta^*}}^{1/2}(\theta_p^{\Delta^*} + \theta_{\Delta^*} - \alpha_{\Delta^*}^W) \\ &\quad \times \mathcal{H}_{\lambda_{\Delta^*}, 0}^{\Lambda_c^+ \rightarrow \Delta^{++*} K^-} d_{\nu_{\Lambda_c^+}, \lambda_{\Delta^*}}^{1/2}(\theta_{\Delta^*}) d_{\lambda_{\Delta^*}, \lambda_p^{\Delta^*}}^{J_{\Delta^*}}(\theta_p^{\Delta^*}) \mathcal{R}(m_{p\pi^+}^2). \end{aligned} \quad (41)$$

683 It is important to stress that all the signed polar angles on which the amplitude depends  
 684 do not constitute independent degrees of freedom, being function of  $m_{pK^-}^2$  and  $m_{K^-\pi^+}^2$   
 685 invariant masses.

686 The complete amplitude for the  $\Lambda_c^+ \rightarrow pK^-\pi^+$  decay is obtained summing the ampli-  
 687 tudes for all the intermediate resonances and their allowed helicity states,

$$\begin{aligned} \mathcal{O}_{\nu_{\Lambda_c^+}, m_p}(m_{pK^-}^2, m_{K^-\pi^+}^2) &= \sum_{i=1}^{N_{K^*}} \sum_{\bar{\lambda}_{K^*}} \mathcal{A}_{\nu_{\Lambda_c^+}, m_p, \bar{\lambda}_{K^*}}^{K_i^*} \\ &+ \sum_{j=1}^{N_{\Lambda^*}} \sum_{\lambda_{\Lambda^*}} \mathcal{A}_{\nu_{\Lambda_c^+}, \lambda_{\Lambda^*}, m_p}^{\Lambda_j^*} \\ &+ \sum_{k=1}^{N_{\Delta^{++*}}} \sum_{\lambda_{\Delta^{++*}}} \mathcal{A}_{\nu_{\Lambda_c^+}, \lambda_{\Delta^{++*}}, m_p}^{\Delta_k^{++*}}. \end{aligned} \quad (42)$$

#### 688 4.4.2 Model without Dalitz-plot decomposition

689 An equivalent amplitude model is written without Dalitz-plot decomposition, applying  
 690 helicity transformations directly from the  $\Lambda_c^+$  polarisation system without referring to  
 691 the decay plane. This way, invariant mass and decay orientation degrees of freedom are  
 692 mixed; moreover, the functional form of the amplitude model is more complicated, since  
 693 helicity transformations are not forced to act within the decay plane. Nonetheless, it  
 694 is worth considering this model as a useful cross-check because the properties following  
 695 from rotational invariance are no more ensured by construction, so that any issue in the  
 696 implementation of the model would show up by breaking these properties.

697 The  $\Lambda_c^+ \rightarrow pK^-\pi^+$  amplitude model without Dalitz-plot decomposition considered  
 698 follows the three-body decay model described in Ref. [37], adapted to the  $\Lambda_c^+ \rightarrow pK^-\pi^+$   
 699 decay case.

700 Starting from the decay chain  $\Lambda_c^+ \rightarrow pK^*(\rightarrow K^-\pi^+)$ , the weak decay  $\Lambda_c^+ \rightarrow pK^*$  is  
 701 described by

$$\mathcal{A}_{m_{\Lambda_c^+}, \lambda_p, \bar{\lambda}_{K^*}}^{\Lambda_c^+ \rightarrow pK^*} = \mathcal{H}_{\lambda_p, \bar{\lambda}_{K^*}}^{\Lambda_c^+ \rightarrow pK^*} D_{m_{\Lambda_c^+}, \lambda_p + \bar{\lambda}_{K^*}}^{*1/2}(\phi_p, \theta_p, 0), \quad (43)$$

702 in which proton and  $K^*$  helicities  $\lambda_p$  and  $\bar{\lambda}_{K^*}$  are defined in the proton helicity system  
 703 reached from the  $\Lambda_c^+$  baryon polarisation system. The number of allowed helicity couplings  
 704 is the same as for the other model in Sec. 4.4.1, however the definition of the couplings  
 705 is different from before, since they refer to different helicity systems. The strong decay  
 706  $K^* \rightarrow K^-\pi^+$  contribution is

$$\mathcal{A}_{\bar{\lambda}_{K^*}}^{K^* \rightarrow K^-\pi^+} = \mathcal{H}_{0,0}^{K^* \rightarrow K^-\pi^+} D_{\bar{\lambda}_{K^*}, 0}^{*J_{K^*}}(\bar{\phi}_K, \bar{\theta}_K, 0) \mathcal{R}(m_{K^-\pi^+}^2), \quad (44)$$

707 in which  $\bar{\phi}_K$  and  $\bar{\theta}_K$  are the kaon azimuthal and polar angles in the  $K^*$  opposite-helicity  
 708 system. The coupling  $\mathcal{H}_{0,0}^{K^* \rightarrow K^-\pi^+}$  is set to 1 as in Sec. 4.4.1. The transformation of proton  
 709 helicity states  $\lambda_p$  to canonical ones  $m_p$ , is simple since only one rotation  $R(\phi_p, \theta_p, 0)$  has  
 710 to be applied.

711 Considering the decay chain  $\Lambda_c^+ \rightarrow \Lambda^*(\rightarrow pK^-)\pi^+$ , the weak decay  $\Lambda_c^+ \rightarrow \Lambda^*\pi^+$  is  
 712 described by

$$\mathcal{A}_{m_{\Lambda_c^+}, \lambda_{\Lambda^*}}^{\Lambda_c^+ \rightarrow \Lambda^*\pi^+} = \mathcal{H}_{\lambda_{\Lambda^*}, 0}^{\Lambda_c^+ \rightarrow \Lambda^*\pi^+} D_{m_{\Lambda_c^+}, \lambda_{\Lambda^*}}^{*1/2}(\phi_{\Lambda^*}, \theta_{\Lambda^*}, 0), \quad (45)$$

713 with  $\lambda_{A^*}$  the  $A^*$  helicity and  $\theta_{A^*}, \phi_{A^*}$  the polar and azimuthal angles of the  $A^*$  momentum,  
 714 in the  $\Lambda_c^+$  polarisation system. The strong decay  $A^* \rightarrow pK^-$  is described by

$$\mathcal{A}_{\lambda_{A^*}, \lambda_p^{A^*}}^{A^* \rightarrow pK^-} = \mathcal{H}_{\lambda_p^{A^*}, 0}^{A^* \rightarrow pK^-} D_{\lambda_{A^*}, \lambda_p^{A^*}}^{*J_{A^*}}(\phi_p^{A^*}, \theta_p^{A^*}, 0) \mathcal{R}(m_{pK^-}^2), \quad (46)$$

715 with  $\phi_p^{A^*}$  and  $\theta_p^{A^*}$  the azimuthal and polar angles of the proton momentum in the  $A^*$   
 716 helicity system and  $\lambda_p^{A^*}$  the proton helicity in the system reached from the  $A^*$  resonance.  
 717 Helicity couplings corresponding to  $\lambda_p^{A^*} = \pm 1/2$  are related by Eq. (12) and absorbed into  
 718 the weak decay ones as in Sec. 4.4.1.

719 Three rotations must be applied to the proton helicity states  $\lambda_p^{A^*}$  to obtain canonical  
 720 states  $m_p$ : two related to the helicity transformations,  $R(\phi_p^{A^*}, \theta_p^{A^*}, 0)$  and  $R(\phi_{A^*}, \theta_{A^*}, 0)$ ,  
 721 plus a Wigner rotation accounting for the different boost sequence applied. The Wigner  
 722 rotation expressed using the axis-angle expressions [43] is written as an Euler rotation  
 723  $R(\alpha_{A^*}^W, \beta_{A^*}^W, \gamma_{A^*}^W)$ , with angles calculated applying Eq. (90) between original and Wigner-  
 724 rotated systems.

725 Considering the third decay chain  $\Lambda_c^+ \rightarrow \Delta^{++*} (\rightarrow p\pi^+) K^-$ , the weak decay  $\Lambda_c^+ \rightarrow$   
 726  $\Delta^{++*} K^-$  is described by

$$\mathcal{A}_{m_{\Lambda_c^+}, \lambda_{\Delta^*}}^{\Lambda_c^+ \rightarrow \Delta^{++*} K^-} = \mathcal{H}_{\lambda_{\Delta^*}, 0}^{\Lambda_c^+ \rightarrow \Delta^{++*} K^-} D_{m_{\Lambda_c^+}, \lambda_{\Delta^*}}^{*1/2}(\phi_{\Delta^*}, \theta_{\Delta^*}, 0), \quad (47)$$

727 with  $\lambda_{\Delta^*}$  the  $\Delta^*$  helicity and  $\theta_{\Delta^*}, \phi_{\Delta^*}$  the polar and azimuthal angles of the  $\Delta^*$  momentum,  
 728 in the  $\Lambda_c^+$  polarisation system. The strong decay  $\Delta^{++*} \rightarrow p\pi^+$  amplitude is written as

$$\mathcal{A}_{\lambda_{\Delta^*}, \lambda_p^{\Delta^*}}^{\Delta^{++*} \rightarrow p\pi^+} = \mathcal{H}_{\lambda_p^{\Delta^*}, 0}^{\Delta^{++*} \rightarrow p\pi^+} D_{\lambda_{\Delta^*}, \lambda_p^{\Delta^*}}^{*J_{\Delta^*}}(\phi_p^{\Delta^*}, \theta_p^{\Delta^*}, 0) \mathcal{R}(m_{p\pi^+}^2), \quad (48)$$

729 with  $\phi_p^{\Delta^*}$  and  $\theta_p^{\Delta^*}$  the azimuthal and polar angles of the proton momentum in the  $\Delta^*$   
 730 helicity system and  $\lambda_p^{\Delta^*}$  the proton helicity in the system reached from the  $\Delta^*$  resonance.  
 731 Helicity couplings are defined as for the  $A^*$  decay chain. Also the transformation of proton  
 732 helicity states  $\lambda_p^{\Delta^*}$  to canonical states  $m_p$  is analogous, done applying three rotations  
 733  $R(\phi_p^{\Delta^*}, \theta_p^{\Delta^*}, 0)$ ,  $R(\phi_{\Delta^*}, \theta_{\Delta^*}, 0)$  and the Wigner rotation  $R(\alpha_{\Delta^*}^W, \beta_{\Delta^*}^W, \gamma_{\Delta^*}^W)$ .

734 The decay amplitudes for each decay chain are the product of the two two-body decay  
 735 amplitudes for each decay chain, to which the specific sequential proton spin rotations are  
 736 applied

$$\begin{aligned} \mathcal{A}_{\nu_{\Lambda_c^+}, m_p, \bar{\lambda}_{K^*}}^{K^*} &= \sum_{\lambda_p} D_{m_p, \lambda_p}^{1/2}(\phi_p, \theta_p, 0) \\ &\times \mathcal{H}_{\lambda_p, \bar{\lambda}_{K^*}}^{\Lambda_c^+ \rightarrow pK^*} D_{m_{\Lambda_c^+}, \lambda_p + \bar{\lambda}_{K^*}}^{*1/2}(\phi_p, \theta_p, 0) D_{\bar{\lambda}_{K^*}, 0}^{*J_{K^*}}(\bar{\phi}_K, \bar{\theta}_K, 0) \mathcal{R}(m_{K^-\pi^+}^2) \\ \mathcal{A}_{\nu_{\Lambda_c^+}, \lambda_{A^*}, m_p}^{A^*} &= \sum_{\lambda_p^{A^*}, \mu_p^{A^*}, \nu_p^{A^*}} D_{m_p, \nu_p^{A^*}}^{1/2}(\alpha_{A^*}^W, \beta_{A^*}^W, \gamma_{A^*}^W) D_{\nu_p^{A^*}, \mu_p^{A^*}}^{1/2}(\phi_{A^*}, \theta_{A^*}, 0) D_{\mu_p^{A^*}, \lambda_p^{A^*}}^{1/2}(\phi_p^{A^*}, \theta_p^{A^*}, 0) \\ &\times \mathcal{H}_{\lambda_{A^*}, 0}^{\Lambda_c^+ \rightarrow A^*\pi^+} D_{m_{\Lambda_c^+}, \lambda_{A^*}}^{*1/2}(\phi_{A^*}, \theta_{A^*}, 0) D_{\lambda_{A^*}, \lambda_p^{A^*}}^{*J_{A^*}}(\phi_p^{A^*}, \theta_p^{A^*}, 0) \mathcal{R}(m_{pK^-}^2) \\ \mathcal{A}_{\nu_{\Lambda_c^+}, \lambda_{\Delta^*}, m_p}^{\Delta^{++*}} &= \sum_{\lambda_p^{\Delta^*}, \mu_p^{\Delta^*}, \nu_p^{\Delta^*}} D_{m_p, \nu_p^{\Delta^*}}^{1/2}(\alpha_{\Delta^*}^W, \beta_{\Delta^*}^W, \gamma_{\Delta^*}^W) D_{\nu_p^{\Delta^*}, \mu_p^{\Delta^*}}^{1/2}(\phi_{\Delta^*}, \theta_{\Delta^*}, 0) D_{\mu_p^{\Delta^*}, \lambda_p^{\Delta^*}}^{1/2}(\phi_p^{\Delta^*}, \theta_p^{\Delta^*}, 0) \\ &\times \mathcal{H}_{\lambda_{\Delta^*}, 0}^{\Lambda_c^+ \rightarrow \Delta^{++*} K^-} D_{m_{\Lambda_c^+}, \lambda_{\Delta^*}}^{*1/2}(\phi_{\Delta^*}, \theta_{\Delta^*}, 0) D_{\lambda_{\Delta^*}, \lambda_p^{\Delta^*}}^{*J_{\Delta^*}}(\phi_p^{\Delta^*}, \theta_p^{\Delta^*}, 0) \mathcal{R}(m_{p\pi^+}^2). \end{aligned} \quad (49)$$

in which  $\mu_p^{A^*}, \nu_p^{A^*}, \mu_p^{\Delta^*}, \nu_p^{\Delta^*}$  represent intermediate proton helicity states; their physical meaning is explained in Ref. [37]. The complete amplitude for the  $\Lambda_c^+ \rightarrow pK^-\pi^+$  decay is obtained summing the amplitudes for all the intermediate resonances and their allowed helicity states as in Eq. (42).

## 4.5 Polarised decay rate

The differential decay rate for  $\Lambda_c^+$  baryons in a generic state of polarisation to be measured from the amplitude fit, is given by Eq. (18). The most general spin 1/2 density matrix is

$$\rho^{\Lambda_c^+} = \frac{1}{2} (\mathbb{I} + \boldsymbol{P} \cdot \boldsymbol{\sigma}) = \frac{1}{2} \begin{pmatrix} 1 + P_z & P_x - iP_y \\ P_x + iP_y & 1 - P_z \end{pmatrix}, \quad (50)$$

in which  $P_x, P_y, P_z$  are the polarisation components in the polarisation system Sec. 4.1 and  $\boldsymbol{\sigma}$  the three Pauli matrices. The density matrix representing the  $pK^-\pi^+$  polarisation is that of a maximally mixed state (in any proton spin basis)

$$\rho^{pK^-\pi^+} = \frac{\mathbb{I}}{2}, \quad (51)$$

since the proton polarisation can not be measured.

The transition operator matrix elements in the  $\Lambda_c^+$  and proton spin bases are the helicity amplitudes  $\mathcal{A}_{m_{\Lambda_c^+}, \lambda_p}(\Omega)$

$$T = \begin{pmatrix} \mathcal{A}_{1/2,1/2}(\Omega) & \mathcal{A}_{1/2,-1/2}(\Omega) \\ \mathcal{A}_{-1/2,1/2}(\Omega) & \mathcal{A}_{-1/2,-1/2}(\Omega) \end{pmatrix}, \quad (52)$$

and the differential rate Eq. (18) turns out to be proportional to

$$\begin{aligned} p(\Omega, \vec{P}) \propto & \sum_{\lambda_p=\pm 1/2} [(1 + P_z)|\mathcal{A}_{1/2,\lambda_p}(\Omega)|^2 + (1 - P_z)|\mathcal{A}_{-1/2,\lambda_p}(\Omega)|^2 \\ & + (P_x - iP_y)\mathcal{A}_{1/2,\lambda_p}^*(\Omega)\mathcal{A}_{-1/2,\lambda_p}(\Omega) \\ & + (P_x + iP_y)\mathcal{A}_{1/2,\lambda_p}(\Omega)\mathcal{A}_{-1/2,\lambda_p}^*(\Omega)]. \end{aligned} \quad (53)$$

The properties of the decay rate following from rotational invariance described in Sec. 3.3 are apparent from the properties of the  $D$  rotation matrices when applying the Dalitz plot decomposition Eq. (27) to Eq. (53),

$$\begin{aligned} p(\Omega, \vec{P}) \propto & \sum_{m_{\Lambda_c^+}, m'_{\Lambda_c^+}} \rho_{m_{\Lambda_c^+}, m'_{\Lambda_c^+}} \sum_{\nu_{\Lambda_c^+}, \nu'_{\Lambda_c^+}} D_{m_{\Lambda_c^+}, \nu_{\Lambda_c^+}}^{*1/2}(\cos \theta_p, \phi_p, \chi) D_{m'_{\Lambda_c^+}, \nu'_{\Lambda_c^+}}^{1/2}(\cos \theta_p, \phi_p, \chi) \\ & \times \sum_{\lambda_p} \mathcal{O}_{\nu_{\Lambda_c^+}, m_p}(m_{pK^-}^2, m_{K^-\pi^+}^2) \mathcal{O}_{\nu'_{\Lambda_c^+}, m_p}(m_{pK^-}^2, m_{K^-\pi^+}^2). \end{aligned} \quad (54)$$

For unpolarised baryons,  $\rho_{m_{\Lambda_c^+}, m'_{\Lambda_c^+}} = \delta_{m_{\Lambda_c^+}, m'_{\Lambda_c^+}}/2$ , isotropy follows from the orthogonality of the rotation operators

$$\sum_{m_{\Lambda_c^+}} D_{m_{\Lambda_c^+}, \nu_{\Lambda_c^+}}^{*1/2}(\cos \theta_p, \phi_p, \chi) D_{m_{\Lambda_c^+}, \nu'_{\Lambda_c^+}}^{1/2}(\cos \theta_p, \phi_p, \chi) \propto \delta_{\nu_{\Lambda_c^+}, \nu'_{\Lambda_c^+}}, \quad (55)$$

756 while the independence of invariant mass distributions from the polarisation vector follows  
 757 from the orthogonality relation

$$\int_{-\pi}^{\pi} d\phi_p \int_{-\pi}^{\pi} d\chi \int_0^{\pi} d\cos\theta_p D_{m_{\Lambda_c^+}^{*1/2}, \nu_{\Lambda_c^+}}^{1/2}(\cos\theta_p, \phi_p, \chi) D_{m'_{\Lambda_c^+}, \nu'_{\Lambda_c^+}}^{1/2}(\cos\theta_p, \phi_p, \chi) \propto \delta_{m,m'} \delta_{\nu,\nu'}. \quad (56)$$

## 758 4.6 Relation between amplitude model determination and po- 759 larisation measurement

760 The possibility of determining simultaneously the  $\Lambda_c^+ \rightarrow pK^-\pi^+$  amplitude model and  
 761 the  $\Lambda_c^+$  polarization vector has been demonstrated in Ref. [3], here, the relation between  
 762 the two is discussed.

763 Eq. (27) shows how the five phase space degrees-of-freedom of the  $\Lambda_c^+ \rightarrow pK^-\pi^+$   
 764 decay can be separated between Dalitz squared invariant masses  $m_{pK^-}^2$ ,  $m_{K^-\pi^+}^2$  and decay  
 765 orientation angles  $\theta_p, \phi_p, \chi$ . All the information about the amplitude model is contained in  
 766 the  $\mathcal{O}_{\nu_{\Lambda_c^+}, m_p}(m_{pK^-}^2, m_{K^-\pi^+}^2)$  term, which, depending uniquely on squared invariant masses,  
 767 is independent on both the polarisation vector and the polarisation frame definition.  
 768 Different definitions of the latter lead to different values of the decay orientation angles  
 769 and of the polarisation vector, but can not lead to different amplitude models.

770 The magnitude of the polarisation vector influences the sensitivity to the parity-  
 771 violating part of the amplitude model, instead. The larger the polarisation, the better the  
 772 precision on such amplitude model component; in particular, in absence of polarisation  
 773 (or, equivalently, when performing a Dalitz plot fit ignoring decay orientation angles  
 774 degrees-of-freedom) the parity-violating part of the  $\Lambda_c^+ \rightarrow pK^-\pi^+$  amplitude model can  
 775 not be determined [3].

776 In the present analysis, the independence of the amplitude model determination on  
 777 the polarisation frame definition is explicitly tested, see Secs. 6.9 and 8.

## 778 5 Test and comparison of amplitude models written 779 with different proton spin matching methods

780 In this section,  $\Lambda_c^+ \rightarrow pK^-\pi^+$  amplitude models written with different proton spin  
 781 matching methods are tested and compared.

782 These amplitude models are tested using a toy description of the  $\Lambda_c^+ \rightarrow pK^-\pi^+$   
 783 decay including one resonance per decay channel, with spin-parity  $J^P$  assignments  $K^*(1^-)$ ,  
 784  $\Lambda^*(1/2^-)$  and  $\Delta^*(1/2^-)$ . The values of the helicity couplings and the resonance parameters  
 785 have been chosen in such a way to have non-negligible interference effects; these are reported  
 786 in Table 6. Relativistic Breit-Wigner lineshapes have been used.

787 First, we consider two amplitude models in which helicity transformations are performed  
 788 directly from the  $\Lambda_c^+$  polarisation system: the one described in Sec. 4.4.2 (denoted PF)  
 789 and one in which the proton spin has been matched according to the method used in  
 790 Refs. [44, 45] (denoted PQ). For the  $\Lambda_c^+ \rightarrow pK^-\pi^+$  case, the latter method consists  
 791 in applying a single rotation to the proton states aligning their quantisation axes to a  
 792 reference one, which are defined as the direction opposite to the momentum of the particle

Parameter	Value
$K^*(1^-)$	
$\mathcal{H}_{1/2,0}$	1
$\mathcal{H}_{1/2,-1}$	$0.5 + 0.5i$
$\mathcal{H}_{-1/2,1}$	$i$
$\mathcal{H}_{-1/2,0}$	$-0.5 - 0.5i$
BW $m$	0.9 GeV
BW $\Gamma$	0.2 GeV
$J^P$	$1^+$
$\Lambda^*(1/2^-)$	
$\mathcal{H}_{-1/2,0}$	$i$
$\mathcal{H}_{1/2,0}$	$0.8 - 0.4i$
BW $m$	1.6 GeV
BW $\Gamma$	0.2 GeV
$J^P$	$1/2^-$
$\Delta^*(1/2^-)$	
$\mathcal{H}_{-1/2,0}$	$0.6 - 0.4i$
$\mathcal{H}_{1/2,0}$	$0.1i$
BW $m$	1.4 GeV
BW $\Gamma$	0.2 GeV
$J^P$	$1/2^-$

Table 6: Toy amplitude model parameters.

recoiling against the proton in the proton rest frame. Taking the  $K^*(\rightarrow K^-\pi^+)$  decay chain as reference, the rotation applied to the proton helicity states is

$$\hat{R}(0, \beta_p^R, 0) |1/2, \lambda_p\rangle = \sum_{\lambda'_p} d_{\lambda'_p, \lambda_p}^{1/2}(\beta_p^R) |1/2, \lambda'_p\rangle, \quad (57)$$

with angles

$$\cos \beta_p^{A^*} = \hat{\mathbf{p}}_{K^*}^p \cdot \hat{\mathbf{p}}_{K^-}^p, \quad \cos \beta_p^{\Delta^*} = \hat{\mathbf{p}}_{K^*}^p \cdot \hat{\mathbf{p}}_{\pi^+}^p, \quad (58)$$

for the  $\Lambda^*(\rightarrow pK^-)$  and  $\Delta^{*++}(\rightarrow p\pi^+)$  decay chains, respectively.

As argued in Sec. 4.4.2, properties following from rotational invariance are not guaranteed by the structure of these amplitude model: nonetheless, if their implementation is correct, such properties must arise naturally. The tests outlined in Sec. 3.3 therefore provide a simple and necessary condition for the models to be valid. Here we consider whether the decay plane orientation distributions  $\cos \theta_p, \phi_p, \chi$  are uniform for zero polarisation. The model isotropy is checked using 5 millions Monte Carlo events generated according to the amplitude model. The distributions for the PF amplitude model are reported in Fig. 26, showing this model is isotropic to a very high accuracy. The distributions for the PQ amplitude model are reported in Fig. 27, showing this model is clearly unphysical, violating rotational invariance. Moreover, the description of the invariant mass distributions is different for the two models.

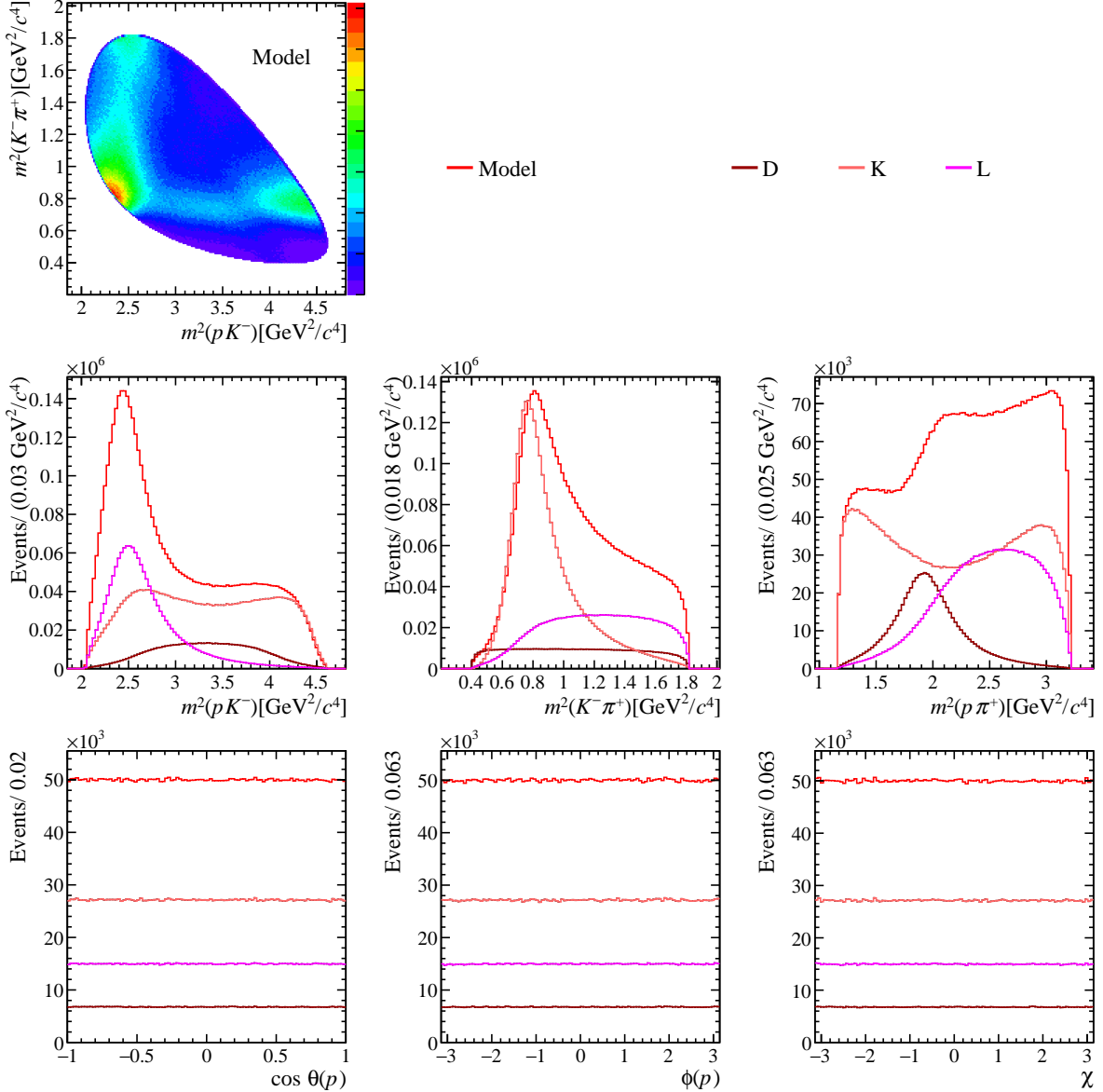


Figure 26: Phase space distributions for the PF amplitude model, described in Sec. 4.4.2, generated using 5 millions Monte Carlo events for zero polarisation.

We showed the PF amplitude model satisfies rotational invariance for zero polarisation, Fig. 26, but also the independence of the invariant mass distributions for varying polarisation must be checked. We generate 5 millions Monte Carlo events according to the PF amplitude model this time requiring full polarisation in the three different components. Figs. 28, 29 and 30 display the amplitude model phase space distribution for  $P_z = 1$ ,  $P_x = 1$  and  $P_y = 1$  polarisation values.

The invariant mass distributions are indeed identical for the different polarisation values, including the unpolarised case Fig. 26, up to irrelevant statistical fluctuations due to the Monte Carlo generation. It is also important to note that the decay orientation angle distributions follow the expected dependencies obtained from the general study of the  $\Lambda_c^+ \rightarrow pK^-\pi^+$  polarised decay [3]: a  $P_z$  component introduces a  $\cos \theta_p$  linear

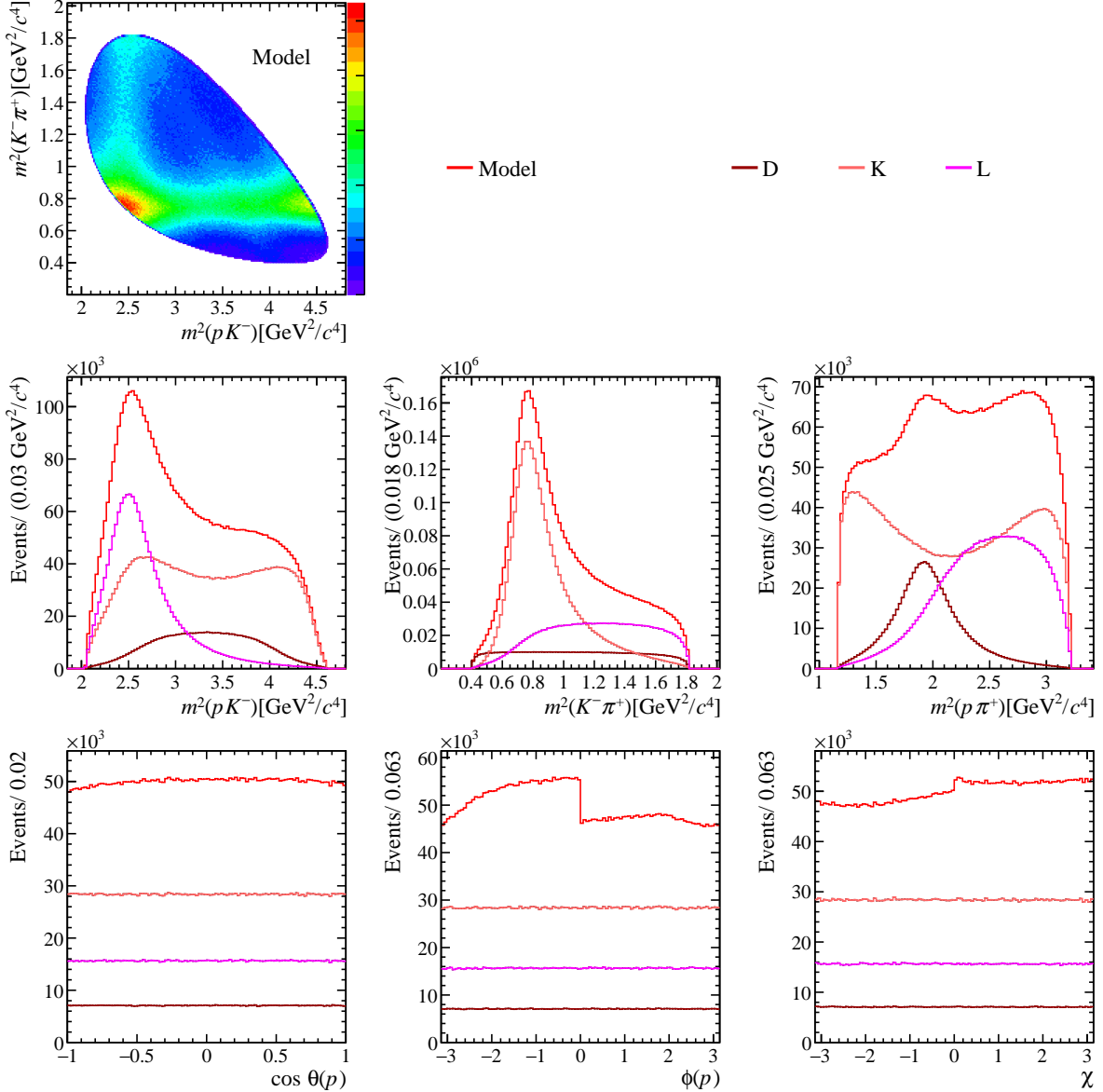


Figure 27: Phase space distributions for the PQ amplitude model, built following the method of Ref. [45], generated using 5 millions Monte Carlo events for zero polarisation.

dependence and a sinusoidal modulation in  $\chi$  (with amplitude and phase determined by the specific decay model), while a  $P_x$  ( $P_y$ ) contribution produces a cosine (minus sine) dependence in  $\phi_p$ .

These tests showed the need to go beyond the spin matching method used in previous analyses. Indeed, the impossibility of fitting the  $\phi_p$  distribution of  $\Lambda_c^+ \rightarrow pK^-\pi^+$  data at the earlier stages of the analysis, see the thesis [46], turn out to be caused by the incorrect spin matching employed, whose rationale was taken from the method of Refs. [44, 45].

Next, we consider amplitude models exploiting the decomposition Eq. (27): the one described in Sec. 4.4.1 (denoted N, for “nominal”) and one following the implementation proposed in Ref. [42]<sup>3</sup> (denoted DPD).

<sup>3</sup>With respect to the paper, phase factors related to the particle 2 role in the Jacob-Wick definition of

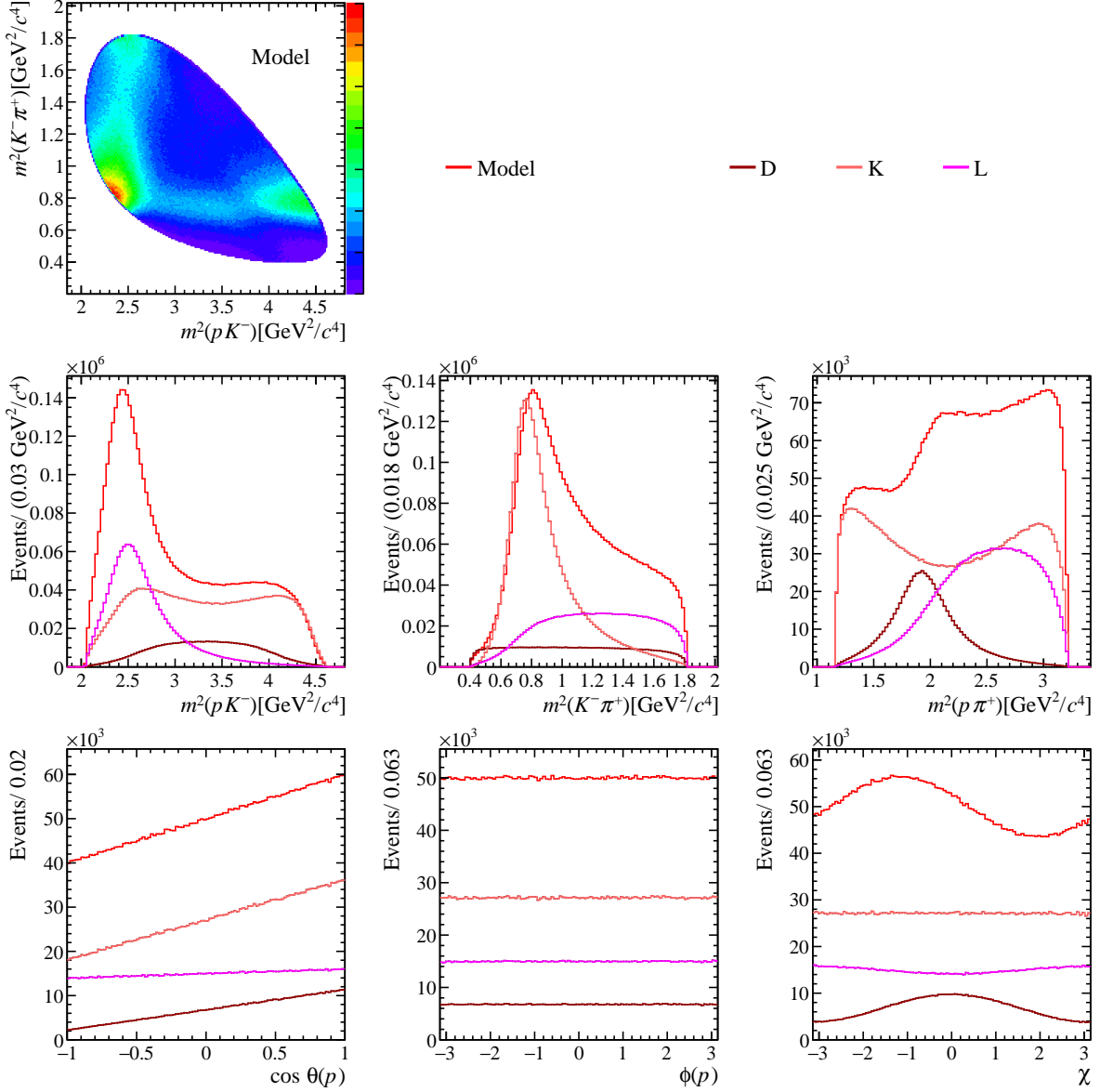


Figure 28: Phase space distributions for the PF amplitude model, described in Sec. 4.4.2, generated using 5 millions Monte Carlo events for full  $P_z = 1$  polarisation.

829     The two amplitude models differ in the method used for the spin matching, however, by  
 830     comparing the analytical form of the two, exploiting the Wigner  $d$ -matrix properties, it is  
 831     possible to show these amplitude models are equivalent<sup>4</sup>, leading to the same  $\Lambda_c^+ \rightarrow p K^- \pi^+$   
 832     decay rate expression. Indeed, the relation between amplitudes is

$$\mathcal{O}_{\nu_{\Lambda_c^+}, m_p}^N = (-1)^{1/2+m_p} \mathcal{O}_{\nu_{\Lambda_c^+}, -m_p}^{DPD} \quad (59)$$

833     which leads to the same decay rate when summing over  $m_p$ , provided the definition of the

---

two-particle helicity states must be added to the  $K^*$  and  $\Delta^*$  decay chains.

<sup>4</sup>We thank Alessandro Pilloni for contributing to this comparison.

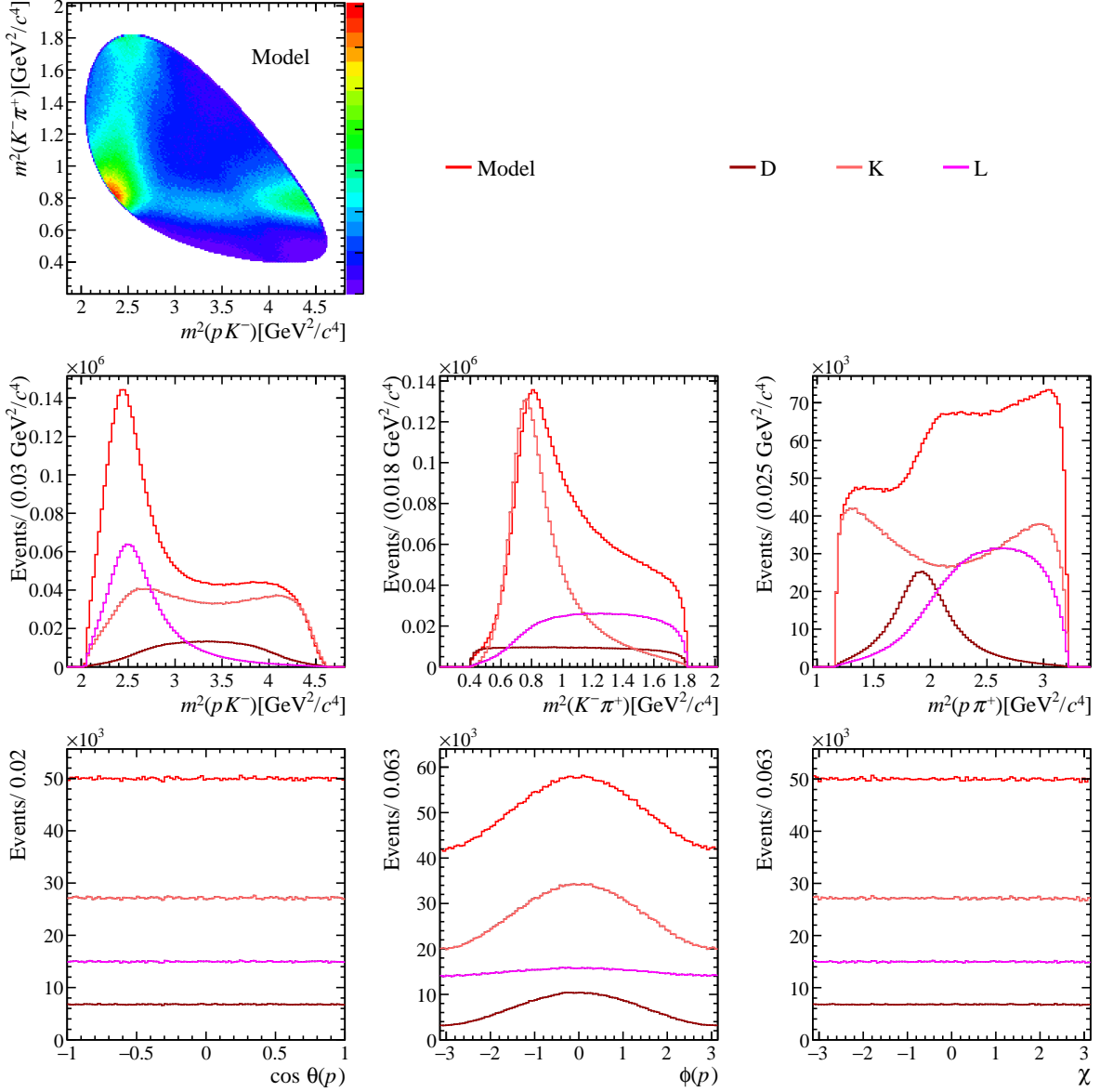


Figure 29: Phase space distributions for the PF amplitude model, described in Sec. 4.4.2, generated using 5 millions Monte Carlo events for full  $P_x = 1$  polarisation.

834 helicity coupling is changed according to

$$\begin{aligned} \mathcal{H}_{\bar{\lambda}_{K^*}, m_p}^{N, K^*} &= \mathcal{H}_{\bar{\lambda}_{K^*}, -m_p}^{DPD, K^*}, \\ \mathcal{H}_{\lambda_{\Delta^*}}^{N, \Delta^*} &= (-1)^{J_{\Delta^*} + 3/2} \mathcal{H}_{\lambda_{\Delta^*}}^{DPD, \Delta^*} \end{aligned} \quad (60)$$

835 The equivalence of N and DPD models is also checked numerically, plotting the  
 836 difference between their distributions. The toy amplitude model of Table 6 is employed,  
 837 with values changed following Eq. (60) for the DPD model. This comparison is reported in  
 838 Fig. 31, done using 5 millions Monte Carlo events for zero polarisation. The two amplitude  
 839 models are exactly equal: the per-bin differences of order  $10^{-12}$  are due to numerical  
 840 rounding effects. A further comparison is performed for  $P_z = 1$ , reported in Fig. 32, giving  
 841 similar result.

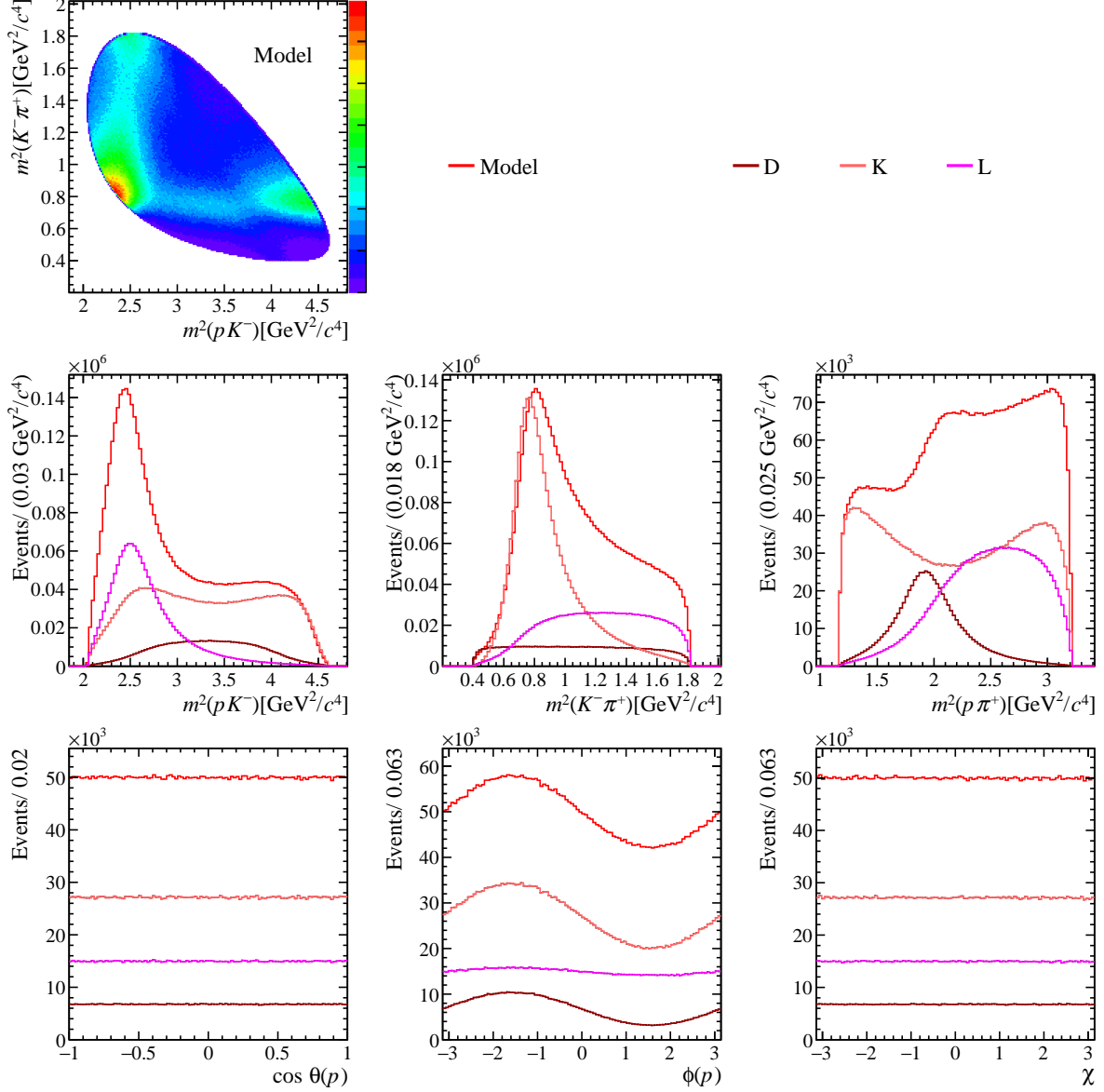


Figure 30: Phase space distributions for the PF amplitude model, described in Sec. 4.4.2, generated using 5 millions Monte Carlo events for full  $P_y = 1$  polarisation.

## 842 5.1 Interference patterns over the Dalitz plot

843 In this section the interference patterns over the Dalitz plot are shown for the toy amplitude  
 844 model described in the previous section, Table 6: Fig. 33 for the full, three-resonance,  
 845 toy model; Fig. 34 for the toy model with  $\Lambda^*$  and  $K^*$  contributions only; Fig. 35 for the  
 846 toy model with  $\Lambda^*$  and  $\Delta^*$  contributions only; Fig. 36 for the toy model with  $\Delta^*$  and  $K^*$   
 847 contributions only;

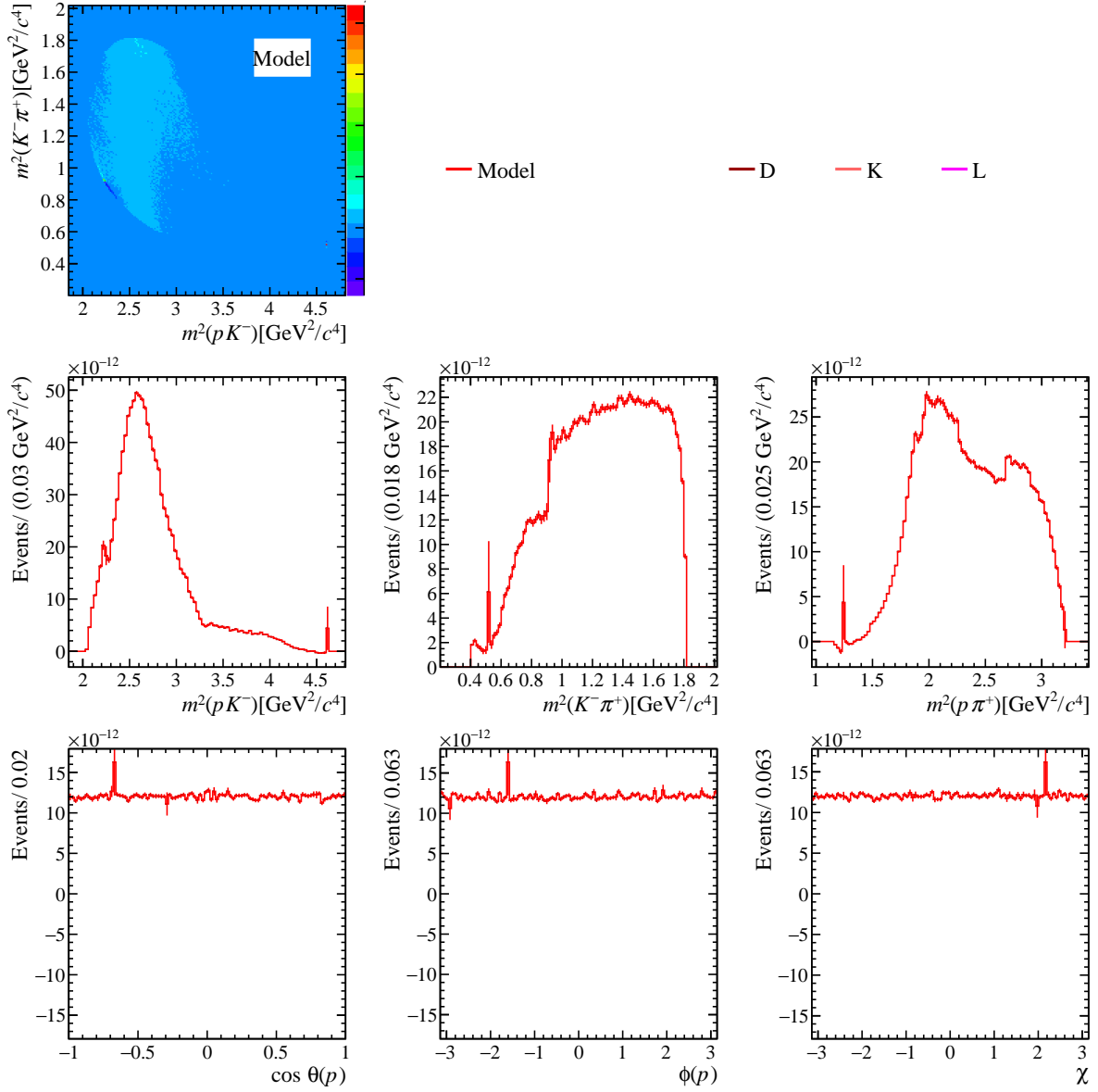


Figure 31: Phase space distribution differences between N and DPD amplitude models, generated using 5 millions Monte Carlo events for zero polarisation.

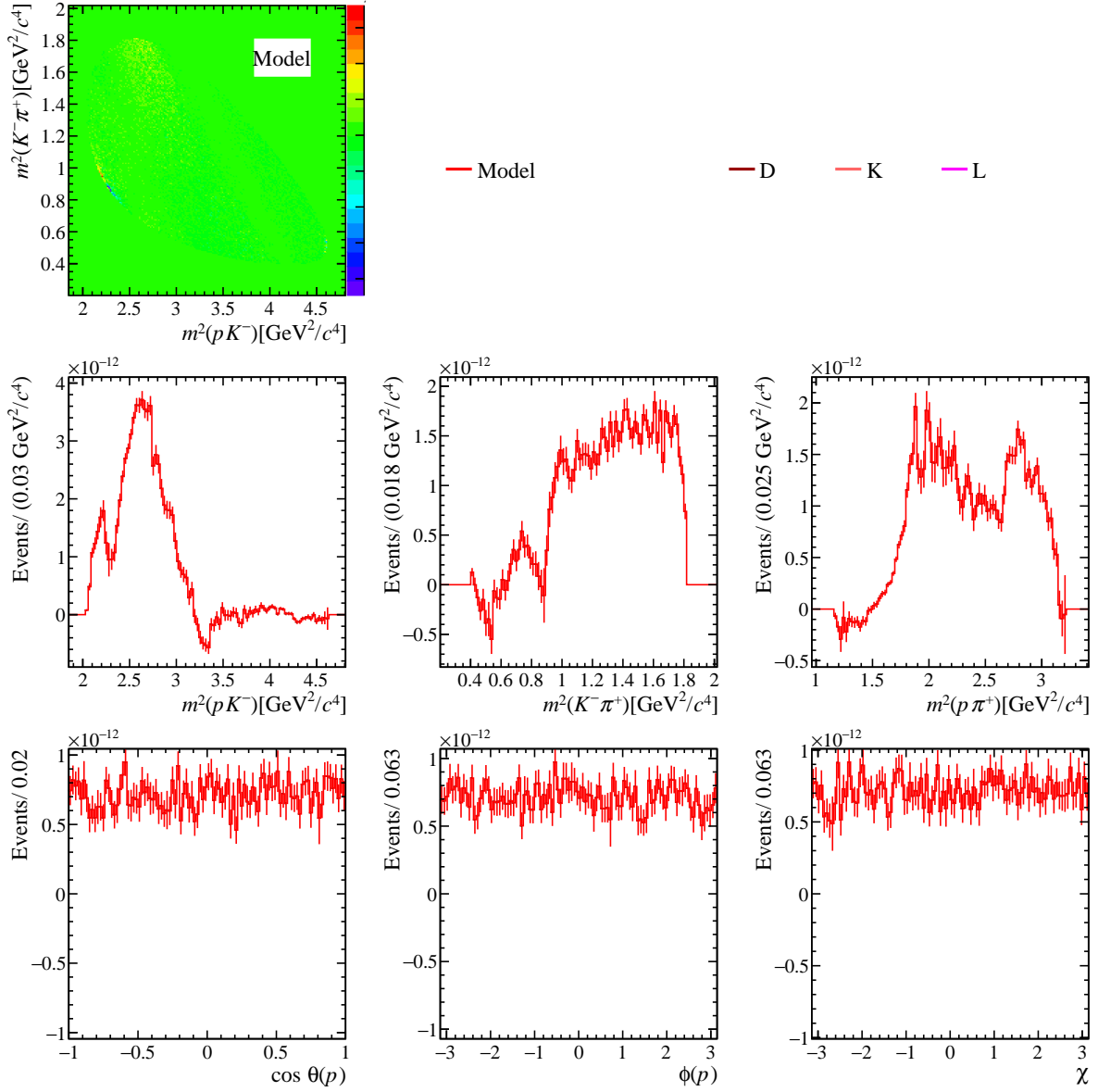


Figure 32: Phase space distribution differences between N and DPD amplitude models, generated using 5 millions Monte Carlo events for  $P_z = 1$ .

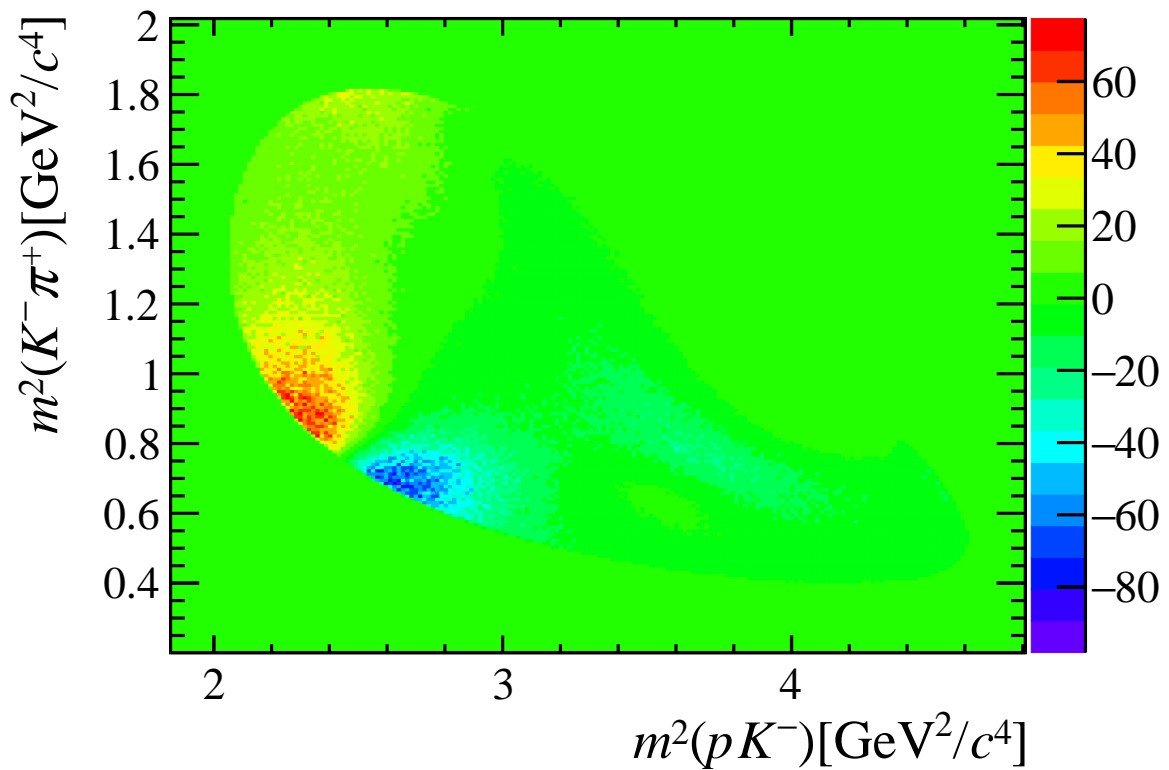


Figure 33: Interference effects over the  $\Lambda_c^+ \rightarrow p K^- \pi^+$  Dalitz plot for the toy amplitude model described in Table 6, obtained plotting the difference between the model and the incoherent sum of each resonant contribution, using 1 million generated MC events.

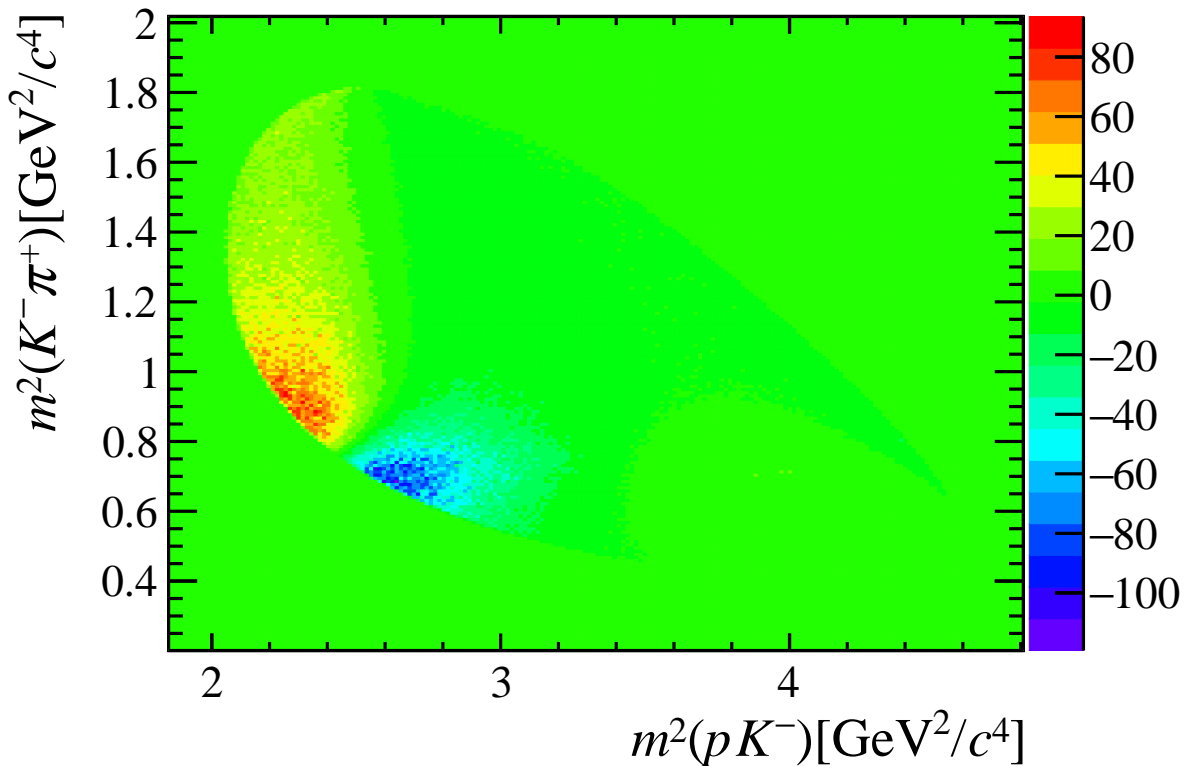


Figure 34: Interference effects over the  $\Lambda_c^+ \rightarrow p K^- \pi^+$  Dalitz plot for the toy amplitude model described in Table 6 with  $\Lambda^*$  and  $K^*$  contributions only, obtained plotting the difference between the model and the incoherent sum of each resonant contribution, using 1 million generated MC events.

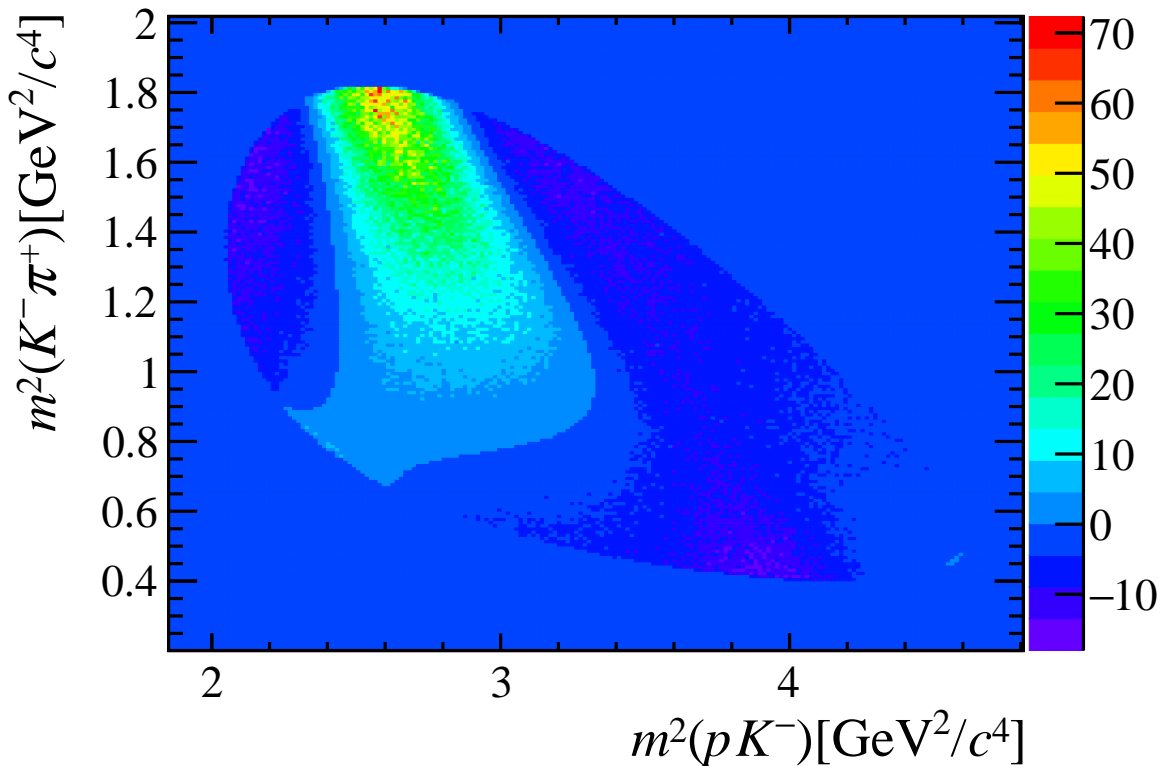


Figure 35: Interference effects over the  $\Lambda_c^+ \rightarrow p K^- \pi^+$  Dalitz plot for the toy amplitude model described in Table 6 with  $\Lambda^*$  and  $\Delta^*$  contributions only, obtained plotting the difference between the model and the incoherent sum of each resonant contribution, using 1 million generated MC events.

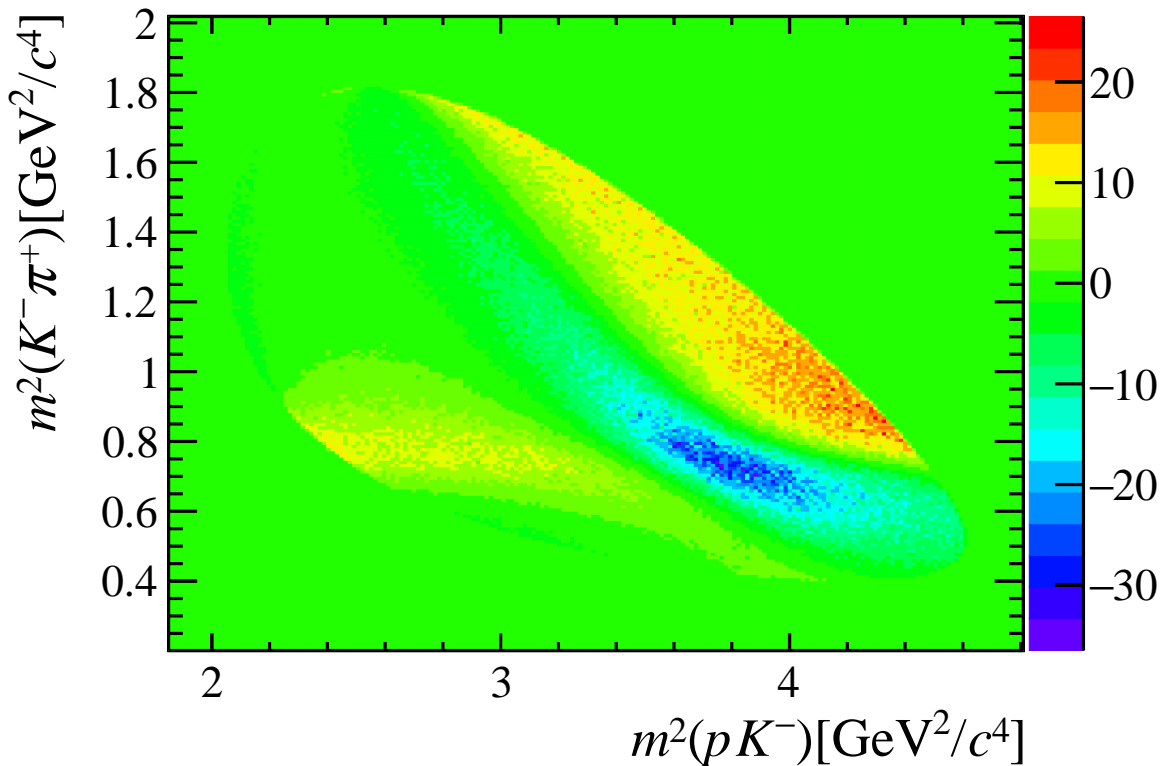


Figure 36: Interference effects over the  $\Lambda_c^+ \rightarrow p K^- \pi^+$  Dalitz plot for the toy amplitude model described in Table 6 with  $\Delta^*$  and  $K^*$  contributions only, obtained plotting the difference between the model and the incoherent sum of each resonant contribution, using 1 million generated MC events.

## 848 6 Amplitude fit

### 849 6.1 Maximum-likelihood fit

850 The amplitude model free parameters, collectively indicated as  $\omega$ , are determined from  
 851 a maximum likelihood (ML) fit to the data sample  $\{\Omega_i\}$  by minimising the negative  
 852 logarithmic likelihood (NLL)

$$853 -\log \mathcal{L}(\omega) = -\sum_{i=1}^N \log p_{tot}(\Omega_i|\omega), \quad (61)$$

853 in which  $p_{tot}(\Omega_i|\omega)$  represents the total fitting PDF,

$$853 p_{tot}(\Omega_i|\omega) = \frac{p(\Omega_i|\omega)\epsilon(\Omega_i)}{I(\omega)} \frac{n_{sig}}{N} + p_{bkg}(\Omega_i) \frac{n_{bkg}}{N}, \quad (62)$$

854 describing the conditional probability of having the experimental points  $\Omega_i$  given the  
 855 parameters  $\omega$ . This PDF includes the  $\Lambda_c^+ \rightarrow pK^-\pi^+$  decay rate Eq. (53) now indicated as  
 856  $p(\Omega_i|\omega)$ , the detector efficiency variation over the phase space  $\epsilon(\Omega)$  and the background  
 857 contribution, which, in this approach, is included in the amplitude model with a parametric  
 858 (normalised) PDF  $p_{bkg}(\Omega)$  rather than statistically subtracted (see Ref. [45] for a comparison  
 859 of the two methods). The number of signal and background events,  $n_{sig}$  and  $n_{bkg}$ , is  
 860 determined from the fit to the  $\Lambda_c^+$  invariant mass, Fig. 2.  $I(\omega)$  is the normalisation of the  
 861 signal part of the total PDF,

$$861 I(\omega) = \int p(\Omega|\omega)\epsilon(\Omega)d\Omega, \quad (63)$$

862 which can be computed numerically without explicitly knowing the efficiency function  $\epsilon(\Omega)$ ,  
 863 by using simulated flat phase space events reconstructed through the detector. Indeed,  
 864 the integration variables can be changed from the decay phase space  $d\Omega$  to the phase  
 865 space as seen from the detector viewpoint  $d\Omega' = \epsilon(\Omega)d\Omega$ , like in [45], so that

$$866 I(\omega) = \int p(\Omega|\omega)d\Omega' = \frac{\sum_i p(\Omega_i^{\text{MC}}|\omega)}{N^{\text{MC}}}, \quad (64)$$

866 in which  $\{\Omega_i^{\text{MC}}\}$ ,  $i = \{1, \dots, N^{\text{MC}}\}$  are the phase space points of the simulated sample.

867 Exploiting the logarithm properties, the log-likelihood Eq. (61) can be rewritten as

$$868 -\log \mathcal{L}(\omega) = -\sum_{i=1}^N \log \left[ p(\Omega_i|\omega) + \frac{p_{bkg}(\Omega_i)I(\omega)}{\epsilon(\Omega_i)} \frac{n_{bkg}}{n_{sig}} \right] \\ + N \log I(\omega) + \text{constant}, \quad (65)$$

868 showing that in presence of a background contribution, both the efficiency and background  
 869 functions over the decay phase space  $\epsilon(\Omega)$  and  $p_{bkg}(\Omega)$  need to be parametrised<sup>5</sup>. However,  
 870 their contribution to the parameter estimation is proportional to the ratio  $n_{bkg}/n_{sig}$ , which  
 871 for a good background rejection is small, and any systematic uncertainty associated to the  
 872 choice of the parametrisation is suppressed by this ratio. The tight selection presented in  
 873 Section 2.1 reduces the ratio to  $n_{bkg}/n_{sig} \approx 1.7\%$ .

---

<sup>5</sup>The use of an efficiency parametrisation may be avoided by obtaining background distributions weighting the reconstructed simulation sample, see e.g. [47].

874 **6.2 Code**

875 For performing the  $\Lambda_c^+ \rightarrow pK^-\pi^+$  amplitude analysis the TensorFlowAnalysis (TFA)  
876 package [48] is chosen. TensorFlowAnalysis is a collection of useful functions to perform  
877 amplitude fits, developed within the LHCb Collaboration, based on top of the machine-  
878 learning framework TensorFlow [49]. An already implemented amplitude model for  $\Lambda_c^+ \rightarrow$   
879  $pK^-\pi^+$  decays has been generalised from Dalitz plot to full phase space 5-dimensional  
880 fit, including the extraction of the  $\Lambda_c^+$  polarisation vector and the inclusion of detector  
881 efficiency effects. The main advantages of the TFA with respect to other amplitude fit  
882 frameworks are those following from Tensorflow features.

883 Tensorflow is based on the computer algebra paradigm, in which users do not run  
884 directly calculations, but specify the computational graph describing what has to be  
885 computed. For example, the definition of the amplitude model can be more flexible  
886 since the explicit data flow behind its definition needs not to be specified, but it is  
887 handled automatically by Tensorflow. Tensorflow is able to handle tensor data, optimise  
888 automatically the computational graph, and compile for different architectures. This is  
889 very important for the present analysis, since the amplitude model is complicated due  
890 to the presence of sequential decays, involving many rotations, and a large number of  
891 resonant states, which would be prohibitive to build from basic, hard-coded functions.  
892 One important feature of TFA is the possibility to memorise parts of the decay amplitude  
893 independent of fit parameters, like angular structure and background, which are reused at  
894 each minimisation step without being recalculated.

895 One drawback is that Tensorflow built-in minimisation functions are not suitable for  
896 physics, since they do not deal with the errors associated to fit parameters. For this  
897 reason TFA exploits the MINUIT package for ML fits. In MINUIT, the NLL minimisation  
898 algorithm MIGRAD is employed, based on gradient-descent method. The  $1\sigma$  standard  
899 deviations on the fit parameters are computed using the HESSE method, via the Hessian  
900 matrix. MINUIT also provides the MINOS method for error computation, which is not  
901 used by default since it is very demanding in terms of computational resources; tests on  
902 simplified amplitude models showed that MINOS errors are not significantly different  
903 from HESSE ones.

904 **6.3 Fit strategy**

905 Amplitude fits are performed choosing the amplitude model with Dalitz-plot decompo-  
906 sition of Sec. 4.4.1. The free parameters  $\omega$  include the real and imaginary parts of the  
907 complex helicity couplings, resonance parameters like masses and widths and the three  
908  $\Lambda_c^+$  polarisation components. Since the normalisation of the model is fixed, Eq. (63),  
909 one of the helicity couplings must be fixed to a constant value, so that the value of the  
910 other couplings is expressed relative to the reference one. The  $K^*(892)$  helicity coupling  
911  $\mathcal{H}_{1,2,0}^{\Lambda_c^+ \rightarrow pK^*}$  is chosen as reference coupling, fixed to one, with zero imaginary part.

912 Fits are carried out on a datasample of 400'000  $\Lambda_c^+ \rightarrow pK^-\pi^+$  data candidates selected  
913 as described in Sec. 2.2 using a simulation sample of  $\approx 450'000$  events passing the selection  
914 process. The fit is performed with initial values of the floating parameters thrown randomly  
915 in their allowed range, and the best result according to the minimum NLL is selected  
916 among 20 different fits.

917 Fit fractions for each resonance  $R$  are obtained by computing the integral of the

amplitude model over the phase space in which only the  $R$  contribution is left,

$$\int d\Omega \sum_{m_{\Lambda_c^+}, m_p} \left| \sum_{\lambda_R} \mathcal{A}_{m_{\Lambda_c^+}, \lambda_R, m_p}^{\Lambda_c^+ \rightarrow Rh}(\Omega) \right|^2. \quad (66)$$

For each two-body contribution, the decay asymmetry parameter  $\alpha$  is measured. It characterises the two-body decay angular distribution,

$$\frac{dN}{d \cos \theta_R} \propto \frac{1}{2} (1 + \alpha P \cos \theta_R), \quad (67)$$

in which  $\cos \theta_R = \mathbf{P} \cdot \hat{\mathbf{p}}(R)$  is the cosine of the angle between the polarisation vector and the direction of the intermediate resonance in the  $\Lambda_c^+$  rest frame. In two-body decays, the  $\alpha$  parameters can be expressed as a combination of helicity coupling squared moduli: for a decay to a spin 1/2, 0 pair ( $\Lambda^*$ ,  $\Delta^*$ ,  $K^*$  spin zero channels) it is

$$\alpha = \frac{|\mathcal{H}_{1/2,0}|^2 - |\mathcal{H}_{-1/2,0}|^2}{|\mathcal{H}_{1/2,0}|^2 + |\mathcal{H}_{-1/2,0}|^2}, \quad (68)$$

for a decay to a spin 1/2, 1 pair (higher  $K^*$  spin channels) it is

$$\alpha = \frac{|\mathcal{H}_{1/2,0}|^2 + |\mathcal{H}_{1/2,-1}|^2 - |\mathcal{H}_{-1/2,0}|^2 - |\mathcal{H}_{-1/2,1}|^2}{|\mathcal{H}_{1/2,0}|^2 + |\mathcal{H}_{1/2,-1}|^2 + |\mathcal{H}_{-1/2,0}|^2 + |\mathcal{H}_{-1/2,1}|^2}. \quad (69)$$

An important quantity to be measured in light of  $\Lambda_c^+$  polarisation measurement is the sensitivity of the amplitude model to the polarisation, measured by the squared average event Fisher information at zero polarisation, see Refs. [46, 50, 51],

$$S^2 = \frac{1}{N\sigma^2} = \left\langle \frac{g^2}{f^2}(\Omega) \right\rangle = \int \frac{g^2}{f}(\Omega) d\Omega, \quad (70)$$

in which

$$\begin{aligned} f(\Omega) &\propto \sum_{m_p=\pm 1/2} [| \mathcal{A}_{1/2, m_p}(\Omega) |^2 + | \mathcal{A}_{-1/2, m_p}(\Omega) |^2] \\ &= p(\Omega, P_z = 0) \\ g(\Omega) &\propto \sum_{m_p=\pm 1/2} [| \mathcal{A}_{1/2, m_p}(\Omega) |^2 - | \mathcal{A}_{-1/2, m_p}(\Omega) |^2] \\ &\propto p(\Omega, P_z = 1) - p(\Omega, P_z = -1), \end{aligned} \quad (71)$$

normalised in such a way that

$$\int p(\Omega, P_z) d\Omega = \int f(\Omega) d\Omega = 1, \quad (72)$$

with the  $g$  function integrating to zero over the phase space,

$$\int g(\Omega) d\Omega = 0. \quad (73)$$

932 For two-body decays, the relation between Fisher information and decay asymmetry  
 933 parameter  $\alpha$ , applying Eq. (67) to Eq. (70), is

$$S^2 = \frac{\alpha^2}{3}, \quad (74)$$

934 so that the decay asymmetry parameter can be seen as a measure of the sensitivity of the  
 935 decay to the polarisation.

936 The sensitivity to polarisation of the  $\Lambda_c^+ \rightarrow pK^-\pi^+$  three-body decay is obtained from  
 937 Eq. 70 using its amplitude model. For an easier comparison to two-body decays it is  
 938 useful to quote the sensitivity to the polarisation as  $\sqrt{3}S$ , which, like decay asymmetry  
 939 parameters, is a measure of parity violation. If parity is conserved in the decay, the  
 940 amplitudes do not depend on the  $\Lambda_c^+$  polarisation, leading to  $g(\Omega) = 0$  and  $S = 0$ .  
 941 Maximum parity-violation corresponds to the case  $\sqrt{3}S = 1$ , since the maximum Fisher  
 942 information is  $S = 1/\sqrt{3}$  [50]. From the polarisation measurement perspective  $\sqrt{3}S$  can be  
 943 considered as a generalisation of two-body decay asymmetry parameters for a multi-body  
 944 decay.

## 945 6.4 Fit quality

946 The fit quality can be assessed in different ways. The simplest method is to compare 1-  
 947 or 2- dimensional phase space distributions between data and model. Pull distributions  
 948 among data and model histograms are computed, the latter obtained by weighing the flat  
 949 phase space simulated events  $\Omega_i^{MC}$  according to amplitude model values,  $w_i = p(\Omega_i^{MC}|\omega)$ ,  
 950 in order to include detector efficiency effects. Pulls related to the 2-dimensional Dalitz plot  
 951 are also computed using an adaptive binning. This is the most straightforward method to  
 952 spot manifest discrepancies and their location in the decay phase space, but its sensitivity  
 953 is limited by the use of projections. A  $\chi^2$ -based test is performed to increase sensitivity to  
 954 differences in the full phase space distributions. The  $\chi^2$  statistics is defined as in Ref. [52]

$$\chi^2 = \sum_i^N \delta_i^2 \quad \delta_i = \frac{D_i - F_i}{\sqrt{\sigma(D_i)^2 + \sigma(F_i)^2}} \quad (75)$$

955 in which  $D_i$  is the number of data candidates in bin  $i$ ,  $F_i = \sum_i^{N_{MC}} w_i$  the model sum-of-  
 956 weights of MC events in bin  $i$  and  $\sigma(F_i)^2 = \sum_i^{N_{MC}} w_i^2$  the associated per-bin uncertainty.  
 957 An adaptive binning of the phase space (that provided by the ROOT package) is chosen  
 958 in order to have the same amount of data points per bin, each one being a 5-D hyperpar-  
 959 allelogram<sup>6</sup>, this way the  $\chi^2$  test is no more dependent on the data dimensionality<sup>7</sup>. The  
 960  $\chi^2$  is computed using 1000 “adapted” bins: on the one hand, such binning is fine enough  
 961 to be sensitive to localised discrepancies in the phase space; on the other hand, each bin  
 962 will has  $\approx 100$  data or MC events per bin, a value much higher than the minimum limit  
 963 of 5 considered in the statistics literature for a valid  $\chi^2$  test.

---

<sup>6</sup>This is a different one with respect that used to compute the Dalitz plot pulls.

<sup>7</sup>Indeed, the  $\chi^2$  test is independent of the data dimensionality; problems with multiple dimensions arise when considering partitions given by products of 1-D binnings, leading to a huge number of mostly empty bins, invalidating the assumptions behind the  $\chi^2$  test. This is a consequence of the “curse of dimensionality” problem: data become sparser with the increase of its dimensionality. All this can be avoided by using adaptive binning techniques, as already done in other analyses, like in Ref. [47]

Another measure of fit quality is given by the probability value obtained from the  $\chi^2$  distribution given the number of degrees of freedom (ndf). These are estimated as  $ndf = nbins - npars - 1$ , with  $nbins$  the number of bins used to compute the  $\chi^2$  value,  $npars$  the number of free fit parameters and the  $-1$  for the normalisation imposed to the PDF. For maximum-likelihood fits, in which the  $\chi^2$  is not used for the determination of the fit parameters, this is an approximation, the number of effective degrees-of-freedom lying between  $nbins$  and  $ndf = nbins - npars - 1$ . The true ndf can be estimated using toy simulations; for our purposes we consider the lower ndf limit in order to have probability values favouring simpler models (with less free parameters) for similar  $\chi^2$  values.

## 6.5 Resonance lineshapes

By default resonances are parametrised with relativistic Breit-Wigner lineshapes, which are well-suited for relatively narrow resonances far from other nearby resonances and the threshold of additional decay channels. To reproduce the typical suppression of transitions involving non-zero orbital angular momentum, the Breit-Wigner parametrisation is multiplied by angular barrier terms involving Blatt-Weisskopf form factors [53, 54]

$$\mathcal{R}_{BW}(m^2) = \left[ \frac{q(m)}{q_0} \right]^{L_{\Lambda_c^+}} \left[ \frac{p(m)}{p_0} \right]^{L_R} \frac{F_{\Lambda_c^+}(m, L_{\Lambda_c^+}) F_R(m, L_R)}{m_0^2 - m^2 - im_0 \Gamma(m)}, \quad (76)$$

in which the mass-dependent width

$$\Gamma(m) = \Gamma_0 \left[ \frac{p(m)}{p_0} \right]^{2L_R+1} \frac{m_0}{m} F_R^2(m, L_R), \quad (77)$$

is introduced. The definition of the different quantities entering the above expressions are the following:  $m$  is the invariant mass of the resonance,  $m_0$  and  $\Gamma_0$  are its Breit-Wigner mass and width,  $p(m)$  is the momentum of one of the decay products in the resonance two-body decay,  $p_0 \equiv p(m_0)$ ,  $q(m)$  is the momentum of one of the decay products in the  $\Lambda_c^+$  two-body decay  $\Lambda_c^+ \rightarrow Rh$ ,  $q_0 = q(m_0)$ , both defined in the rest frame of the decaying particle,  $L_{\Lambda_c^+}$  and  $L_R$  are the orbital angular momenta associated to the  $\Lambda_c^+$  and  $R$  decays, respectively. The Blatt-Weisskopf form factors for the resonance,  $F_R(m, L_R)$ , and for the  $\Lambda_c^+$ ,  $F_{\Lambda_c^+}(m, L_{\Lambda_c^+})$ , are parametrised as

$$F_{R,\Lambda_c^+}(m, L) = \begin{cases} 1 & L = 0 \\ \sqrt{\frac{1+z_0^2}{1+z^2(m)}} & L = 1 \\ \sqrt{\frac{9+3z_0^2+z_0^4}{9+3z^2(m)+z^4(m)}} & L = 2 \\ \sqrt{\frac{225+45z_0^2+6z_0^4+z_0^6}{225+45z^2(m)+6z^4(m)+z^6(m)}} & L = 3 \end{cases}, \quad (78)$$

in which the definitions of the terms  $z(m)$  and  $z_0$  depend on whether the form factor for the resonance  $R$  or for the  $\Lambda_c^+$  is being considered. For  $R$  these terms are given by  $z(m) = p(m)d$  and  $z_0 = p_0d$ , in which  $p(m)$  is the momentum of one of the decay products in the resonance two-body decay,  $p_0 \equiv p(m_0)$ , and  $d$  is a radial<sup>8</sup> parameter taken to be

---

<sup>8</sup>The angular barrier factors arise from the non-relativistic quantisation of a particle in a radial potential, and  $d$  represents, loosely speaking, the radius of the resonance.

1.5 GeV<sup>-1</sup>. For the  $\Lambda_c^+$  baryon the respective functions are  $z(m) = q(m)d$  and  $z_0 = q_0d$ , in which  $q(m)$  is the momentum of one of the decay products in the  $\Lambda_c^+$  two-body decay  $\Lambda_c^+ \rightarrow Rh$ ,  $q_0 = q(m_0)$ , and  $d = 5.0$  GeV<sup>-1</sup>. Previous studies showed the amplitude analysis is very weakly sensitive to the  $d$  values [55].

The mass-dependent width and the form factors depend on the orbital angular momenta of the two-body decays. For the  $\Lambda_c^+$  weak decay, the orbital angular momentum is not constrained: the minimum possible one is assumed, since one can expect higher assignments to be energetically disfavoured. For half-integer spin  $\Lambda^*$ ,  $\Delta^{++}$  resonances it is  $L_{\Lambda_c^+} = J_R - 1/2$ ,  $J_R$  being the resonance spin, it is  $L_{\Lambda_c^+} = 0$  for spin zero  $K^*$  resonances and  $L_{\Lambda_c^+} = J_R - 1$  for higher spin  $K^*$  resonances. These assignments are employed for the nominal amplitude fit; as an alternative approach, the amplitude fit is also performed using  $LS$  couplings instead of helicity ones, Sec. 7.1.14, this allowing to fit also for higher orbital angular momentum states.

For the strong decay of  $\Lambda^*$ ,  $\Delta^{*++}$  resonance, the orbital angular momentum  $L_R$  is determined by the conservation of angular momentum, which requires  $L_R = J_R \pm 1/2$ , and the parity of the resonance<sup>9</sup>,  $P_R = -(-1)^{L_R}$ , which chooses one of the  $L_R$  values. For  $K^*$  resonances, decaying into two mesons, the orbital angular momentum is  $L_R = J_R$ .

Some of the resonances employed in the amplitude model can not be parametrised by relativistic Breit-Wigner lineshapes. After a through study the  $K^*$  spin-zero contribution is described as two  $K^*(700)$  and  $K^*(1430)$  resonant states described by a simplified version of the parametrisation proposed in Ref. [56], called hereafter Bugg lineshape,

$$\mathcal{R}_{\text{Bugg}}(m_{K-\pi^+}^2) = \frac{1}{m_0^2 - m_{K-\pi^+}^2 - ig_{K\pi}^2(s)\rho_{K\pi}} \quad (79)$$

$$g_{K\pi}^2(s) = \frac{m_{K-\pi^+}^2 - s_A}{m_0^2 - s_A} \Gamma_0^2 e^{-\gamma m_{K-\pi^+}^2}. \quad (80)$$

It consists of a Breit-Wigner-like term featuring a singularity (Adler zero) at  $s_A = m_K^2 - 0.5m_\pi^2$  and an exponential form factor on the  $K\pi$  width driven by the parameter  $\gamma$ . In the amplitude fit,  $m_0$  and  $\Gamma_0$  are the Breit-Wigner mass and widths, while the  $\gamma$  parameter is floated separately for each contribution.

With respect to the full parametrisation in Ref. [56], an additional overall exponential form factor  $\exp(-\alpha q^2)$  and the opening of  $K\eta$ ,  $K\eta'$  decay channels are neglected in the nominal fit. The overall form factor is considered as an alternative model, with floating  $\alpha$  parameters, while introducing  $K\eta$ ,  $K\eta'$  associated widths leads to instabilities.

This parametrisation of the  $K^*$  spin-zero contribution is found to better describe the low  $m_{K-\pi^+}^2$  region of the Dalitz plot than the often used LASS parametrisation [57].

The  $\Lambda(1405)$  resonance has its pole mass below the threshold of  $pK^-$  production, and it contributes to the  $\Lambda_c^+ \rightarrow pK^-\pi^+$  decay due to its higher mass tail. Its contribution is parametrised by a Flatté lineshape [58] which describes the opening of the  $pK$  decay channel in addition to the  $\Sigma\pi$  one, following [45]. It is basically composed by a Breit-Wigner lineshape with a total width being the sum of the widths associated to the two decay channels,

$$\Gamma(m) = \Gamma_{pK}(m) + \Gamma_{\Sigma\pi}(m) \quad (81)$$

where  $q$  in the second term and  $q_0$  in both terms are calculated assuming the decay to  $\Sigma\pi$ . Assuming that both channels are dynamically equally likely and differ only by the phase

---

<sup>9</sup>The additional minus sign is given by the negative parity of the final state meson.

1031 space factors we set  $\Gamma_0$  to the total width of the  $\Lambda(1405)$  resonance in both terms, so no  
1032 floating parameter characterise the resonance. Possible variation of the two widths are  
1033 considered as a contribution to the systematic uncertainty associated to the amplitude  
1034 model choice, by floating them independently in the amplitude fit, Sec. 7.1.3.

## 1035 6.6 Efficiency and background parametrisation

1036 The inclusion of the background contribution in the ML fit Eq. (65) requires the explicit  
1037 parametrisation of both detector efficiency and combinatorial background over the decay  
1038 phase space. Legendre polynomial expansions are employed because they consist of  
1039 regular and derivable functions, easily obtained from the relevant data samples. Since  
1040 Legendre polynomials are defined in the range  $[-1, 1]$ , the five phase-space variables must  
1041 be transformed in order to be defined in the same interval. The two invariant masses can  
1042 be replaced by the so-called “square Dalitz plot” variables

$$m'_{pK^-} = 2 \frac{m_{pK^-} - m_{pK^-}^{\min}}{m_{pK^-}^{\max} - m_{pK^-}^{\min}} - 1, \quad (82)$$

1043 in which  $m_{pK^-}^{\min} = \sqrt{(m_p + m_{K^-})^2}$  and  $m_{pK^-}^{\max} = \sqrt{(m_{\Lambda_c^+} - m_{\pi^+})^2}$  are the minimum and  
1044 maximum  $pK^-$  invariant mass values allowed by kinematics, and the cosine of the angle  
1045 between the kaon and the pion in the  $\Lambda^*$  rest frame,  $\cos \theta_{K\pi}^{\Lambda^*}$ , which can be computed as

$$\cos \theta_{K\pi}^{\Lambda^*} = \frac{m_{K^-}^2 + m_{\pi^+}^2 + 2E_{K^-}E_{\pi^+} - m_{pK^-}^2}{2p_{K^-}p_{\pi^+}}. \quad (83)$$

1046 The choice of the decay plane orientation variables is trivial,  $\cos(\theta_p)$ ,  $\phi'_p = \phi_p/\pi$ ,  $\chi' = \chi/\pi$ .  
1047 This way, the phase space is defined on a 5-dimensional hypercube; note however that the  
1048 phase space density is not uniform in  $m'_{pK^-}$ , this is taken into account when constructing  
1049 the efficiency parametrisation.

1050 Exploiting the completeness and orthogonality of Legendre polynomials, a generic  
1051 function  $f(\Omega)$  over the phase space can be expanded as

$$f(\Omega) = \sum_{i,j,k,l,m} c_{i,j,k,l,m} L(m'_{pK^-}, i) L(\cos \theta_{K\pi}^{\Lambda^*}, j) L(\cos \theta_p, k) L(\phi'_p, l) L(\chi', m), \quad (84)$$

1052 with  $L(x, l)$  being the Legendre polynomial of order  $l$ . The coefficients  $c_{i,j,k,l,m}$  are  
1053 determined from phase space points as

$$c_{i,j,k,l,m} = \sum_{n=0}^N \frac{w_n}{\rho(m'_{pK^-})} (2i+1)(2j+1)(2k+1)(2l+1)(2m+1) \\ \times L(m'_{pK^-}, i) L(\cos \theta_{K\pi}^{\Lambda^*}, j) L(\cos \theta_p, k) L(\phi'_p, l) L(\chi'), \quad (85)$$

1054 in which  $w_n$  represents the weight associated to each phase space point and  $\rho(m'_{pK^-})$   
1055 represent the non-uniform phase space density.

1056 The efficiency parametrisation  $\epsilon(\Omega)$  is obtained from the ReDecay simulated  $\Lambda_c^+ \rightarrow$   
1057  $pK^-\pi^+$  decays, uniformly generated in phase space, passing the data selection requirements,  
1058 with the per-event weight computed in Sec. 2.4 to include residual data/simulation

1059 discrepancies. The background parametrisation  $p_{bkg}(\Omega)$  is obtained from the data signal  
 1060 sidebands  $|m(pK^-\pi^+) - m(\Lambda_c^+)_\text{PDG}| > 40 \text{ MeV}$ .

1061 The full 5D Legendre expansion Eq. (84) presents some practical problems. One is that  
 1062 data points become sparser with increasing dimensionality (“the curse of dimensionality”  
 1063 problem), lesser able to determine the parametrisation. This is especially relevant for  
 1064 background events, which are  $\approx 40k$  only after selection. In particular, the parametrisation  
 1065 can become negative in regions with few data points, which is not acceptable by the ML  
 1066 fit. Another issue is that the number of coefficients is exponential in the phase space  
 1067 dimensionality, which can make the parametrisation complicated.

1068 Before exploring different methods, the possibility to factorise parametrisations is  
 1069 considered evaluating the correlations among phase space variables for the simulation and  
 1070 background samples: the correlation plots are reported in Fig. 37 and 38, respectively.  
 1071 The correlations measured using mutual information<sup>10</sup> are found to be small, at 2 – 3%  
 1072 level at maximum.

1073 Efficiency and background parametrisation are therefore obtained by building five  
 1074 one-dimensional polynomial expansions multiplied together. For instance the efficiency  
 1075 parametrisation is

$$\begin{aligned}\epsilon(\Omega) &= \varepsilon(m'_{pK^-}) \varepsilon(\cos \theta_{K\pi}^{*}) \varepsilon(\cos \theta_p) \varepsilon(\phi'_p) \varepsilon(\chi') \\ \varepsilon(x) &= \sum_i c_i L(x, i) \\ c_i &= \sum_{n=0}^N \frac{w_n}{\rho(x)} (2i + 1) L(x, i).\end{aligned}\quad (87)$$

1076 The comparison between simulated sample and efficiency parametrisation phase space  
 1077 projections is reported in Fig. 39. For each phase space variable the Legendre expansion  
 1078 is built up to order 10, enough to well reproduce the observed dependencies.

1079 The comparison between background sample and parametrisation is reported in  
 1080 Fig. 39. The background distribution is regular for  $\cos \theta_{K\pi}^{*}$ ,  $\cos \theta_p$  and  $\phi'_p$  variables, and  
 1081 their Legendre expansion is built up to order 10. To reproduce the peaking structures  
 1082 in  $m'_{pK^-}$  and  $\chi$  variables polynomials up to order 50 are employed. However, since  
 1083 Legendre polynomial coefficients increase very rapidly (like a factorial) with the order, the  
 1084 inclusion of high orders cause problems in computing the log-likelihood. So, these peaking  
 1085 contribution are neglected limiting the maximum polynomial to 10 also for  $m'_{pK^-}$  and  $\chi$   
 1086 variables. This parametrisation is used for the nominal amplitude fit, reported in Sec. 6.9.

1087 The  $m'_{pK^-}$  peak is present in the lower mass sideband only, while the one in the  $\chi$   
 1088 distribution is present in both sidebands. The comparison between upper mass sideband  
 1089 background sample and parametrisation (Legendre expansion up to order 10) is reported  
 1090 in Fig. 41. The shapes are more regular but the available statistics is lower. This  
 1091 parametrisation is used for evaluating the systematic uncertainty associated to background  
 1092 modelling, Sec. 7.3.

---

<sup>10</sup>The mutual information between two random variables  $X$ ,  $Y$ , given their joint and marginalized probability distributions  $p(X, Y)$  and  $p(X)$ ,  $p(Y)$ , defined as

$$I(X : Y) = \sum_{X,Y} p(X, Y) \log \frac{p(X, Y)}{p(X)p(Y)}, \quad (86)$$

is sensitive to any form of relationship.

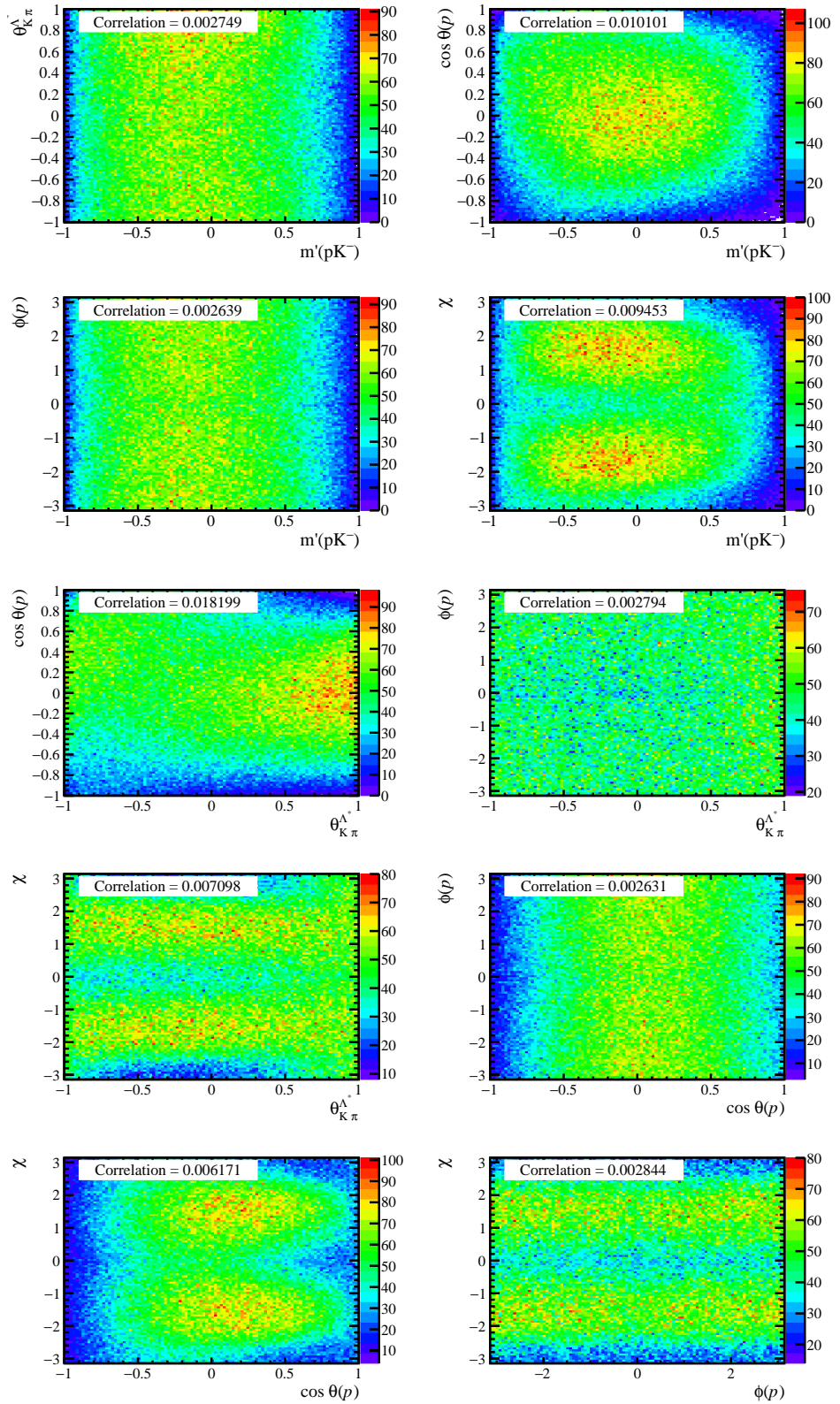


Figure 37: Phase space correlation plots for the simulated sample used for efficiency parametrisation. The mutual information is used as a measure of correlation.

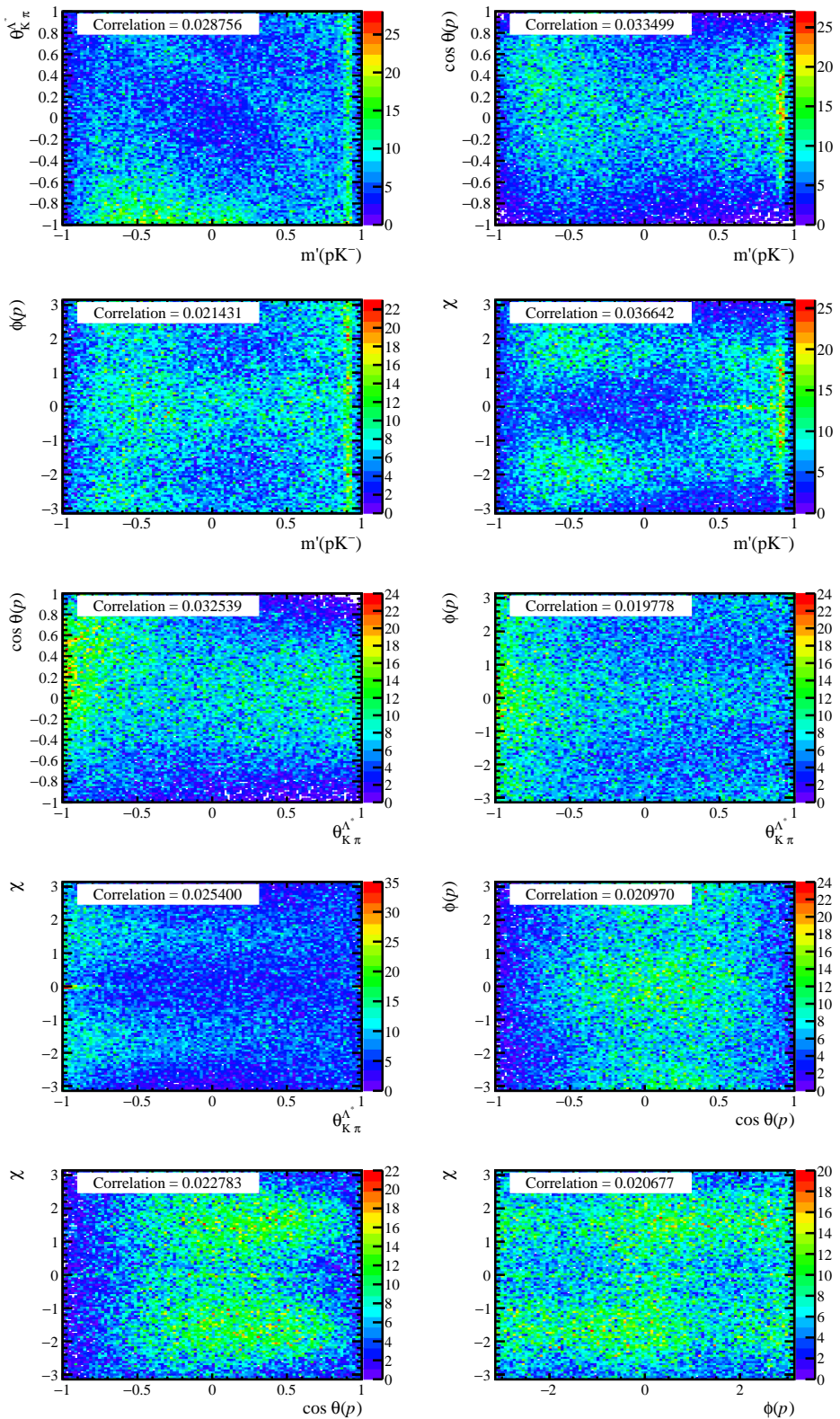


Figure 38: Phase space correlation plots for the background sample. The mutual information is used as a measure of correlation.

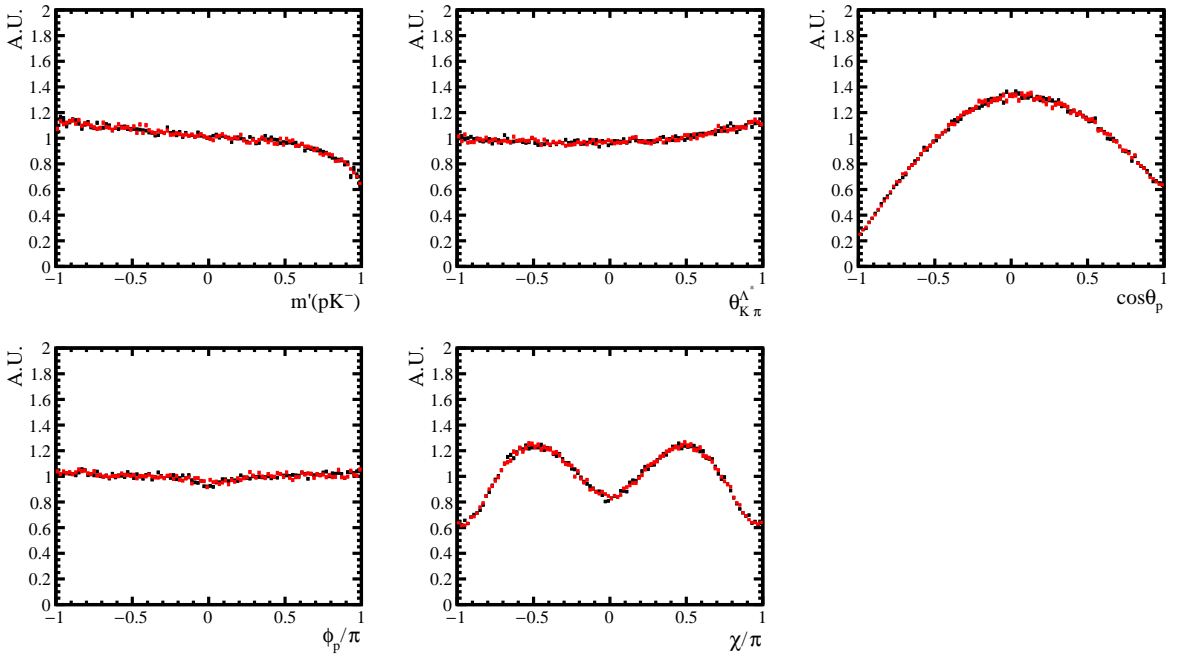


Figure 39: Comparison between (black) simulated  $\Lambda_c^+ \rightarrow p K^- \pi^+$  sample and (red) efficiency Legendre parametrisation phase space projections.

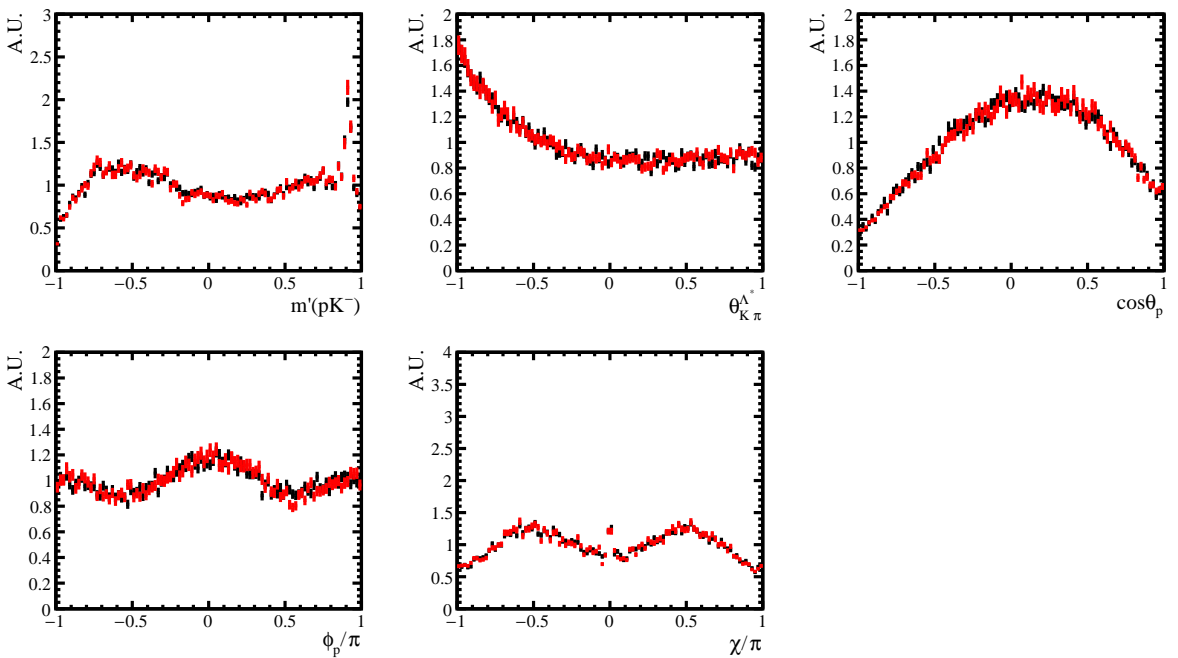


Figure 40: Comparison between (black) background sample from both mass sidebands and (red) background Legendre parametrisation phase space projections.

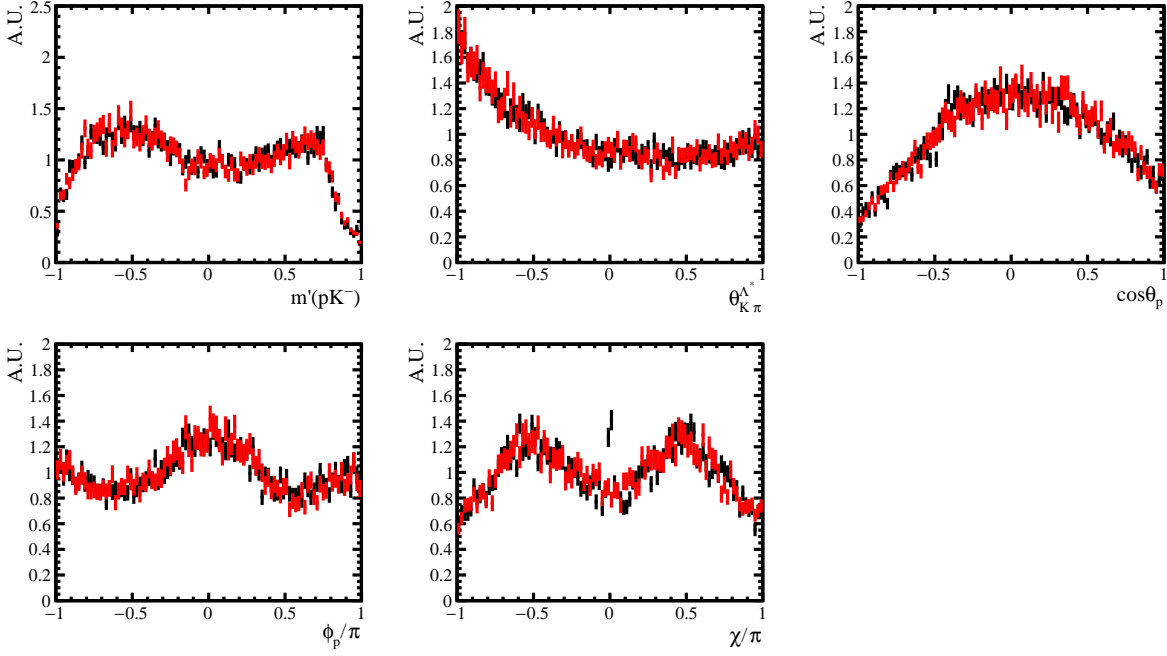


Figure 41: Comparison between (black) background sample from upper mass sideband and (red) background Legendre parametrisation phase space projections.

## 1093 6.7 Amplitude model building

1094 The  $\Lambda_c^+ \rightarrow pK^-\pi^+$  amplitude model is built by adding helicity amplitudes corresponding  
 1095 to a set of intermediate states, Eq. (42), to be chosen in order to describe the decay  
 1096 phase-space distributions. As a starting point we consider the knowledge about  $\Lambda^*$ ,  $\Delta^{++}$   
 1097 and  $K^*$  resonances according to the PDG [1], which is summarised in Table 7. The  
 1098 contribution of  $\Sigma^* \rightarrow pK^-$  resonances is possible but expected to be suppressed since  
 1099 it involves a  $\Delta I = 1$  strong isospin difference in the  $\Lambda_c^+ \rightarrow \Sigma$  process, contrary to  $\Lambda^*$   
 1100 resonances having zero isospin [1]. Moreover, their contribution would be difficult to  
 1101 separate from that of  $\Lambda^*$  resonances, so they are neglected as done in Ref. [45]. A check  
 1102 for their presence is described in Sec. 7.2.4.

1103 The efficiency-uncorrected Dalitz plot for the full sample of 2016  $\Lambda_c^+ \rightarrow pK^-\pi^+$   
 1104 selected candidates is shown in Fig. 42:  $\Lambda^* \rightarrow pK^-$  resonances are visible as vertical  
 1105 bands,  $K^* \rightarrow K^-\pi^+$  as horizontal bands and  $\Delta^{++} \rightarrow p\pi^+$  as diagonal bands, in which  
 1106 the different intensity patterns can be given by the spin of the resonance, by interference  
 1107 patterns or non-uniform detector efficiency. Regarding the  $\Lambda^*$  pattern, there are two clear  
 1108 narrow bands corresponding to the  $\Lambda(1520)$  and  $\Lambda(1670)$  resonances, plus broader bands  
 1109 in between and below the  $\Lambda(1520)$  mass, possible signs of  $\Lambda(1405)$  (whose pole mass is  
 1110 below the  $pK^-$  mass threshold) and  $\Lambda(1600)$  resonances. The only other vertical band  
 1111 is an excess of events in the region  $m_{pK^-}^2 \in 3.8 - 4.0 \text{ GeV}^2$ , better visible in the  $m_{pK^-}^2$   
 1112 projection Fig. 7, which can be a sign of additional  $\Lambda^*$  resonances for which there is no  
 1113 clear evidence according to the PDG [1]. Regarding the  $K^*$  resonances the only clear  
 1114 band is that of the  $K^*(892)$ ; higher mass  $K^*(1410)$  and  $K_0^*(1430)$  resonances, having pole  
 1115 masses outside the allowed phase-space, may contribute thanks to the lower mass tail  
 1116 of their broad distribution, possibly explaining the presence of a large number of events

Resonance	$J^P$	BW mass ( MeV)	BW width ( MeV)	Existence
$\Lambda(1405)$	$1/2^-$	$1405.1^{+1.3}_{-1.0}$	$50.5 \pm 2.0$	certain
$\Lambda(1520)$	$3/2^-$	$1518 - 1520$	$15 - 17$	certain
$\Lambda(1600)$	$1/2^+$	$1570 - 1630$	$150 - 250$	certain
$\Lambda(1670)$	$1/2^-$	$1670 - 1678$	$25 - 35$	certain
$\Lambda(1690)$	$3/2^-$	$1685 - 1695$	$60 - 80$	certain
$\Lambda(1710)$	$1/2^+$	$1713 \pm 13$	$180 \pm 40$	poor
$\Lambda(1800)$	$1/2^-$	$1750 - 1850$	$150 - 250$	very likely
$\Lambda(1810)$	$1/2^+$	$1740 - 1840$	$50 - 170$	very likely
$\Lambda(1820)$	$5/2^+$	$1815 - 1825$	$70 - 90$	certain
$\Lambda(1830)$	$5/2^-$	$1820 - 1830$	$60 - 120$	certain
$\Lambda(1890)$	$3/2^+$	$1870 - 1910$	$80 - 160$	certain
$\Lambda(2000)$	$1/2^-$	$\approx 2000$		poor
$\Lambda(2050)$	$3/2^-$	$2056 \pm 22$	$493 \pm 60$	poor
$\Lambda(2070)$	$3/2^+$	$2076 \pm 24$	$370 \pm 50$	poor
$\Lambda(2080)$	$5/2^-$	$2082 \pm 13$	$181 \pm 29$	poor
$\Lambda(2085)$	$7/2^+$	$\approx 2020$		fair
$\Lambda(2100)$	$7/2^-$	$2090 - 2110$	$100 - 250$	certain
$\Lambda(2110)$	$5/2^+$	$2050 - 2130$	$200 - 300$	very likely
$\Delta^{++}(1232)$	$3/2^+$	$1230 - 1234$	$114 - 120$	certain
$\Delta^{++}(1600)$	$3/2^+$	$1500 - 1640$	$200 - 300$	certain
$\Delta^{++}(1620)$	$1/2^-$	$1590 - 1630$	$110 - 150$	certain
$\Delta^{++}(1700)$	$3/2^-$	$1690 - 1730$	$220 - 380$	certain
$K_0^*(700)$	$0^+$	$824 \pm 30$	$478 \pm 50$	certain
$K^*(892)$	$1^-$	$895.55 \pm 0.20$	$47.3 \pm 0.5$	certain
$K^*(1410)$	$1^-$	$1414 \pm 15$	$232 \pm 21$	certain
$K_0^*(1430)$	$0^+$	$1425 \pm 50$	$270 \pm 80$	certain

Table 7: List of  $\Lambda^*$ ,  $\Delta^{++}$  and  $K^*$  resonances possibly contributing to the  $\Lambda_c^+ \rightarrow p K^- \pi^+$  phase space according to the PDG [1]. Here,  $J^P$  is the spin-parity assignment, BW mass and widths represent the approximate values assuming relativistic Breit-Wigner lineshape and the last column reports the degree of experimental evidence for the resonance existence.

at high  $m_{K^-\pi^+}^2$  invariant mass. Even if a spin-zero non-resonant component cannot be excluded, the center of the Dalitz plot is interestingly almost empty of events. Finally, the diagonal band of the  $\Delta^{++}(1232)$  is apparent, plus an unclear band at higher  $m_{p\pi^+}^2$  mass which may be a sign of additional  $\Delta^{++}$  resonances. The Dalitz plot shows at least two interesting interference effects among resonances belonging to different decay chains, which are needed for the simultaneous measurement of helicity amplitudes and  $\Lambda_c^+$  polarization vector [3]: the  $K^*(892)$  band gets shifted when crossing the  $\Lambda(1670)$  contribution, while the  $\Lambda(1520)$  shows a destructive interference pattern with the high mass  $K^*$  contributions at the upper corner of the Dalitz plot.

The nominal amplitude model is built starting from the contributions identified from the qualitative inspection of the Dalitz plot and adding resonant states according to those listed in the PDG. Four quantities are monitored when comparing different amplitude

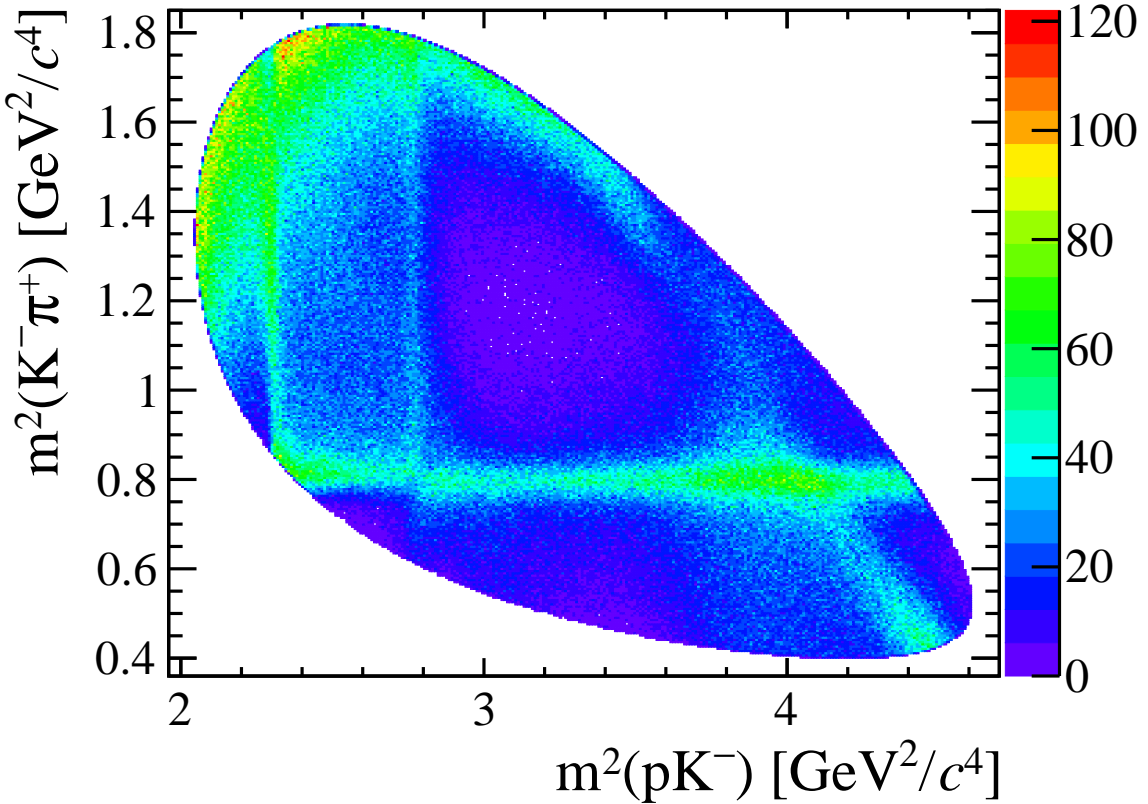


Figure 42: Efficiency-uncorrected Dalitz plot for 2016  $\Lambda_c^+ \rightarrow p K^- \pi^+$  candidates.

fits: NLL variation, as a measure of significance of the added contributions,  $\chi^2$  and its  
 associated probability, as a measure of fit quality, and the sum of fit fractions, as a measure  
 of interference effects. Contributions which significantly improve the fit quality are added  
 to the nominal model; those giving similar fit quality are considered as possible alternative  
 models for systematic uncertainty evaluation, see Sec. 7.1 for more details. When adding  
 a new contribution or variation to the temporary nominal model, the free parameters are  
 fitted starting first from the nominal model results, then they are fitted again 20 times  
 starting from random initial values. Interestingly, the fits with random initial values have  
 never found a better NLL minimum than the first one: they converged either to the same  
 minimum or to greater NLL values. This makes sure the fits are converging to the global  
 NLL minimum.

The resulting nominal model is specified in Table 8. All the contributions give a  
 significant contribution to the amplitude fit, both in terms of NLL decrease and fit quality  
 improvement. Most resonance parameters are fixed in the amplitude fits, the only left  
 floating being those related to the  $\Lambda(1520)$  and the  $\Lambda(2000)$  contributions. The mass  
 and width of the narrow  $\Lambda(1520)$  state are floated to account for possible resolution  
 effects, while those of the  $\Lambda(2000)$  contribution are floated because unknown. Most of the  
 fixed resonance parameters are set to the PDG mean values, but for the broad  $\Lambda(1600)$ ,  
 $\Delta^{++}(1600)$  and  $\Delta^{++}(1700)$  contributions: when floated their parameters are found to be  
 outside the ranges given by the PDG, which indicates that these contributions are likely  
 not well constrained by the amplitude fit. Therefore we fix their parameters at the edges

Resonance	$J^P$	BW mass ( MeV)	BW width ( MeV)
$\Lambda(1405)$	$1/2^-$	1405.1	50.5
$\Lambda(1520)$	$3/2^-$	1515 – 1523	10 – 20
$\Lambda(1600)$	$1/2^+$	1630	250
$\Lambda(1670)$	$1/2^-$	1670	30
$\Lambda(1690)$	$3/2^-$	1690	70
$\Lambda(2000)$	$1/2^-$	1900 – 2100	20 – 400
$\Delta^{++}(1232)$	$3/2^+$	1232	117
$\Delta^{++}(1600)$	$3/2^+$	1640	300
$\Delta^{++}(1700)$	$3/2^-$	1690	380
$K_0^*(700)$	$0^+$	824	478
$K^*(892)$	$1^-$	895.5	47.3
$K_0^*(1430)$	$0^+$	1375	190

Table 8: Resonant composition of the nominal  $\Lambda_c^+ \rightarrow pK^-\pi^+$  amplitude model, with  $J^P$  the spin-parity assignment, and the Breit-Wigner parameters which, in the amplitude fit, are floated within the reported range, or fixed to the given value if no interval is quoted.

of the ranges quoted by the PDG, towards the directions suggested by the amplitude fit: this choice affects very marginally the fit quality, see Sec. 7.1.2 for more details. The same method has been followed to fix the  $K^*(1430)$  parameters: its mass and width are set to the lower PDG limits, while PDG mean values lead to a worser fit quality. The best spin-parity assignment of the  $\Lambda(2000)$  contribution is  $1/2^-$ , see Sec. 7.2.3.

## 6.8 Definition of the amplitude fit parameters

Here the naming conventions for the amplitude fit parameters are detailed.

### 6.8.1 Resonances

Resonant states are indicated as L ( $\Lambda^*$ ), D ( $\Delta^*$ ), K ( $K^*$  nonzero spin) and K0 ( $K^*$  spin zero), followed by their mass identification as assigned by the PDG, Table 7.

### 6.8.2 Lineshape parameters

For most resonances, parametrised using relativistic Breit-Wigner or its modification for sub-threshold resonances, Sec. 6.5, the Breit-Wigner mass and width are indicated as M or G (for “Gamma”), respectively, and expressed in GeV units. The  $\gamma$  parameters driving the exponential form factors of Bugg lineshapes is indicated as gamma, expressed in  $\text{GeV}^{-2}$  units.

### 6.8.3 Helicity couplings

Each complex helicity coupling is introduced in the amplitude fit via two real fit parameters representing its real, Ar, and imaginary, Ai, parts. The number after the resonance

Resonance type	Coupling number	$\lambda_R$	$\lambda_p$
$\Lambda^*, \Delta^*$	1	1/2	
	2	-1/2	
$K^*, S \geq 1$	1	0	1/2
	2	-1	1/2
	3	1	-1/2
	4	0	-1/2
$K^*, S = 0$	1		-1/2
	2		1/2

Table 9: Definition of the helicity couplings.  $\lambda_R$  and  $\lambda_p$  are the resonance and proton helicities as defined for the specific decay channel (*e.g.* for  $K^*$  resonances is the opposite helicity  $\bar{\lambda}_{K^*}$ ), see Secs. 4.4.1, 4.4.2.

1169 specification labels the helicity coupling for specific resonance and proton helicities, as  
1170 described in Table 9<sup>11</sup>.

#### 1171 6.8.4 Polarisation components

1172 The three polarisation components are indicated as Px, Py and Pz.

### 1173 6.9 Nominal amplitude fit results

1174 The amplitude fit results for the nominal model, Table 8, are reported in Table 10 and  
1175 shown in Figs. 43, 44. The associated fit fractions are reported in Table 11, decay  
1176 asymmetry parameters in Table 12. The fit is performed on the fit dataset described in  
1177 Sec. 2.2.

1178 The fit quality is fairly good: there are no big discrepancies between data and model  
1179 distributions. The probability value drawn from the  $\chi^2$  value is  $4.2 \times 10^{-5}$ , which is  
1180 actually a lower limit given that the effective degrees of freedom may be larger than  
1181 assumed (see Sec. 6.4).

1182 The largest contributions to the amplitude model, measured by fit fractions, come  
1183 from  $\Delta^{++}(1232)$ ,  $K^*(892)$  and  $K_0^*(1430)$  resonances. Among  $\Lambda^*$  resonances the larger  
1184 contributions come from  $\Lambda(1405)$  and  $\Lambda(2000)$  states, the latter well reproducing the peak  
1185 at high  $m_{pK^-}^2$  mass.

1186 The sum of fit fractions is close to one, however significant interference effects, as  
1187 anticipated by the visual inspection of the Dalitz plot, are present. Interference effects  
1188 over the  $\Lambda_c^+ \rightarrow pK^-\pi^+$  Dalitz plot for the nominal model are reported in Fig. 45, obtained  
1189 plotting the difference between the model and the incoherent sum of each resonant  
1190 contribution.

1191 The  $\Lambda(2000)$  Breit-Wigner parameters are found to be  $m \approx 1.98$  GeV and  $\Gamma \approx 180$  MeV;  
1192 those of the  $\Lambda(1520)$  are compatible with the ranges quoted by the PDG. The fact that

---

<sup>11</sup>Helicity couplings for baryonic resonances  $\Lambda^*$  and  $\Delta^*$  do not depend on proton helicities for parity conservation in their decay.

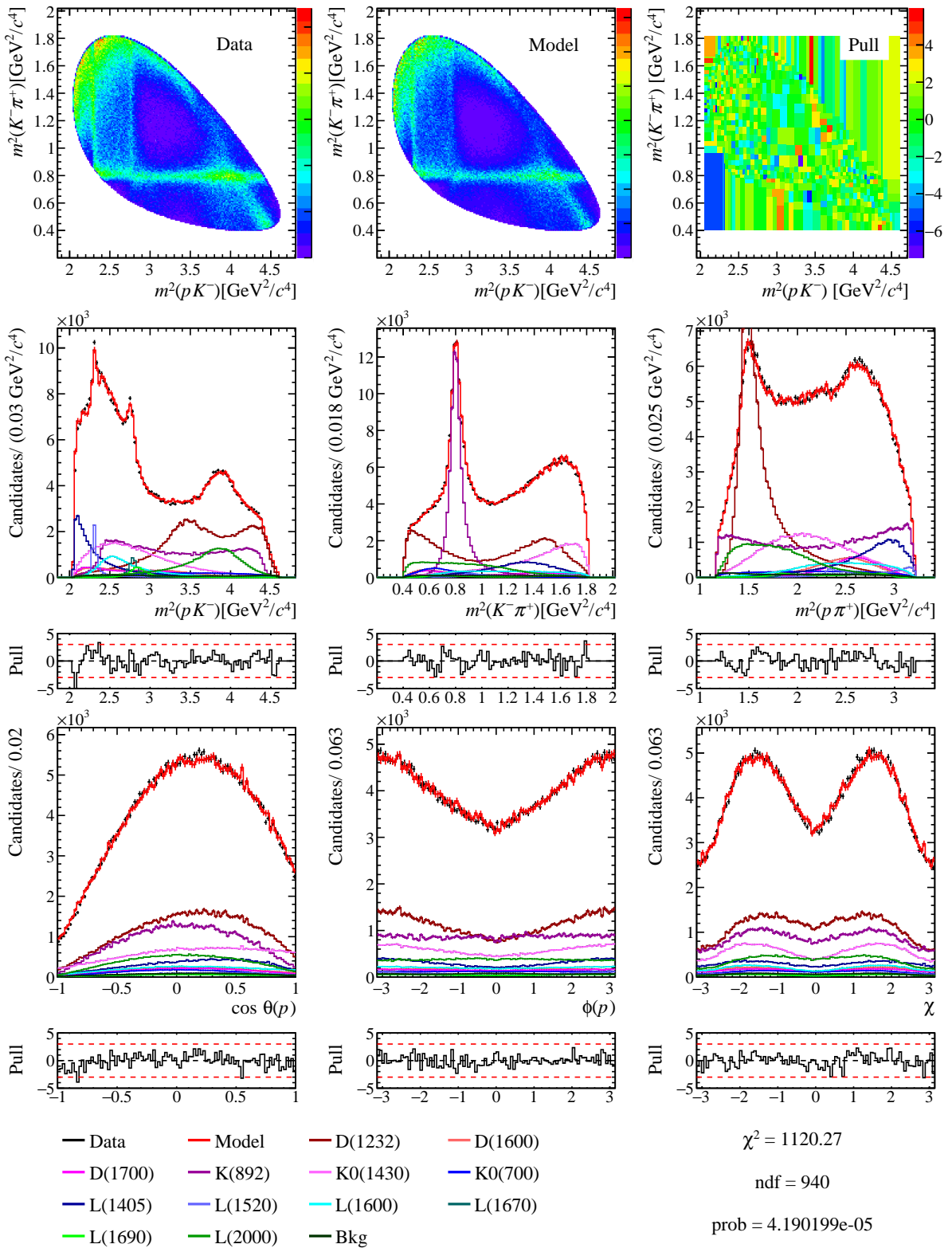


Figure 43: Phase space projections for the amplitude fit with nominal model.

Parameter	Central value	Uncertainty
gammaK0(700)	0.941060	$\pm$ 0.042406
ArK0(700)1	0.068908	$\pm$ 0.122603
AiK0(700)1	2.521444	$\pm$ 0.084235
ArK0(700)2	-2.685630	$\pm$ 0.124151
AiK0(700)2	0.038490	$\pm$ 0.123867
ArK(892)2	1.192614	$\pm$ 0.066524
AiK(892)2	-1.025814	$\pm$ 0.041453
ArK(892)3	-3.141446	$\pm$ 0.092448
AiK(892)3	-3.293410	$\pm$ 0.206014
ArK(892)4	-0.727145	$\pm$ 0.181956
AiK(892)4	-4.155027	$\pm$ 0.119153
gammaK0(1430)	0.020981	$\pm$ 0.011062
ArK0(1430)1	-6.715160	$\pm$ 0.602836
AiK0(1430)1	10.479411	$\pm$ 0.267895
ArK0(1430)2	0.219754	$\pm$ 0.381936
AiK0(1430)2	8.741196	$\pm$ 0.250855
Arl(1405)1	-4.572486	$\pm$ 0.231833
AiL(1405)1	3.190144	$\pm$ 0.169851
Arl(1405)2	10.446080	$\pm$ 0.128799
AiL(1405)2	2.787441	$\pm$ 0.607833
ML(1520)	1.518467	$\pm$ 0.000100
GL(1520)	0.015195	$\pm$ 0.000265
ArL(1520)1	0.293998	$\pm$ 0.012158
AiL(1520)1	0.044324	$\pm$ 0.022276
ArL(1520)2	-0.160687	$\pm$ 0.075604
AiL(1520)2	1.498833	$\pm$ 0.032468
ArL(1600)1	4.840649	$\pm$ 0.080342
AiL(1600)1	3.082786	$\pm$ 0.313304
ArL(1600)2	-6.971233	$\pm$ 0.180278
AiL(1600)2	0.842435	$\pm$ 0.300438
ArL(1670)1	-0.339585	$\pm$ 0.013871
AiL(1670)1	-0.144678	$\pm$ 0.022591
ArL(1670)2	-0.570978	$\pm$ 0.059400
AiL(1670)2	1.011833	$\pm$ 0.017816
ArL(1690)1	-0.385772	$\pm$ 0.046657
AiL(1690)1	-0.110235	$\pm$ 0.045896
ArL(1690)2	-2.730592	$\pm$ 0.052811
AiL(1690)2	-0.353613	$\pm$ 0.136240
ML(2000)	1.988190	$\pm$ 0.000911
GL(2000)	0.179260	$\pm$ 0.002766
ArL(2000)1	-8.014857	$\pm$ 0.267813
AiL(2000)1	-7.614006	$\pm$ 0.529630
ArL(2000)2	-4.336255	$\pm$ 0.137963
AiL(2000)2	-3.796192	$\pm$ 0.285036
ArD(1232)1	-6.778191	$\pm$ 0.268436
AiD(1232)1	3.051805	$\pm$ 0.264359
ArD(1232)2	-12.987193	$\pm$ 0.433180
AiD(1232)2	4.528336	$\pm$ 0.493430
ArD(1600)1	11.401585	$\pm$ 0.437580
AiD(1600)1	-3.125511	$\pm$ 0.473191
ArD(1600)2	6.729211	$\pm$ 0.283501
AiD(1600)2	-1.002383	$\pm$ 0.331137
ArD(1700)1	10.378280	$\pm$ 0.253080
AiD(1700)1	1.434872	$\pm$ 0.485532
ArD(1700)2	12.874102	$\pm$ 0.233827
AiD(1700)2	2.105570	$\pm$ 0.644916
Px	0.603214	$\pm$ 0.002419
Py	-0.004078	$\pm$ 0.000763
Pz	-0.246958	$\pm$ 0.003603

Table 10: Fit parameters returned by MINUIT for the amplitude fit with nominal model. Uncertainties are the  $1\sigma$  standard deviations returned by HESSE. Fit parameters are defined in Sec. 6.8.

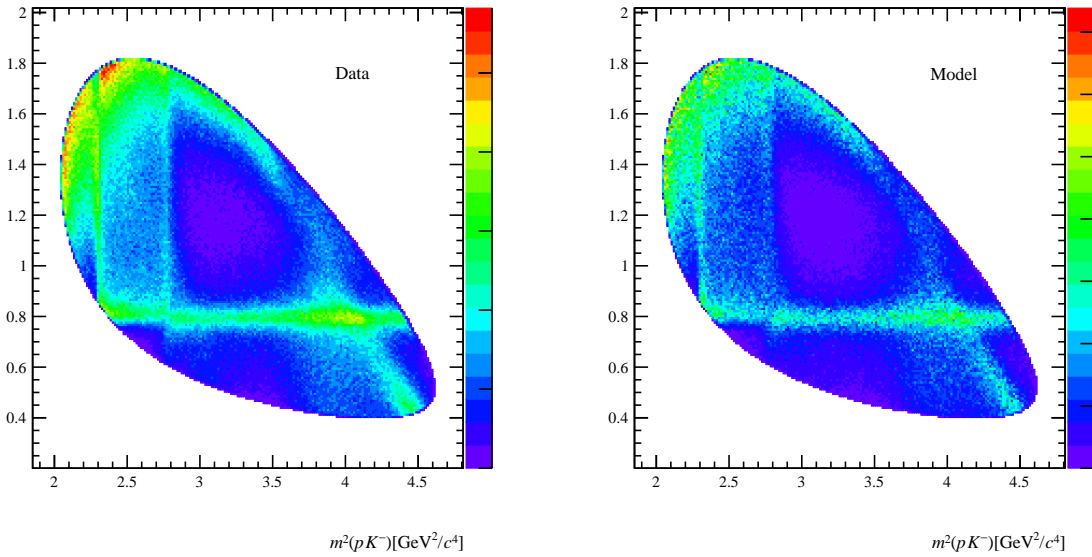


Figure 44: (left) Data and (right) Model Dalitz Plots. Here, the entire 2016 selected data and MC samples are used.

Resonance	Fit Fraction		Uncertainty
$\Delta^{++}(1232)$	0.285997	$\pm$	0.010696
$\Delta^{++}(1600)$	0.045180	$\pm$	0.002434
$\Delta^{++}(1700)$	0.039025	$\pm$	0.001893
$K^*(892)$	0.221389	$\pm$	0.008538
$K^*0(1430)$	0.147098	$\pm$	0.006617
$K^*0(700)$	0.030178	$\pm$	0.001578
$\Lambda(1405)$	0.077164	$\pm$	0.003007
$\Lambda(1520)$	0.018621	$\pm$	0.000838
$\Lambda(1600)$	0.051787	$\pm$	0.002177
$\Lambda(1670)$	0.011787	$\pm$	0.000478
$\Lambda(1690)$	0.011943	$\pm$	0.000549
$\Lambda(2000)$	0.095805	$\pm$	0.003874
Sum	1.035972	$\pm$	0.016526

Table 11: Fit fractions for the amplitude fit with nominal model. Uncertainties are computed from the fitted parameters in Table 10 and the covariance returned by the MINUIT minimisation.

Resonance	$\alpha$	Uncertainty
Model ( $\sqrt{3}S$ )	0.662306	$\pm$ 0.012681
$\Delta^{++}(1232)$	-0.547868	$\pm$ 0.108512
$\Delta^{++}(1600)$	0.502429	$\pm$ 0.132945
$\Delta^{++}(1700)$	-0.215788	$\pm$ 0.144851
$K^*(892)$	-0.834474	$\pm$ 0.067141
$K^*0(1430)$	-0.339090	$\pm$ 0.145169
$K^*0(700)$	0.062731	$\pm$ 0.930468
$\Lambda(1405)$	-0.579866	$\pm$ 0.066536
$\Lambda(1520)$	-0.925108	$\pm$ 0.062745
$\Lambda(1600)$	-0.199072	$\pm$ 0.205708
$\Lambda(1670)$	-0.816631	$\pm$ 0.082630
$\Lambda(1690)$	-0.958417	$\pm$ 0.057190
$\Lambda(2000)$	0.572602	$\pm$ 0.122557

Table 12: Decay asymmetry parameters for the amplitude fit with nominal model, computed as described in Sec. 6.3. Uncertainties are computed from the fitted parameters in Table 10 and the covariance returned by the MINUIT minimisation.

the width of the  $\Lambda(1520)$  state is not overestimated is a sign that detector resolution effects are very small.

A significant polarisation is measured by the fit in the  $\Lambda_c^+$  helicity frame reached from the laboratory, with a modulus  $P \approx 66\%$ . Its direction is in the  $\Lambda_c^+ - \mu^-$  plane, as expected following the discussion in Sec. 4.1, mainly orthogonal to the  $\Lambda_c^+$  momentum. The normal polarisation  $P_y$  is close to zero.

To check the fit convergence, the nominal fit is also repeated 100 times with randomised starting fit parameters instead of 20, but no better NLL minima are found.

The amplitude fit with the nominal model is repeated changing the polarisation frame to the  $\Lambda_c^+$  helicity frame reached from an approximate  $\Lambda_b^0$  rest frame, for the two reconstruction algorithms presented in Sec. 4.1.

The amplitude fit results for polarisation measured in the  $\Lambda_c^+$  helicity frame reached from the approximate  $\Lambda_b^0$  frame reconstructed via the “Full reconstruction” algorithm are reported in Table 13 and shown in Fig. 46. The associated fit fractions are reported in Table 14, decay asymmetry parameters in Table 15. The fit quality is good but for a discrepancy in the  $\phi_p$  distribution. A disagreement in decay orientation angles is not surprising because of the differences between data and MC samples regarding beauty hadron semileptonic decays: while the simulation contains only  $\Lambda_b^0 \rightarrow \Lambda_c^+ \mu^- \nu_\mu$  decays, the selection criteria applied to data do not reject other decay modes, *e.g.*  $\Lambda_b^0 \rightarrow \Lambda_c^+ \tau^- \nu_\tau$ .

The amplitude model obtained is compatible with that referring to the  $\Lambda_c^+$  helicity frame reached from the laboratory, see Sec. 8 and Appendix D for a quantitative comparison. A large polarisation is found,  $P \approx 69\%$ , in this frame being more longitudinal  $P_z \approx -61\%$  than transverse  $P_x \approx 32\%$ , with the latter value which could be biased due to the  $\phi_p$  discrepancy. Normal polarisation is close to zero. This polarisation frame is not considered for providing final results: the understanding of the observed discrepancies would require a specific analysis of the semileptonic decays contributing to the fit datasample.

Parameter	Central value	Uncertainty
gammaK0(700)	0.953402	$\pm$ 0.048903
ArK0(700)1	0.035344	$\pm$ 0.126013
AiK0(700)1	2.289112	$\pm$ 0.131573
ArK0(700)2	-2.448281	$\pm$ 0.154688
AiK0(700)2	0.031553	$\pm$ 0.134912
ArK(892)2	1.066743	$\pm$ 0.064163
AiK(892)2	-1.041785	$\pm$ 0.063938
ArK(892)3	-2.810232	$\pm$ 0.193033
AiK(892)3	-3.096465	$\pm$ 0.184678
ArK(892)4	-0.737698	$\pm$ 0.179377
AiK(892)4	-3.839400	$\pm$ 0.171281
gammaK0(1430)	0.015284	$\pm$ 0.011147
ArK0(1430)1	-6.062540	$\pm$ 0.529582
AiK0(1430)1	9.785043	$\pm$ 0.575240
ArK0(1430)2	0.201531	$\pm$ 0.408674
AiK0(1430)2	8.005151	$\pm$ 0.375570
ArL(1405)1	-4.252359	$\pm$ 0.230162
AiL(1405)1	2.846311	$\pm$ 0.272235
ArL(1405)2	9.863916	$\pm$ 0.454255
AiL(1405)2	2.711975	$\pm$ 0.538033
ML(1520)	1.518669	$\pm$ 0.000108
GL(1520)	0.015447	$\pm$ 0.000219
ArL(1520)1	0.295168	$\pm$ 0.023516
AiL(1520)1	0.057651	$\pm$ 0.020788
ArL(1520)2	-0.163641	$\pm$ 0.068104
AiL(1520)2	1.399628	$\pm$ 0.065432
ArL(1600)1	4.430041	$\pm$ 0.259323
AiL(1600)1	2.621279	$\pm$ 0.280010
ArL(1600)2	-6.474293	$\pm$ 0.301619
AiL(1600)2	0.728392	$\pm$ 0.329073
ArL(1670)1	-0.301619	$\pm$ 0.025201
AiL(1670)1	-0.119691	$\pm$ 0.023973
ArL(1670)2	-0.534195	$\pm$ 0.050422
AiL(1670)2	0.934233	$\pm$ 0.052706
ArL(1690)1	-0.389931	$\pm$ 0.049087
AiL(1690)1	-0.082483	$\pm$ 0.041250
ArL(1690)2	-2.525090	$\pm$ 0.108906
AiL(1690)2	-0.366264	$\pm$ 0.121488
ML(2000)	1.988177	$\pm$ 0.001303
GL(2000)	0.178047	$\pm$ 0.003079
ArL(2000)1	-7.402203	$\pm$ 0.513708
AiL(2000)1	-6.994909	$\pm$ 0.461264
ArL(2000)2	-3.892458	$\pm$ 0.284205
AiL(2000)2	-3.540174	$\pm$ 0.246685
ArD(1232)1	-6.083588	$\pm$ 0.291171
AiD(1232)1	2.747409	$\pm$ 0.297818
ArD(1232)2	-12.138670	$\pm$ 0.525265
AiD(1232)2	4.131741	$\pm$ 0.599419
ArD(1600)1	10.320868	$\pm$ 0.490193
AiD(1600)1	-2.985719	$\pm$ 0.539648
ArD(1600)2	6.070481	$\pm$ 0.442576
AiD(1600)2	-0.961247	$\pm$ 0.357575
ArD(1700)1	9.572884	$\pm$ 0.490874
AiD(1700)1	1.055706	$\pm$ 0.503842
ArD(1700)2	11.477380	$\pm$ 0.581988
AiD(1700)2	1.711539	$\pm$ 0.586431
Px	0.313377	$\pm$ 0.003146
Py	0.012642	$\pm$ 0.000855
Pz	-0.615565	$\pm$ 0.003815

Table 13: Fit parameters returned by MINUIT for the amplitude fit with nominal model, with polarisation measured in the  $\Lambda_c^+$  helicity frame reached from the approximate  $\Lambda_b^0$  rest frame reconstructed using the “Full reconstruction” algorithm. Uncertainties are the  $1\sigma$  standard deviations returned by HESSE. Fit parameters are defined in Sec. 6.8.

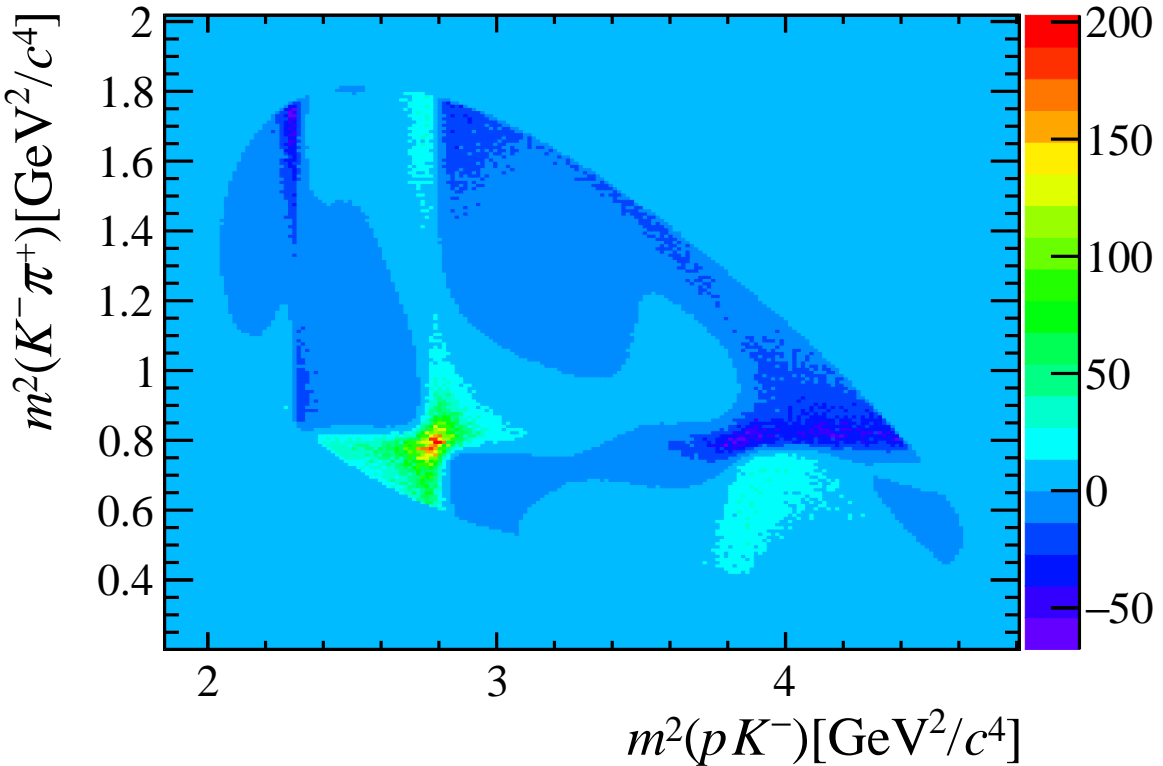


Figure 45: Interference effects over the  $\Lambda_c^+ \rightarrow p K^- \pi^+$  Dalitz plot for the nominal model, obtained plotting the difference between the model and the incoherent sum of each resonant contribution, using 1 million generated MC events.

Resonance	Fit Fraction		Uncertainty
$\Delta^{++}(1232)$	0.286589	$\pm$	0.024218
$\Delta^{++}(1600)$	0.043600	$\pm$	0.004284
$\Delta^{++}(1700)$	0.037155	$\pm$	0.003604
$K^*(892)$	0.222586	$\pm$	0.018569
$K^*0(1430)$	0.145787	$\pm$	0.013989
$K^*0(700)$	0.029620	$\pm$	0.002830
$\Lambda(1405)$	0.079964	$\pm$	0.006588
$\Lambda(1520)$	0.018868	$\pm$	0.001701
$\Lambda(1600)$	0.050874	$\pm$	0.004787
$\Lambda(1670)$	0.011733	$\pm$	0.001045
$\Lambda(1690)$	0.012050	$\pm$	0.001019
$\Lambda(2000)$	0.095700	$\pm$	0.008405
Sum	1.034526	$\pm$	0.036171

Table 14: Fit fractions for the amplitude fit with nominal model, with polarisation measured in the  $\Lambda_c^+$  helicity frame reached from the approximate  $\Lambda_b^0$  rest frame reconstructed using the “Full reconstruction” algorithm. Uncertainties are computed from the fitted parameters in Table 10 and the covariance returned by the MINUIT minimisation.

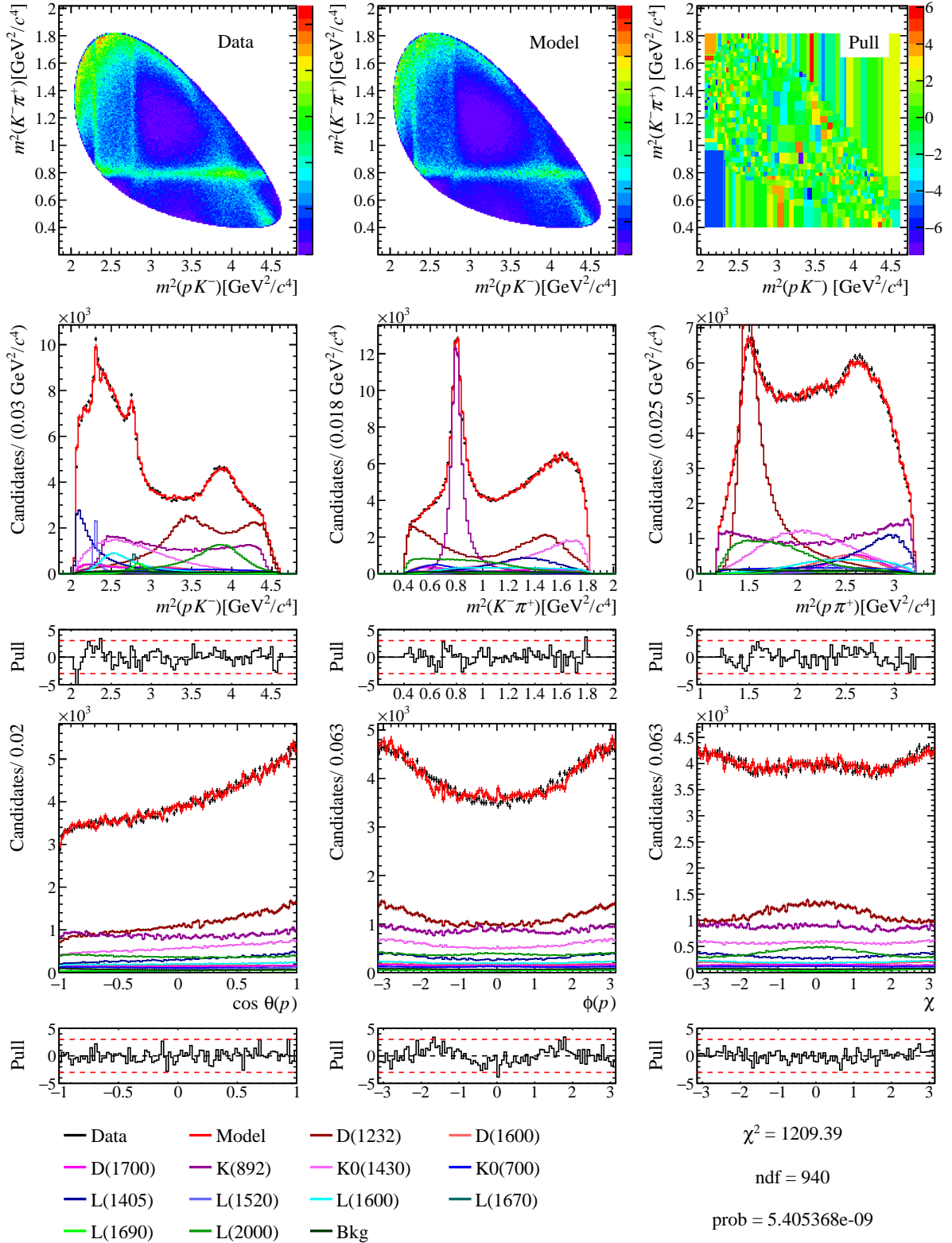


Figure 46: Phase space projections for the amplitude fit, with polarisation measured in the  $\Lambda_c^+$  helicity frame reached from the approximate  $\Lambda_b^0$  rest frame reconstructed using the “Full reconstruction” algorithm.

Resonance	$\alpha$	Uncertainty
Model ( $\sqrt{3}S$ )	0.668572	$\pm$ 0.029248
$\Delta^{++}(1232)$	-0.573558	$\pm$ 0.136825
$\Delta^{++}(1600)$	0.506888	$\pm$ 0.172097
$\Delta^{++}(1700)$	-0.184267	$\pm$ 0.400164
$K^*(892)$	-0.820900	$\pm$ 0.091025
$K^*0(1430)$	-0.347761	$\pm$ 0.221229
$K^*0(700)$	0.067085	$\pm$ 1.286848
$\Lambda(1405)$	-0.599742	$\pm$ 0.144885
$\Lambda(1520)$	-0.912871	$\pm$ 0.132200
$\Lambda(1600)$	-0.231359	$\pm$ 0.308052
$\Lambda(1670)$	-0.833314	$\pm$ 0.140227
$\Lambda(1690)$	-0.952362	$\pm$ 0.121432
$\Lambda(2000)$	0.578647	$\pm$ 0.157485

Table 15: Decay asymmetry parameters for the amplitude fit with nominal model, computed as described in Sec. 6.3, with polarisation measured in the  $\Lambda_c^+$  helicity frame reached from the approximate  $\Lambda_b^0$  rest frame reconstructed using the “Full reconstruction” algorithm. Uncertainties are computed from the fitted parameters in Table 10 and the covariance returned by the MINUIT minimisation.

The amplitude fit results for polarisation measured in the  $\Lambda_c^+$  helicity frame reached from the approximate  $\Lambda_b^0$  frame reconstructed via the “Equal boost” algorithm are reported in Table 16 and shown in Fig. 47. The associated fit fractions are reported in Table 17, decay asymmetry parameters in Table 18. The fit quality is good, no significant discrepancies are visible.

The amplitude model obtained is compatible with that referring to the  $\Lambda_c^+$  helicity frame reached from the laboratory, see Sec. 8 and Appendix D for a quantitative comparison. The polarisation vector is similar to that obtained with the “Full reconstruction” algorithms: same polarisation modulus  $P \approx 69\%$ , more longitudinal than transverse; in this case it is even more longitudinal,  $P_z \approx -66\%$  and  $P_x \approx 21\%$ . Normal polarisation is close to zero. The difference in polarisation between the two reconstruction algorithms gives an idea of the uncertainty caused by the limited knowledge of the  $\Lambda_b^0$  rest frame.

## 6.10 Resolution effects

The typical resolution on invariant masses expected from the LHCb detector is order few MeV, which may be important for resonances featuring a narrow width in invariant mass spectrum. In  $\Lambda_c^+ \rightarrow pK^-\pi^+$  data, the only peaking structures are those related to  $\Lambda(1520)$  and  $\Lambda(1670)$  contributions, having widths between 15 – 17 and 25 – 35 MeV, respectively. The resolution on  $m(pK^-)$  is checked comparing the true and reconstructed invariant mass values on simulation. Two regions around the narrow  $\Lambda^*$  contributions are studied:  $1520 \pm 20$  and  $1670 \pm 40$  MeV, Fig. 48. The width of the distribution is found to be around 1.5 and 2 MeV in the  $\Lambda(1520)$  and  $\Lambda(1670)$  regions, respectively. Since these values are one order of magnitude less than the narrower structures in the  $m(pK^-)$  phase

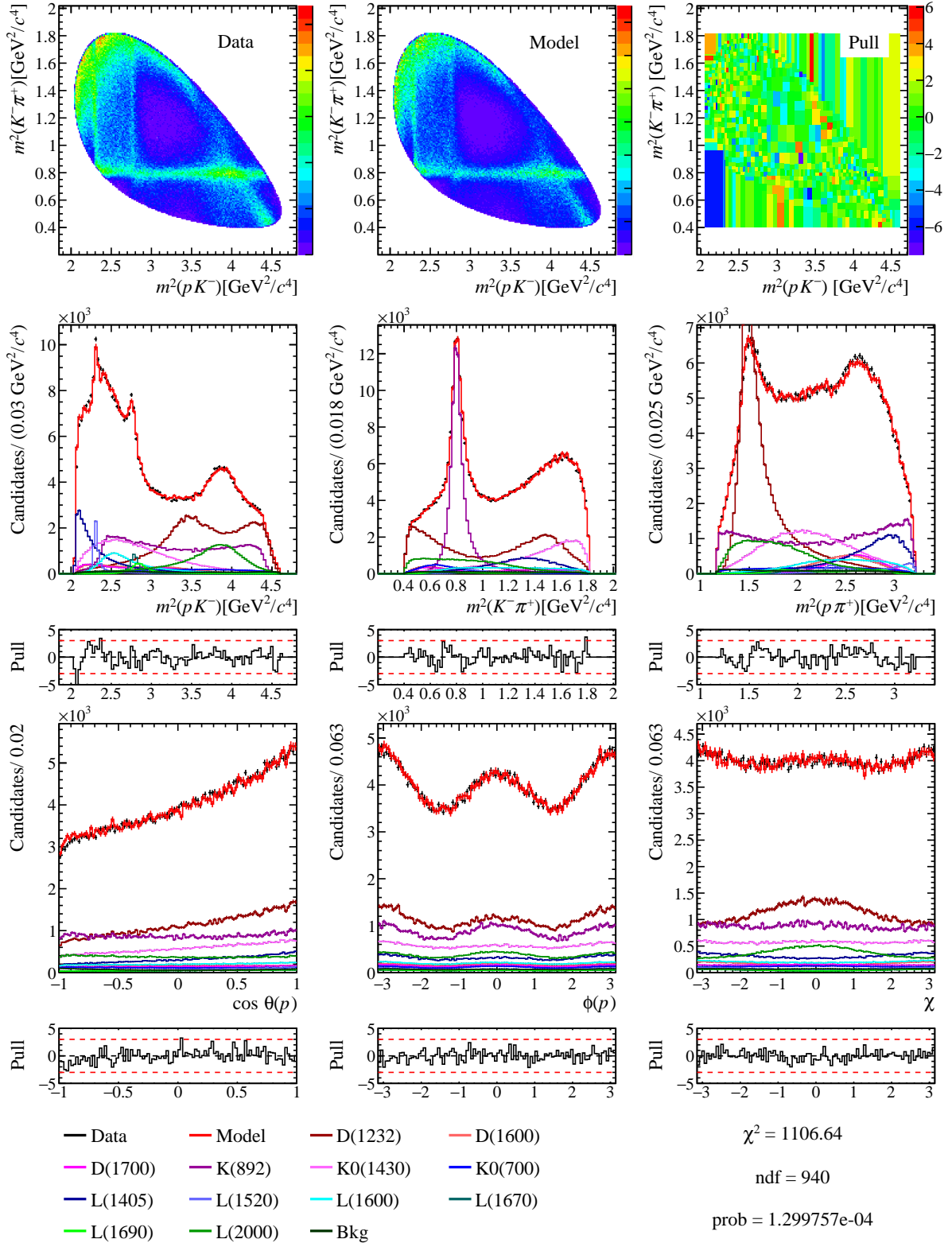


Figure 47: Phase space projections for the amplitude fit with nominal model, with polarisation measured in the  $\Lambda_c^+$  helicity frame reached from the approximate  $\Lambda_b^0$  rest frame reconstructed using the “Equal boost” algorithm.

Parameter	Central value	Uncertainty
gammaK0(700)	0.938580	$\pm$ 0.046941
ArK0(700)1	0.022646	$\pm$ 0.123230
AiK0(700)1	2.280049	$\pm$ 0.129922
ArK0(700)2	-2.430080	$\pm$ 0.148641
AiK0(700)2	0.058299	$\pm$ 0.130188
ArK(892)2	1.052461	$\pm$ 0.065589
AiK(892)2	-1.039656	$\pm$ 0.060802
ArK(892)3	-2.742634	$\pm$ 0.187119
AiK(892)3	-3.103361	$\pm$ 0.180268
ArK(892)4	-0.706763	$\pm$ 0.174646
AiK(892)4	-3.805224	$\pm$ 0.166020
gammaK0(1430)	0.014334	$\pm$ 0.011454
ArK0(1430)1	-6.084784	$\pm$ 0.520049
AiK0(1430)1	9.669191	$\pm$ 0.560763
ArK0(1430)2	0.199384	$\pm$ 0.404587
AiK0(1430)2	7.916568	$\pm$ 0.367259
ArL(1405)1	-4.244215	$\pm$ 0.226963
AiL(1405)1	2.787281	$\pm$ 0.272178
ArL(1405)2	9.711310	$\pm$ 0.438046
AiL(1405)2	2.781865	$\pm$ 0.528438
ML(1520)	1.518624	$\pm$ 0.000139
GL(1520)	0.015449	$\pm$ 0.000346
ArL(1520)1	0.304763	$\pm$ 0.024741
AiL(1520)1	0.048655	$\pm$ 0.020889
ArL(1520)2	-0.165283	$\pm$ 0.068340
AiL(1520)2	1.383250	$\pm$ 0.066388
ArL(1600)1	4.450771	$\pm$ 0.249106
AiL(1600)1	2.634823	$\pm$ 0.279108
ArL(1600)2	-6.361192	$\pm$ 0.291049
AiL(1600)2	0.665379	$\pm$ 0.319392
ArL(1670)1	-0.301522	$\pm$ 0.026005
AiL(1670)1	-0.104016	$\pm$ 0.021453
ArL(1670)2	-0.537159	$\pm$ 0.049520
AiL(1670)2	0.915069	$\pm$ 0.050883
ArL(1690)1	-0.402047	$\pm$ 0.048219
AiL(1690)1	-0.108668	$\pm$ 0.036793
ArL(1690)2	-2.511521	$\pm$ 0.107002
AiL(1690)2	-0.408117	$\pm$ 0.120072
ML(2000)	1.988321	$\pm$ 0.001215
GL(2000)	0.178368	$\pm$ 0.003073
ArL(2000)1	-7.266493	$\pm$ 0.498915
AiL(2000)1	-7.008131	$\pm$ 0.444914
ArL(2000)2	-3.897619	$\pm$ 0.281606
AiL(2000)2	-3.499512	$\pm$ 0.242301
ArD(1232)1	-6.071763	$\pm$ 0.285506
AiD(1232)1	2.689754	$\pm$ 0.293255
ArD(1232)2	-12.044884	$\pm$ 0.509552
AiD(1232)2	3.973336	$\pm$ 0.578979
ArD(1600)1	10.123785	$\pm$ 0.475835
AiD(1600)1	-2.898388	$\pm$ 0.513764
ArD(1600)2	6.008779	$\pm$ 0.427624
AiD(1600)2	-0.955054	$\pm$ 0.349606
ArD(1700)1	9.427164	$\pm$ 0.472989
AiD(1700)1	1.092168	$\pm$ 0.477279
ArD(1700)2	11.319597	$\pm$ 0.559953
AiD(1700)2	1.781636	$\pm$ 0.563509
Px	0.216509	$\pm$ 0.002782
Py	0.010822	$\pm$ 0.000719
Pz	-0.664688	$\pm$ 0.004158

Table 16: Fit parameters returned by MINUIT for the amplitude fit with nominal model, with polarisation measured in the  $\Lambda_c^+$  helicity frame reached from the approximate  $\Lambda_b^0$  rest frame reconstructed using the “Equal boost” algorithm. Uncertainties are the  $1\sigma$  standard deviations returned by HESSE. Fit parameters are defined in Sec. 6.8.

Resonance	Fit Fraction		Uncertainty
$\Delta^{++}(1232)$	0.286632	$\pm$	0.023659
$\Delta^{++}(1600)$	0.042919	$\pm$	0.004129
$\Delta^{++}(1700)$	0.036880	$\pm$	0.003495
$K^*(892)$	0.222762	$\pm$	0.018150
$K^*0(1430)$	0.145969	$\pm$	0.013725
$K^*0(700)$	0.029436	$\pm$	0.002763
$\Lambda(1405)$	0.079662	$\pm$	0.006409
$\Lambda(1520)$	0.018860	$\pm$	0.001689
$\Lambda(1600)$	0.050909	$\pm$	0.004697
$\Lambda(1670)$	0.011621	$\pm$	0.001005
$\Lambda(1690)$	0.012246	$\pm$	0.001021
$\Lambda(2000)$	0.095810	$\pm$	0.008210
Sum	1.033706	$\pm$	0.035354

Table 17: Fit fractions for the amplitude fit with nominal model, with polarisation measured in the  $\Lambda_c^+$  helicity frame reached from the approximate  $\Lambda_b^0$  rest frame reconstructed using the “Equal boost” algorithm. Uncertainties are computed from the fitted parameters in Table 10 and the covariance returned by the MINUIT minimisation.

Resonance	$\alpha$		Uncertainty
Model ( $\sqrt{3}S$ )	0.667672	$\pm$	0.028534
$\Delta^{++}(1232)$	-0.569678	$\pm$	0.134550
$\Delta^{++}(1600)$	0.499456	$\pm$	0.171554
$\Delta^{++}(1700)$	-0.186308	$\pm$	0.386323
$K^*(892)$	-0.819451	$\pm$	0.089312
$K^*0(1430)$	-0.350909	$\pm$	0.216282
$K^*0(700)$	0.063879	$\pm$	1.319613
$\Lambda(1405)$	-0.596618	$\pm$	0.142449
$\Lambda(1520)$	-0.906434	$\pm$	0.135791
$\Lambda(1600)$	-0.209223	$\pm$	0.330511
$\Lambda(1670)$	-0.834258	$\pm$	0.137942
$\Lambda(1690)$	-0.947817	$\pm$	0.119781
$\Lambda(2000)$	0.575768	$\pm$	0.154278

Table 18: Decay asymmetry parameters for the amplitude fit with nominal model, computed as described in Sec. 6.3, with polarisation measured in the  $\Lambda_c^+$  helicity frame reached from the approximate  $\Lambda_b^0$  rest frame reconstructed using the “Equal boost” algorithm. Uncertainties are computed from the fitted parameters in Table 10 and the covariance returned by the MINUIT minimisation.

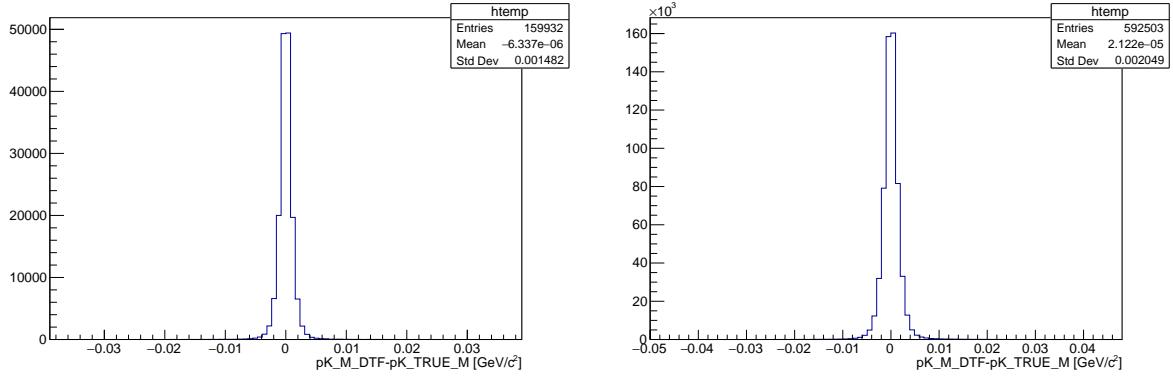


Figure 48: Distribution of the difference between reconstructed and true  $m(pK^-)$  values in the *ReDecay* simulation samples for (left)  $1520 \pm 20$  and (right)  $1670 \pm 40$  MeV  $m(pK^-)$  regions.

space projections, resolution effects are negligible, and not studied further.

## 1242 7 Systematic uncertainties

### 1243 7.1 Amplitude model choice

1244 To estimate the systematic uncertainty associated to the choice of the amplitude model,  
1245 many variations of the nominal model are considered. In this section we report those  
1246 leading to a fit quality comparable to that of the nominal model (alternative models) and  
1247 are considered for systematic uncertainty evaluation. For each fit parameter, fit fraction  
1248 and  $\alpha$  parameter, the maximum absolute variation with respect to the nominal fit results  
1249 among the alternative models is considered as systematic uncertainty due to the choice of  
1250 the amplitude model. The numerical values are reported in Sec. 7.7.

1251 Variations of the nominal model which have not been considered for systematic  
1252 uncertainties evaluation are reported in Sec. 7.2.

#### 1253 7.1.1 Breit-Wigner parameters for $K^*(892)$ , $\Lambda(1670)$ , $\Lambda(1690)$ , $\Delta(1232)$ contributions

1255 Amplitude fits in which the mass and width parameters for specific resonances have been  
1256 left floating are tried, one resonance at a time.

1257 The  $K^*(892)$  and  $\Lambda(1670)$  BW parameters are found to be compatible with the PDG  
1258 values used in the amplitude fits within PDG uncertainties, with basically same  $\chi^2$  value  
1259 as for the nominal fit.

1260 The  $\Delta(1232)$  parameters are found to be larger than the mean PDG values: the mass  
1261 is shifted from 1232 to  $\approx 1244$  MeV; the width from 117 to  $\approx 130$  MeV, beyond PDG upper  
1262 limits. The fit shows a decrease of 2  $\chi^2$  units, similar probability; slight improvement in  
1263 the  $m_{p\pi^+}^2$  pull distribution around the  $\Delta(1232)$  peak. The sum of fit fraction is increased  
1264 to 1.07.

1265 The  $\Lambda(1690)$  parameters are found to be larger than the mean PDG values: the mass  
1266 is shifted from 1690 to  $\approx 1700$  MeV (not far from the PDG upper limit 1695 MeV); the  
1267 width from 70 to  $\approx 94$  MeV (beyond the PDG upper limit 80 MeV). The fit shows a  
1268 decrease of 2  $\chi^2$  unit, similar probability; no significant variations in the pull distributions.  
1269 The sum of fit fraction is unchanged with respect to the nominal model one.

1270 While the first two fits are basically identical to the nominal fit, the latter two show  
1271 some difficulty in constraining the resonance BW parameters: different values lead to very  
1272 similar fit qualities. This four amplitude fits are considered as alternative models.

#### 1273 7.1.2 Breit-Wigner parameters for broad $\Lambda(1600)$ , $\Delta^{++}(1600)$ and $\Delta^{++}(1700)$ 1274 contributions

1275 An amplitude fit in which the Breit-Wigner mass and width parameters of the broad  
1276  $\Lambda(1600)$ ,  $\Delta^{++}(1600)$  and  $\Delta^{++}(1700)$  resonances are left floating is performed. The  
1277 resulting fit shows a decrease of 10  $\chi^2$  units and a modest probability improvement to  
1278  $5.4 \times 10^{-5}$ ; no appreciable differences in the pull distributions are observed; the sum of  
1279 fit fraction is similar to the nominal model. However, most of the fitted Breit-Wigner  
1280 parameters for the three contributions are forced far outside the ranges quoted by the  
1281 PDG:

- 1282 •  $\Lambda(1600)$  mass: found at 1.64 GeV, near the 1.63 GeV upper limit;

- $\Lambda(1600)$  width: found at 280 MeV, beyond the 250 MeV upper limit;
- $\Delta^{++}(1600)$  mass: found at 1.65 GeV, near the 1.64 GeV upper limit;
- $\Delta^{++}(1600)$  width: found at 400 MeV, beyond the 300 MeV upper limit;
- $\Delta^{++}(1700)$  mass: found at 1.76 GeV, beyond the 1.73 MeV upper limit;
- $\Delta^{++}(1700)$  width: found at 580 MeV, beyond the 380 MeV upper limit;

Thus, it has been decided to fix masses and widths in the nominal amplitude model at the edges of the ranges quoted by the PDG, towards the directions suggested by the amplitude fit; a worser fit quality is obtained if these parameters are fixed to the PDG mean values.

Even if the fitted Breit-Wigner parameters are well outside the PDG ranges we consider this fit as an alternative model, given the large uncertainties associated to the knowledge of the  $\Lambda(1600)$ ,  $\Delta^{++}(1600)$  and  $\Delta^{++}(1700)$  resonances.

### 7.1.3 $\Lambda(1405)$ widths

An amplitude fit in which the two  $\Lambda(1405)$  widths, associated to the two-component Flatté lineshape, are left floating is performed. The fit quality is basically unchanged: 2  $\chi^2$  unit decrease with basically equal probability value; pull distributions almost equal. The widths are different than the  $\Gamma = 50.5$  MeV value assumed: around 36 and 95 MeV for those associated to  $pK$  and  $\Sigma\pi$  decay channel, respectively. The sum of fit fractions is similar to the nominal model one. We consider this fit as an alternative model.

### 7.1.4 $\Lambda(1800)$ contribution

An amplitude fit adding the broad  $\Lambda(1800)$  contribution is performed, first with parameters fixed to the PDG mean values. The fit quality is basically unchanged: 1  $\chi^2$  units decrease with probability decreased to  $3.1 \times 10^{-5}$  due to the larger ndf; no visible changes in pull distributions; sum of fit fractions unchanged. The  $\Lambda(1800)$  fit fraction is  $(0.7 \pm 0.2)\%$ .

A second fit with the  $\Lambda(1800)$  contribution is performed, this time with floating mass and width parameters. The fit quality is not improved: 1  $\chi^2$  unit increase with respect to the nominal fit with probability decreased to  $2.2 \times 10^{-5}$  due to the larger ndf; no visible changes in pull distributions; sum of fit fractions increased to 1.07. The  $\Lambda(1800)$  fit fraction is 2.3%, with mass and width parameters forced beyond PDG ranges,  $m \approx 1.72$  GeV and  $\Gamma \approx 400$  MeV.

We consider the first fit (with fixed parameters) as an alternative model, given its slightly higher fit quality.

### 7.1.5 $\Lambda(1810)$ contribution

An amplitude fit adding the  $\Lambda(1810)$  contribution is performed, first with parameters fixed to the PDG mean values. The fit quality is basically unchanged: 3  $\chi^2$  units decrease with probability decreased to  $3.9 \times 10^{-5}$  due to the larger ndf; no visible changes in pull distributions; sum of fit fractions increased to 1.06. The  $\Lambda(1810)$  fit fraction is  $(0.8 \pm 0.2)\%$ .

A second fit with the  $\Lambda(1810)$  contribution is performed, this time with floating mass and width parameters. The fit quality is not improved with respect the previous fit, with  $\Lambda(1810)$  width forced beyond PDG range,  $\Gamma \approx 360$  MeV.

1322 We consider the first fit (with fixed parameters) as an alternative model, given its  
1323 better fit quality.

### 1324 7.1.6 $\Delta^{++}(1620)$ contribution

1325 An amplitude fit adding the  $\Delta^{++}(1620)$  contribution is performed, with floating mass  
1326 and width parameters. The fit quality is basically unchanged: 6  $\chi^2$  unit decrease but  
1327 probability slightly decreased to  $4.0 \times 10^{-5}$  due to the larger ndf; no visible changes in pull  
1328 distributions; fit fractions decreased to 0.99. The  $\Delta^{++}(1620)$  fit fraction is  $(1.0 \pm 0.2)\%$ ,  
1329 with mass and width parameters forced beyond the PDG ranges,  $m \approx 1.56$  GeV and  
1330  $\Gamma \approx 181$  MeV. A fit with mass and width parameters fixed to the PDG mean values is  
1331 also tried but leads to a worse fit quality.

1332 Even if the mass and width parameters are far from the PDG values, probably indicating  
1333 difficulties in constraining this contribution, this fit is considered as an alternative model.

### 1334 7.1.7 Relativistic Breit-Wigner for $K_0^*(700)$

1335 An amplitude fit in which a relativistic Breit-Wigner is used as  $K_0^*(700)$  lineshape, instead  
1336 of the Bugg parametrisation, is tried. The fit quality measured by the  $\chi^2$  test is slightly  
1337 worse: 4  $\chi^2$  units increase and probability decreased to  $3.3 \times 10^{-5}$ ; sum of fit fractions  
1338 slightly increased from 1.03 to 1.06. It is considered as an alternative model.

### 1339 7.1.8 $K_0^*(700)$ parameters

1340 An amplitude fit in which the  $K_0^*(700)$  Breit-Wigner parameters are left floating is  
1341 performed. The fit quality is basically unchanged: same  $\chi^2$  and probability decreased to  
1342  $3.5 \times 10^{-5}$ ; no visible changes in pull distributions; similar sum of fit fractions. The mass  
1343 is found to be stable near the PDG mean value, while the width is forced outside PDG  
1344 ranges towards higher widths; the fit shows to be poorly sensitive to the latter parameter.  
1345 The  $K_0^*(700)$  Breit-Wigner parameters are fixed to the mean PDG values in the nominal  
1346 model, with the fit with floating parameters considered as an alternative model.

### 1347 7.1.9 $K^*(1410)$ contribution

1348 An amplitude fit is performed adding the  $K_0^*(1410)$  state with fixed Breit-Wigner pa-  
1349 rameters. The fit quality is not improved:  $\chi^2$  reduced by 6 units but probability slightly  
1350 decreased to  $3.4 \times 10^{-5}$  due to the larger ndf; no visible changes in pull distributions;  
1351 sum of fit fractions decreased to 1.00. The  $K^*(1410)$  fit fraction is  $1.0 \pm 0.2\%$ . This fit is  
1352 considered as an alternative model.

### 1353 7.1.10 Relativistic Breit-Wigner for $K_0^*(1430)$

1354 An amplitude fit in which a relativistic Breit-Wigner is used as  $K_0^*(1430)$  lineshape,  
1355 instead of the Bugg parametrisation, is tried. The fit quality measured by the  $\chi^2$  test is  
1356 basically unchanged, with the sum of fit fractions slightly increased from 1.03 to 1.05. It  
1357 is considered as an alternative model.

1358 **7.1.11  $K_0^*(1430)$  width**

1359 An amplitude fit in which the  $K_0^*(1430)$  Breit-Wigner width is floated is performed. The fit  
1360 quality is basically unchanged: same  $\chi^2$  and probability decreased to  $3.9 \times 10^{-5}$ ; no visible  
1361 changes in pull distributions; stable sum of fit fractions. The fitted width is 150 MeV,  
1362 smaller than the lower PDG limit assumed. In the nominal fit the  $K_0^*(1430)$  width is set  
1363 to the PDG lower limit, with this fit considered as an alternative model.

1364 **7.1.12 Overall exponential form factor for Bugg lineshape**

1365 An amplitude fit in which an additional overall exponential form factor  $\exp(-\alpha q^2)$  multi-  
1366 plies the Bugg lineshape for spin-zero  $K^*$  resonances is tried, with floating  $\alpha$  coefficients.  
1367 The fit quality is not improved: same  $\chi^2$  with probability decreased to  $3.5 \times 10^{-5}$ . The  
1368  $\alpha$  coefficients are found to be compatible to zero within  $2\sigma$ : therefore these exponential  
1369 factors are not added to the nominal model but considered as an alternative one.

1370 **7.1.13  $\Lambda_c^+$   $d$  radial parameter**

1371 The effect of the choice radial parameter  $d$  for the  $\Lambda_c^+$  resonance used to describe barrier  
1372 effects in the resonance lineshapes (Sec. 6.5) is estimated leaving it as free parameter  
1373 in the amplitude fit. The fit quality is basically unchanged:  $\chi^2$  decreased by 1 unit and  
1374 same probability; no visible changes in pull distributions; similar sum of fit fractions. The  
1375 fitted  $d$  value is  $\approx 4.2$  GeV. The fit shows to be weakly sensitive to the precise value of  
1376  $d$ , as seen in other analyses [55]: the previously assumed  $d = 5$  GeV value is kept for the  
1377 nominal model, with this fit considered as an alternative model.

1378 **7.1.14  $\Lambda_c^+ \rightarrow Rh$  decay orbital angular momentum**

1379 For the angular barrier terms in the resonance lineshapes, Sec. 6.5, the minimum orbital  
1380 angular momentum for the  $\Lambda_c^+ \rightarrow Rh$  decay has been assigned. To check for the possible  
1381 contribution of higher orbital angular momentum states, the fit with the nominal model is  
1382 repeated decomposing helicity couplings in terms of LS couplings (see *e.g.* [45]), associating  
1383 to each coupling the lineshape with the corresponding orbital angular momentum value.  
1384 The fitted LS couplings are reported in Table 19.

1385 The fit quality is similar:  $\chi^2$  increased by 3 units and probability decreased to  $3.4 \times 10^{-5}$ ;  
1386 no visible changes in pull distributions with respect the nominal model; similar sum of  
1387 fit fractions. Since the use of LS couplings brings no significant improvements to the fit,  
1388 helicity couplings are kept for the nominal fit; the fit with LS couplings is considered as  
1389 an alternative model.

1390 **7.2 Other amplitude models not considered for evaluating sys-  
1391 tematic uncertainties**

1392 **7.2.1 “PDG extended” model**

1393 The nominal model is built via an “additive” approach, Sec. 6.7: starting from a minimal  
1394 set of resonances, contributions are added one at a time. As a cross-check, a “subtractive”  
1395 approach is also tried. An amplitude model reflecting the knowledge of the PDG is  
1396 built: all the resonances listed in Table 7 are considered, but the  $\Lambda(1710)$  and the  $\Lambda^*$

Parameter	Central value		Uncertainty
ArK0(700)1	-0.000167	±	0.019096
AiK0(700)1	-0.684890	±	0.026946
ArK0(700)2	-0.631117	±	0.024065
AiK0(700)2	0.040435	±	0.023737
ArK(892)2	0.341792	±	0.007302
AiK(892)2	-0.064047	±	0.004810
ArK(892)3	-0.755199	±	0.014376
AiK(892)3	-0.592176	±	0.014062
ArK(892)4	0.093754	±	0.007945
AiK(892)4	0.379956	±	0.005135
ArK0(1430)1	-1.352114	±	0.098594
AiK0(1430)1	-3.150814	±	0.057482
ArK0(1430)2	0.598156	±	0.054311
AiK0(1430)2	-0.955655	±	0.046918
ArL(1405)1	-1.224670	±	0.034198
AiL(1405)1	-0.039521	±	0.052576
ArL(1405)2	-1.811842	±	0.039381
AiL(1405)2	1.625622	±	0.034881
ArL(1520)1	0.191708	±	0.004957
AiL(1520)1	0.167003	±	0.005131
ArL(1520)2	0.115638	±	0.006304
AiL(1520)2	0.242542	±	0.004908
ArL(1600)1	-0.134004	±	0.032490
AiL(1600)1	-0.628117	±	0.032433
ArL(1600)2	1.712637	±	0.029718
AiL(1600)2	-1.128953	±	0.032192
ArL(1670)1	0.009197	±	0.004825
AiL(1670)1	-0.200899	±	0.003052
ArL(1670)2	-0.114543	±	0.004976
AiL(1670)2	-0.167795	±	0.005083
ArL(1690)1	-0.378966	±	0.012153
AiL(1690)1	0.331114	±	0.009513
ArL(1690)2	-0.286413	±	0.009060
AiL(1690)2	0.247902	±	0.011125
ArL(2000)1	2.807070	±	0.049100
AiL(2000)1	0.071483	±	0.066689
ArL(2000)2	-0.890941	±	0.023480
AiL(2000)2	-0.087397	±	0.028816
ArD(1232)1	-1.499936	±	0.054859
AiD(1232)1	3.161477	±	0.040932
ArD(1232)2	-0.586497	±	0.031930
AiD(1232)2	0.838665	±	0.019560
ArD(1600)1	1.595876	±	0.050522
AiD(1600)1	-2.460301	±	0.074787
ArD(1600)2	-0.432377	±	0.049114
AiD(1600)2	0.688543	±	0.027446
ArD(1700)1	3.161722	±	0.068890
AiD(1700)1	-2.292309	±	0.099002
ArD(1700)2	0.179027	±	0.031955
AiD(1700)2	-0.298638	±	0.021052

Table 19: LS couplings returned by MINUIT for the amplitude fit with nominal model. Uncertainties are the  $1\sigma$  standard deviations returned by HESSE. The numbering convention of the fit parameters is reported in Table 20.

Resonance type	Coupling number	$L$	$S$
$\Lambda^*, \Delta^*$	1	$S - 1/2$	$S$
	2	$S + 1/2$	$S$
$K^*, S \geq 1$	1	0	$1/2$
	2	1	$1/2$
	3	1	$3/2$
	4	2	$3/2$
$K^*, S = 0$	1	0	$1/2$
	2	1	$1/2$

Table 20: Definition of the LS couplings. Here,  $s$  is the resonance spin.

contributions beyond the  $\Lambda(2000)$ , plus the  $K^*$  non-resonant component. Resonance parameters with non-negligible uncertainties are floated following PDG ranges; also the two  $\Lambda(1405)$  widths are floated. The fit results show that all the resonances included in nominal model give significant contributions; however, many resonance mass and width parameters are forced to the edges of the PDG ranges. The  $\Lambda^*(1800)$ ,  $\Lambda(1810)$ ,  $\Lambda^*(1890)$  and  $\Delta^{++}(1620)$  contributions give a modest contribution, fit fractions around 1% with mass and width parameters forced to the edges of the PDG ranges. The  $\Lambda(1820)$  and  $\Lambda(1830)$  contributions are negligible. The fit results are in line with those of the nominal model, Sec. 6.9, and of the alternative model, Sec. 7.1.

This model is not considered as an alternative model due to the higher number of fit parameters making the fit more complex and leading to much lower probability value.

### 7.2.2 $\Lambda(1890)$ contribution

An amplitude fit adding the  $\Lambda(1890)$  contribution is performed both with parameters fixed to the PDG mean values and floating ones. In the both cases the fit quality is worser, in the second fit mass and width parameters are also forced well beyond PDG ranges. For these reasons this fit is not considered as an alternative model.

### 7.2.3 $\Lambda(2000)$ spin-parity assignment

The spin-parity assignment for the  $\Lambda(2000)$  contribution included in the fit model is checked testing  $J^\pm$  assignments up to spin  $7/2$ . All the assignments different from  $1/2^-$  lead to significantly worser fits, both in terms of NLL increase and  $\chi^2$  decrease. Therefore the  $\Lambda(2000)$  contribution is considered as a  $1/2^-$  resonance, while other assignments are not considered as alternative models.

### 7.2.4 Addition of $\Sigma^*$ states

The contribution of  $\Sigma^* \rightarrow pK^-$  resonances is expected to be suppressed since it involves a  $\Delta I = 1$  strong isospin difference in the  $\Lambda_c^+ \rightarrow \Sigma$  process. Two  $\Sigma^*$  are added to the decay model,  $\Sigma(1670)$  and  $\Sigma(1775)$ , classified as certain in the PDG, introduced with floating parameters following the ranges quoted by the PDG. The  $\Sigma(1670)$  gives rise to unphysical large interference effects with the  $\Lambda(1690)$ : the two are indistinguishable

1425 having the same spin-parity. The contribution of the  $\Sigma(1775)$  is null, with fit fraction  
1426 below 0.1%. Other  $\Sigma^*$  states are not tested because of their weaker experimental evidence  
1427 and large parameter uncertainties, which makes their separation from  $\Lambda^*$  states difficult.  
1428 No  $\Sigma^*$  states are considered for systematic uncertainty evaluation.

### 1429 7.2.5 Removal of resonance barrier factors

1430 To see the effect of the barrier factors introduced in the resonance description (the first  
1431 two factors in Eq. (76), see Sec. 6.5) an amplitude fit in which such factors are removed  
1432 is tried. The fit quality is significantly reduced: barrier factors are therefore seen to be  
1433 important for properly describing resonance lineshapes.

### 1434 7.2.6 $K\eta$ , $K\eta'$ decay channel widths in Bugg lineshape

1435 An amplitude fit in which the opening of  $K\eta$ ,  $K\eta'$  decay channels is considered in the  
1436 Bugg lineshape is tried. However, the fit does not converge to a minimum, indicating a  
1437 tiny sensitivity on  $K\eta$ ,  $K\eta'$  associated widths, which are not added to the nominal model.

### 1438 7.2.7 $K^*$ spin zero as a single contribution

1439 An amplitude fit in which the  $K_0^*(700)$  and  $K_0^*(1430)$  contribution are considered as a  
1440 single contribution is tried: a contribution with one set of helicity couplings is considered  
1441 with a lineshape being the sum of the  $K_0^*(700)$  and  $K_0^*(1430)$  Bugg lineshapes used in the  
1442 nominal model; an approach resembling the LASS parametrisation. A worser fit quality is  
1443 obtained, so this fit variation is discarded.

### 1444 7.2.8 Pole model for $K_0^*(700)$ state

1445 An amplitude fit in which the  $K_0^*(700)$  state is described by a simple pole lineshape is  
1446 tried. If the pole mass is floated, the minimisation pulls it beyond the  $K\pi$  threshold,  
1447 leading to numerical errors. Otherwise, the pole mass has been fixed to some test values,  
1448 400 MeV, 450 MeV,  $m_K^2 - 0.5m_\pi^2$ , in all cases obtaining a worser fit quality.

### 1449 7.2.9 Flatté lineshape for $K_0^*(1430)$ state

1450 An amplitude fit in which the  $K_0^*(1430)$  state is described by a Flatté lineshape is tried,  
1451 but leads to instabilities in the fit minimisation: the fit is not able to constrain the width  
1452 associated to the  $K\eta$  channel opening.

### 1453 7.2.10 $K_0^*(1430)$ floating mass

1454 An amplitude fit in which the  $K_0^*(1430)$  mass is left floating is tried, but the fit does not  
1455 converge to a minimum, with the mass forced beyond the lower PDG limit. Therefore the  
1456  $K_0^*(1430)$  mass is fixed to the lower PDG limit, after checking that the PDG mean value  
1457 leads to a worser fit quality.

1458 **7.2.11 Change of  $\Lambda_c^+ \rightarrow Rh$  decay orbital angular momentum assignment**

1459 For the  $\Lambda_c^+ \rightarrow Rh$  weak decay, the orbital angular momentum is not constrained a priori.  
1460 As presented in Sec. 6.5 the minimum possible one is taken. An amplitude fit in which  
1461 the orbital angular momentum assignments are assumed to be equally probable (among  
1462 the values allowed by angular momentum conservation) is tried. This means that the  
1463 resonance lineshapes are an unweighted sum of the contributions corresponding to the  
1464 different orbital angular momentum assignments.

1465 The fit quality is much worse with respect to the nominal fit results, therefore, the  
1466 original orbital momentum assignments are kept and this fit is not considered as an  
1467 alternative model.

1468 **7.3 Background contribution**

1469 To evaluate the systematic effect due to the modelling of the background contribution,  
1470 two amplitude fits having different treatment of the background component with respect  
1471 to the nominal fit are performed. First, a fit using the parametrisation built using the  
1472 background upper mass sideband only, Fig. 41, is performed; second, a fit with the  
1473 background fraction modified from 1.69% (obtained from the invariant mass fit of Fig. 2)  
1474 to 1.79% (obtained from the alternative invariant mass fit of Fig. 5) is done. Systematic  
1475 uncertainties are assigned summing in quadrature the results variations of the two fits  
1476 with respect to the nominal one. The numerical values are reported in Sec. 7.7.

1477 **7.4 Simulation weighting**

1478 The systematic effect due to the choice of the simulation weighting is evaluated changing  
1479 the way weights are computed. In the weighting presented in Sec. 2.4, weights are  
1480 obtained starting from data and MC samples after stripping and trigger requirements,  
1481 before selection. For systematic evaluation, new weights are derived in the same way but  
1482 starting from data and MC samples after selection, and applied to the MC sample used  
1483 in the amplitude fit, like in Ref. [47]. Systematic uncertainties are assigned taking the  
1484 results variations of the fit with respect to the nominal one. The numerical values are  
1485 reported in Sec. 7.7.

1486 **7.5 PID**

1487 The particle identification ProbNN variables used in the selection have been corrected  
1488 using the PIDCorr package, which also provides the tools needed to evaluate PID-related  
1489 systematic uncertainties. Two different PID corrections are considered: one in which the  
1490 calibration sample used to derive the PID variable transformation is changed, to consider  
1491 the effect due to its limited statistics; and a second in which the kernel-density-estimation  
1492 used to derive the transformation are taken to be 50% wider than the standard correction.  
1493 Two MC samples with these different PID corrections are obtained applying the the  
1494 selection criteria and used to perform two amplitude fits. Systematic uncertainties are  
1495 assigned summing in quadrature the results variations of the two fits with respect to the  
1496 nominal one. The numerical values are reported in Sec. 7.7.

## 1497 7.6 Fit bias and finite MC integration statistics

1498 To check whether the amplitude fit is unbiased and to provide an independent estimation  
1499 of statistical uncertainties, pseudoexperiments are performed, generating a signal sample  
1500 according to the nominal amplitude fit results, Table 10, and fitting it back. The  
1501 pseudodata sample has the same size of the data sample used for amplitude fits, 400'000  
1502 events. For each pseudoexperiment a different MC sample is generated, of the same size of  
1503 the MC sample used for amplitude fits,  $\approx 450'000$ . This way, this toy study also includes  
1504 the effect of the finite MC integration statistics. 1'000 toy experiments are performed.

1505 From pseudoexperiment fit results have been considered: the mean and standard  
1506 deviation of the measured quantities (fit parameters, fit fractions and  $\alpha$  parameters), of  
1507 their statistical uncertainties (computed with HESSE and propagated using covariance  
1508 matrix) and of the pulls (ratio of the difference from nominal fit results over the computed  
1509 statistical uncertainty). These are reported in Table 21 for fit parameters, Table 22 for fit  
1510 fractions and Table 23 for  $\alpha$  parameters.

1511 For an unbiased fit, the pull mean should be zero: its deviation from zero, multiplied  
1512 by the average statistical uncertainty, is assigned as systematic uncertainty. The numerical  
1513 values are reported in Sec. 7.7.

1514 If the statistical uncertainties computed from HESSE were correct, the pull distributions  
1515 should have a standard deviation of 1; in practice a larger value should be expected due to  
1516 statistical fluctuations of the MC integration sample. The smallest pulls are observed for  
1517 some parameters including polarisation values, with  $\sigma \approx 1.4 - 1.5$ ; for other fit parameters  
1518 the standard deviations are larger, especially for those parameters related to contributions  
1519 difficult to constrain, mostly at 2,3  $\sigma$  level, with a few cases up to 4,5 $\sigma$ . For the fit  
1520 parameters, the statistical uncertainties provided by HESSE are seen to underestimate  
1521 the actual ones.

1522 On the contrary, for some fit fractions and all the  $\alpha$  parameters the pull standard deviation  
1523 is smaller than 1, indicating that the statistical uncertainties obtained propagating  
1524 HESSE estimates via the fit covariance matrix tend to overestimate the actual ones.

1525 The statistical uncertainties in the nominal fit are therefore substituted when quoting  
1526 final results, Sec. 9, with the mean computed statistical uncertainties rescaled by the pull  
1527 standard deviation.

## 1528 7.7 Summary of systematic uncertainties

1529 This section reports the numerical values of the different sources of systematic uncertainties:  
1530 Table 24 for the fit parameters, Table 25 for fit fractions and Table 26 for  $\alpha$  parameters.  
1531 The total systematic uncertainty is the sum in quadrature of the different sources.

1532 The systematic uncertainty associated to the amplitude model choice is by far the  
1533 leading contribution for all the measured quantities; the only exceptions are  $P_z$ , whose  
1534 leading systematic contribution is that coming from the MC weighting and  $P_y$ , which is  
1535 dominated by statistical uncertainty. The latter can be explained by the fact that  $P_y$  is  
1536 compatible with zero: the presence of a polarisation component is model-independent  
1537 (can be seen directly from decay orientation angle distribution), while the determination  
1538 of the polarisation magnitude depends on the resonance interference pattern described by  
1539 the amplitude model [3].

1540 Table 27 reports the systematic uncertainties for the polarisation measured in the

Parameter	Mean Value	$\sigma$ Value	Mean Uncertainty	$\sigma$ Uncertainty	Mean Pull	$\sigma$ Pull
gammaK0(700)	0.941475	0.066788	0.046909	0.001791	0.007838	1.421796
ArK0(700)1	0.063766	0.230355	0.097655	0.008431	-0.086844	2.365836
AiK0(700)1	2.523885	0.228966	0.111117	0.009784	-0.142784	2.024228
ArK0(700)2	-2.682293	0.250854	0.111437	0.009804	0.206124	2.241360
AiK0(700)2	0.033091	0.255799	0.110259	0.009945	-0.106390	2.324267
ArK(892)2	1.192394	0.129541	0.048986	0.003876	-0.105784	2.623371
AiK(892)2	-1.019397	0.122093	0.051011	0.004303	0.170320	2.387374
ArK(892)3	-3.129423	0.356949	0.102597	0.009418	0.212715	3.475788
AiK(892)3	-3.286741	0.347840	0.084463	0.008667	0.201370	4.094364
ArK(892)4	-0.716397	0.342299	0.103671	0.009800	0.084423	3.303249
AiK(892)4	-4.145658	0.313989	0.058148	0.006527	0.570115	5.443216
gammaK0(1430)	0.021036	0.017558	0.010625	0.000236	-0.002185	1.652445
ArK0(1430)1	-6.704101	0.999402	0.328164	0.029151	0.072100	3.032705
AiK0(1430)1	10.466666	0.978122	0.318869	0.028166	-0.154023	3.042529
ArK0(1430)2	0.220377	0.775524	0.312256	0.026272	-0.110071	2.477440
AiK0(1430)2	8.721966	0.686495	0.226365	0.018665	-0.284729	3.007807
ArL(1405)1	-4.559964	0.521372	0.259090	0.023752	0.031380	2.008382
AiL(1405)1	3.189748	0.535164	0.254066	0.019773	-0.035255	2.099605
ArL(1405)2	10.389835	0.834685	0.228292	0.022049	-0.449952	3.647837
AiL(1405)2	2.803625	1.045646	0.383506	0.032491	0.054424	2.747950
ML(1520)	1.518479	0.000360	0.000210	0.000013	0.024972	1.709755
GL(1520)	0.015212	0.000782	0.000474	0.000029	-0.050399	1.651524
ArL(1520)1	0.293816	0.053688	0.032356	0.002660	-0.058031	1.636794
AiL(1520)1	0.045389	0.053717	0.031417	0.002595	0.003452	1.705250
ArL(1520)2	-0.164884	0.139687	0.051085	0.004552	-0.068562	2.737737
AiL(1520)2	1.496553	0.127471	0.044509	0.003900	-0.279369	2.863538
ArL(1600)1	4.826489	0.465286	0.169114	0.014346	-0.231840	2.738209
AiL(1600)1	3.090852	0.538645	0.200649	0.016104	-0.054079	2.676447
ArL(1600)2	-6.948653	0.542173	0.161937	0.013713	0.377953	3.347847
AiL(1600)2	0.834423	0.629497	0.215353	0.018983	-0.153587	2.912796
ArL(1670)1	-0.338543	0.051276	0.032014	0.002418	0.087592	1.597007
AiL(1670)1	-0.145336	0.051037	0.032572	0.002517	0.019152	1.554715
ArL(1670)2	-0.570382	0.098613	0.036447	0.003001	0.049530	2.694090
AiL(1670)2	1.008765	0.093645	0.031296	0.002549	-0.225794	2.984182
ArL(1690)1	-0.381564	0.102075	0.070836	0.005034	0.067050	1.432490
AiL(1690)1	-0.112903	0.094509	0.067801	0.004858	-0.022723	1.384398
ArL(1690)2	-2.720917	0.199076	0.076411	0.005898	0.297117	2.593196
AiL(1690)2	-0.355443	0.227134	0.089949	0.007051	-0.016252	2.508620
ML(2000)	1.988256	0.001977	0.001329	0.000037	0.046437	1.490997
GL(2000)	0.179522	0.003956	0.002492	0.000074	0.068252	1.586533
ArL(2000)1	-7.985259	0.898615	0.288038	0.024541	0.193034	3.101335
AiL(2000)1	-7.615442	0.843279	0.250480	0.023280	0.089097	3.327661
ArL(2000)2	-4.334535	0.494957	0.181993	0.014971	0.153593	2.707480
AiL(2000)2	-3.799920	0.450830	0.168856	0.014446	0.100556	2.635484
ArD(1232)1	-6.768267	0.539704	0.127527	0.012424	0.318834	4.219262
AiD(1232)1	3.029790	0.585216	0.215093	0.017782	-0.137825	2.724090
ArD(1232)2	-12.955183	0.964245	0.184885	0.021157	0.543814	5.238667
AiD(1232)2	4.503148	1.098147	0.345791	0.029203	-0.121159	3.173800
ArD(1600)1	11.382321	0.942038	0.295472	0.023841	-0.248285	3.171662
AiD(1600)1	-3.096454	1.020871	0.364658	0.029963	0.092561	2.803368
ArD(1600)2	6.731015	0.689902	0.320144	0.023855	-0.118531	2.156424
AiD(1600)2	-0.963446	0.661122	0.302646	0.024304	0.148102	2.159727
ArD(1700)1	10.336445	0.849938	0.288114	0.022226	-0.336943	2.957230
AiD(1700)1	1.447891	0.929404	0.379543	0.030302	0.045932	2.449771
ArD(1700)2	12.825294	1.037891	0.312430	0.025630	-0.388867	3.338335
AiD(1700)2	2.161504	1.104059	0.422678	0.035617	0.112690	2.607718
Px	0.603683	0.006780	0.004463	0.000034	0.101645	1.519470
Py	-0.004071	0.006140	0.003959	0.000028	0.001903	1.551395
Pz	-0.247109	0.005968	0.004047	0.000028	-0.034529	1.474543

Table 21: Pseudoexperiments results for the fit parameters of the nominal amplitude model.  $\sigma$  indicates standard deviation; uncertainties are statistical, computed by the HESSE method. Fit parameters are defined in Appendix 6.8.

Resonance	Mean Value	$\sigma$ Value	Mean Uncertainty	$\sigma$ Uncertainty	Mean Pull	$\sigma$ Pull
$\Delta^{++}(1232)$	0.285771	0.002931	0.007603	0.000680	-0.032544	0.386028
$\Delta^{++}(1600)$	0.045336	0.002714	0.002275	0.000119	0.024870	1.192771
$\Delta^{++}(1700)$	0.039000	0.001969	0.001700	0.000093	-0.050177	1.166990
$K^*(892)$	0.221158	0.002258	0.005785	0.000511	-0.039794	0.392198
$K^*0(1430)$	0.147626	0.005628	0.005099	0.000342	0.072275	1.109019
$K^*0(700)$	0.030327	0.001584	0.001381	0.000074	0.066395	1.151655
$\Lambda(1405)$	0.077502	0.002439	0.002483	0.000167	0.114891	0.982850
$\Lambda(1520)$	0.018860	0.000918	0.000779	0.000044	0.265642	1.174966
$\Lambda(1600)$	0.051848	0.002227	0.001980	0.000131	-0.008961	1.127958
$\Lambda(1670)$	0.011767	0.000579	0.000512	0.000029	-0.081765	1.135456
$\Lambda(1690)$	0.011949	0.000881	0.000670	0.000034	-0.048849	1.316799
$\Lambda(2000)$	0.095752	0.002710	0.002876	0.000222	-0.045312	0.949013

Table 22: Pseudoexperiments results for fit fractions.  $\sigma$  indicates standard deviation; uncertainties are statistical, computed propagating uncertainties from the fit parameters via covariance matrix.

Resonance	Mean Value	$\sigma$ Value	Mean Uncertainty	$\sigma$ Uncertainty	Mean Pull	$\sigma$ Pull
Model	0.668933	0.004795	0.009264	0.000801	0.714801	0.516986
$\Delta^{++}(1232)$	-0.547302	0.014398	0.052194	0.004556	0.008372	0.277779
$\Delta^{++}(1600)$	0.500692	0.047297	0.100671	0.008437	0.016113	0.474625
$\Delta^{++}(1700)$	-0.215985	0.034740	0.178537	0.030330	-0.031174	0.203987
$K^*(892)$	-0.833474	0.012384	0.037182	0.002277	0.026709	0.334885
$K^*0(1430)$	-0.339157	0.033544	0.120753	0.011521	-0.022983	0.279375
$K^*0(700)$	0.060284	0.068997	0.194489	0.013234	0.012581	0.355121
$\Lambda(1405)$	-0.575717	0.050799	0.081248	0.007679	0.007198	0.629022
$\Lambda(1520)$	-0.921222	0.024725	0.084684	0.003032	0.043426	0.290938
$\Lambda(1600)$	-0.196890	0.051735	0.219000	0.279336	-0.058067	0.284214
$\Lambda(1670)$	-0.812331	0.042678	0.084536	0.004139	0.039040	0.498161
$\Lambda(1690)$	-0.954508	0.020034	0.079705	0.003082	0.049272	0.251208
$\Lambda(2000)$	0.571439	0.025830	0.081647	0.004095	-0.006004	0.316520

Table 23: Pseudoexperiments results for  $\alpha$  parameters.  $\sigma$  indicates standard deviation; uncertainties are statistical, computed propagating uncertainties from the fit parameters via covariance matrix.

<sup>1541</sup> “Equal boost” approximate  $\Lambda_b^0$  rest frame. The leading contribution is the amplitude model  
<sup>1542</sup> choice for  $P_x$ ,  $P_z$ , with  $P_y$  dominated by statistical uncertainty.

Parameter	Model Choice	Total*	Background	MC weighting	PID	Fit Bias
gammaK0(700)	0.352595	0.037569	0.032168	0.019036	0.003761	0.000368
ArK0(700)1	0.929106	0.08887	0.073958	0.003866	0.048387	0.008481
AiK0(700)1	3.206334	0.136353	0.128939	0.038354	0.015627	0.015866
ArK0(700)2	2.054513	0.200919	0.186207	0.070681	0.013114	0.02297
AiK0(700)2	1.338656	0.054253	0.02472	0.028815	0.036938	0.01173
ArK(892)2	0.850822	0.051234	0.044638	0.012333	0.021295	0.005182
AiK(892)2	0.961767	0.020692	0.017974	0.004336	0.00329	0.008688
ArK(892)3	2.386247	0.057544	0.025089	0.00671	0.046482	0.021824
AiK(892)3	2.701234	0.09741	0.074903	0.033243	0.049838	0.017008
ArK(892)4	1.479561	0.084137	0.022528	0.041127	0.069307	0.008752
AiK(892)4	4.534983	0.097391	0.086946	0.016506	0.023535	0.033151
gammaK0(1430)	0.332961	0.005049	0.00461	0.000285	0.002039	2.3e-05
ArK0(1430)1	5.363046	0.357129	0.293736	0.104063	0.172834	0.023661
AiK0(1430)1	13.630225	0.182603	0.138678	0.072028	0.080698	0.049113
ArK0(1430)2	2.426869	0.269459	0.210532	0.116648	0.116175	0.03437
AiK0(1430)2	9.696851	0.113639	0.087796	0.006623	0.031743	0.064453
ArL(1405)1	3.347816	0.051749	0.021158	0.00418	0.046333	0.00813
AiL(1405)1	3.229665	0.117856	0.077394	0.006671	0.088179	0.008957
ArL(1405)2	12.257922	0.159029	0.086396	0.076388	0.037939	0.10272
AiL(1405)2	3.713678	0.268249	0.174121	0.120491	0.163359	0.020872
ML(1520)	0.000647	2.9e-05	2.5e-05	1.1e-05	8e-06	5e-06
GL(1520)	0.001307	0.000135	5e-05	7.8e-05	9.5e-05	2.4e-05
ArL(1520)1	0.123946	0.005822	0.004628	0.00097	0.002829	0.001878
AiL(1520)1	0.122679	0.016106	0.007539	0.000652	0.014218	0.000108
ArL(1520)2	0.685141	0.034413	0.011571	0.023862	0.02165	0.003502
AiL(1520)2	1.256291	0.03382	0.028233	0.009287	0.010289	0.012434
ArL(1600)1	4.974653	0.1221	0.102833	0.03554	0.039159	0.039207
AiL(1600)1	3.710903	0.134333	0.088027	0.035302	0.094513	0.010851
ArL(1600)2	8.68387	0.079794	0.04722	0.009703	0.017238	0.061205
AiL(1600)2	1.971388	0.173032	0.037757	0.06794	0.151013	0.033075
ArL(1670)1	0.348782	0.009082	0.003237	0.002866	0.007479	0.002804
AiL(1670)1	0.224407	0.018522	0.007386	0.00149	0.016909	0.000624
ArL(1670)2	0.456435	0.023003	0.014096	0.008122	0.016162	0.001805
AiL(1670)2	1.179628	0.014798	0.01208	0.000224	0.004803	0.007066
ArL(1690)1	0.227841	0.017978	0.009973	0.010001	0.010057	0.00475
AiL(1690)1	0.441349	0.023154	0.020657	0.000319	0.010341	0.001541
ArL(1690)2	2.444179	0.046494	0.037293	0.003722	0.015546	0.022703
AiL(1690)2	0.601515	0.061425	0.039036	0.033086	0.033947	0.001462
ML(2000)	0.021189	0.001289	0.001282	1.7e-05	0.000122	6.2e-05
GL(2000)	0.015787	0.002924	0.002746	0.00097	0.0002	0.00017
ArL(2000)1	10.821927	0.22646	0.177541	0.092493	0.090094	0.055601
AiL(2000)1	7.685489	0.235687	0.205101	0.010521	0.113459	0.022317
ArL(2000)2	3.445314	0.15085	0.119719	0.047795	0.073193	0.027953
AiL(2000)2	3.708795	0.066898	0.050473	0.007601	0.039772	0.016979
ArD(1232)1	5.278255	0.170592	0.153347	0.04268	0.04595	0.04066
AiD(1232)1	1.422528	0.14629	0.067222	0.03048	0.122776	0.029645
ArD(1232)2	12.400696	0.2592	0.213169	0.067613	0.084045	0.100543
AiD(1232)2	3.689671	0.319639	0.253632	0.067729	0.177476	0.041896
ArD(1600)1	9.805709	0.235312	0.173873	0.105325	0.093085	0.073361
AiD(1600)1	1.430495	0.175824	0.044899	0.056344	0.156793	0.033753
ArD(1600)2	7.161588	0.221083	0.179154	0.057627	0.109639	0.037947
AiD(1600)2	2.123592	0.076526	0.031455	0.01012	0.052492	0.044822
ArD(1700)1	7.216558	0.319345	0.282193	0.106259	0.040409	0.097078
AiD(1700)1	5.154101	0.173366	0.106382	0.085305	0.105631	0.017433
ArD(1700)2	12.695075	0.291225	0.255406	0.055186	0.042113	0.121494
AiD(1700)2	6.035012	0.25295	0.153605	0.125939	0.149197	0.047632
Px	0.009797	0.002109	0.00099	0.001735	0.000504	0.000454
Py	0.001643	0.000719	0.000328	0.000441	0.000464	8e-06
Pz	0.003462	0.010527	0.000483	0.010335	0.001939	0.00014

Table 24: Summary of the systematic uncertainties on fit parameters. Total\* includes all contributions but for the amplitude choice one. Fit parameters are defined in Appendix 6.8

Resonance	FF	Model Choice	Total*	Background	MC weighting	PID	Fit Bias
$\Delta^{++}(1232)$	0.007625	0.00158	0.001429	0.000254	0.000571	0.000247	
$\Delta^{++}(1600)$	0.014757	0.000598	4e-05	0.000448	0.00039	5.7e-05	
$\Delta^{++}(1700)$	0.009402	0.000685	0.000533	0.000404	0.000121	8.5e-05	
$K^*(892)$	0.006355	0.000381	4.7e-05	0.00026	0.000151	0.00023	
$K^*0(1430)$	0.026717	0.001234	0.000839	0.000771	0.000298	0.000369	
$K^*0(700)$	0.00922	0.00182	0.001716	0.000548	0.000246	9.2e-05	
$\Lambda(1405)$	0.02998	0.001837	0.001513	0.000889	0.000461	0.000285	
$\Lambda(1520)$	0.002328	0.000279	2.8e-05	0.000152	0.000104	0.000207	
$\Lambda(1600)$	0.019351	0.000587	0.000539	8e-05	0.000218	1.8e-05	
$\Lambda(1670)$	0.003164	0.000127	8.4e-05	3.3e-05	7.8e-05	4.2e-05	
$\Lambda(1690)$	0.003361	0.000133	7.8e-05	7e-05	7.5e-05	3.3e-05	
$\Lambda(2000)$	0.009317	0.002271	0.001992	0.001019	0.000364	0.00013	

Table 25: Summary of the systematic uncertainties on fit fractions. Total\* includes all contributions but for the amplitude choice one.

Resonance $\alpha$	Model Choice	Total*	Background	MC weighting	PID	Fit Bias
Model ( $\sqrt{3}S$ )	0.010359	0.007032	0.001525	0.001652	0.000742	0.006622
$\Delta^{++}(1232)$	0.035625	0.004079	0.003488	0.00037	0.002037	0.000437
$\Delta^{++}(1600)$	0.171375	0.012903	0.008408	0.000921	0.009607	0.001622
$\Delta^{++}(1700)$	0.074887	0.01058	0.006938	0.005122	0.002568	0.005566
$K^*(892)$	0.036	0.002435	0.001433	0.00011	0.001696	0.000993
$K^*0(1430)$	0.13889	0.013803	0.010919	0.000727	0.007942	0.002775
$K^*0(700)$	0.238346	0.226548	0.01592	0.010704	0.00222	0.225724
$\Lambda(1405)$	0.27771	0.010235	0.009691	0.002536	0.002018	0.000585
$\Lambda(1520)$	0.084296	0.004649	3.2e-05	0.001047	0.002645	0.003677
$\Lambda(1600)$	0.498706	0.025045	0.018188	0.010572	0.004792	0.012717
$\Lambda(1670)$	0.072945	0.005625	0.001185	0.001697	0.004057	0.0033
$\Lambda(1690)$	0.026588	0.006169	0.004058	0.001967	0.001515	0.003927
$\Lambda(2000)$	0.191026	0.009023	0.00754	0.001155	0.004794	0.00049

Table 26: Summary of the systematic uncertainties on  $\alpha$  parameters. Total\* includes all contributions but for the amplitude choice one.

Parameter	Model Choice	Total*	Background	MC weighting	PID	Fit Bias
Px	0.00363	0.001538	0.000178	0.001452	0.000136	0.000454
Py	0.00087	0.000806	0.000187	0.000572	0.000537	8e-06
Pz	0.010584	0.00122	0.000811	0.000594	0.000676	0.00014

Table 27: Summary of the systematic uncertainties on polarisation components measured in the “Equal boost” approximate  $\Lambda_b^0$  rest frame. Total\* includes all contributions but for the amplitude choice one.

## 1543 8 Cross-checks

1544 A set of cross-checks have been performed to check the stability of the results under change  
1545 of magnet polarity,  $\Lambda_c^+$  charge, polarisation frame,  $\Lambda_c^+$  transverse momentum and lifetime.  
1546 All fits have been done with the nominal model detailed in Table 8 and the datasample  
1547 used in the nominal fit with additional requirements applied. For each check, results are  
1548 compared to the nominal fit results, Tables 10-12, computing the pull normalised to the  
1549 final total uncertainties (sum in quadrature of statistical and systematic uncertainties)  
1550 reported in Tables 29-31 and the associated  $\chi^2$  and probability values. All the amplitude  
1551 model found are well compatible with the nominal one.

### 1552 8.1 MagDown data sample

1553 The amplitude fit is performed selecting events collected with MagDown magnet polarity  
1554 from the fit datasample. The amplitude fit results are reported in Table 35, shown in  
1555 Fig. 60. Fit fractions are reported in Table 36, decay asymmetry parameters in Table 37.

1556 The fit quality is good, no significant discrepancies in phase space distributions are  
1557 visible. Fit results are well compatible with the nominal model.

### 1558 8.2 MagUp data sample

1559 The amplitude fit is performed selecting events collected with MagUp magnet polarity  
1560 from the fit datasample. The amplitude fit results are reported in Table 38, shown in  
1561 Fig. 61. Fit fractions are reported in Table 39, decay asymmetry parameters in Table 40.

1562 The fit quality is good, no significant discrepancies in phase space distributions are  
1563 visible. Fit results are well compatible with the nominal model.

### 1564 8.3 $\Lambda_c^+$ -only data sample

1565 The amplitude fit is performed selecting  $\Lambda_c^+$  (positive charge) decays. The amplitude  
1566 fit results are reported in Table 41, shown in Fig. 62. Fit fractions are reported in  
1567 Table 42, decay asymmetry parameters in Table 43. The fit quality is good, no significant  
1568 discrepancies in phase space distributions are visible. Fit results are well compatible with  
1569 the nominal model.

### 1570 8.4 $\bar{\Lambda}_c^-$ -only data sample

1571 The amplitude fit is performed selecting  $\bar{\Lambda}_c^-$  (negative charge) decays. The amplitude fit  
1572 results are reported in Table 44, shown in Fig. 63. Fit fractions are reported in Table 45,  
1573 decay asymmetry parameters in Table 46.

1574 The fit quality is good, no significant discrepancies in phase space distributions are  
1575 visible. Fit results are well compatible with the nominal model. First, the good fit quality  
1576 shows that the amplitude fit on the  $CP$ -conjugated  $\bar{\Lambda}_c^- \rightarrow \bar{p}K^+\pi^-$  decays is equally valid  
1577 as the one on  $\Lambda_c^+ \rightarrow pK^-\pi^+$  decays, with no visible differences in detector efficiency effects.  
1578 Second, the compatibility of  $\Lambda_c^+ \rightarrow pK^-\pi^+$  and  $\bar{\Lambda}_c^- \rightarrow \bar{p}K^+\pi^-$  amplitude models suggests  
1579 no significant  $CP$ -violation effects, at the level of precision allowed by the chosen data  
1580 sample size.

1581    **8.5 Polarisation in  $\Lambda_b^0$  rest frame from “Full reconstruction” al-**  
1582    **gorithm**

1583    The amplitude fit is performed changing polarisation frame to the  $\Lambda_c^+$  helicity frame  
1584    reached from the approximate  $\Lambda_b^0$  rest frame reconstructed with the “Full reconstruction”  
1585    algorithm. The amplitude fit results compared to the nominal fit are reported in Table 47,  
1586    shown in Fig. 46, fit fractions are reported in Table 48, decay asymmetry parameters in  
1587    Table 49.

1588    The fit quality is good but for a discrepancy in the  $\phi_p$  distribution, an effect of the  
1589    different behaviour of the “Full reconstruction” algorithm between data and simulated  
1590    events. Fit results are well compatible with the nominal model. Polarisation values are  
1591    not included in the comparison since referring to different frames. This check shows that  
1592    the determination of the amplitude model does not depend on the choice of polarisation  
1593    frame.

1594    **8.6 Polarisation in  $\Lambda_b^0$  rest frame from “Equal boost” algorithm**

1595    The amplitude fit is performed changing polarisation frame to the  $\Lambda_c^+$  helicity frame reached  
1596    from the approximate  $\Lambda_b^0$  rest frame reconstructed with the “Equal boost” algorithm.  
1597    The amplitude fit results compared to the nominal fit are reported in Table 50, shown in  
1598    Fig. 47, fit fractions are reported in Table 51, decay asymmetry parameters in Table 18.

1599    The fit quality is good, no significant discrepancies in phase space distributions are  
1600    visible. Fit results are well compatible with the nominal model. Polarisation values are  
1601    not included in the comparison since referring to different frames. This check shows that  
1602    the determination of the amplitude model does not depend on the choice of polarisation  
1603    frame.

1604    **8.7 Data split according to  $\Lambda_c^+$  transverse momentum**

1605    To check whether detector efficiency effects are well reproduced as a function of the  $\Lambda_c^+$   
1606    kinematics, which had to be corrected in the MC sample, two amplitude fits have been  
1607    performed splitting the fit dataset into two datasets requiring the  $\Lambda_c^+$  transverse momentum  
1608    to be greater or smaller than 5 GeV. The background and efficiency parametrisation, as  
1609    well as the estimation of the background contribution, have been done separately for the  
1610    two samples.

1611    The amplitude fit results for  $p_T(\Lambda_c^+) > 5$  GeV are reported in Table 53, shown in  
1612    Fig. 64. Fit fractions are reported in Table 54, decay asymmetry parameters in Table 55.

1613    The fit quality is good, no significant discrepancies in phase space distributions are  
1614    visible. Fit results are well compatible with the nominal model. A larger longitudinal  
1615    polarisation than the nominal fit is found,  $\approx -32\%$ : a different polarisation value is not  
1616    surprising since the  $\Lambda_c^+$  kinematic requirement is correlated with the semileptonic decay  
1617    kinematics. Polarisation values are thus not included in the  $\chi^2$  test.

1618    The amplitude fit results for  $p_T(\Lambda_c^+) \leq 5$  GeV are reported in Table 56, shown in  
1619    Fig. 65. Fit fractions are reported in Table 57, decay asymmetry parameters in Table 58.

1620    The fit quality is good, no significant discrepancies in phase space distributions are  
1621    visible. Fit results related to the amplitude model are well compatible with the nominal

1622 model. A smaller longitudinal polarisation than the nominal fit is found, consistently with  
1623 the results found for larger  $p_T$ .

1624 This check shows that the determination of the amplitude model does not significantly  
1625 depend on the  $\Lambda_c^+$  transverse momentum.

## 1626 8.8 Data split according to $\Lambda_c^+$ lifetime

1627 To check whether detector efficiency effects are well reproduced as a function of the decay  
1628 topology, two amplitude fits have been performed splitting the fit dataset into two datasets  
1629 requiring the  $\Lambda_c^+$  lifetime to be greater or smaller than 0.2 ps. The background and  
1630 efficiency parametrisation, as well as the estimation of the background contribution, have  
1631 been done separately for the two samples.

1632 The amplitude fit results for  $\tau(\Lambda_c^+) > 0.2$  ps are reported in Table 59, shown in Fig. 66.  
1633 Fit fractions are reported in Table 60, decay asymmetry parameters in Table 61.

1634 The fit quality is good, no significant discrepancies in phase space distributions are  
1635 visible. Fit results are well compatible with the nominal model.

1636 The amplitude fit results for  $\tau(\Lambda_c^+) \leq 0.2$  ps are reported in Table 62, shown in Fig. 67.  
1637 Fit fractions are reported in Table 63, decay asymmetry parameters in Table 64.

1638 The fit quality is good, no significant discrepancies in phase space distributions are  
1639 visible. Fit results are well compatible with the nominal model.

1640 This check shows that the determination of  $\Lambda_c^+$  polarisation and amplitude model does  
1641 not significantly depend on the  $\Lambda_c^+$  lifetime.

## 1642 9 Final results

1643 The final results of the amplitude analysis of the  $\Lambda_c^+ \rightarrow pK^-\pi^+$  decay from semileptonic  
1644 production are summarised in this section: besides polarisation values, the results refers  
1645 to the fit using the  $\Lambda_c^+$  helicity frame reached from the laboratory. The final values  
1646 including corrected statistical uncertainties (see Sec. 7.6) and systematic uncertainties are  
1647 reported for polarisation components, Table 28, nominal model fit parameters, Table 29, fit  
1648 fractions, Table 30, and decay asymmetry  $\alpha$  parameters, Table 31. The amplitude model  
1649 choice systematic uncertainty contribution is reported separately from the other sources  
1650 being the leading one for most quantities. The data and amplitude model projections are  
1651 shown in Fig. 43. Table 32 summarises the resonant composition of the fitted nominal  
1652  $\Lambda_c^+ \rightarrow pK^-\pi^+$  amplitude model.

1653 This analysis has showed the possibility of a precision measurement of the full po-  
1654 larisation vector of the  $\Lambda_c^+$  baryon, with uncertainties of order 0.01 on the polarisation  
1655 components. A large polarisation is measured in the  $\Lambda_c^+$  helicity frames considered. In  
1656 the one reached from the laboratory frame it has a modulus  $P \approx 65\%$ , with a transverse  
1657  $P_x$  component larger than the longitudinal  $P_z$  component; in those reached from the  
1658 approximate  $\Lambda_b^0$  rest frame it has a modulus  $P \approx 69\%$ , with a longitudinal component  
1659 larger than the transverse one. For the latter frame, final results are provided for the  
1660 frame reconstructed via the “Equal boost” algorithm.

1661 The normal polarisation  $P_y$ , sensitive to time-reversal violation effects and final-state  
1662 interactions, is compatible with zero at 0.01 level, for all the polarisation frames considered.

1663 Following [3], the  $\Lambda_c^+ \rightarrow pK^-\pi^+$  amplitude analysis is sensitive to all the parameters  
1664 of describing the  $\Lambda_c^+ \rightarrow pK^-\pi^+$  amplitude model. In practice, not all the contributions  
1665 composing the amplitude model can be constrained in the same way: some resonant  
1666 contributions are well determined by the fit, measured with relatively small uncertainties;  
1667 others which are difficult to disentangle among each other are measured with large  
1668 uncertainties. Nonetheless, the  $\Lambda_c^+$  polarisation is weakly sensitive to amplitude model  
1669 uncertainties.

1670 A large contribution from a resonant state in the  $m(pK^-) \approx 2$  GeV region, where no  
1671 clear resonances have been reported by the PDG, has been established. This contribution is  
1672 well described as a single  $J^P = 1/2^-$  state, with Breit-Wigner parameters  $m = 1988 \pm 2 \pm 21$   
1673 MeV and  $\Gamma = 179 \pm 4 \pm 16$  MeV. The closest resonance reported by the PDG is the  $\Lambda(2000)$ :  
1674 the measured values are fairly compatible with those quoted by Ref. [59],  $m = 2020 \pm 16$   
1675 MeV and  $\Gamma = 255 \pm 63$  MeV, and Ref. [60],  $m = 2030 \pm 30$  MeV and  $\Gamma = 125 \pm 25$  MeV.

1676 The largest contributions to the amplitude model, measured from fit fractions, come  
1677 from  $\Delta^{++}(1232)$ ,  $K^*(892)$  and  $K_0^*(1430)$  resonances. Among  $\Lambda^*$  resonances the larger  
1678 contributions come from  $\Lambda(1405)$  and  $\Lambda(2000)$  states.

1679 A large sensitivity to the polarisation,  $\sqrt{3}S = 0.662 \pm 0.005 \pm 0.013$  is observed, an  
1680 essential information for  $\Lambda_c^+$  polarisation and electromagnetic dipole moments from spin  
1681 precession measurements.

1682 The amplitude fit has also been performed separately for  $\Lambda_c^+ \rightarrow pK^-\pi^+$  decays and  
1683 its  $CP$ -conjugated mode  $\bar{\Lambda}_c^- \rightarrow \bar{p}K^+\pi^-$ : no significant differences are observed between  
1684 the amplitude models obtained.

Parameter	Central Value		Stat. Unc.		Model Unc.		Syst. Unc.
Px (lab)	0.603214	±	0.006781	±	0.009797	±	0.002109
Py (lab)	-0.004078	±	0.006142	±	0.001643	±	0.000719
Pz (lab)	-0.246958	±	0.005967	±	0.003462	±	0.010527
Px ( $\Lambda_b^0$ )	0.216509	±	0.006781	±	0.00363	±	0.001538
Py ( $\Lambda_b^0$ )	0.010822	±	0.006142	±	0.00087	±	0.000806
Pz ( $\Lambda_b^0$ )	-0.664688	±	0.005967	±	0.010584	±	0.00122

Table 28: Final results for the polarisation components, measured in the  $\Lambda_c^+$  helicity frame reached from the laboratory (lab) or the  $\Lambda_b^0$  approximate rest frame reconstructed via the “Equal boost” algorithm ( $\Lambda_b^0$ ). **Rounding to be applied.**

Parameter	Central Value	Stat. Unc.	Model Unc.	Syst. Unc.
gammaK0(700)	0.94106	± 0.066695	± 0.352595	± 0.037569
ArK0(700)1	0.068908	± 0.231036	± 0.929106	± 0.08887
AiK0(700)1	2.521444	± 0.224926	± 3.206334	± 0.136353
ArK0(700)2	-2.68563	± 0.24977	± 2.054513	± 0.200919
AiK0(700)2	0.03849	± 0.256271	± 1.338656	± 0.054253
ArK(892)2	1.192614	± 0.128508	± 0.850822	± 0.051234
AiK(892)2	-1.025814	± 0.121782	± 0.961767	± 0.020692
ArK(892)3	-3.141446	± 0.356605	± 2.386247	± 0.057544
AiK(892)3	-3.29341	± 0.345822	± 2.701234	± 0.09741
ArK(892)4	-0.727145	± 0.342451	± 1.479561	± 0.084137
AiK(892)4	-4.155027	± 0.316512	± 4.534983	± 0.097391
gammaK0(1430)	0.020981	± 0.017557	± 0.332961	± 0.005049
ArK0(1430)1	-6.71516	± 0.995225	± 5.363046	± 0.357129
AiK0(1430)1	10.479411	± 0.970168	± 13.630225	± 0.182603
ArK0(1430)2	0.219754	± 0.773596	± 2.426869	± 0.269459
AiK0(1430)2	8.741196	± 0.680862	± 9.696851	± 0.113639
ArL(1405)1	-4.572486	± 0.520352	± 3.347816	± 0.051749
AiL(1405)1	3.190144	± 0.533438	± 3.229665	± 0.117856
ArL(1405)2	10.44608	± 0.832772	± 12.257922	± 0.159029
AiL(1405)2	2.787441	± 1.053855	± 3.713678	± 0.268249
ML(1520)	1.518467	± 0.000359	± 0.000647	± 2.9e-05
GL(1520)	0.015195	± 0.000783	± 0.001307	± 0.000135
ArL(1520)1	0.293998	± 0.05296	± 0.123946	± 0.005822
AiL(1520)1	0.044324	± 0.053574	± 0.122679	± 0.016106
ArL(1520)2	-0.160687	± 0.139857	± 0.685141	± 0.034413
AiL(1520)2	1.498833	± 0.127453	± 1.256291	± 0.03382
ArL(1600)1	4.840649	± 0.463069	± 4.974653	± 0.1221
AiL(1600)1	3.082786	± 0.537026	± 3.710903	± 0.134333
ArL(1600)2	-6.971233	± 0.54214	± 8.68387	± 0.079794
AiL(1600)2	0.842435	± 0.627279	± 1.971388	± 0.173032
ArL(1670)1	-0.339585	± 0.051127	± 0.348782	± 0.009082
AiL(1670)1	-0.144678	± 0.05064	± 0.224407	± 0.018522
ArL(1670)2	-0.570978	± 0.098191	± 0.456435	± 0.023003
AiL(1670)2	1.011833	± 0.093393	± 1.179628	± 0.014798
ArL(1690)1	-0.385772	± 0.101472	± 0.227841	± 0.017978
AiL(1690)1	-0.110235	± 0.093864	± 0.441349	± 0.023154
ArL(1690)2	-2.730592	± 0.198149	± 2.444179	± 0.046494
AiL(1690)2	-0.353613	± 0.225648	± 0.601515	± 0.061425
ML(2000)	1.98819	± 0.001982	± 0.021189	± 0.001289
GL(2000)	0.17926	± 0.003954	± 0.015787	± 0.002924
ArL(2000)1	-8.014857	± 0.893302	± 10.821927	± 0.22646
AiL(2000)1	-7.614006	± 0.833513	± 7.685489	± 0.235687
ArL(2000)2	-4.336255	± 0.492742	± 3.445314	± 0.15085
AiL(2000)2	-3.796192	± 0.445017	± 3.708795	± 0.066898
ArD(1232)1	-6.778191	± 0.53807	± 5.278255	± 0.170592
AiD(1232)1	3.051805	± 0.585933	± 1.422528	± 0.14629
ArD(1232)2	-12.987193	± 0.968551	± 12.400696	± 0.2592
AiD(1232)2	4.528336	± 1.097471	± 3.689671	± 0.319639
ArD(1600)1	11.401585	± 0.937137	± 9.805709	± 0.235312
AiD(1600)1	-3.125511	± 1.022271	± 1.430495	± 0.175824
ArD(1600)2	6.729211	± 0.690366	± 7.161588	± 0.221083
AiD(1600)2	-1.002383	± 0.653633	± 2.123592	± 0.076526
ArD(1700)1	10.37828	± 0.852019	± 7.216558	± 0.319345
AiD(1700)1	1.434872	± 0.929793	± 5.154101	± 0.173366
ArD(1700)2	12.874102	± 1.042996	± 12.695075	± 0.291225
AiD(1700)2	2.10557	± 1.102225	± 6.035012	± 0.25295

Table 29: Final results for the fit parameters of the nominal amplitude model. **Rounding to be applied.** Fit parameters are defined in Appendix 6.8.

Resonance	Fit Fraction		Stat. Unc.		Model Unc.		Syst. Unc.
$\Delta^{++}(1232)$	0.285997	$\pm$	0.002935	$\pm$	0.007625	$\pm$	0.00158
$\Delta^{++}(1600)$	0.04518	$\pm$	0.002714	$\pm$	0.014757	$\pm$	0.000598
$\Delta^{++}(1700)$	0.039025	$\pm$	0.001984	$\pm$	0.009402	$\pm$	0.000685
$K^*(892)$	0.221389	$\pm$	0.002269	$\pm$	0.006355	$\pm$	0.000381
$K^*0(1430)$	0.147098	$\pm$	0.005655	$\pm$	0.026717	$\pm$	0.001234
$K^*0(700)$	0.030178	$\pm$	0.00159	$\pm$	0.00922	$\pm$	0.00182
$\Lambda(1405)$	0.077164	$\pm$	0.00244	$\pm$	0.02998	$\pm$	0.001837
$\Lambda(1520)$	0.018621	$\pm$	0.000915	$\pm$	0.002328	$\pm$	0.000279
$\Lambda(1600)$	0.051787	$\pm$	0.002233	$\pm$	0.019351	$\pm$	0.000587
$\Lambda(1670)$	0.011787	$\pm$	0.000581	$\pm$	0.003164	$\pm$	0.000127
$\Lambda(1690)$	0.011943	$\pm$	0.000882	$\pm$	0.003361	$\pm$	0.000133
$\Lambda(2000)$	0.095805	$\pm$	0.002729	$\pm$	0.009317	$\pm$	0.002271

Table 30: Final results for the fit fractions of the resonant contributions included in the nominal amplitude model. **Rounding to be applied.**

Resonance	$\alpha$		Stat. Unc.		Model Unc.		Syst. Unc.
Model ( $\sqrt{3}S$ )	0.662306	$\pm$	0.004789	$\pm$	0.010359	$\pm$	0.007032
$\Delta^{++}(1232)$	-0.547868	$\pm$	0.014498	$\pm$	0.035625	$\pm$	0.004079
$\Delta^{++}(1600)$	0.502429	$\pm$	0.047781	$\pm$	0.171375	$\pm$	0.012903
$\Delta^{++}(1700)$	-0.215788	$\pm$	0.036419	$\pm$	0.074887	$\pm$	0.01058
$K^*(892)$	-0.834474	$\pm$	0.012452	$\pm$	0.036	$\pm$	0.002435
$K^*0(1430)$	-0.33909	$\pm$	0.033735	$\pm$	0.13889	$\pm$	0.013803
$K^*0(700)$	0.062731	$\pm$	0.655995	$\pm$	0.238346	$\pm$	0.226548
$\Lambda(1405)$	-0.579866	$\pm$	0.051107	$\pm$	0.27771	$\pm$	0.010235
$\Lambda(1520)$	-0.925108	$\pm$	0.024638	$\pm$	0.084296	$\pm$	0.004649
$\Lambda(1600)$	-0.199072	$\pm$	0.062243	$\pm$	0.498706	$\pm$	0.025045
$\Lambda(1670)$	-0.816631	$\pm$	0.042113	$\pm$	0.072945	$\pm$	0.005625
$\Lambda(1690)$	-0.958417	$\pm$	0.020023	$\pm$	0.026588	$\pm$	0.006169
$\Lambda(2000)$	0.572602	$\pm$	0.025843	$\pm$	0.191026	$\pm$	0.009023

Table 31: Final results for the decay asymmetry  $\alpha$  parameters of the nominal amplitude model and single resonant contributions. **Rounding to be applied.**

Resonance	$J^P$	BW mass ( MeV)	BW width ( MeV)
$\Lambda(1405)$	$1/2^-$	1405.1	50.5
$\Lambda(1520)$	$3/2^-$	1518.4	15.2
$\Lambda(1600)$	$1/2^+$	1630	250
$\Lambda(1670)$	$1/2^-$	1670	30
$\Lambda(1690)$	$3/2^-$	1690	70
$\Lambda(2000)$	$1/2^-$	1988	179
$\Delta^{++}(1232)$	$3/2^+$	1232	117
$\Delta^{++}(1600)$	$3/2^+$	1640	300
$\Delta^{++}(1700)$	$3/2^-$	1690	380
$K_0^*(700)$	$0^+$	824	478
$K^*(892)$	$1^-$	895.5	47.3
$K_0^*(1430)$	$0^+$	1375	190

Table 32: Resonant composition of the fitted  $\Lambda_c^+ \rightarrow pK^-\pi^+$  amplitude model, with  $J^P$  the spin-parity assignment, and the Breit-Wigner parameters. Those related to  $\Lambda(1520)$  and  $\Lambda(2000)$  contributions are determined from the fit.

System	$P_x$	$P_y$	$P_z$	$P(\%)$
approx $\Lambda_b^0$ (initial)	0.2165	0.010822	-0.6646	69
lab (fit)	$0.603 \pm 0.012$	$-0.0041 \pm 0.0064$	$-0.247 \pm 0.013$	65
lab (MC study)	0.57	-0.012	-0.23	62

Table 33: Summary of the simulation-based study transforming  $\Lambda_c^+$  polarisation from the  $\Lambda_c^+$  helicity systems reached from the approximate  $\Lambda_b^0$  rest frame to that reached from the laboratory frame. Initial refers to the polarisation vector used as input to the MC study; fit refers the polarisation measured in the amplitude fit; MC study is the rotated polarisation vector.

## 9.1 Interpretation of the measured $\Lambda_c^+$ polarisation

To better understand the  $\Lambda_c^+$  polarisation values observed in the two reference systems considered, a simulation-based study is performed. Indeed, the dynamics of the semileptonic decay produces a  $\Lambda_c^+$  polarisation which is better expressed in the hardly accessible helicity system reached from the beauty hadron rest frame. It is therefore interesting to have an understanding of how such polarisation can be seen in the two  $\Lambda_c^+$  helicity frames considered in the present analysis. Moreover, this study also aims at understanding the relation between the polarisation values measured in the two polarisation systems.

In this study, we consider an initial value of the polarisation vector, expressed in one reference system, which is then rotated to a second reference system. The rotation between systems is determined from their event-by-event definition, taking events from the full simulation sample with selection applied. This way, the relation between reference systems is obtained from the  $\Lambda_b^0 \rightarrow \Lambda_c^+ \mu^- \bar{\nu}_\mu$  kinematics corresponding to the same simulation sample used in the amplitude fit ( $\approx 450'000$  events). The rotated polarisation vectors are then averaged over the event-by-event coordinate system of the second polarisation system, obtaining a mean polarisation vector.

Two cases are considered. First, the transformation from the  $\Lambda_c^+$  helicity systems reached from the approximate  $\Lambda_b^0$  rest frame to that reached from the laboratory frame is studied. Starting from the  $\Lambda_c^+$  polarisation measured in the approximate  $\Lambda_b^0$  rest frame, Table 28, a  $\Lambda_c^+$  polarisation of  $P_x = 0.57$ ,  $P_y = -0.012$ ,  $P_z = -0.23$  is obtained in the laboratory frame. This polarisation vector is compared to that obtained in the amplitude fit in Table 33, while the distributions of the event-by-event rotated polarisation components are reported in Figure 49. This study reproduces what observed in the amplitude analysis: the mostly longitudinal polarisation in the  $\Lambda_c^+$  helicity system reached from the approximate  $\Lambda_b^0$  frame becomes mostly transverse when expressed using the laboratory frame, as a consequence of the different way  $\Lambda_c^+$  and  $\mu^-$  momenta (defining the polarisation systems, Eq. (19)) are expressed in the two reference frames. The study also predicts a dilution (reduction) of the polarisation magnitude from 69% to 62%, even if slightly larger than the one observed in the laboratory frame (65%).

Second, the transformation from the  $\Lambda_c^+$  helicity systems reached from the true  $\Lambda_b^0$  rest frame (known in the simulation sample) and that reached from the approximate  $\Lambda_b^0$  one is considered. In this case the study is aimed at giving a qualitative understanding of how the  $\Lambda_c^+$  polarisation in the  $\Lambda_b^0$  rest frame (the one interesting for a comparison with theoretical predictions) is seen when considering an approximate definition of the  $\Lambda_b^0$  frame. It is important to note that the mismatch between the simulation employed,

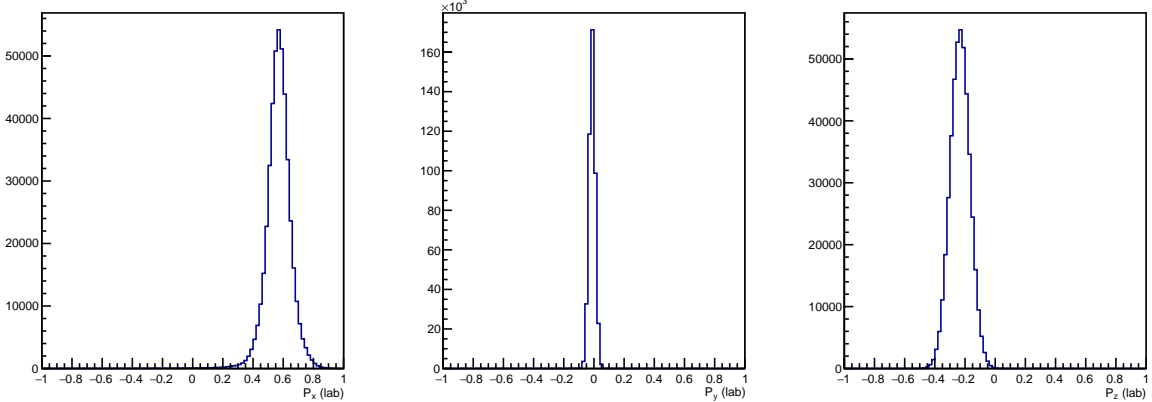


Figure 49: Distributions of the event-by-event rotated polarisation components in the  $\Lambda_c^+$  helicity system reached from the laboratory frame, obtained transforming the  $\Lambda_c^+$  polarisation measured in the  $\Lambda_c^+$  helicity system reached from the approximate  $\Lambda_b^0$  rest frame.

1720 constituted by exclusive  $\Lambda_b^0 \rightarrow \Lambda_c^+ \mu^- \bar{\nu}_\mu$  decays, and the real data, for which an inclusive  
 1721 selection based on  $\Lambda_c^+ \mu^-$  vertices has been applied, may be important in this case. A  
 1722 quantitative evaluation of these effects requires a precise understanding of the semileptonic  
 1723 decays contributing to data, which is beyond the scope of the present analysis.

1724 Two polarisation vectors in the true  $\Lambda_b^0$  rest frame are considered. For full negative  
 1725 polarisation  $P_z = -1$ , a  $\Lambda_c^+$  polarisation of  $P_x = 0.17$ ,  $P_y = -7.1 \times 10^{-5}$ ,  $P_z = -0.89$  is  
 1726 obtained in the approximate  $\Lambda_b^0$  frame. The distributions of the event-by-event rotated  
 1727 polarisation components are reported in Figure 50. This shows that a full negative  
 1728 longitudinal polarisation in the true  $\Lambda_b^0$  frame gets a positive transverse polarisation  
 1729 component when expressed in the approximate frame. The polarisation magnitude is  
 1730 diluted from 100% to 91%. A second polarisation vector is considered,  $P_x = 0.4$ ,  $P_y = 0$ ,  
 1731  $P_z = -0.85$ , corresponding to the prediction of Ref. [7] for  $q^2 = 5.8 \text{ GeV}^2$ , the mean value  
 1732 obtained from the simulation sample. The corresponding  $\Lambda_c^+$  polarisation expressed in the  
 1733 approximate  $\Lambda_b^0$  rest frame is  $P_x = 0.32$ ,  $P_y = 4.8 \times 10^{-5}$ ,  $P_z = -0.76$ , with polarisation  
 1734 magnitude reduced from 94% to 82%. The distributions of the event-by-event rotated  
 1735 polarisation components are reported in Figure 51. The  $\Lambda_c^+$  polarisation vectors obtained  
 1736 are compared to the results of the amplitude fit in Table 34

1737 In both cases the same polarisation pattern observed in data is reproduced: a dominant  
 1738 negative longitudinal polarisation together with a positive transverse component. It is also  
 1739 important to highlight that for both cases a dilution of the polarisation degree is expected.  
 1740 Even if the quantitative determination of the  $\Lambda_c^+$  polarisation in the  $\Lambda_c^+$  helicity system  
 1741 reached from the real  $\Lambda_b^0$  rest frame would require a more thorough study, with the folding  
 1742 of the partial reconstruction effects into the amplitude fit, the present simulation-based  
 1743 study shows that the interpretation of the  $\Lambda_c^+$  polarisation measured in the approximate  
 1744 rest frame from the perspective of available theoretical predictions is in principle possible.

System	$P_x$	$P_y$	$P_z$	$P(\%)$
true $\Lambda_b^0$ (initial)	0	0	-1	100
approx $\Lambda_b^0$ (MC study)	0.17	$-7.1 \times 10^{-5}$	-0.89	91
true $\Lambda_b^0$ (initial)	0.4	0	-0.85	94
approx $\Lambda_b^0$ (MC study)	0.32	$4.8 \times 10^{-5}$	-0.76	82
approx $\Lambda_b^0$ (fit)	$0.2165 \pm 0.0078$	$0.0108 \pm 0.0063$	$-0.665 \pm 0.012$	69

Table 34: Summary of the simulation-based study transforming  $\Lambda_c^+$  polarisation from the true  $\Lambda_b^0$  rest frame (known in the simulation sample) and that reached from the approximate  $\Lambda_b^0$  one. Initial refers to the polarisation vector used as input to the MC study; MC study is the rotated polarisation vector; fit refers the polarisation measured in the amplitude fit.

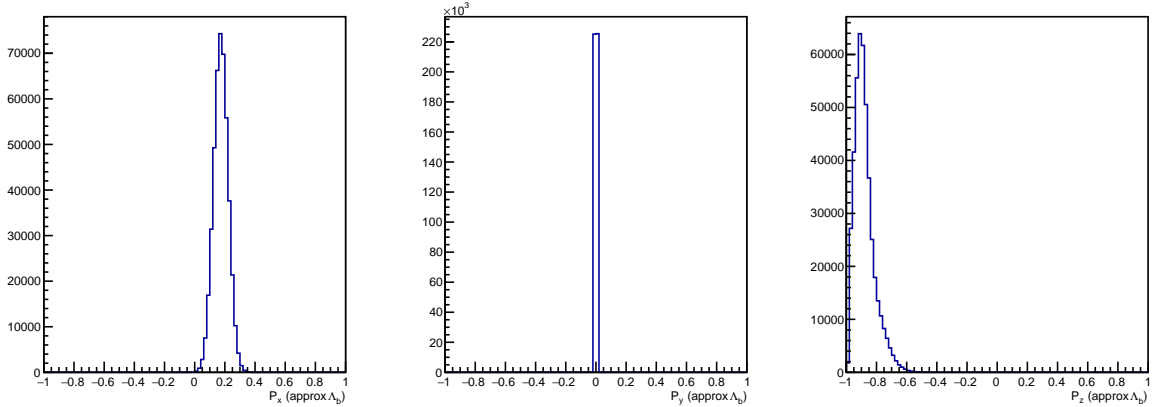


Figure 50: Distributions of the event-by-event rotated polarisation components in the  $\Lambda_c^+$  helicity system reached from the approximate  $\Lambda_b^0$  frame, obtained transforming a full negative longitudinal  $\Lambda_c^+$  polarisation in the  $\Lambda_c^+$  helicity system reached from the true  $\Lambda_b^0$  rest frame.

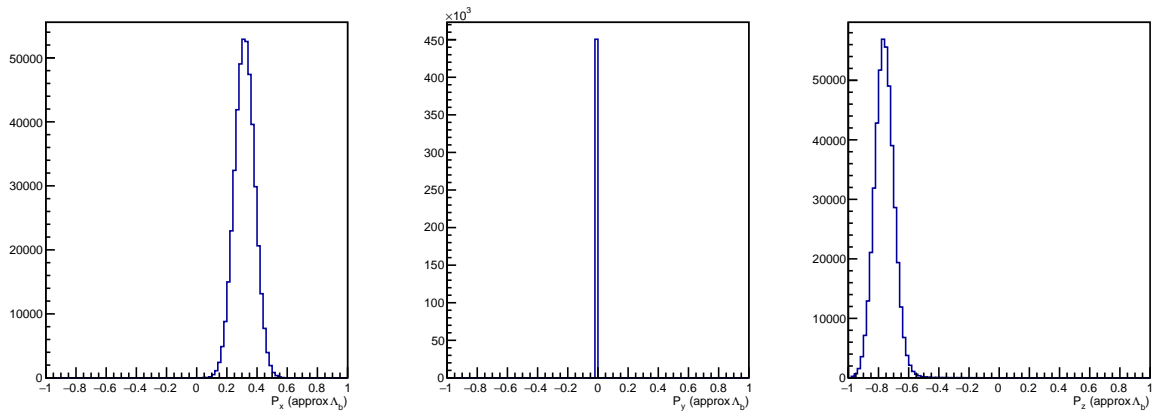


Figure 51: Distributions of the event-by-event rotated polarisation components in the  $A_c^+$  helicity system reached from the approximate  $\Lambda_b^0$  frame, obtained transforming an initial  $A_c^+$  polarisation taken a theoretical prediction in the  $A_c^+$  helicity system reached from the true  $\Lambda_b^0$  rest frame.

Figure 52: Comparison between full (red) and ReDecay (blue) invariant mass,  $\Lambda_c^+$  lifetime, number of tracks distributions.

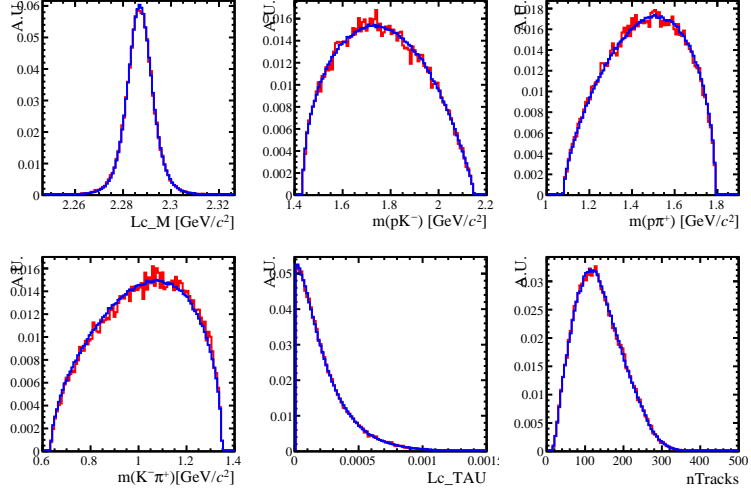
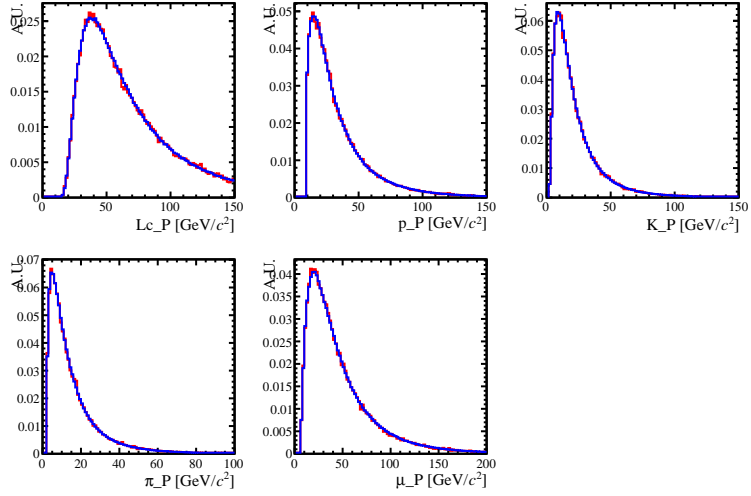


Figure 53: Comparison between full (red) and ReDecay (blue) momentum distributions.



## 1745 A ReDecay faster simulation validation

1746 The validity of the *ReDecay* faster simulation for the description of the detector efficiency  
 1747 effects is studied comparing a large set of distributions against the full simulation sample,  
 1748 in which only the flat phase space  $\Lambda_c^+ \rightarrow pK^-\pi^+$  events are considered, to avoid effects  
 1749 of the full simulation decay model on the distributions. The following distributions are  
 1750 checked: invariant masses,  $\Lambda_c^+$  lifetime, number of tracks (Fig. 52), momenta (Fig. 53),  
 1751 transverse momenta (Fig. 54), uncorrected particle identification delta log-likelihoods  
 1752 (Fig. 55), uncorrected neural network based ProbNN variables (Fig. 56) and the one-  
 1753 dimensional projections of the detector efficiency over the  $\Lambda_c^+ \rightarrow pK^-\pi^+$  phase space  
 1754 (Fig. 57). No significant discrepancies are visible.

Figure 54: Comparison between full (red) and ReDecay (blue) transverse momentum distributions.

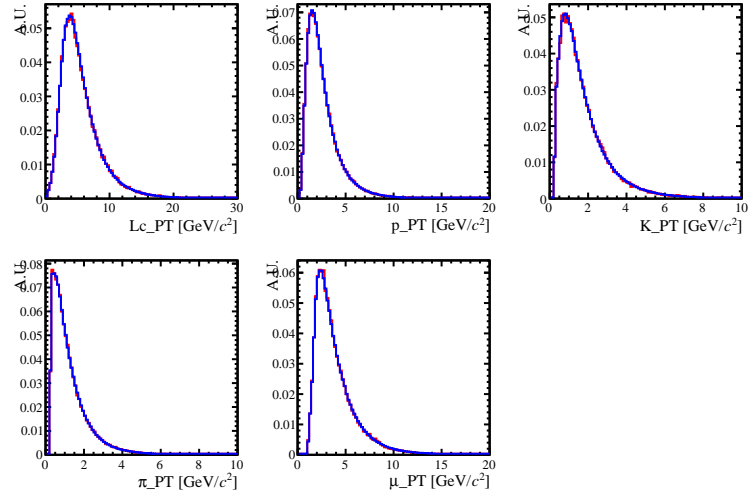


Figure 55: Comparison between full (red) and ReDecay (blue) uncorrected PID distributions.

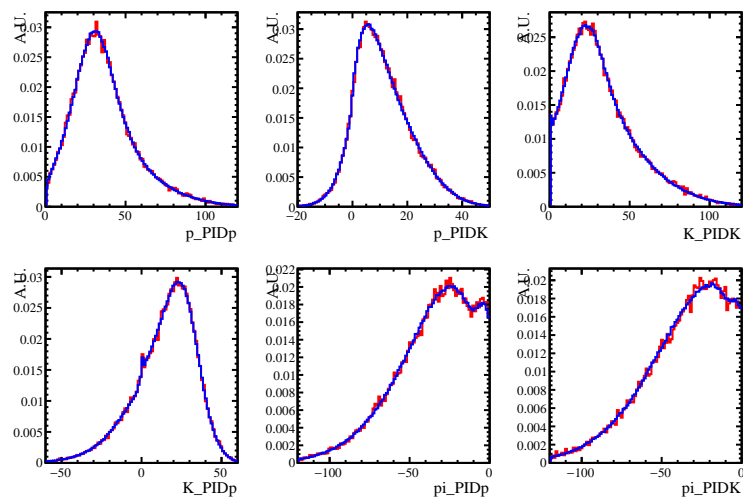


Figure 56: Comparison between full (red) and ReDecay (blue) uncorrected ProbNN distributions.

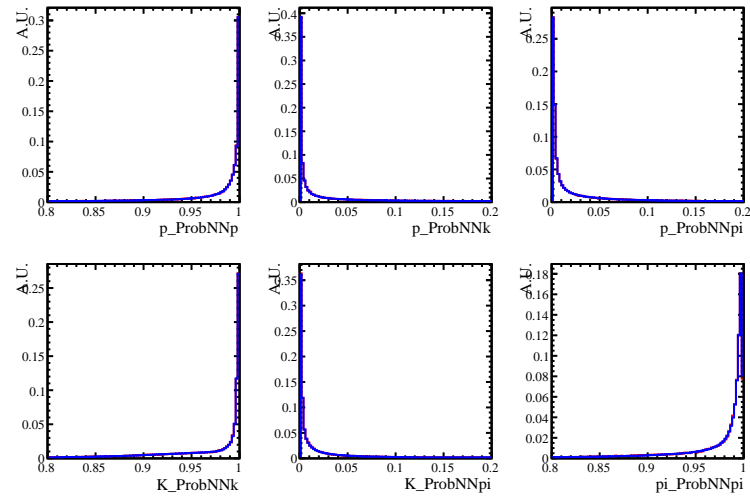
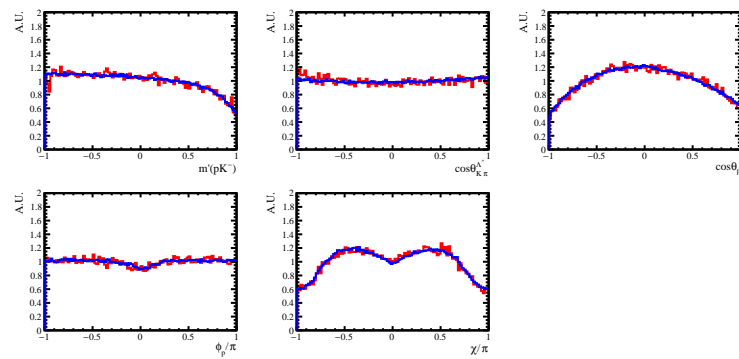


Figure 57: Comparison between full (red) and ReDecay (blue)  $\Lambda_c^+$  efficiency distributions in  $\Lambda_c^+$  phase space.



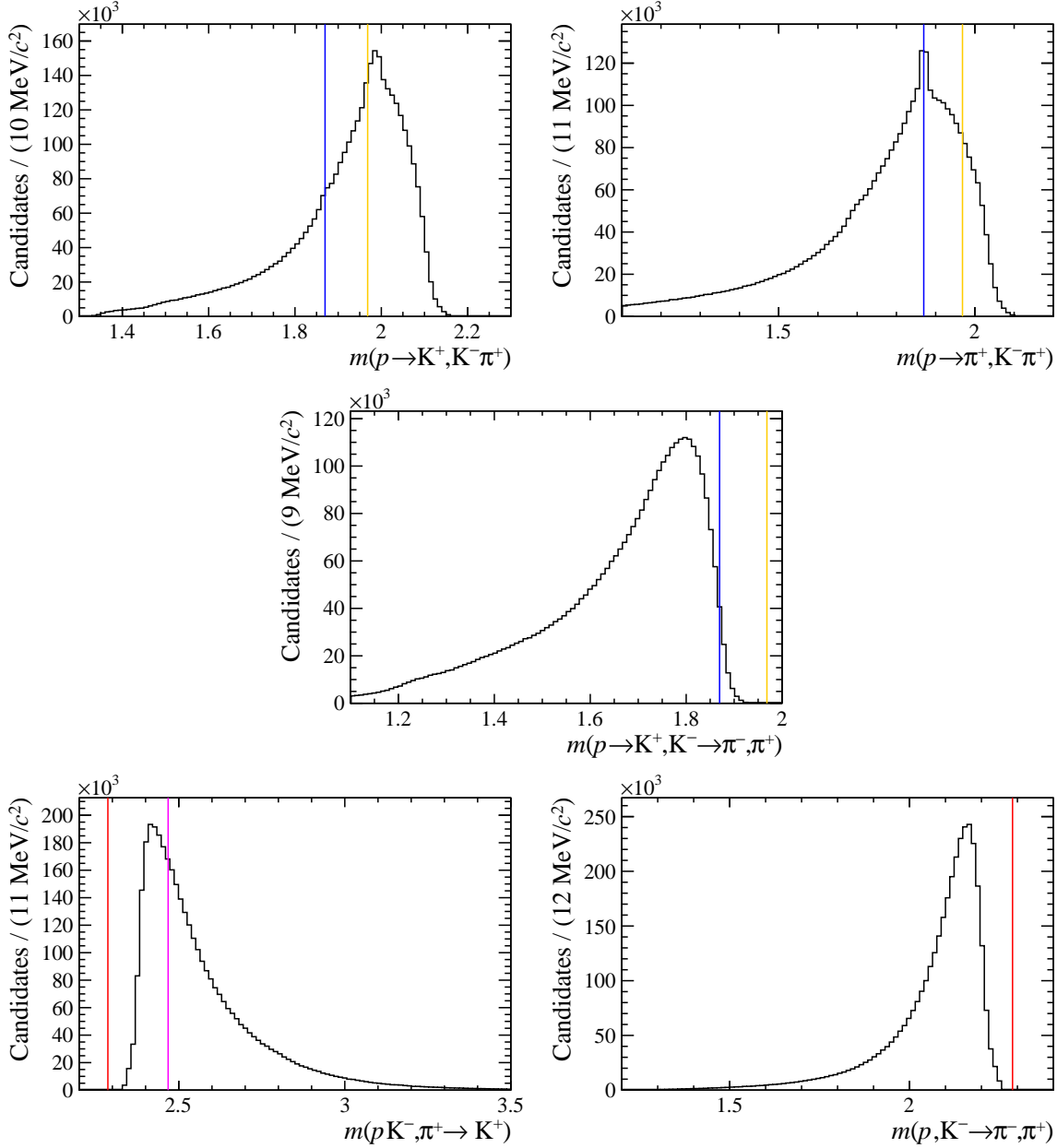


Figure 58: Invariant mass distributions for  $D_{(s)}^+ \rightarrow h^+h^-h^+$  and (Bottom)  $\Lambda_c^+/\Xi_c^+ \rightarrow ph^-h^+$  alternative mass hypothesis for candidates passing stripping and trigger requirements. Dashed lines correspond to (blue)  $D^+$ , (orange)  $D_s^+$ , (red)  $\Lambda_c^+$  and (magenta)  $\Xi_c^+$  PDG masses [1].

## <sup>1755</sup> B Additional misidentified background plots

<sup>1756</sup> The invariant mass distributions of the three daughter particles with different mass  
<sup>1757</sup> hypothesis before and after selection are reported in Figs. 58 and 59, respectively.

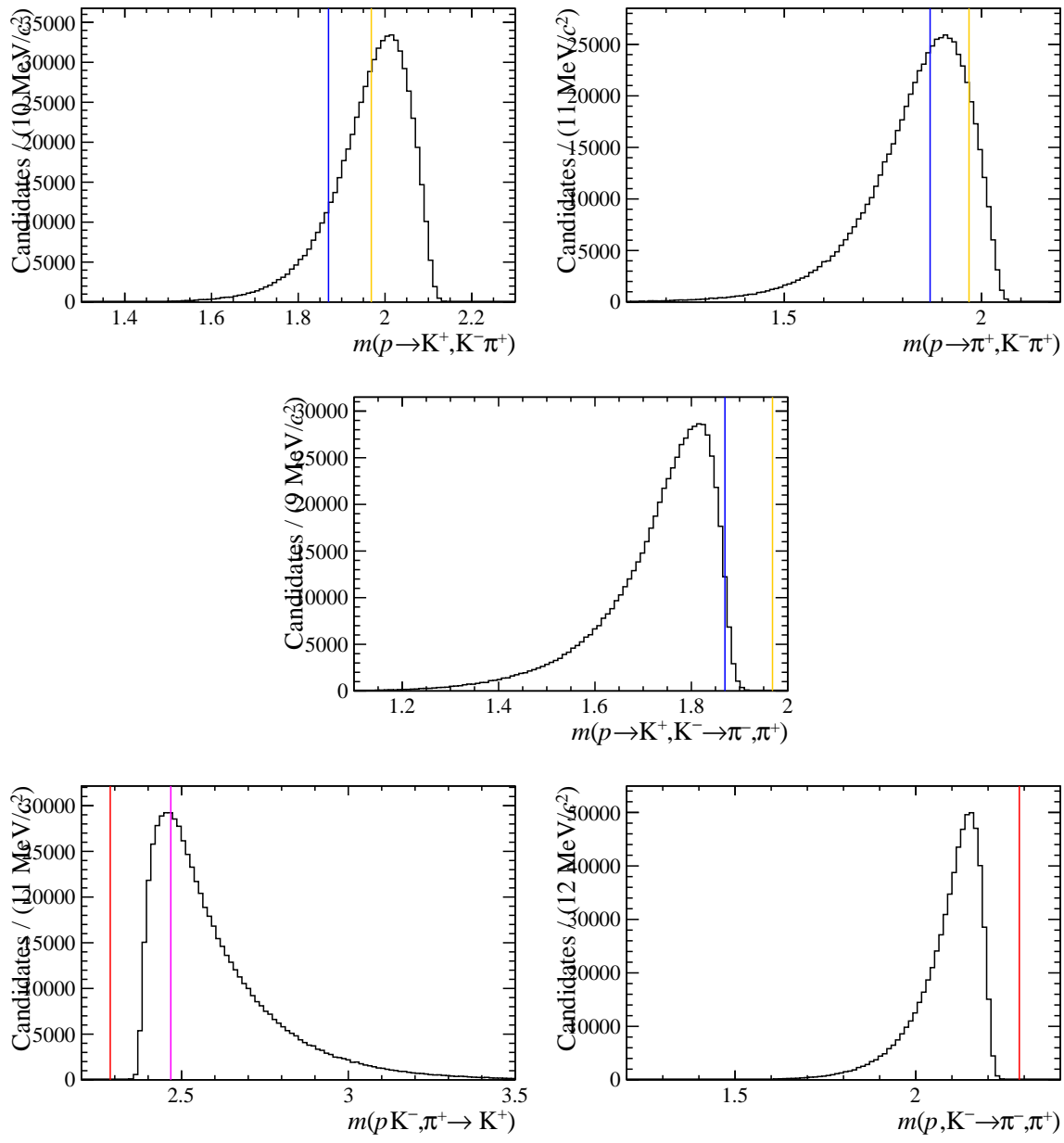


Figure 59: Invariant mass distributions for  $D_{(s)}^+ \rightarrow h^+ h^- h^+$  and (Bottom)  $\Lambda_c^+/\Xi_c^+ \rightarrow ph^- h^+$  alternative mass hypothesis for candidates passing the full selection process. Dashed lines correspond to (blue)  $D^+$ , (orange)  $D_s^+$ , (red)  $\Lambda_c^+$  and (magenta)  $\Xi_c^+$  PDG masses [1].

## 1758 C Rotation of reference frames

1759 The rotation of an initial Cartesian reference frame  $(x, y, z)$  into a final one  $(X, Y, Z)$  can  
 1760 be univocally described by an Euler rotation parametrised by three Euler angles  $\alpha, \beta, \gamma$ .  
 1761 Taking the  $z$ - $y$ - $z$  convention for the rotation axes, the Euler rotation is composed by a  
 1762 first rotation of angle  $\alpha$  around the  $z$  axis, a second rotation of angle  $\beta$  around the rotated  
 1763  $y'$  axis and a third one of angle  $\gamma$  around the two-times rotated  $z''$  axis,

$$\mathcal{R}(\alpha, \beta, \gamma) = R_{z''}(\gamma)R_{y'}(\beta)R_z(\alpha) = e^{-i\gamma\hat{J}_{z''}}e^{-i\beta\hat{J}_{y'}}e^{-i\alpha\hat{J}_z}. \quad (88)$$

1764 The latter equality expresses rotations in terms of the generating angular momentum  
 1765 operators. Here, active rotations are considered, in which the normalised vectors  $\hat{\mathbf{x}}, \hat{\mathbf{y}}, \hat{\mathbf{z}}$   
 1766 defining the initial reference frame are actively rotated to those describing the final  
 1767 reference frame  $\hat{\mathbf{X}}, \hat{\mathbf{Y}}, \hat{\mathbf{Z}}$ ,

$$\hat{\mathbf{X}}^i = \mathcal{R}(\alpha, \beta, \gamma)\hat{\mathbf{x}}^i. \quad (89)$$

1768 The three Euler angles can be computed as follows: given the vector  $\mathbf{N} = \hat{\mathbf{z}} \times \hat{\mathbf{Z}}$ ,  $\alpha$  is the  
 1769 angle between  $\hat{\mathbf{y}}$  and  $\hat{\mathbf{N}}$ ,  $\beta$  is the angle between  $\hat{\mathbf{z}}$  and  $\hat{\mathbf{Z}}$  axes and  $\gamma$  is the angle between  
 1770  $\hat{\mathbf{N}}$  and  $\hat{\mathbf{Y}}$  axes. In formulae<sup>12</sup>,

$$\begin{aligned} \alpha &= \text{atan2}\left(\hat{\mathbf{y}} \cdot \hat{\mathbf{Z}}, \hat{\mathbf{x}} \cdot \hat{\mathbf{Z}}\right) \in [-\pi, \pi], \\ \beta &= \arccos\left(\hat{\mathbf{z}} \cdot \hat{\mathbf{Z}}\right) \in [0, \pi], \\ \gamma &= \text{atan2}\left(\hat{\mathbf{z}} \cdot \hat{\mathbf{Y}}, -\hat{\mathbf{z}} \cdot \hat{\mathbf{X}}\right) \in [-\pi, \pi]. \end{aligned} \quad (90)$$

1771 The Euler rotation can be also expressed in terms of rotations around the initial reference  
 1772 frame axes only, by means of the equality, shown in Ref. [61],

$$\mathcal{R}(\alpha, \beta, \gamma) = R_z(\alpha)R_y(\beta)R_z(\gamma) = e^{-i\alpha\hat{J}_z}e^{-i\beta\hat{J}_y}e^{-i\gamma\hat{J}_z}. \quad (91)$$

1773 The active action of an Euler rotation on a vector  $\mathbf{v}$  can be written in matrix notation as

$$V_i = \mathcal{R}_{ij}(\alpha, \beta, \gamma)v_j \quad (92)$$

1774 in which the vector and matrix components are expressed in the same, but arbitrary,  
 1775 reference frame. Instead, the passive action on vector components, expressed in the initial  
 1776 ( $v_i$ ) or the final ( $v_I$ ) reference frames connected by an Euler rotation  $\mathcal{R}(\alpha, \beta, \gamma)$ , is

$$v_I = v_i \mathcal{R}(\alpha, \beta, \gamma)_{iI} = \mathcal{R}^T(\alpha, \beta, \gamma)_{Ii} v_i = \mathcal{R}(-\gamma, -\beta, -\alpha)_{ij} v_j, \quad (93)$$

1777 in which the latter equality follows from  $\mathcal{R}^T = \mathcal{R}^{-1}$  and Eq. (91).

1778 The action of the rotation operators  $\mathcal{R}(\alpha, \beta, \gamma)$  on angular momentum eigenstates  
 1779  $|J, m\rangle$  can be written as

$$\mathcal{R}(\alpha, \beta, \gamma) |J, m\rangle = \sum_{m'=-J}^J D_{m', m}^J(\alpha, \beta, \gamma) |J, m'\rangle, \quad (94)$$

---

<sup>12</sup>The function  $\text{atan2}(y, x) \in [-\pi, \pi]$  computes the signed angle between the  $x$  axis and the vector having components  $(x, y)$ .

<sub>1780</sub> in which the Wigner  $D$ -matrices  $D_{m'm}^J(\alpha, \beta, \gamma)$  are the matrix elements of the rotation  
<sub>1781</sub> operator in the given spin reference frame,

$$D_{m',m}^J(\alpha, \beta, \gamma) = \langle J, m' | \mathcal{R}(\alpha, \beta, \gamma) | J, m \rangle. \quad (95)$$

<sub>1782</sub> From the latter equality of Eq. (91), the Wigner  $D$ -matrices can be factorised as

$$\begin{aligned} D_{m',m}^J(\alpha, \beta, \gamma) &= \langle J, m' | e^{-i\alpha \hat{J}_z} e^{-i\beta \hat{J}_y} e^{-i\gamma \hat{J}_z} | J, m \rangle \\ &= e^{-im'\alpha} d_{m',m}^J(\beta) e^{-im\gamma}, \end{aligned} \quad (96)$$

<sub>1783</sub> in which the Wigner  $d$ -matrices elements are known combinations of trigonometric functions  
<sub>1784</sub> of  $\beta$  depending on  $J, m, m'$  parameters [61].

<sub>1785</sub> **D Cross-checks fit results**

<sub>1786</sub> In this appendix, the results of the amplitude fits considered as cross-checks, Sec. 8, are  
<sub>1787</sub> presented.

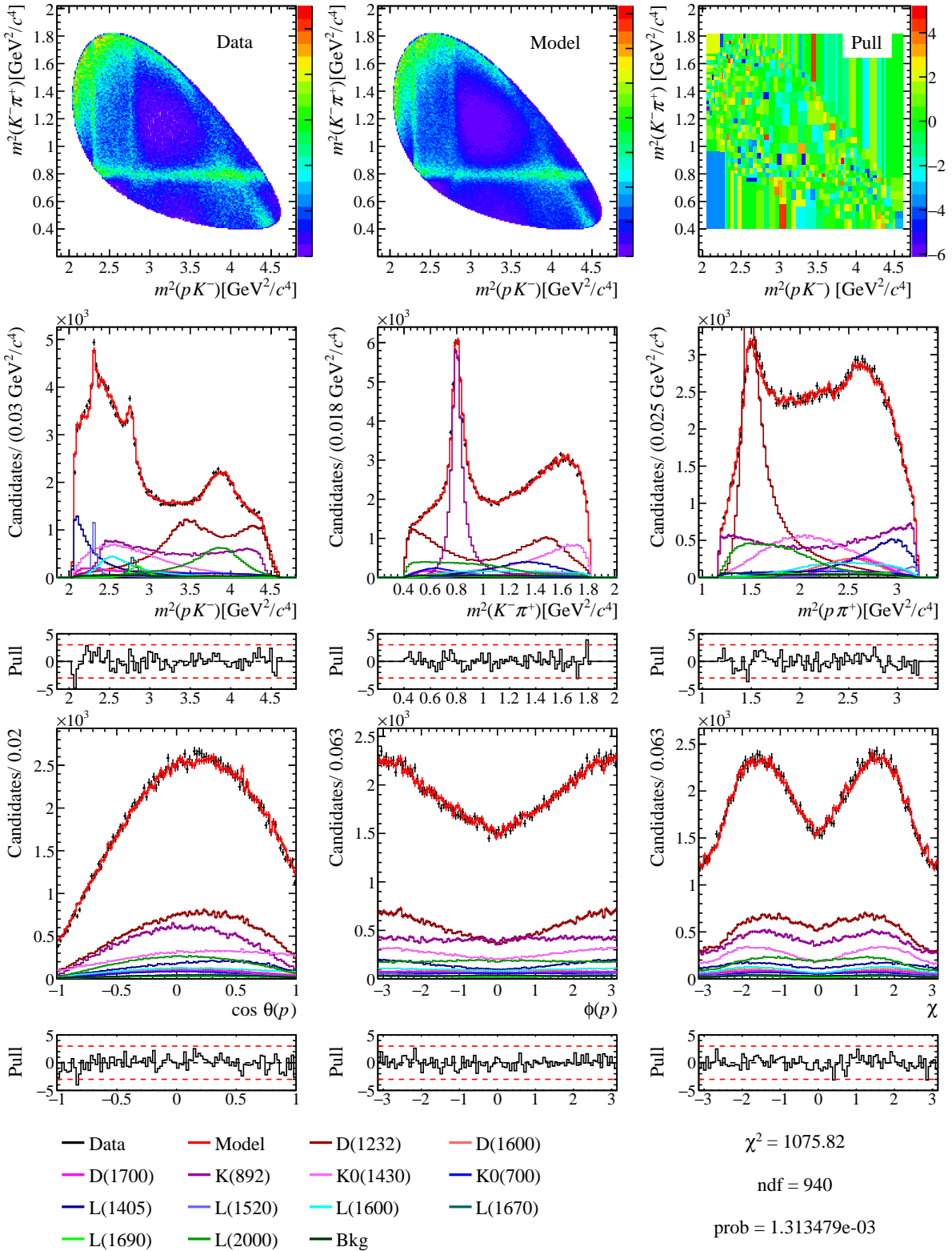


Figure 60: Phase space projections for the amplitude fit with nominal model selecting  $\Lambda_c^+ \rightarrow pK^-\pi^+$  candidates collected with MagDown polarity.

Parameter	Central Value	Pull
gammaK0(700)	0.91274	-0.3
ArK0(700)1	0.139884	0.22
AiK0(700)1	2.602766	0.26
ArK0(700)2	-2.767348	-0.23
AiK0(700)2	0.001152	-0.1
ArK(892)2	1.185011	-0.04
AiK(892)2	-1.040785	-0.09
ArK(892)3	-3.21498	-0.15
AiK(892)3	-3.288458	0.01
ArK(892)4	-0.69884	0.06
AiK(892)4	-4.246994	-0.21
gammaK0(1430)	0.020673	-0.01
ArK0(1430)1	-6.625833	0.06
AiK0(1430)1	10.399828	-0.06
ArK0(1430)2	-0.143075	-0.33
AiK0(1430)2	8.762502	0.02
ArL(1405)1	-4.530902	0.06
AiL(1405)1	2.980059	-0.28
ArL(1405)2	10.741687	0.25
AiL(1405)2	3.032812	0.16
ML(1520)	1.518703	0.46
GL(1520)	0.015063	-0.12
ArL(1520)1	0.256511	-0.5
AiL(1520)1	0.121152	1.01
ArL(1520)2	-0.169461	-0.04
AiL(1520)2	1.554461	0.31
ArL(1600)1	4.937357	0.15
AiL(1600)1	3.091193	0.01
ArL(1600)2	-7.123871	-0.2
AiL(1600)2	0.913846	0.08
ArL(1670)1	-0.324327	0.21
AiL(1670)1	-0.196078	-0.72
ArL(1670)2	-0.617654	-0.34
AiL(1670)2	1.028934	0.13
ArL(1690)1	-0.597084	-1.47
AiL(1690)1	-0.132015	-0.16
ArL(1690)2	-2.943614	-0.76
AiL(1690)2	-0.483909	-0.41
ML(2000)	1.98736	-0.3
GL(2000)	0.172704	-1.17
ArL(2000)1	-7.821873	0.15
AiL(2000)1	-7.70559	-0.08
ArL(2000)2	-4.283772	0.08
AiL(2000)2	-4.065494	-0.43
ArD(1232)1	-6.807744	-0.04
AiD(1232)1	3.218786	0.2
ArD(1232)2	-13.507882	-0.38
AiD(1232)2	4.173852	-0.23
ArD(1600)1	11.601584	0.15
AiD(1600)1	-3.172299	-0.03
ArD(1600)2	6.36744	-0.37
AiD(1600)2	-1.059176	-0.06
ArD(1700)1	10.157901	-0.18
AiD(1700)1	1.444618	0.01
ArD(1700)2	12.943673	0.05
AiD(1700)2	1.700791	-0.26
Px	0.609978	0.71
Py	0.004212	0.95
Pz	-0.236398	1.25
$\chi^2$	11.10	
prob	1.00	

Table 35: Fit parameters returned by MINUIT for the amplitude fit with nominal model selecting  $A_c^+ \rightarrow pK^-\pi^+$  candidates collected with MagDown polarity. Pulls are computed with respect to nominal fit results using the final statistical uncertainties reported in Table 29. Fit parameters are defined in Sec. 6.8.

Resonance	Fit Fraction	Pull
$\Delta^{++}(1232)$	0.290737	1.14
$\Delta^{++}(1600)$	0.043818	-0.35
$\Delta^{++}(1700)$	0.037219	-0.64
$K^*(892)$	0.220419	-0.3
$K^*0(1430)$	0.140869	-0.78
$K^*0(700)$	0.030272	0.04
$\Lambda(1405)$	0.077766	0.17
$\Lambda(1520)$	0.019476	0.66
$\Lambda(1600)$	0.052148	0.11
$\Lambda(1670)$	0.012166	0.46
$\Lambda(1690)$	0.013852	1.53
$\Lambda(2000)$	0.097204	0.36
Sum	1.035946	

Table 36: Fit fractions for the amplitude fit with nominal model selecting  $\Lambda_c^+ \rightarrow pK^-\pi^+$  candidates collected with MagDown polarity. Pulls are computed with respect to nominal fit results using the final statistical uncertainties reported in Table 30.

Resonance	$\alpha$	Pull
Model	0.668289	0.88
$\Delta^{++}(1232)$	0.55737	0.49
$\Delta^{++}(1600)$	0.552474	0.75
$\Delta^{++}(1700)$	0.236197	0.42
$K^*(892)$	0.878003	0.31
$K^*0(1430)$	0.328725	-0.22
$K^*0(700)$	0.059822	-0.04
$\Lambda(1405)$	0.618108	0.53
$\Lambda(1520)$	0.936222	0.32
$\Lambda(1600)$	0.206447	0.1
$\Lambda(1670)$	0.818654	0.03
$\Lambda(1690)$	0.919072	-1.39
$\Lambda(2000)$	0.551555	-0.58

Table 37: Decay asymmetry parameters for the amplitude fit with nominal model selecting  $\Lambda_c^+ \rightarrow pK^-\pi^+$  candidates collected with MagDown polarity. Pulls are computed with respect to nominal fit results using the final statistical uncertainties reported in Table 31.

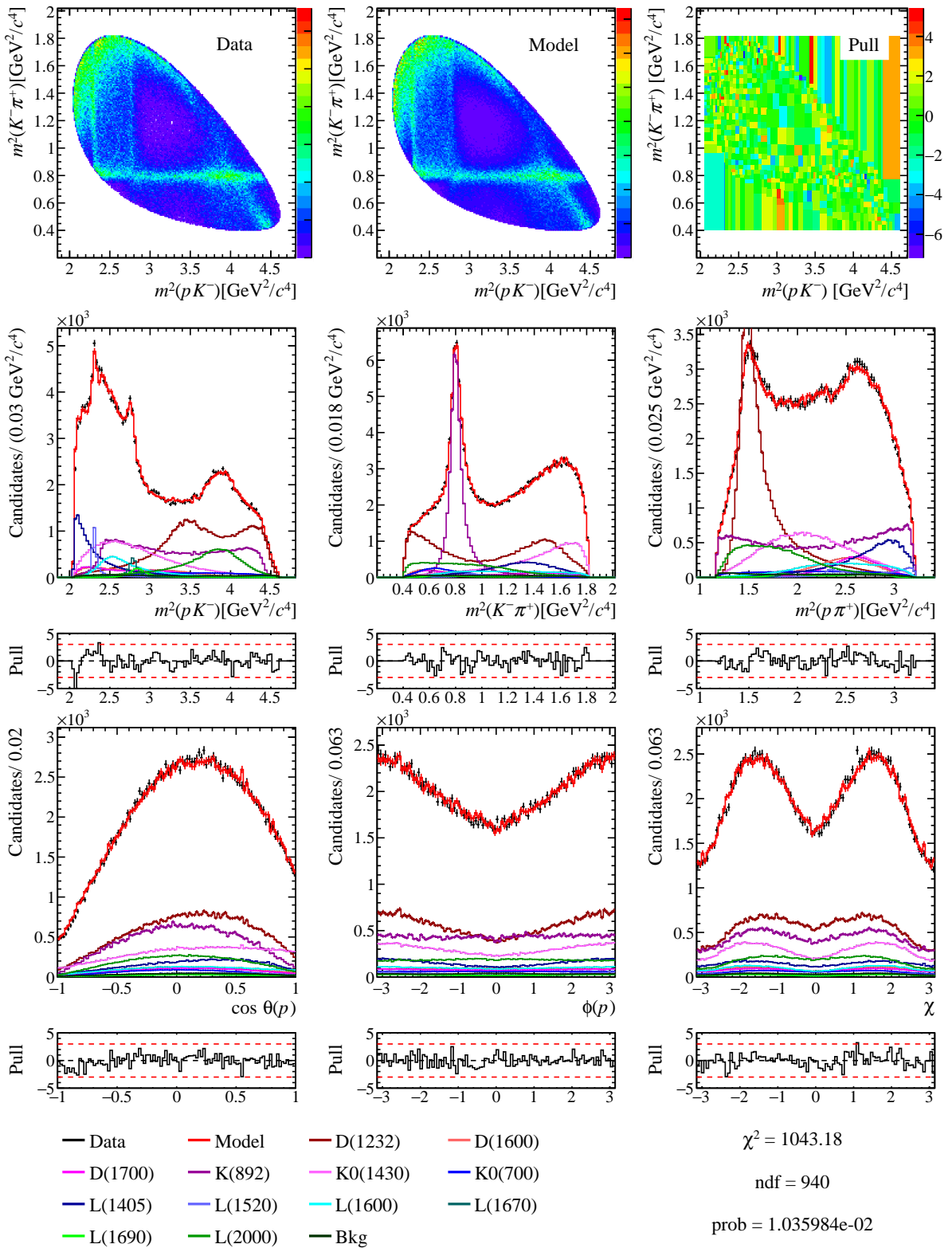


Figure 61: Phase space projections for the amplitude fit with nominal model selecting  $\Lambda_c^+ \rightarrow pK^-\pi^+$  candidates collected with MagUp polarity.

Parameter	Central Value	Pull
gammaK0(700)	0.991477	0.53
ArK0(700)1	0.060957	-0.02
AiK0(700)1	2.470734	-0.16
ArK0(700)2	-2.55451	0.37
AiK0(700)2	0.107155	0.19
ArK(892)2	1.179715	-0.07
AiK(892)2	-1.069224	-0.25
ArK(892)3	-3.127221	0.03
AiK(892)3	-3.232306	0.12
ArK(892)4	-0.851697	-0.26
AiK(892)4	-4.06751	0.2
gammaK0(1430)	0.022554	0.06
ArK0(1430)1	-6.569834	0.1
AiK0(1430)1	10.700587	0.16
ArK0(1430)2	0.598808	0.35
AiK0(1430)2	8.658388	-0.09
ArL(1405)1	-4.672136	-0.14
AiL(1405)1	3.439883	0.33
ArL(1405)2	10.26233	-0.16
AiL(1405)2	2.324977	-0.31
ML(1520)	1.518111	-0.7
GL(1520)	0.015115	-0.07
ArL(1520)1	0.331773	0.5
AiL(1520)1	-0.038641	-1.1
ArL(1520)2	-0.107607	0.27
AiL(1520)2	1.432584	-0.37
ArL(1600)1	4.696678	-0.22
AiL(1600)1	2.918057	-0.22
ArL(1600)2	-6.85413	0.15
AiL(1600)2	0.857354	0.02
ArL(1670)1	-0.372239	-0.45
AiL(1670)1	-0.08892	0.78
ArL(1670)2	-0.510901	0.43
AiL(1670)2	1.001908	-0.08
ArL(1690)1	-0.207354	1.24
AiL(1690)1	-0.078434	0.24
ArL(1690)2	-2.555784	0.62
AiL(1690)2	-0.221902	0.41
ML(2000)	1.988791	0.21
GL(2000)	0.184886	1.01
ArL(2000)1	-8.342995	-0.26
AiL(2000)1	-7.291422	0.27
ArL(2000)2	-4.406423	-0.1
AiL(2000)2	-3.540212	0.41
ArD(1232)1	-6.765846	0.02
AiD(1232)1	3.083099	0.04
ArD(1232)2	-12.419325	0.41
AiD(1232)2	5.044617	0.33
ArD(1600)1	11.214131	-0.14
AiD(1600)1	-3.231804	-0.07
ArD(1600)2	6.994455	0.27
AiD(1600)2	-1.136004	-0.14
ArD(1700)1	10.532595	0.13
AiD(1700)1	1.347142	-0.07
ArD(1700)2	12.811364	-0.04
AiD(1700)2	2.225571	0.08
Px	0.597481	-0.6
Py	-0.010955	-0.79
Pz	-0.255602	-1.02
$\chi^2$	10.38	
prob	1.0	

Table 38: Fit parameters returned by MINUIT for the amplitude fit with nominal model selecting  $\Lambda_c^+ \rightarrow p K^- \pi^+$  candidates collected with MagUp polarity. Pulls are computed with respect to nominal fit results using the final statistical uncertainties reported in Table 29. Fit parameters are defined in Sec. 6.8.

Resonance	Fit Fraction	Pull
$\Delta^{++}(1232)$	0.282162	-0.92
$\Delta^{++}(1600)$	0.046458	0.33
$\Delta^{++}(1700)$	0.040322	0.46
$K^*(892)$	0.222069	0.21
$K^*0(1430)$	0.152233	0.64
$K^*0(700)$	0.030268	0.04
$\Lambda(1405)$	0.077268	0.03
$\Lambda(1520)$	0.017692	-0.72
$\Lambda(1600)$	0.050593	-0.38
$\Lambda(1670)$	0.011488	-0.36
$\Lambda(1690)$	0.010497	-1.16
$\Lambda(2000)$	0.094195	-0.42
Sum	1.035245	

Table 39: Fit fractions for the amplitude fit with nominal model selecting  $\Lambda_c^+ \rightarrow pK^-\pi^+$  candidates collected with MagUp polarity. Pulls are computed with respect to nominal fit results using the final statistical uncertainties reported in Table 30.

Resonance	$\alpha$	Pull
Model	0.656374	-0.88
$\Delta^{++}(1232)$	0.528848	-0.9
$\Delta^{++}(1600)$	0.461045	-0.61
$\Delta^{++}(1700)$	0.199754	-0.32
$K^*(892)$	0.868358	-0.35
$K^*0(1430)$	0.353288	0.3
$K^*0(700)$	0.033919	-0.38
$\Lambda(1405)$	0.533799	-0.64
$\Lambda(1520)$	0.897355	-0.79
$\Lambda(1600)$	0.218979	0.27
$\Lambda(1670)$	0.792495	-0.4
$\Lambda(1690)$	0.984876	0.95
$\Lambda(2000)$	0.587353	0.39

Table 40: Decay asymmetry parameters for the amplitude fit with nominal model selecting  $\Lambda_c^+ \rightarrow pK^-\pi^+$  candidates collected with MagUp polarity. Pulls are computed with respect to nominal fit results using the final statistical uncertainties reported in Table 31.

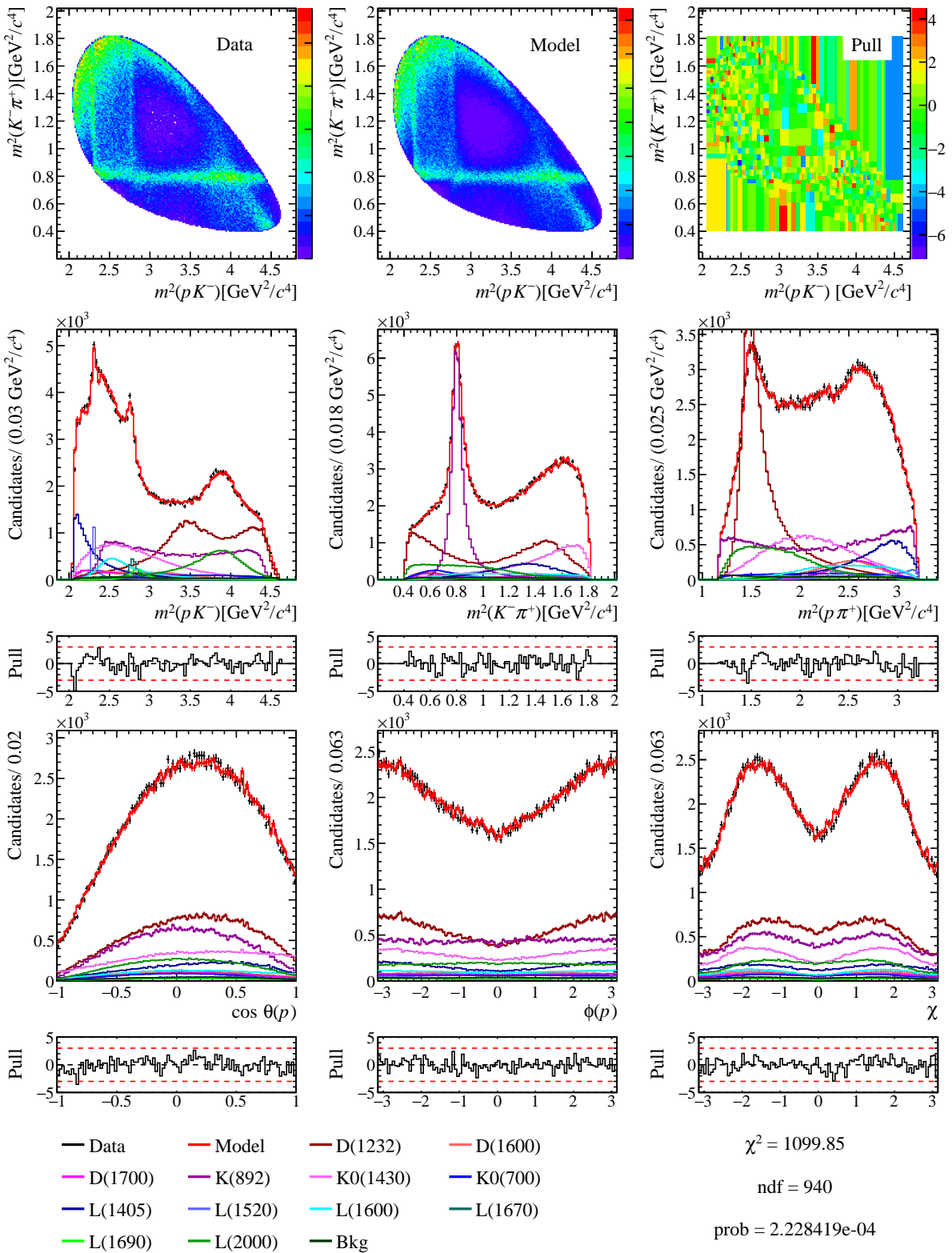


Figure 62: Phase space projections for the amplitude fit with nominal model selecting  $\Lambda_c^+$ -only candidates.

Parameter	Central Value	Pull
gammaK0(700)	0.887258	-0.57
ArK0(700)1	0.072997	0.01
AiK0(700)1	2.580396	0.19
ArK0(700)2	-2.705528	-0.06
AiK0(700)2	-0.01667	-0.15
ArK(892)2	1.205029	0.07
AiK(892)2	-1.080793	-0.32
ArK(892)3	-3.210542	-0.14
AiK(892)3	-3.09311	0.41
ArK(892)4	-0.811374	-0.17
AiK(892)4	-4.033214	0.27
gammaK0(1430)	0.027828	0.28
ArK0(1430)1	-6.323827	0.28
AiK0(1430)1	10.289853	-0.14
ArK0(1430)2	-0.02547	-0.22
AiK0(1430)2	8.711782	-0.03
ArL(1405)1	-4.713905	-0.19
AiL(1405)1	3.051313	-0.18
ArL(1405)2	10.436951	-0.01
AiL(1405)2	2.569965	-0.15
ML(1520)	1.518186	-0.55
GL(1520)	0.014668	-0.48
ArL(1520)1	0.306175	0.16
AiL(1520)1	-0.050117	-1.25
ArL(1520)2	-0.120416	0.2
AiL(1520)2	1.412951	-0.48
ArL(1600)1	4.672309	-0.26
AiL(1600)1	2.772364	-0.41
ArL(1600)2	-6.934572	0.05
AiL(1600)2	0.863836	0.02
ArL(1670)1	-0.414833	-1.04
AiL(1670)1	-0.114805	0.42
ArL(1670)2	-0.506996	0.46
AiL(1670)2	1.016387	0.03
ArL(1690)1	-0.205097	1.26
AiL(1690)1	-0.145432	-0.27
ArL(1690)2	-2.67658	0.19
AiL(1690)2	-0.260598	0.29
ML(2000)	1.99152	1.19
GL(2000)	0.179912	0.12
ArL(2000)1	-7.779616	0.19
AiL(2000)1	-7.551862	0.05
ArL(2000)2	-4.039597	0.43
AiL(2000)2	-4.00736	-0.34
ArD(1232)1	-6.567816	0.28
AiD(1232)1	3.039135	-0.02
ArD(1232)2	-12.617708	0.27
AiD(1232)2	4.64984	0.08
ArD(1600)1	10.951545	-0.34
AiD(1600)1	-3.366372	-0.17
ArD(1600)2	6.262897	-0.48
AiD(1600)2	-1.407334	-0.44
ArD(1700)1	9.71231	-0.55
AiD(1700)1	1.272522	-0.12
ArD(1700)2	12.300462	-0.39
AiD(1700)2	1.604508	-0.32
Px	0.607791	0.48
Py	6.2e-05	0.48
Pz	-0.244751	0.26
$\chi^2$	10.54	
prob	1.0	

Table 41: Fit parameters returned by MINUIT for the amplitude fit with nominal model selecting  $\Lambda_c^+$ -only candidates. Pulls are computed with respect to nominal fit results using the final statistical uncertainties reported in Table 29. Fit parameters are defined in Sec. 6.8.

Resonance	Fit Fraction	Pull
$\Delta^{++}(1232)$	0.284879	-0.27
$\Delta^{++}(1600)$	0.043729	-0.38
$\Delta^{++}(1700)$	0.03636	-0.95
$K^*(892)$	0.222544	0.36
$K^*0(1430)$	0.148083	0.12
$K^*0(700)$	0.030808	0.28
$\Lambda(1405)$	0.080069	0.84
$\Lambda(1520)$	0.017981	-0.49
$\Lambda(1600)$	0.05151	-0.09
$\Lambda(1670)$	0.012217	0.52
$\Lambda(1690)$	0.01175	-0.15
$\Lambda(2000)$	0.094899	-0.23
Sum	1.034829	

Table 42: Fit fractions for the amplitude fit with nominal model selecting  $\Lambda_c^+$ -only candidates. Pulls are computed with respect to nominal fit results using the final statistical uncertainties reported in Table 30.

Resonance	$\alpha$	Pull
Model	0.658889	-0.5
$\Delta^{++}(1232)$	0.55021	0.14
$\Delta^{++}(1600)$	0.521925	0.29
$\Delta^{++}(1700)$	0.231725	0.33
$K^*(892)$	0.86514	-0.57
$K^*0(1430)$	0.315437	-0.5
$K^*0(700)$	0.046955	-0.21
$\Lambda(1405)$	0.571273	-0.12
$\Lambda(1520)$	0.908547	-0.47
$\Lambda(1600)$	0.246602	0.65
$\Lambda(1670)$	0.748916	-1.13
$\Lambda(1690)$	0.982359	0.86
$\Lambda(2000)$	0.568457	-0.12

Table 43: Decay asymmetry parameters for the amplitude fit with nominal model selecting  $\Lambda_c^+$ -only candidates. Pulls are computed with respect to nominal fit results using the final statistical uncertainties reported in Table 31.

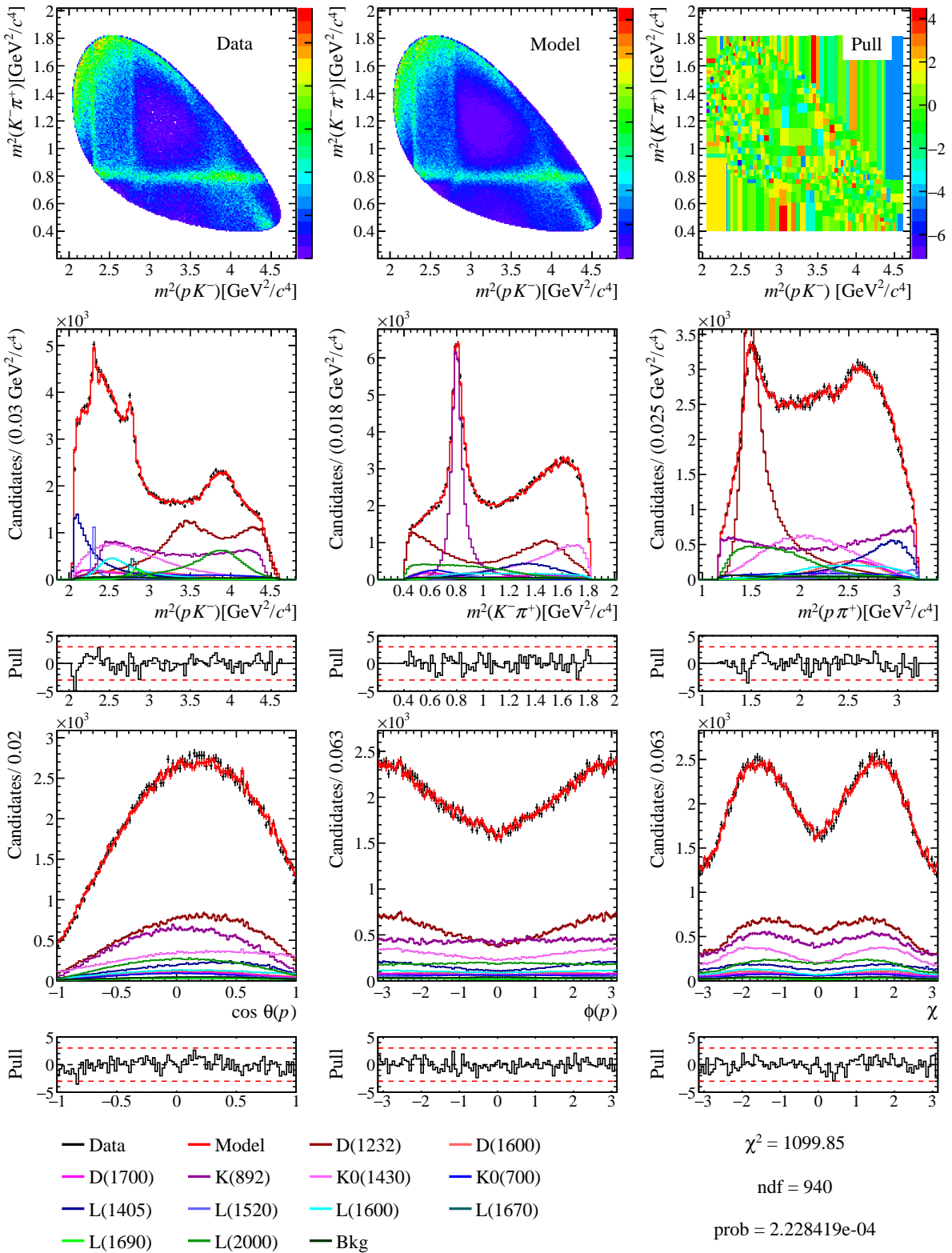


Figure 63: Phase space projections for the amplitude fit with nominal model selecting  $\bar{\Lambda}_c^-$ -only candidates.

Parameter	Central Value	Pull
gammaK0(700)	1.03033	0.95
ArK0(700)1	0.039441	-0.09
AiK0(700)1	2.426927	-0.3
ArK0(700)2	-2.59953	0.24
AiK0(700)2	0.101018	0.17
ArK(892)2	1.164818	-0.15
AiK(892)2	-0.98193	0.25
ArK(892)3	-3.08895	0.1
AiK(892)3	-3.480687	-0.38
ArK(892)4	-0.652888	0.15
AiK(892)4	-4.290483	-0.3
gammaK0(1430)	0.011276	-0.39
ArK0(1430)1	-7.131413	-0.3
AiK0(1430)1	10.740185	0.19
ArK0(1430)2	0.557124	0.31
AiK0(1430)2	8.74811	0.01
ArL(1405)1	-4.465155	0.15
AiL(1405)1	3.398024	0.28
ArL(1405)2	10.514657	0.06
AiL(1405)2	3.015811	0.15
ML(1520)	1.518777	0.61
GL(1520)	0.015803	0.55
ArL(1520)1	0.265356	-0.38
AiL(1520)1	0.151506	1.41
ArL(1520)2	-0.208036	-0.24
AiL(1520)2	1.59841	0.55
ArL(1600)1	4.974098	0.2
AiL(1600)1	3.396784	0.41
ArL(1600)2	-7.063382	-0.12
AiL(1600)2	0.877026	0.04
ArL(1670)1	-0.270279	0.96
AiL(1670)1	-0.160485	-0.22
ArL(1670)2	-0.630073	-0.43
AiL(1670)2	0.998576	-0.1
ArL(1690)1	-0.577334	-1.33
AiL(1690)1	-0.101713	0.06
ArL(1690)2	-2.796834	-0.24
AiL(1690)2	-0.464334	-0.35
ML(2000)	1.984669	-1.26
GL(2000)	0.177962	-0.23
ArL(2000)1	-8.271851	-0.2
AiL(2000)1	-7.629597	-0.01
ArL(2000)2	-4.6214	-0.41
AiL(2000)2	-3.523735	0.43
ArD(1232)1	-7.027219	-0.33
AiD(1232)1	3.091117	0.05
ArD(1232)2	-13.375409	-0.28
AiD(1232)2	4.419421	-0.07
ArD(1600)1	11.886758	0.37
AiD(1600)1	-2.857961	0.19
ArD(1600)2	7.190422	0.47
AiD(1600)2	-0.632416	0.4
ArD(1700)1	10.992076	0.51
AiD(1700)1	1.586003	0.11
ArD(1700)2	13.432643	0.38
AiD(1700)2	2.638151	0.34
Px	0.599132	-0.43
Py	-0.007558	-0.4
Pz	-0.249539	-0.31
$\chi^2$	12.21	
prob	1.0	

Table 44: Fit parameters returned by MINUIT for the amplitude fit with nominal model selecting  $\bar{\Lambda}_c^-$ -only candidates. Pulls are computed with respect to nominal fit results using the final statistical uncertainties reported in Table 29. Fit parameters are defined in Sec. 6.8.

Resonance	Fit Fraction	Pull
$\Delta^{++}(1232)$	0.286973	0.24
$\Delta^{++}(1600)$	0.046645	0.38
$\Delta^{++}(1700)$	0.04128	0.8
$K^*(892)$	0.220166	-0.38
$K^*0(1430)$	0.146016	-0.14
$K^*0(700)$	0.029187	-0.44
$\Lambda(1405)$	0.075105	-0.6
$\Lambda(1520)$	0.019443	0.64
$\Lambda(1600)$	0.052169	0.12
$\Lambda(1670)$	0.011285	-0.61
$\Lambda(1690)$	0.012321	0.3
$\Lambda(2000)$	0.096261	0.12
Sum	1.036851	

Table 45: Fit fractions for the amplitude fit with nominal model selecting  $\bar{\Lambda}_c^-$ -only candidates. Pulls are computed with respect to nominal fit results using the final statistical uncertainties reported in Table 30.

Resonance	$\alpha$	Pull
Model	0.665793	0.51
$\Delta^{++}(1232)$	0.541389	-0.29
$\Delta^{++}(1600)$	0.48278	-0.29
$\Delta^{++}(1700)$	0.206005	-0.2
$K^*(892)$	0.882902	0.65
$K^*0(1430)$	0.367582	0.6
$K^*0(700)$	0.069241	0.08
$\Lambda(1405)$	0.58345	0.05
$\Lambda(1520)$	0.930605	0.16
$\Lambda(1600)$	0.16544	-0.46
$\Lambda(1670)$	0.867659	0.85
$\Lambda(1690)$	0.917732	-1.44
$\Lambda(2000)$	0.579243	0.17

Table 46: Decay asymmetry parameters for the amplitude fit with nominal model selecting  $\bar{\Lambda}_c^-$ -only candidates. Pulls are computed with respect to nominal fit results using the final statistical uncertainties reported in Table 31.

Parameter	Central Value	Pull
gammaK0(700)	0.953402	0.13
ArK0(700)1	0.035344	-0.1
AiK0(700)1	2.289112	-0.73
ArK0(700)2	-2.448281	0.67
AiK0(700)2	0.031553	-0.02
ArK(892)2	1.066743	-0.69
AiK(892)2	-1.041785	-0.09
ArK(892)3	-2.810232	0.66
AiK(892)3	-3.096465	0.4
ArK(892)4	-0.737698	-0.02
AiK(892)4	-3.8394	0.71
gammaK0(1430)	0.015284	-0.23
ArK0(1430)1	-6.06254	0.46
AiK0(1430)1	9.785043	-0.51
ArK0(1430)2	0.201531	-0.02
AiK0(1430)2	8.005151	-0.76
ArL(1405)1	-4.252359	0.44
AiL(1405)1	2.846311	-0.46
ArL(1405)2	9.863916	-0.49
AiL(1405)2	2.711975	-0.05
ML(1520)	1.518669	0.4
GL(1520)	0.015447	0.23
ArL(1520)1	0.295168	0.02
AiL(1520)1	0.057651	0.18
ArL(1520)2	-0.163641	-0.01
AiL(1520)2	1.399628	-0.55
ArL(1600)1	4.430041	-0.63
AiL(1600)1	2.621279	-0.61
ArL(1600)2	-6.474293	0.65
AiL(1600)2	0.728392	-0.13
ArL(1670)1	-0.301619	0.53
AiL(1670)1	-0.119691	0.35
ArL(1670)2	-0.534195	0.26
AiL(1670)2	0.934233	-0.59
ArL(1690)1	-0.389931	-0.03
AiL(1690)1	-0.082483	0.21
ArL(1690)2	-2.52509	0.73
AiL(1690)2	-0.366264	-0.04
ML(2000)	1.988177	-0.0
GL(2000)	0.178047	-0.22
ArL(2000)1	-7.402203	0.48
AiL(2000)1	-6.994909	0.53
ArL(2000)2	-3.892458	0.64
AiL(2000)2	-3.540174	0.41
ArD(1232)1	-6.083588	0.91
AiD(1232)1	2.747409	-0.37
ArD(1232)2	-12.13867	0.62
AiD(1232)2	4.131741	-0.26
ArD(1600)1	10.320868	-0.82
AiD(1600)1	-2.985719	0.1
ArD(1600)2	6.070481	-0.67
AiD(1600)2	-0.961247	0.04
ArD(1700)1	9.572884	-0.67
AiD(1700)1	1.055706	-0.29
ArD(1700)2	11.47738	-0.95
AiD(1700)2	1.711539	-0.25
$\chi^2$	12.65	
prob	1.0	

Table 47: Fit parameters returned by MINUIT for the amplitude fit with nominal model, with polarisation measured in the  $\Lambda_c^+$  helicity frame reached from the approximate  $\Lambda_b^0$  rest frame reconstructed using the “Full reconstruction” algorithm. Pulls are computed with respect to nominal fit results using the final statistical uncertainties reported in Table 29. Polarisation values are not compared because referring to different polarisation frames. Fit parameters are defined in Sec. 6.8.

Resonance	Fit Fraction	Pull
$\Delta^{++}(1232)$	0.286589	0.14
$\Delta^{++}(1600)$	0.0436	-0.41
$\Delta^{++}(1700)$	0.037155	-0.67
$K^*(892)$	0.222586	0.37
$K^*0(1430)$	0.145787	-0.16
$K^*0(700)$	0.02962	-0.25
$\Lambda(1405)$	0.079964	0.81
$\Lambda(1520)$	0.018868	0.19
$\Lambda(1600)$	0.050874	-0.29
$\Lambda(1670)$	0.011733	-0.07
$\Lambda(1690)$	0.01205	0.09
$\Lambda(2000)$	0.0957	-0.03
Sum	1.034526	

Table 48: Fit fractions for the amplitude fit with nominal model, with polarisation measured in the  $\Lambda_c^+$  helicity frame reached from the approximate  $\Lambda_b^0$  rest frame reconstructed using the “Full reconstruction” algorithm. Pulls are computed with respect to nominal fit results using the final statistical uncertainties reported in Table 30.

Resonance	$\alpha$	Pull
Model	0.668572	0.93
$\Delta^{++}(1232)$	0.572885	1.25
$\Delta^{++}(1600)$	0.506654	0.07
$\Delta^{++}(1700)$	0.184148	-0.64
$K^*(892)$	0.863963	-0.65
$K^*0(1430)$	0.347649	0.18
$K^*0(700)$	0.067109	0.06
$\Lambda(1405)$	0.599813	0.27
$\Lambda(1520)$	0.913103	-0.34
$\Lambda(1600)$	0.231411	0.44
$\Lambda(1670)$	0.8338	0.29
$\Lambda(1690)$	0.952343	-0.21
$\Lambda(2000)$	0.578974	0.16

Table 49: Decay asymmetry parameters for the amplitude fit with nominal model, with polarisation measured in the  $\Lambda_c^+$  helicity frame reached from the approximate  $\Lambda_b^0$  rest frame reconstructed using the “Full reconstruction” algorithm. Pulls are computed with respect to nominal fit results using the final statistical uncertainties reported in Table 31.

Parameter	Central Value	Pull
gammaK0(700)	0.93858	-0.03
ArK0(700)1	0.022646	-0.14
AiK0(700)1	2.280049	-0.76
ArK0(700)2	-2.43008	0.72
AiK0(700)2	0.058299	0.05
ArK(892)2	1.052461	-0.77
AiK(892)2	-1.039656	-0.08
ArK(892)3	-2.742634	0.79
AiK(892)3	-3.103361	0.39
ArK(892)4	-0.706763	0.04
AiK(892)4	-3.805224	0.78
gammaK0(1430)	0.014334	-0.27
ArK0(1430)1	-6.084784	0.45
AiK0(1430)1	9.669191	-0.59
ArK0(1430)2	0.199384	-0.02
AiK0(1430)2	7.916568	-0.86
ArL(1405)1	-4.244215	0.45
AiL(1405)1	2.787281	-0.53
ArL(1405)2	9.71131	-0.62
AiL(1405)2	2.781865	-0.0
ML(1520)	1.518624	0.31
GL(1520)	0.015449	0.23
ArL(1520)1	0.304763	0.14
AiL(1520)1	0.048655	0.06
ArL(1520)2	-0.165283	-0.02
AiL(1520)2	1.38325	-0.64
ArL(1600)1	4.450771	-0.6
AiL(1600)1	2.634823	-0.59
ArL(1600)2	-6.361192	0.8
AiL(1600)2	0.665379	-0.2
ArL(1670)1	-0.301522	0.53
AiL(1670)1	-0.104016	0.57
ArL(1670)2	-0.537159	0.24
AiL(1670)2	0.915069	-0.73
ArL(1690)1	-0.402047	-0.11
AiL(1690)1	-0.108668	0.01
ArL(1690)2	-2.511521	0.78
AiL(1690)2	-0.408117	-0.17
ML(2000)	1.988321	0.05
GL(2000)	0.178368	-0.16
ArL(2000)1	-7.266493	0.59
AiL(2000)1	-7.008131	0.51
ArL(2000)2	-3.897619	0.63
AiL(2000)2	-3.499512	0.47
ArD(1232)1	-6.071763	0.93
AiD(1232)1	2.689754	-0.44
ArD(1232)2	-12.044884	0.69
AiD(1232)2	3.973336	-0.36
ArD(1600)1	10.123785	-0.96
AiD(1600)1	-2.898388	0.16
ArD(1600)2	6.008779	-0.74
AiD(1600)2	-0.955054	0.05
ArD(1700)1	9.427164	-0.79
AiD(1700)1	1.092168	-0.26
ArD(1700)2	11.319597	-1.05
AiD(1700)2	1.781636	-0.21
$\chi^2$	15.41	
prob	1.0	

Table 50: Fit parameters returned by MINUIT for the amplitude fit with nominal model, with polarisation measured in the  $\Lambda_c^+$  helicity frame reached from the approximate  $\Lambda_b^0$  rest frame reconstructed using the “Equal boost” algorithm. Pulls are computed with respect to nominal fit results using the final statistical uncertainties reported in Table 29. Polarisation values are not compared because referring to different polarisation frames. Fit parameters are defined in Sec. 6.8.

Resonance	Fit Fraction	Pull
$\Delta^{++}(1232)$	0.286632	0.15
$\Delta^{++}(1600)$	0.042919	-0.59
$\Delta^{++}(1700)$	0.03688	-0.76
$K^*(892)$	0.222762	0.43
$K^*0(1430)$	0.145969	-0.14
$K^*0(700)$	0.029436	-0.33
$\Lambda(1405)$	0.079662	0.72
$\Lambda(1520)$	0.01886	0.18
$\Lambda(1600)$	0.050909	-0.28
$\Lambda(1670)$	0.011621	-0.2
$\Lambda(1690)$	0.012246	0.24
$\Lambda(2000)$	0.09581	0.0
Sum	1.033706	

Table 51: Fit fractions for the amplitude fit with nominal model, with polarisation measured in the  $\Lambda_c^+$  helicity frame reached from the approximate  $\Lambda_b^0$  rest frame reconstructed using the “Equal boost” algorithm. Pulls are computed with respect to nominal fit results using the final statistical uncertainties reported in Table 30.

Resonance	$\alpha$	Pull
Model	0.667672	0.79
$\Delta^{++}(1232)$	0.569002	1.06
$\Delta^{++}(1600)$	0.499234	-0.04
$\Delta^{++}(1700)$	0.186187	-0.6
$K^*(892)$	0.862696	-0.74
$K^*0(1430)$	0.350795	0.25
$K^*0(700)$	0.063901	0.02
$\Lambda(1405)$	0.596699	0.23
$\Lambda(1520)$	0.906744	-0.53
$\Lambda(1600)$	0.209271	0.14
$\Lambda(1670)$	0.834856	0.3
$\Lambda(1690)$	0.947868	-0.37
$\Lambda(2000)$	0.576085	0.09

Table 52: Decay asymmetry parameters for the amplitude fit with nominal model, with polarisation measured in the  $\Lambda_c^+$  helicity frame reached from the approximate  $\Lambda_b^0$  rest frame reconstructed using the “Equal boost” algorithm. Pulls are computed with respect to nominal fit results using the final statistical uncertainties reported in Table 31.

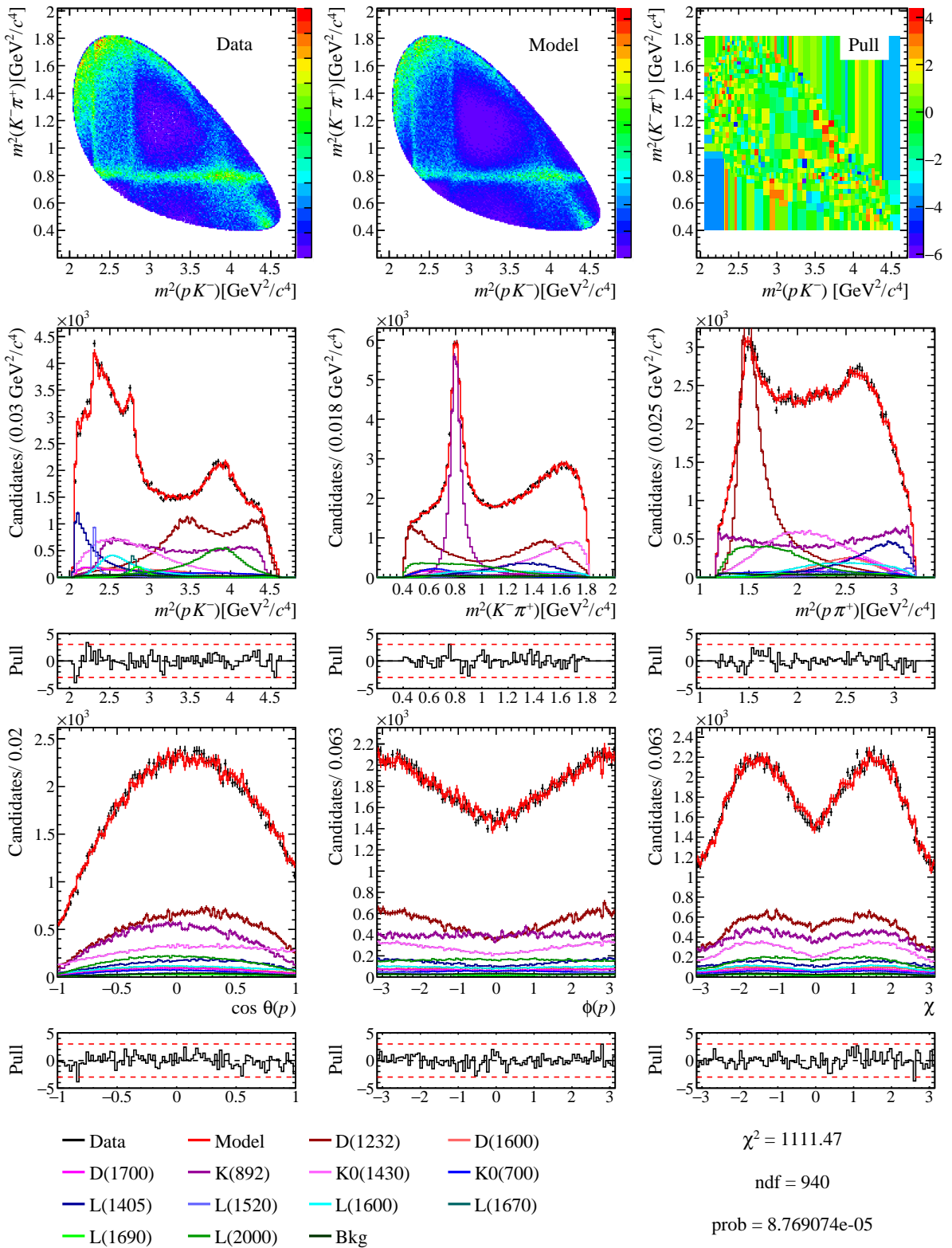


Figure 64: Phase space projections for the amplitude fit with nominal model selecting candidates having  $p_T(\Lambda_c^+) > 5$  GeV.

Parameter	Central Value	Pull
gammaK0(700)	0.932589	-0.09
ArK0(700)1	-0.064737	-0.41
AiK0(700)1	2.347292	-0.55
ArK0(700)2	-2.894494	-0.59
AiK0(700)2	0.09135	0.15
ArK(892)2	1.232986	0.22
AiK(892)2	-0.942868	0.48
ArK(892)3	-3.261079	-0.24
AiK(892)3	-3.415524	-0.25
ArK(892)4	-0.676359	0.1
AiK(892)4	-4.231854	-0.17
gammaK0(1430)	0.042577	0.87
ArK0(1430)1	-7.871303	-0.82
AiK0(1430)1	10.314681	-0.12
ArK0(1430)2	-0.164587	-0.35
AiK0(1430)2	9.077995	0.35
ArL(1405)1	-5.209093	-0.87
AiL(1405)1	3.627007	0.58
ArL(1405)2	10.336804	-0.09
AiL(1405)2	2.646839	-0.09
ML(1520)	1.5177	-1.51
GL(1520)	0.015674	0.43
ArL(1520)1	0.341531	0.63
AiL(1520)1	-0.033072	-1.02
ArL(1520)2	-0.008119	0.77
AiL(1520)2	1.52634	0.15
ArL(1600)1	4.724077	-0.18
AiL(1600)1	3.309122	0.3
ArL(1600)2	-7.299051	-0.43
AiL(1600)2	0.522748	-0.36
ArL(1670)1	-0.364157	-0.34
AiL(1670)1	-0.091486	0.74
ArL(1670)2	-0.609083	-0.27
AiL(1670)2	1.030579	0.14
ArL(1690)1	-0.322995	0.44
AiL(1690)1	-0.147174	-0.28
ArL(1690)2	-2.775139	-0.16
AiL(1690)2	-0.418538	-0.2
ML(2000)	1.989815	0.58
GL(2000)	0.174346	-0.88
ArL(2000)1	-7.385818	0.5
AiL(2000)1	-7.964594	-0.3
ArL(2000)2	-4.072065	0.38
AiL(2000)2	-3.858463	-0.1
ArD(1232)1	-7.241842	-0.61
AiD(1232)1	3.029462	-0.03
ArD(1232)2	-13.219959	-0.17
AiD(1232)2	4.517609	-0.01
ArD(1600)1	11.774679	0.28
AiD(1600)1	-2.773109	0.24
ArD(1600)2	7.128447	0.41
AiD(1600)2	-0.458522	0.59
ArD(1700)1	10.318437	-0.05
AiD(1700)1	1.280482	-0.12
ArD(1700)2	13.185886	0.21
AiD(1700)2	2.38794	0.18
$\chi^2$	12.89	
prob	1.0	

Table 53: Fit parameters returned by MINUIT for the amplitude fit with nominal model selecting candidates having  $p_T(\Lambda_c^+) > 5 \text{ GeV}$ . Pulls are computed with respect to nominal fit results using the final statistical uncertainties reported in Table 29. Polarisation values are not included in the  $\chi^2$  test since they may differ due to different  $\Lambda_c^+$  kinematic requirements. Fit parameters are defined in Sec. 6.8.

Resonance	Fit Fraction	Pull
$\Delta^{++}(1232)$	0.288043	0.49
$\Delta^{++}(1600)$	0.045943	0.2
$\Delta^{++}(1700)$	0.038444	-0.21
$K^*(892)$	0.222826	0.45
$K^*0(1430)$	0.155723	1.08
$K^*0(700)$	0.02938	-0.35
$\Lambda(1405)$	0.077053	-0.03
$\Lambda(1520)$	0.017892	-0.56
$\Lambda(1600)$	0.052405	0.2
$\Lambda(1670)$	0.011967	0.22
$\Lambda(1690)$	0.011833	-0.09
$\Lambda(2000)$	0.090675	-1.33
Sum	1.042185	

Table 54: Fit fractions for the amplitude fit with nominal model selecting candidates having  $p_T(\Lambda_c^+) > 5 \text{ GeV}$ . Pulls are computed with respect to nominal fit results using the final statistical uncertainties reported in Table 30.

Resonance	$\alpha$	Pull
Model	0.659501	-0.41
$\Delta^{++}(1232)$	0.51948	-1.35
$\Delta^{++}(1600)$	0.482677	-0.29
$\Delta^{++}(1700)$	0.248243	0.66
$K^*(892)$	0.879383	0.41
$K^*0(1430)$	0.342466	0.07
$K^*0(700)$	0.206717	1.88
$\Lambda(1405)$	0.477325	-1.42
$\Lambda(1520)$	0.903663	-0.61
$\Lambda(1600)$	0.233665	0.47
$\Lambda(1670)$	0.820967	0.07
$\Lambda(1690)$	0.968248	0.36
$\Lambda(2000)$	0.57924	0.17

Table 55: Decay asymmetry parameters for the amplitude fit with nominal model selecting candidates having  $p_T(\Lambda_c^+) > 5 \text{ GeV}$ . Pulls are computed with respect to nominal fit results using the final statistical uncertainties reported in Table 31.

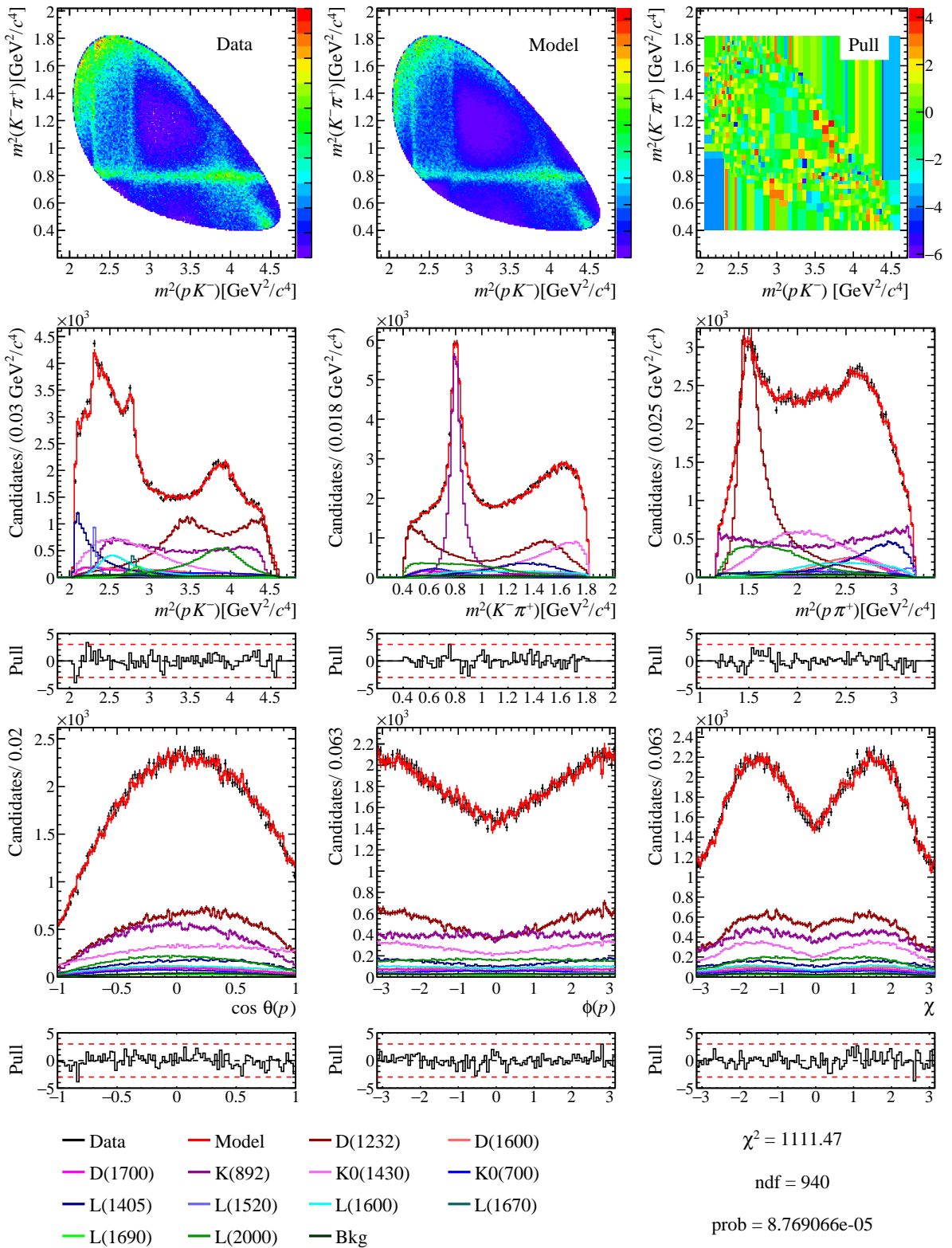


Figure 65: Phase space projections for the amplitude fit with nominal model selecting candidates having  $p_T(\Lambda_c^+) \leq 5$  GeV.

Parameter	Central Value	Pull
gammaK0(700)	0.933209	-0.08
ArK0(700)1	0.211975	0.44
AiK0(700)1	2.593162	0.23
ArK0(700)2	-2.45152	0.66
AiK0(700)2	0.01529	-0.06
ArK(892)2	1.121871	-0.39
AiK(892)2	-1.064703	-0.23
ArK(892)3	-2.925531	0.43
AiK(892)3	-3.06778	0.46
ArK(892)4	-0.706049	0.04
AiK(892)4	-3.938561	0.48
gammaK0(1430)	-0.000966	-0.88
ArK0(1430)1	-5.519848	0.85
AiK0(1430)1	10.122283	-0.26
ArK0(1430)2	0.381314	0.15
AiK0(1430)2	8.164209	-0.6
ArL(1405)1	-4.150677	0.57
AiL(1405)1	2.833148	-0.47
ArL(1405)2	10.071062	-0.32
AiL(1405)2	2.990029	0.14
ML(1520)	1.518953	0.96
GL(1520)	0.015037	-0.14
ArL(1520)1	0.240842	-0.71
AiL(1520)1	0.10816	0.84
ArL(1520)2	-0.2827	-0.62
AiL(1520)2	1.435586	-0.35
ArL(1600)1	4.739456	-0.15
AiL(1600)1	2.787024	-0.39
ArL(1600)2	-6.376	0.78
AiL(1600)2	0.988188	0.16
ArL(1670)1	-0.328408	0.15
AiL(1670)1	-0.172299	-0.39
ArL(1670)2	-0.53581	0.25
AiL(1670)2	0.949789	-0.47
ArL(1690)1	-0.423259	-0.26
AiL(1690)1	-0.070255	0.3
ArL(1690)2	-2.65819	0.26
AiL(1690)2	-0.383649	-0.09
ML(2000)	1.98641	-0.64
GL(2000)	0.181677	0.43
ArL(2000)1	-8.051232	-0.03
AiL(2000)1	-6.899301	0.61
ArL(2000)2	-4.45321	-0.17
AiL(2000)2	-3.618242	0.28
ArD(1232)1	-6.21065	0.75
AiD(1232)1	3.060456	0.01
ArD(1232)2	-12.406741	0.42
AiD(1232)2	4.094577	-0.28
ArD(1600)1	10.801201	-0.45
AiD(1600)1	-3.328879	-0.14
ArD(1600)2	6.15927	-0.58
AiD(1600)2	-1.348573	-0.37
ArD(1700)1	9.879466	-0.41
AiD(1700)1	1.46405	0.02
ArD(1700)2	11.967379	-0.61
AiD(1700)2	1.688024	-0.27
$\chi^2$	11.51	
prob	1.0	

Table 56: Fit parameters returned by MINUIT for the amplitude fit with nominal model selecting candidates having  $p_T(\Lambda_c^+) \leq 5$  GeV. Pulls are computed with respect to nominal fit results using the final statistical uncertainties reported in Table 29. Polarisation values are not included in the  $\chi^2$  test since they may differ due to different  $\Lambda_c^+$  kinematic requirements. Fit parameters are defined in Sec. 6.8.

Resonance	Fit Fraction	Pull
$\Delta^{++}(1232)$	0.284907	-0.26
$\Delta^{++}(1600)$	0.045303	0.03
$\Delta^{++}(1700)$	0.038165	-0.31
$K^*(892)$	0.219489	-0.59
$K^*0(1430)$	0.138742	-1.04
$K^*0(700)$	0.031399	0.54
$\Lambda(1405)$	0.078766	0.46
$\Lambda(1520)$	0.019651	0.8
$\Lambda(1600)$	0.050396	-0.44
$\Lambda(1670)$	0.011722	-0.08
$\Lambda(1690)$	0.01271	0.61
$\Lambda(2000)$	0.098876	0.8
Sum	1.030126	

Table 57: Fit fractions for the amplitude fit with nominal model selecting candidates having  $p_T(\Lambda_c^+) \leq 5$  GeV. Pulls are computed with respect to nominal fit results using the final statistical uncertainties reported in Table 30.

Resonance	$\alpha$	Pull
Model	0.662062	-0.04
$\Delta^{++}(1232)$	0.560829	0.66
$\Delta^{++}(1600)$	0.525046	0.34
$\Delta^{++}(1700)$	0.188314	-0.55
$K^*(892)$	0.863987	-0.65
$K^*0(1430)$	0.330989	-0.17
$K^*0(700)$	0.059432	-0.04
$\Lambda(1405)$	0.627654	0.66
$\Lambda(1520)$	0.936926	0.34
$\Lambda(1600)$	0.15867	-0.55
$\Lambda(1670)$	0.792665	-0.4
$\Lambda(1690)$	0.949912	-0.29
$\Lambda(2000)$	0.547297	-0.7

Table 58: Decay asymmetry parameters for the amplitude fit with nominal model selecting candidates having  $p_T(\Lambda_c^+) \leq 5$  GeV. Pulls are computed with respect to nominal fit results using the final statistical uncertainties reported in Table 31.

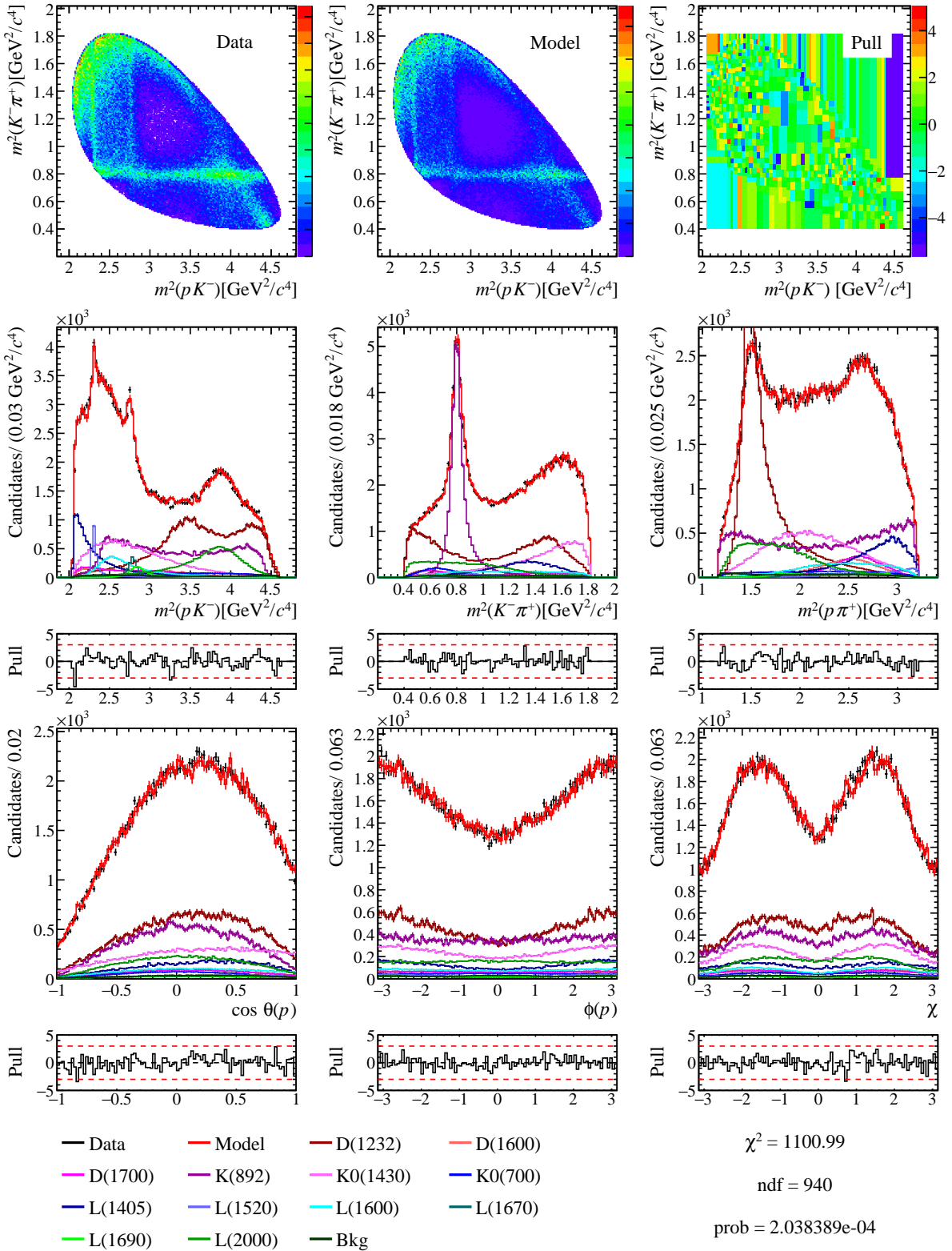


Figure 66: Phase space projections for the amplitude fit with nominal model selecting candidates having  $\tau(\Lambda_c^+) > 0.2$  ps.

Parameter	Central Value	Pull
gammaK0(700)	1.048853	1.14
ArK0(700)1	0.061529	-0.02
AiK0(700)1	2.445128	-0.24
ArK0(700)2	-2.697159	-0.03
AiK0(700)2	0.242484	0.56
ArK(892)2	0.995988	-1.08
AiK(892)2	-1.439508	-2.4
ArK(892)3	-3.362575	-0.44
AiK(892)3	-3.335847	-0.09
ArK(892)4	-1.25372	-1.09
AiK(892)4	-4.38517	-0.51
gammaK0(1430)	0.016352	-0.19
ArK0(1430)1	-6.53591	0.13
AiK0(1430)1	11.719788	0.9
ArK0(1430)2	0.228976	0.01
AiK0(1430)2	9.372398	0.66
ArL(1405)1	-4.811965	-0.33
AiL(1405)1	3.414764	0.3
ArL(1405)2	11.351088	0.77
AiL(1405)2	1.706058	-0.73
ML(1520)	1.518564	0.19
GL(1520)	0.014915	-0.25
ArL(1520)1	0.226447	-0.9
AiL(1520)1	-0.000356	-0.59
ArL(1520)2	-0.096471	0.32
AiL(1520)2	1.550605	0.29
ArL(1600)1	5.276922	0.67
AiL(1600)1	2.777085	-0.4
ArL(1600)2	-7.176394	-0.27
AiL(1600)2	1.22694	0.43
ArL(1670)1	-0.346684	-0.1
AiL(1670)1	-0.086821	0.81
ArL(1670)2	-0.55729	0.1
AiL(1670)2	1.129325	0.89
ArL(1690)1	-0.856604	-3.28
AiL(1690)1	-0.252996	-1.08
ArL(1690)2	-2.894978	-0.59
AiL(1690)2	-0.260758	0.29
ML(2000)	1.98769	-0.18
GL(2000)	0.175689	-0.64
ArL(2000)1	-8.791946	-0.62
AiL(2000)1	-7.482456	0.11
ArL(2000)2	-4.587822	-0.36
AiL(2000)2	-4.173042	-0.6
ArD(1232)1	-6.922646	-0.19
AiD(1232)1	3.950261	1.08
ArD(1232)2	-13.517597	-0.39
AiD(1232)2	5.378947	0.55
ArD(1600)1	11.883783	0.36
AiD(1600)1	-3.371065	-0.17
ArD(1600)2	6.006337	-0.74
AiD(1600)2	-1.479343	-0.52
ArD(1700)1	11.49619	0.93
AiD(1700)1	0.577816	-0.65
ArD(1700)2	13.628981	0.51
AiD(1700)2	1.144703	-0.62
Px	0.60069	-0.26
Py	-0.000219	0.44
Pz	-0.240922	0.72
$\chi^2$	35.67	
prob	0.99	

Table 59: Fit parameters returned by MINUIT for the amplitude fit with nominal model selecting candidates having  $\tau(\Lambda_c^+) > 0.2$  ps. Pulls are computed with respect to nominal fit results using the final statistical uncertainties reported in Table 29. Fit parameters are defined in Sec. 6.8.

Resonance	Fit Fraction	Pull
$\Delta^{++}(1232)$	0.290744	1.14
$\Delta^{++}(1600)$	0.041851	-0.87
$\Delta^{++}(1700)$	0.040225	0.43
$K^*(892)$	0.225221	1.19
$K^*0(1430)$	0.153219	0.77
$K^*0(700)$	0.0296	-0.26
$\Lambda(1405)$	0.078434	0.37
$\Lambda(1520)$	0.017899	-0.56
$\Lambda(1600)$	0.050356	-0.45
$\Lambda(1670)$	0.012274	0.59
$\Lambda(1690)$	0.012879	0.75
$\Lambda(2000)$	0.098048	0.58
Sum	1.050751	

Table 60: Fit fractions for the amplitude fit with nominal model selecting candidates having  $\tau(\Lambda_c^+) > 0.2$  ps. Pulls are computed with respect to nominal fit results using the final statistical uncertainties reported in Table 30.

Resonance	$\alpha$	Pull
Model	0.665057	0.41
$\Delta^{++}(1232)$	0.53768	-0.47
$\Delta^{++}(1600)$	0.598701	1.43
$\Delta^{++}(1700)$	0.170637	-0.91
$K^*(892)$	0.878224	0.33
$K^*0(1430)$	0.343879	0.1
$K^*0(700)$	0.101495	0.51
$\Lambda(1405)$	0.582058	0.03
$\Lambda(1520)$	0.958329	0.96
$\Lambda(1600)$	0.197044	-0.03
$\Lambda(1670)$	0.850956	0.57
$\Lambda(1690)$	0.827226	-4.66
$\Lambda(2000)$	0.552444	-0.56

Table 61: Decay asymmetry parameters for the amplitude fit with nominal model selecting candidates having  $\tau(\Lambda_c^+) > 0.2$  ps. Pulls are computed with respect to nominal fit results using the final statistical uncertainties reported in Table 31.

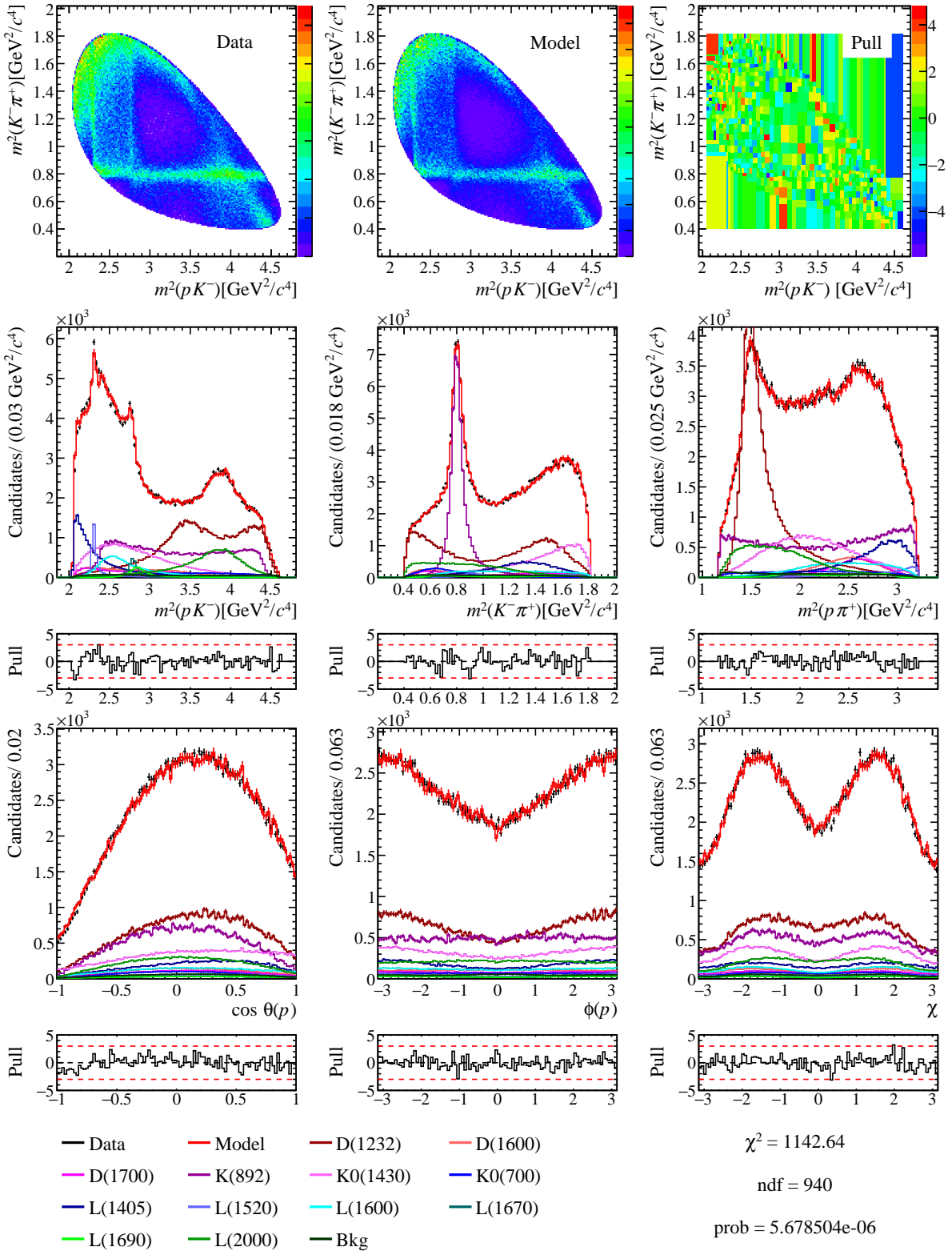


Figure 67: Phase space projections for the amplitude fit with nominal model selecting candidates having  $\tau(\Lambda_c^+) \leq 0.2$  ps.

Parameter	Central Value	Pull
gammaK0(700)	0.893067	-0.51
ArK0(700)1	0.077315	0.03
AiK0(700)1	2.54553	0.08
ArK0(700)2	-2.623206	0.18
AiK0(700)2	-0.110946	-0.41
ArK(892)2	1.2718	0.44
AiK(892)2	-0.801667	1.3
ArK(892)3	-3.026186	0.23
AiK(892)3	-3.234865	0.12
ArK(892)4	-0.429231	0.62
AiK(892)4	-3.988196	0.37
gammaK0(1430)	0.027182	0.25
ArK0(1430)1	-6.74973	-0.02
AiK0(1430)1	9.642886	-0.61
ArK0(1430)2	0.169331	-0.05
AiK0(1430)2	8.364286	-0.39
ArL(1405)1	-4.569544	0.0
AiL(1405)1	3.152783	-0.05
ArL(1405)2	9.880009	-0.48
AiL(1405)2	3.450213	0.44
ML(1520)	1.518324	-0.28
GL(1520)	0.015279	0.08
ArL(1520)1	0.339629	0.61
AiL(1520)1	0.078909	0.46
ArL(1520)2	-0.18567	-0.13
AiL(1520)2	1.463144	-0.2
ArL(1600)1	4.51333	-0.5
AiL(1600)1	3.201911	0.16
ArL(1600)2	-6.910502	0.08
AiL(1600)2	0.619217	-0.25
ArL(1670)1	-0.349349	-0.14
AiL(1670)1	-0.173863	-0.41
ArL(1670)2	-0.579464	-0.06
AiL(1670)2	0.928811	-0.63
ArL(1690)1	-0.099421	2.0
AiL(1690)1	0.002097	0.85
ArL(1690)2	-2.654712	0.27
AiL(1690)2	-0.439631	-0.27
ML(2000)	1.988355	0.06
GL(2000)	0.180286	0.18
ArL(2000)1	-7.471343	0.43
AiL(2000)1	-7.51221	0.09
ArL(2000)2	-4.180096	0.22
AiL(2000)2	-3.604032	0.31
ArD(1232)1	-6.68174	0.13
AiD(1232)1	2.599097	-0.55
ArD(1232)2	-12.660445	0.24
AiD(1232)2	3.916785	-0.39
ArD(1600)1	11.113172	-0.22
AiD(1600)1	-3.007552	0.08
ArD(1600)2	7.012184	0.29
AiD(1600)2	-0.68069	0.35
ArD(1700)1	9.454447	-0.77
AiD(1700)1	1.870293	0.33
ArD(1700)2	12.155338	-0.49
AiD(1700)2	2.498889	0.25
Px	0.607841	0.48
Py	-0.004858	-0.09
Pz	-0.251561	-0.55
$\chi^2$	13.14	
prob	1.0	

Table 62: Fit parameters returned by MINUIT for the amplitude fit with nominal model selecting candidates having  $\tau(\Lambda_c^+) \leq 0.2$  ps. Pulls are computed with respect to nominal fit results using the final statistical uncertainties reported in Table 29. Fit parameters are defined in Sec. 6.8.

Resonance	Fit Fraction	Pull
$\Delta^{++}(1232)$	0.283338	-0.64
$\Delta^{++}(1600)$	0.047188	0.52
$\Delta^{++}(1700)$	0.036709	-0.83
$K^*(892)$	0.219215	-0.68
$K^*0(1430)$	0.142177	-0.62
$K^*0(700)$	0.030284	0.05
$\Lambda(1405)$	0.078058	0.26
$\Lambda(1520)$	0.019208	0.45
$\Lambda(1600)$	0.052899	0.35
$\Lambda(1670)$	0.011427	-0.44
$\Lambda(1690)$	0.01193	-0.01
$\Lambda(2000)$	0.093153	-0.69
Sum	1.025588	

Table 63: Fit fractions for the amplitude fit with nominal model selecting candidates having  $\tau(\Lambda_c^+) \leq 0.2$  ps. Pulls are computed with respect to nominal fit results using the final statistical uncertainties reported in Table 30.

Resonance	$\alpha$	Pull
Model	0.659978	-0.34
$\Delta^{++}(1232)$	0.546564	-0.03
$\Delta^{++}(1600)$	0.454887	-0.7
$\Delta^{++}(1700)$	0.247378	0.64
$K^*(892)$	0.867387	-0.41
$K^*0(1430)$	0.328639	-0.22
$K^*0(700)$	0.030492	-0.42
$\Lambda(1405)$	0.560847	-0.26
$\Lambda(1520)$	0.894074	-0.89
$\Lambda(1600)$	0.222436	0.32
$\Lambda(1670)$	0.774591	-0.7
$\Lambda(1690)$	0.996956	1.38
$\Lambda(2000)$	0.573457	0.01

Table 64: Decay asymmetry parameters for the amplitude fit with nominal model selecting candidates having  $\tau(\Lambda_c^+) \leq 0.2$  ps. Pulls are computed with respect to nominal fit results using the final statistical uncertainties reported in Table 31.

## 1788 References

- 1789 [1] Particle Data Group, P. A. Zyla *et al.*, *Review of Particle Physics*, PTEP **2020** (2020)  
1790 083C01.
- 1791 [2] E791 collaboration, E. M. Aitala *et al.*, *Multidimensional resonance analysis of*  
1792  $\Lambda_c^+ \rightarrow p K^- \pi^+$ , Phys. Lett. **B471** (2000) 449, [arXiv:hep-ex/9912003](#).
- 1793 [3] D. Marangotto, *Extracting Maximum Information from Polarised Baryon Decays via*  
1794 *Amplitude Analysis: The  $\Lambda_c^+ \rightarrow p K^- \pi^+$  Case*, Adv. High Energy Phys. **2020** (2020)  
1795 7463073, [arXiv:2004.12318](#).
- 1796 [4] G. Durieux and Y. Grossman, *Probing CP violation systematically in differential*  
1797 *distributions*, Phys. Rev. **D92** (2015) 076013, [arXiv:1508.03054](#).
- 1798 [5] B. Konig, J. G. Korner, M. Kramer, and P. Kroll, *Infinite momentum frame calcula-*  
1799 *tion of semileptonic heavy Lambda(b) —> Lambda(c) transitions including HQET*  
1800 *improvements*, Phys. Rev. D **56** (1997) 4282, [arXiv:hep-ph/9701212](#).
- 1801 [6] M. Pervin, W. Roberts, and S. Capstick, *Semileptonic decays of heavy lambda baryons*  
1802 *in a quark model*, Phys. Rev. C **72** (2005) 035201, [arXiv:nucl-th/0503030](#).
- 1803 [7] T. Gutsche *et al.*, *Semileptonic decay  $\Lambda_b \rightarrow \Lambda_c + \tau^- + \bar{\nu}_\tau$  in the covariant confined quark*  
1804 *model*, Phys. Rev. D **91** (2015) 074001, [arXiv:1502.04864](#), [Erratum: Phys. Rev. D  
1805 91, 119907 (2015)].
- 1806 [8] S. Shivashankara, W. Wu, and A. Datta,  $\Lambda_b \rightarrow \Lambda_c \tau \bar{\nu}_\tau$  *Decay in the Standard Model*  
1807 *and with New Physics*, Phys. Rev. **D91** (2015) 115003, [arXiv:1502.07230](#).
- 1808 [9] R. Dutta,  $\Lambda_b \rightarrow (\Lambda_c, p) \tau \nu$  *decays within standard model and beyond*, Phys. Rev.  
1809 **D93** (2016) 054003, [arXiv:1512.04034](#).
- 1810 [10] R. N. Faustov and V. O. Galkin, *Semileptonic decays of  $\Lambda_b$  baryons in the relativistic*  
1811 *quark model*, Phys. Rev. D **94** (2016) 073008, [arXiv:1609.00199](#).
- 1812 [11] X.-Q. Li, Y.-D. Yang, and X. Zhang,  $\Lambda_b \rightarrow \Lambda_c \tau \bar{\nu}_\tau$  *decay in scalar and vector leptoquark*  
1813 *scenarios*, JHEP **02** (2017) 068, [arXiv:1611.01635](#).
- 1814 [12] A. Celis, M. Jung, X.-Q. Li, and A. Pich, *Scalar contributions to  $b \rightarrow c(u) \tau \nu$*   
1815 *transitions*, Phys. Lett. B **771** (2017) 168, [arXiv:1612.07757](#).
- 1816 [13] A. Datta, S. Kamali, S. Meinel, and A. Rashed, *Phenomenology of  $\Lambda_b \rightarrow \Lambda_c \tau \bar{\nu}_\tau$  using*  
1817 *lattice QCD calculations*, JHEP **08** (2017) 131, [arXiv:1702.02243](#).
- 1818 [14] J. Zhu *et al.*, *Probing the R-parity violating supersymmetric effects in  $B_c \rightarrow$*   
1819  *$J/\psi \ell^- \bar{\nu}_\ell, \eta_c \ell^- \bar{\nu}_\ell$  and  $\Lambda_b \rightarrow \Lambda_c \ell^- \bar{\nu}_\ell$  decays*, Nucl. Phys. B **934** (2018) 380,  
1820 [arXiv:1801.00917](#).
- 1821 [15] E. Di Salvo, F. Fontanelli, and Z. J. Ajaltouni, *Detailed Study of the Decay  $\Lambda_b \rightarrow$*   
1822  *$\Lambda_c \tau \bar{\nu}_\tau$* , Int. J. Mod. Phys. **A33** (2018) 1850169, [arXiv:1804.05592](#).

- [16] A. Ray, S. Sahoo, and R. Mohanta, *Probing new physics in semileptonic  $\Lambda_b$  decays*, Phys. Rev. **D99** (2019) 015015, [arXiv:1812.08314](#).
- [17] F. U. Bernlochner, Z. Ligeti, D. J. Robinson, and W. L. Sutcliffe, *Precise predictions for  $\Lambda_b \rightarrow \Lambda_c$  semileptonic decays*, Phys. Rev. D **99** (2019) 055008, [arXiv:1812.07593](#).
- [18] P. Böer, A. Kokulu, J.-N. Toelstede, and D. van Dyk, *Angular Analysis of  $\Lambda_b \rightarrow \Lambda_c(\rightarrow \Lambda\pi)\ell\bar{\nu}_\ell$* , [arXiv:1907.12554](#).
- [19] N. Penalva, E. Hernández, and J. Nieves, *Further tests of lepton flavour universality from the charged lepton energy distribution in  $b \rightarrow c$  semileptonic decays: The case of  $\Lambda_b \rightarrow \Lambda_c\ell\bar{\nu}_\ell$* , [arXiv:1908.02328](#).
- [20] Q.-Y. Hu, X.-Q. Li, Y.-D. Yang, and D.-H. Zheng, *The measurable angular distribution of  $\Lambda_b^0 \rightarrow \Lambda_c^+(\rightarrow \Lambda^0\pi^+)\tau^- (\rightarrow \pi^- v_\tau)\bar{v}_\tau$  decay*, JHEP **02** (2021) 183, [arXiv:2011.05912](#).
- [21] D. Marangotto, *Angular and CP-Violation Analyses of  $\bar{B} \rightarrow D^{*+}l^-\bar{\nu}_l$  Decays at Hadron Collider Experiments*, Adv. High Energy Phys. **2019** (2019) 5274609, [arXiv:1812.08144](#).
- [22] D. Hill, M. John, W. Ke, and A. Poluektov, *Model-independent method for measuring the angular coefficients of  $B^0 \rightarrow D^{*-}\tau^+\nu_\tau$  decays*, [arXiv:1908.04643](#).
- [23] M. Ferrillo, A. Mathad, P. Owen, and N. Serra, *Probing effects of new physics in  $\Lambda_b^0 \rightarrow \Lambda_c^+\mu^-\bar{\nu}_\mu$  decays*, [arXiv:1909.04608](#).
- [24] T. Mannel and G. A. Schuler, *Semileptonic decays of bottom baryons at LEP*, Phys. Lett. **B279** (1992) 194.
- [25] A. F. Falk and M. E. Peskin, *Production, decay, and polarization of excited heavy hadrons*, Phys. Rev. **D49** (1994) 3320, [arXiv:hep-ph/9308241](#).
- [26] M. Galanti *et al.*, *Heavy baryons as polarimeters at colliders*, JHEP **11** (2015) 067, [arXiv:1505.02771](#).
- [27] B. Konig, J. G. Korner, and M. Kramer, *On the determination of the  $b \rightarrow c$  handedness using nonleptonic lambda( $c$ ) decays*, Phys. Rev. D **49** (1994) 2363, [arXiv:hep-ph/9310263](#).
- [28] X.-L. Mu, Y. Li, Z.-T. Zou, and B. Zhu, *Investigation of effects of new physics in  $\Lambda_b \rightarrow \Lambda_c\tau\bar{\nu}_\tau$  decay*, Phys. Rev. D **100** (2019) 113004, [arXiv:1909.10769](#).
- [29] G. R. Goldstein, *Polarization of inclusively produced  $\Lambda_c^+$  in a QCD based hybrid model*, [arXiv:hep-ph/9907573](#).
- [30] G. R. Goldstein and S. Liuti, *Angular Momentum and Polarization in Hadron Collisions up to LHC Energies*, Int. J. Mod. Phys. Conf. Ser. **37** (2015) 1560038.
- [31] F. J. Botella *et al.*, *On the search for the electric dipole moment of strange and charm baryons at LHC*, Eur. Phys. J. **C77** (2017) 181, [arXiv:1612.06769](#).

- 1859 [32] E. Bagli *et al.*, *Electromagnetic dipole moments of charged baryons with bent crystals*  
 1860 *at the LHC*, Eur. Phys. J. **C77** (2017) 828, arXiv:1708.08483.
- 1861 [33] W. D. Hulsbergen, *Decay chain fitting with a Kalman filter*, Nucl. Instrum. Meth.  
 1862 **A552** (2005) 566, arXiv:physics/0503191.
- 1863 [34] D. Müller, M. Clemencic, G. Corti, and M. Gersabeck, *ReDecay: A novel approach to*  
 1864 *speed up the simulation at LHCb*, Eur. Phys. J. **C78** (2018) 1009, arXiv:1810.10362.
- 1865 [35] M. Pivk and F. R. Le Diberder, *sPlot: A statistical tool to unfold data distributions*,  
 1866 Nucl. Instrum. Meth. **A555** (2005) 356, arXiv:physics/0402083.
- 1867 [36] M. Jacob and G. C. Wick, *On the general theory of collisions for particles with spin*,  
 1868 Annals of Physics **7** (1959) 404 .
- 1869 [37] D. Marangotto, *Helicity Amplitudes for Generic Multibody Particle Decays Fea-*  
 1870 *turing Multiple Decay Chains*, Adv. High Energy Phys. **2020** (2020) 7463073,  
 1871 arXiv:1911.10025.
- 1872 [38] E. Leader, *Spin in particle physics*, vol. 15, Camb. Monogr. Part. Phys. Nucl. Phys.  
 1873 Cosmol., 2011.
- 1874 [39] S. Dambach, U. Langenegger, and A. Starodumov, *Neutrino reconstruction with topo-*  
 1875 *logical information*, Nucl. Instrum. Meth. **A569** (2006) 824, arXiv:hep-ph/0607294.
- 1876 [40] LHCb collaboration, R. Aaij *et al.*, *Measurement of the ratio of branching frac-*  
 1877 *tions  $\mathcal{B}(\bar{B}^0 \rightarrow D^{*+}\tau^-\bar{\nu}_\tau)/\mathcal{B}(\bar{B}^0 \rightarrow D^{*+}\mu^-\bar{\nu}_\mu)$* , Phys. Rev. Lett. **115** (2015) 111803,  
 1878 Publisher's Note ibid. **115** (2015) 159901, arXiv:1506.08614.
- 1879 [41] M. S. Sozzi, *Discrete symmetries and CP violation: from experiment to theory*, Oxford  
 1880 Graduate Texts, Oxford Univ. Press, New York, NY, 2008.
- 1881 [42] JPAC collaboration, M. Mikhasevko *et al.*, *Dalitz-plot decomposition for three-body*  
 1882 *decays*, Phys. Rev. D **101** (2020) 034033, arXiv:1910.04566.
- 1883 [43] E. Gourgoulhon, *Special Relativity in General Frames*, Springer, 2013; *Wigner rotation*  
 1884 — *Wikipedia, the free encyclopedia*, [Online; accessed 04-Apr-2020].
- 1885 [44] Belle collaboration, R. Mizuk *et al.*, *Observation of two resonance-like structures in*  
 1886 *the  $\pi^+\chi_{c1}$  mass distribution in exclusive  $\bar{B}^0 \rightarrow K^-\pi^+\chi_{c1}$  decays*, Phys. Rev. D **78**  
 1887 (2008) 072004, arXiv:0806.4098.
- 1888 [45] LHCb collaboration, R. Aaij *et al.*, *Observation of  $J/\psi p$  resonances consistent with*  
 1889 *pentaquark states in  $\Lambda_b^0 \rightarrow J/\psi p K^-$  decays*, Phys. Rev. Lett. **115** (2015) 072001,  
 1890 arXiv:1507.03414.
- 1891 [46] D. Marangotto, *Amplitude analysis and polarisation measurement of the  $\Lambda_c^+$  baryon*  
 1892 *in  $pK^-\pi^+$  final state for electromagnetic dipole moment experiment*, PhD thesis,  
 1893 Università degli studi di Milano, Presented 16 Mar 2020, <https://cds.cern.ch/record/2713231>.

- 1895 [47] LHCb-ANA-2017-064, *Search for CP violation through an amplitude analysis of*  
 1896  $D^0 \rightarrow K^+ K^- \pi^+ \pi^-$  *decays*, .
- 1897 [48] *TensorFlowAnalysis: A collection of useful functions and example scripts for per-*  
 1898 *forming amplitude fits using TensorFlow*, [https://gitlab.cern.ch/poluekt/](https://gitlab.cern.ch/poluekt/TensorFlowAnalysis)  
 1899 *TensorFlowAnalysis*.
- 1900 [49] M. Abadi *et al.*, *TensorFlow: Large-scale machine learning on heterogeneous systems*,  
 1901 2015. <https://www.tensorflow.org>.
- 1902 [50] M. Davier, L. Duflot, F. Le Diberder, and A. Rouge, *The Optimal method for the*  
 1903 *measurement of tau polarization*, Phys. Lett. **B306** (1993) 411.
- 1904 [51] S. Aiola *et al.*, *Progress towards the first measurement of charm baryon dipole*  
 1905 *moments*, Phys. Rev. D. **103** (2020) 072003, [arXiv:2010.11902](https://arxiv.org/abs/2010.11902).
- 1906 [52] LHCb-ANA-2013-053, *Evidence for the resonant character of the  $Z(4430)^- \rightarrow$*   
 1907  $\psi(2S)\pi^-$  *mass peak observed in  $B^0 \rightarrow \psi(2S)K^+\pi^-$  decays, and determination of the*  
 1908  *$Z(4430)^-$  spin-parity*, .
- 1909 [53] J. M. Blatt and V. F. Weisskopf, *Theoretical nuclear physics*, Springer, New York,  
 1910 1952.
- 1911 [54] F. Von Hippel and C. Quigg, *Centrifugal-barrier effects in resonance partial decay*  
 1912 *widths, shapes, and production amplitudes*, Phys. Rev. **D5** (1972) 624.
- 1913 [55] LHCb collaboration, R. Aaij *et al.*, *Study of the  $D^0 p$  amplitude in  $A_b^0 \rightarrow D^0 p \pi^-$*   
 1914 *decays*, JHEP **05** (2017) 030, [arXiv:1701.07873](https://arxiv.org/abs/1701.07873).
- 1915 [56] D. V. Bugg, *The Kappa in E791 data for  $D \rightarrow K \pi \pi$* , Phys. Lett. B **632** (2006)  
 1916 471, [arXiv:hep-ex/0510019](https://arxiv.org/abs/hep-ex/0510019).
- 1917 [57] D. Aston *et al.*, *A Study of  $K^- \pi^+$  Scattering in the Reaction  $K^- p \rightarrow K^- \pi^+ n$  at*  
 1918 *11-GeV/c*, Nucl. Phys. **B296** (1988) 493.
- 1919 [58] S. M. Flatte, *Coupled - Channel Analysis of the pi eta and K anti-K Systems Near K*  
 1920 *anti-K Threshold*, Phys. Lett. **63B** (1976) 224.
- 1921 [59] H. Zhang, J. Tulpan, M. Shrestha, and D. M. Manley, *Multichannel parametrization*  
 1922 *of  $\bar{K}N$  scattering amplitudes and extraction of resonance parameters*, Phys. Rev. C  
 1923 **88** (2013) 035205, [arXiv:1305.4575](https://arxiv.org/abs/1305.4575).
- 1924 [60] Rutherford-London, W. Cameron *et al.*, *Partial Wave Analysis of  $\bar{K}N \rightarrow \bar{K}^* N$*   
 1925 *Between 1830-{MeV} and 2170-{MeV} Center-of-mass Energy Including New Data*  
 1926 *Below 1960-{MeV}*, Nucl. Phys. B **146** (1978) 327.
- 1927 [61] J. D. Richman, *An experimenter's guide to the helicity formalism*, CALT-68-1148.